UNIVERSITY OF OKLAHOMA

GRADUATE COLLEGE

STIMULI-RESPONSIVE POROUS MEMBRANES FROM LYOTROPIC LIQUID CRYSTAL TEMPLATING

A DISSERTATION

SUBMITTED TO THE GRADUATE FACULTY

in partial fulfillment of the requirements for the

Degree of

DOCTOR OF PHILOSOPHY

By

YOUNES SAADATGHAREHBAGH
Norman, Oklahoma
2023

STIMULI-RESPONSIVE POROUS MEMBRANES FROM LYOTROPIC LIQUID CRYSTAL TEMPLATING

A DISSERTATION APPROVED FOR THE SCHOOL OF SUSTAINABLE CHEMICAL, BIOLOGICAL AND MATERIALS ENGINEERING

BY THE COMMITTEE CONSISTING OF

Dr. Reza Foudazi, Chair

Dr. Brian P. Grady

Dr. Michele Galizia

Dr. Hamidreza Shabgard

Acknowledgment

I would like to express my thanks to all the individuals who assisted me in successfully completing my Ph.D. thesis.

First, I am highly grateful for the continuous guidance and support I received from my advisor, Dr. Reza Foudazi. Not only he provided me technical assistance, but he also created a conducive and peaceful environment that enabled me to fulfill my research goals. I am also indebted to him for his invaluable support to secure my current job opportunity.

I extend my heartfelt thanks to my dissertation committee- Dr. Brian P. Grady, Dr. Michele Galizia, and Dr. Hamidreza Shabgard. I sincerely appreciate the time you invested and the support you provided. In particular, I would like to extend my gratitude to Dr. Grady and Dr. Galizia for generously allowing me access to their laboratory equipment whenever it was needed.

I am truly thankful of all the group membranes in SMaRT lab at both New Mexico State University (NMSU) and OU who played an important role in enhancing my technical and personal experiences.

I would also like to extend my humble regards to the School of Sustainable Chemical, Biological and Materials Engineering (SCBME) for their unwavering financial support, which enabled me to concentrate on my research without any financial concerns. In addition, I would like to thank the support by the National Science Foundation (NSF) under grant no. 2212894 (1840871).

Last but not least, there are no words to show my gratitude towards my wife, Samira, for her patience, understanding, selfless sacrifices, and mental support throughout these years. Thank you very much for everything.

Abstract

Lyotropic liquid crystal (LLC) templating is an efficient approach to synthesize nanostructured polymers with a wide range of applications, particularly in molecular separation. LLCs offer diverse nanostructures, but we focus on the lamellar and normal hexagonal phases due to their ability to facilitate continuous transport paths in two and three dimensions, respectively. This feature is particularly advantageous for membrane applications. The normal hexagonal phase is especially desirable as it eliminates the need for structural alignment. This dissertation presents a comprehensive investigation of transcriptive and synergistic LLC templating approaches for synthesizing stimuli-responsive membranes. These membranes can alter their separation performance in response to external stimuli such as temperature and pH.

When it comes to transcriptive LLC templating, the preservation of the LLC structure after polymerization is highly dependent on polymerization kinetics. Therefore, this dissertation examines the initiator-dependent thermal polymerization kinetics in LLC templates. The results indicate that both water-soluble and oil-soluble initiators effectively preserve the structure after the reaction. However, the use of a water-soluble initiator not only results in higher polymerization rates but also enhances the mechanical properties of the synthesized polymer. Transcriptive templating enables the production of two-step thermoresponsive ultrafiltration (UF) membranes by employing the water-soluble initiator. Thermoresponsive Pluronic F127 (F127) block copolymer is utilized to initiate the thermal response in this study. The formation of an LLC with lamellar structure is achieved by combining the F127 block copolymer with water and hydrophobic monomers. Subsequently, polymerization leads to the creation of a cross-linked network that effectively immobilizes the F127 molecules. The resulting membrane exhibits adjustable pore sizes, ranging from 34.6 nm to 45.7 nm and 59.6 nm, as the temperature is increased from 25 °C

to 35 °C and 50 °C, respectively. Consequently, the membrane permeability is enhanced and molecular weight cutoff (MWCO) can be controlled. The observed two-step thermal response is attributed to the lower critical solution temperature (LCST) of F127 at 35 °C and the melting of the crystalline structure of its PEO bock at 50 °C. The results show that conducting membrane cleaning procedures at higher temperatures can enhance cleaning efficiency and prolong the lifespan of the membrane. This approach takes advantage of the temperature-dependent changes in porosity.

Synergistic LLC templating is employed using in-lab-synthesized polymerizable Pluronic P84 surfactant to produce H_1-structured thermoresponsive ultrafiltration (UF) and nanofiltration (NF) membranes. Our research findings reveal that the synthesized membrane exhibits remarkable adaptability, as evidenced by its ability to modulate thickness-normalized flux from 28 to 68 liters m^{-2} $hour^{-1}$ μm and pore size from 2.5 to 3.2 nm when the temperature is raised from 25 to 45 °C, respectively. Moreover, the membrane demonstrates exceptional resistance to fouling, as its permeability remains largely unaffected even after 60 h of filtering charged and uncharged solutes. This outstanding antifouling behavior is attributed to the highly hydrophilic surface of the membrane. The addition of acrylic acid (AAc) to the LLC formulation allows for the incorporation of additional functionality into this membrane. The resulting membrane exhibits the capability to effectively separate dissolved salts containing trivalent and divalent anion from water. Furthermore, it demonstrates both pH-responsive and thermoresponsive behaviors. By increasing the temperature from 25 to 45 °C, the membrane has the capability to alter its pore size from 2.2 to 2.6 nm, along with adjusting its thickness-normalized flux from 16 to 31 liters m^{-2} $hour^{-1}$ μm, respectively. The membrane effectively removes salts containing trivalent and divalent anion under neutral and alkaline pH conditions, with the option to turn off its ion rejection capability by

reducing the feed pH to 4. Additionally, the membrane displays remarkable selectivity for sulfate ions over chloride ions, making it an ideal choice for salt fractionation applications. Our work on synergistic LLC templating has not only expanded the range of achievable membrane pore sizes through this approach but also successfully produced stimuli-responsive H_1-structured polyLLC membranes, which is a unique accomplishment.

Keywords: Stimuli-responsive membranes, Self-assembly, Lyotropic liquid crystals, Mesophase templating, Fouling resistant, Nanofiltration, Ultrafiltration, Polymerization kinetics

Table of Contents

Abstract v
Table of Contents viii
List of Figures xiv
List of Tables xxi
CHAPTER 1: INTRODUCTION 1
1.1 Self-assembled surfactant phases 1
1.2 Characteristics of LLC structures 16
1.2.1 Hexagonal (H_α) 16
1.2.2 Lamellar (L_α) 19
1.2.3 Bicontinuous cubic (Q_α) 21
1.2.4 Discontinuous cubic (I_α) 22
1.2.5 Other LLC structures 23
1.3 Synergistic LLC templating 26
1.3.1 Hexagonal (H_α) 27
1.3.2 Lamellar (L_α) 28
1.3.3 Bicontinuous cubic (Q_α) 29
1.3.4 Discontinuous cubic (I_α) 31
1.4 Transcriptive LLC templating 37
1.4.1 Hexagonal (H_α) 38
1.4.2 Lamellar (L_α) 40
1.4.3 Bicontinuous cubic (Q_α) 41
1.4.4 Discontinuous cubic (I_α) 41
1.5 Kinetics of polymerization in LLC templates 48

1.5.1 Synergistic LLC templating 48
1.5.2 Transcriptive LLC templating 49
1.6 Synergistic versus transcriptive LLC templating: a summary 52
1.7 Advanced functional materials: opportunities, challenges, and outlook 53
1.8 Overview of thesis research: goal and objectives 64
CHAPTER 2: INITIATOR-DEPENDENT KINETICS OF LYOTROPIC LIQUID CRYSTAL-TEMPLATED THERMAL POLYMERIZATION 69
2.1 Introduction 69
2.2 Experimental 71
2.2.1 Materials 71
2.2.2 Preparation of mesophase samples 71
2.2.3 Structural characterization 71
2.2.4 Polymerization kinetics 72
2.2.5 Chemorheology and mechanical properties 73
2.3 Results and discussion 75
2.3.1 Cross-polarized light microscopy (CPLM) 75
2.3.2 Small angle X-ray scattering (SAXS) 75
2.3.3 Thermal polymerization kinetics 79
2.3.4 Chemorheology and mechanical properties 94
2.4 Conclusion 100
CHAPTER 3: TWO-STEP THERMORESPONSIVE ULTRAFILTRATION MEMBRANE FROM POLYMERIZATION OF LYOTROPIC LIQUID CRYSTALS 101
3.1 Introduction 101
3.2 Experimental 104

3.2.1 Materials 104
3.2.2 Preparation of LLC 104
3.2.3 Characterization of LLC and polyLLC 104
3.2.3.1 Cross-polarized light microscopy (CPLM) 104
3.2.3.2 Small angle X-ray scattering (SAXS) 105
3.2.3.3 Atomic force microscopy (AFM) 105
3.2.3.4 Differential scanning calorimetry (DSC) 105
3.2.4 Preparation of the polyLLC membrane 106
3.2.5 Characterization of the polyLLC membrane 106
3.2.5.1 Hydration capacity 106
3.2.5.2 Water flux and permeability 106
3.2.5.3 Evaluation of fouling resistance and cleaning efficiency 108
3.2.5.4 Molecular weight cut-off measurements 108
3.3 Results and discussions 109
3.3.1 Characterization of LLC and polyLLC 109
3.3.2 Characterization of membranes 113
3.3.2.1 Hydration capacity 114
3.3.2.2 Water flux and permeability 115
3.3.2.3 Fouling resistance and cleaning efficiency 117
3.3.2.4 Molecular weight cut-off 119
3.3.3 Thermoresponsiveness mechanism of polyLLC membrane 122
3.4 Conclusion 126
CHAPTER 4: THERMORESPONSIVE ANTIFOULING ULTRAFILTRATION MEMBRANES FROM MESOPHASE TEMPLATING 128
4.1 Introduction 128
4.2 Experimental 130

4.2.1 Materials 130
4.2.2 Synthesis of P84DA 131
4.2.3 Mesophase preparation 132
4.2.4 Characterization of LLC and polyLLC 132
4.2.4.1 Cross-polarized light microscopy (CPLM) 132
4.2.4.2 Small angle X-ray scattering (SAXS) 133
4.2.4.3 Differential scanning calorimetry (DSC) 133
4.2.4.4 Swelling behavior of the polyLLC 133
4.2.4.5 Rheo-mechanical studies 134
4.2.5 Preparation of the polyLLC membrane 135
4.2.6 Characterization of the polyLLC membrane 136
4.2.6.1 Water flux and permeability 136
4.2.6.2 MWCO, protein and dyes rejection measurements 136
4.2.6.3 Contact angle and fouling resistance 137
4.3 Results and discussions 137
4.3.1 Characterization of LLC and polyLLC 137
4.3.2 Characterization of membranes 149
4.3.2.1 Water flux and permeability 150
4.3.2.2 Rejection characteristics 150
4.3.2.3 Contact angle and fouling resistance 155
4.3.3 Mechanism of thermal response 157
4.4 Conclusion 157
CHAPTER 5: THERMO- and pH-RESPONSIVE ANTIFOULING NANOFILTRATION MEMBRANES FROM LYOTROPIC LIQUID CRYSTAL TEMPLATING 160
5.1 Introduction 160
5.2 Experimental 162

5.2.1 Materials 162
5.2.2 Synthesis of P84DA 163
5.2.3 LLC preparation 163
5.2.4 LLC and polyLLC characterization 163
5.2.4.1 Cross-polarized light microscopy (CPLM) 163
5.2.4.2 Small angle X-ray scattering (SAXS) 164
5.2.4.3 Differential scanning calorimetry (DSC) 164
5.2.4.4 Swelling characteristics of the polyLLC 165
5.2.5 Manufacturing of the supported polyLLC membrane 166
5.2.6 Analysis of the polyLLC membrane performance 166
5.2.6.1 Water flux and permeability 166
5.2.6.2 MWCO, protein, single salt and dye rejection measurements 167
5.2.6.3 Contact angle and fouling resistance 168
5.3 Results and discussions 168
5.3.1 Characterization of LLC and polyLLC 168
5.3.2 Analysis of the polyLLC membrane performance 176
5.3.2.1 Water flux and permeability 177
5.3.2.2 MWCO, protein, single salt, and dye rejection measurements 177
5.3.2.3 Contact angle and fouling resistance 185
5.3.2.4 Mechanisms of thermal and pH response 186
5.4 Conclusion 188
CHAPTER 6: CONCLUSIONS AND FUTURE WORKS 189
6.1 Summary 189
6.2 Future work 194
6.2.1 Mesophases with domain sizes beyond-20 nm 194

6.2.2 Membranes with less than 1 µm active layer thickness 194
6.2.3 Synthesizing positively charged NF membranes 195
6.2.4 PolyLLCs for heavy metal ions removal from wastewater 196
References 198
APPENDIX A 242
NOMENCLATURE AND ACRONYMS 242
APPENDIX B 250
SUPPORTING INFORMATION FOR CHAPTER 1 250
APPENDIX C 254
SUPPORTING INFORMATION FOR CHAPTER 2 254
APPENDIX D 260
SUPPORTING INFORMATION FOR CHAPTER 3 260
APPENDIX E 263
SUPPORTING INFORMATION FOR CHAPTER 4 263
APPENDIX F 268
SUPPORTING INFORMATION FOR CHAPTER 5 268
APPENDIX G 272
MEASUREMENTS UNCERTAINTY CACLULATIONS 272

List of Figures

Figure 1-1. (a) The schematic representation of CPP and its corresponding favorable structure. (b) Schematic diagram of common LLC structures.[9,17–19] Addition/removal of solvents, such as decreasing water content can drive the phase transition. 4

Figure 1-2. (a) Typical CPLM Textures for LLC Mesophases – Representative micrographs for various LLC mesophases when samples are observed in a light microscope with a 90º difference in the Polarizer (P) and Analyzer (A) directions. Birefringent 'fan-like' and 'oily-streak' textures are observed for the normal cylinder (H_1) and lamellar sheet L_α) mesophases. No birefringence is observed for any of the cubic phases i.e. *Im3m*, *Pn3m*, *Ia3d*, *BCC*, and *FCC*. (b) Typical 1D SAXS profiles and corresponding assigned diffraction planes observed for L_α,[20] H_α,[20] I_α (*FCC*[21] and *BCC*[21]), Q_α (*Im3m*,[20], *Pn3m*,[22] and *Ia3d*[23]) and Frank-Kasper phases (A15,[24] σ,[24] C14 Laves,[22] and C15 Laves[22]). (c) Representative example of results acquired from XRD for an L_α LLCs.[25] 5

Figure 1-3. Schematic illustration of typical synergistic, transcriptive, and reconstructive LLC templating using H_2 structure. The reconstructive templating may lead to various structures and the lamellar structure shown here is just one example of the phase transition possible in this method. 7

Figure 1-4. Chemical structure of (a and b) polymerizable ionic, (c) polymerizable non-ionic and (d) non-polymerizable amphiphiles used for LLC templating. 11

Figure 1-5. Chemical structure of (a) (co)monomers and (b) cross-linkers used for LLC templating. 14

Figure 1-6. Chemical structure of the polymerization initiators used for LLC templating: (a) photoinitiators and (b) other (i.e. thermal and ionic) commonly used initiator.....15

Figure 1-7. Typical schematic of H_2 structure with *d*-spacing (*d*), lattice parameter (*a*), radius of micelle (R_m), radius of confined phase in micelle (R_c), intermicellar distance (D_m), and radius of the biggest circle trapped between the micelles ($R_{h,max}$). In this case, ϕ is the volume fraction of the polar phase. In the case of H_1 structure, ϕ is the volume fraction of the apolar phase. 18

Figure 1-8. Typical schematic of L_α structure showing lattice parameter *d*, δ_1 is the thickness of the apolar domain, δ_2 is the thickness of the polar domain, D_1 is the intermicellar distance in apolar

phase, D_2 is the intermicellar distance in polar domain, and $R_{1,max}$ and $R_{2,max}$ are the radii of the biggest circles trapped between the micelles in apolar and polar domains, respectively. 21

Figure 1-9. Typical schematic of (a) normal and (b) reverse primitive Q_α structure with lattice parameter (a) and the thickness of the polar ($2t_{polar}$) and apolar domains ($2l$). 22

Figure 1-10. Typical schematic of inverse *BCC* discontinuous cubic structure with lattice parameter (a), radius of spherical micelles (R_c), polar domain size (α_1) and apolar domain size (α_2). 23

Figure 1-11. Typical schematics of different F-K phases observed for LLCs including A15, C14 and C15 Laves, and σ phases. 25

Figure 1-12. The relative effect of (a) polymerizable group placement on the reactive amphiphile and (b) the lipophilic chain length on the polymerization rate in synergistic templating. Different structures are obtained with an increase in the length of lipophilic chain, resulting in lower reaction rate. Higher proximity of the reactive groups enables higher reaction rates.[27] 51

Figure 1-13. The relative effect of monomer and initiator polarity on the polymerization rate in transcriptive templating.[27] 53

Figure 1-14. Potential applications of LLC templated products.....57

Figure 1-15. The Pluronic block copolymer chart displaying different types of the copolymer based on the PPO molecular weight and the weight percentage of PEO.[142].....65

Figure 1-16. Ternary phase diagram of (a) Pluronic L64,[207] (b) Pluronic P84[212] and (c) Pluronic F127[209] in the presence of water and p-xylene. The concentrations are in wt%. 66

Figure 2-1. (a) Monomers and reaction scheme of their polymerization process in this study; (b-e) Chemical structures of initiators and surfactant: (b) APS, (c) BPO, (d) AIBN, and (e) Pluronic L64; (f) Schematic of polymerization process in lamellar and hexagonal structures. 74

Figure 2-2. CPLM images of LLCs with lamellar and hexagonal structures before and after thermal polymerization by IFW and IFO systems. Scale bar: 50μm. 76

Figure 2-3. 1D SAXS data for (a) lamellar and (b) hexagonal phases before and after polymerization with different initiators. The plots are vertically shifted for clarity. 77

Figure 2-4. Normalized polymerization rate versus time and overall monomer conversion obtained from thermal polymerization in hexagonal and lamellar structures using different initiation systems: (a) APS, (b) BPO, (c) AIBN, (d) APS+AIBN and (e) APS+BPO. For all samples, the total initiator concentration of 5 mol% was used with respect to the total monomer content. 80

Figure 2-5. Normalized polymerization rate versus time and overall monomer conversion obtained from thermal polymerization in (a-c) lamellar and (d-f) hexagonal structures using different initiation systems having varied initiator contents. Arrows denote the time points that show the evidence of reduced termination rate (see main text). 89

Figure 2-6. Normalized polymerization rate versus time and overall monomer conversion obtained from thermal polymerization in (a-c) lamellar and (d-f) hexagonal structures using different initiation systems at varied reaction temperatures. For all samples, the total initiator concentration of 5 mol% was used with respect to the total monomer content. 92

Figure 2-7. Evolution of dynamic moduli during LLC templating with (a-c) lamellar and (d-f) hexagonal structures using different initiation systems. 97

Figure 2-8. Frequency sweep curves of the samples obtained from polymerization in (a) lamellar and (b) hexagonal LLC structures using different initiation systems. 97

Figure 2-9. (a, b) Evolution of dynamic moduli during LLC templating and (c, d) frequency sweep curves of polymerized LLCs using different initiator contents. 99

Figure 2-10. Schematic diagram of the polymerization mechanism in IFW and IFO systems and the consequent difference in the robustness of the polymerized LLCs. 99

Figure 3-1. CPLM images of LLCs with lamellar structure: (a) before and (b) after thermal polymerization (scale bar: 50 μm). (c) 1D SAXS data for LLCs before and after reaction (the plots are vertically shifted for clarity). (d and e) AFM micrograph of the cross section of dried polyLLC in a $5\ \mu m \times 5 \mu m$ area; higher magnification is shown in (f). 112

Figure 3-2. DSC measurement results for poly(nBA-co-EGDMA), F127, and polyLLC. 113

Figure 3-3. Changes in hydration capacity for PAN and polyLLC membranes based on the temperature variation. 114

Figure 3-4. Changes in (a) water flux and (b) permeability for PAN and polyLLC membranes based on the temperature variation. 116

Figure 3-5. Reversibility of the water permeability of the polyLLC membrane under several heating-cooling cycles. 116

Figure 3-6. Change of (a) water flux, (b) normalized water flux, (c) irreversible fouling, and (d) reversible fouling for polyLLC and PAN membranes throughout fouling-cleaning experiment using different cleaning temperatures. The presented temperatures are cleaning temperature and filtrations steps were carried out at 25 °C. 118

Figure 3-7. Temperature-dependent MWCO of polyLLC membrane. 120

Figure 3-8. Temperature-dependent chain size for PEO having different molecular weights. ...122

Figure 3-9. Results of DSC measurement for (a) polyLLCs containing different cross-linker contents and (b) wet and dried polyLLC containing 20 wt% cross-linker with respect to nBA content. 124

Figure 3-10. Formation and thermoresponsiveness mechanism of polyLLC membrane. 126

Figure 4-1. Molecular structure of (a) P84DA, (b) HDDA, (c) [BMIM][BF4] and (d) HCPK. Schematic representation of P84DA and HDDA have also been presented in panel a and b, respectively. (e) Schematic illustration of H1-structured mesophase which is obtained through mixing the components. The micelles are surrounded by [BMIM][BF4]. The apolar domain is made of PPO block and HDDA. Chemically-bonded polymer network is created through the reaction of acrylate groups of P84DA and HDDA. The presence of intermicellar bridges, which form via the reaction of acrylate groups of extended PEO blocks, seems necessary to have an integrated H1-structured membrane.[31] (f) Schematic procedure for preparation of polyLLC membrane. 139

Figure 4-2. (a-c) CPLM images of samples: (a) before reaction, (b) after reaction, and (c) after swelling with water. (d) 1D SAXS scattering profile for samples (the plots are vertically shifted for clarity). 140

Figure 4-3. Schematic representation of structural parameters for H_1 structure. 142

Figure 4-4. DSC results for pure P84DA, water-swollen polyLLC, and dried polyLLC. 145

Figure 4-5. (a-b) PolyLLC sample (a) before and (b) after swelling with water. (c-f) Results of different experiments: (c) swelling capacity changes with temperature; (d) kinetics of thermal response when the temperature changes from 25 to 45 °C; (e) reversibility of the thermoresponsiveness; and (f) viscoelastic behavior of polyLLC film under different conditions. 147

Figure 4-6. (a-f) CPLM images of water-swollen polyLLC at (a) 5, (b) 25, (c) 35, (d) 45, (e) 55, and (f) 65 °C. (g) 1D SAXS scattering profile of the water-swollen polyLLC upon heating and cooling experiment. The experiment starts by heating the sample from 5 to 65 °C and ends by cooling it to 25 °C. The plots are vertically shifted for clarity. 149

Figure 4-7. (a) Circular cut supported polyLLC membrane and (b) typical cross-sectional SEM image of the membrane. (c-d) Variation of (c) thickness-normalized flux and (d) permeability with cyclic change of temperature. (e) MWCO and (f) BSA protein and red dyes rejection at 25 °C, after increasing temperature to 45 °C, and after cooling down back to 25 °C. (g-h) Photos of feed and collected permeates at different temperatures (at 25 °C, after increasing temperature to 45 °C, and after cooling down back to 25 °C) for (g) DR23 and (h) DR80. 153

Figure 4-8. (a) Contact angle of the polyLLC membrane swelled with water at 25 and 45 °C. (b) Ratio of membrane flux at a given time (J) to preliminary flux with DI water (J_0) (filled symbols) and rejection rate of different solutes (open symbols) for the polyLLC membrane. 156

Figure 4-9. Schematic representation of thermoresponsiveness mechanism of the polyLLC membrane. 159

Figure 5-1. Molecular structure of (a) AAc, (b) P84DA, (c) HDDA, (d) [BMIM][BF_4] and (e) HCPK. Schematic illustration of AAc, P84DA and HDDA have also been shown in panel a, b and c, respectively. (f) A schematic depiction of an H_1-structured LLC obtained by blending various components, wherein the micelles are enveloped by a mixture of [BMIM][BF_4] and AAc. Important structural parameters have also been shown in the schematic. The apolar domain consists of PPO block and HDDA. A chemically bound polymer network is formed from reaction of acrylate groups of P84DA, HDDA, and AAc. To achieve a well-integrated H_1-structured membrane, it is crucial to have intermicellar bridges, which are formed from reaction of acrylate groups of extended PEO blocks.[31] 165

Figure 5-2. The images taken using CPLM display the samples in three different stages: (a) their original state (LLC), (b) after undergoing a reaction, and (c) after swelling with water. (d) 1D SAXS profile, in which plots are shifted vertically to enhance comparison. 170

Figure 5-3. The DSC data for pure P84DA, water-swollen polyLLC, and dried polyLLC. 172

Figure 5-4. (a) Variation of polyLLC swelling capacity with temperature (reversibility of the polyLLC thermoresponsiveness is shown as inset). (b) Kinetics of thermal response when the temperature changes from 25 to 45 °C. (c) Changes in swelling capacity with ionic strength at 25 and 45 °C. (d) Variation of the swelling capacity with pH. 175

Figure 5-5. (a-l) CPLM images of water-swollen polyLLC at temperature of (a, e, i) 10, (b, f, j) 25, (c, g, k) 45, and (d, h, l) 65 °C and at pH of (a-d) 9, (e-h) 6, and (i-l) 4. (m) 1D SAXS profile of the water-swollen polyLLC at different temperatures and pH values. To enhance comparison, the plots have been vertically shifted. 176

Figure 5-6. (a) A supported polyLLC membrane with a circular cut and (b) typical cross-sectional SEM image of the membrane. Cyclical changes of (c) thickness-normalized flux and (d) permeability with changes in temperature. (e) MWCO and (f) rejection of BSA, lysozyme, DR23, and DR80 measured at 25 °C, after increasing the temperature to 45 °C, and after cooling back down to 25 °C. 180

Figure 5-7. (a) The results of single salt rejection experiments are presented for different salts and concentrations. The range of rejection observed for different anions is indicated by the shaded areas in the inset. (b) The rejection of different dissolved salts varies with pH. The membrane flux (for K_2SO_4) at different pH values is also presented in the figure. (c) The variation of K_2SO_4 rejection is demonstrated in response to changes in temperature and pH. (d) The pH-dependent rejection rate for different anionic dyes is displayed. Photos of the feed and permeate at different pH values are provided for (e) OG, (f) AR1, and (g) AF. In these photos, the pH value (9, 6, or 4) is indicated by a number and the letter indicates whether it is feed (F) or permeate (P). It should be noted that the color of the feed for AF changes as the pH is altered since this dye is a pH indicator. 184

Figure 5-8. (a) The contact angle of the polyLLC membrane when swelled with water at 25 and 45 °C. (b) The evolution of the ratio of membrane flux at a given time (J) to the initial flux with

DI water (J_0) (represented by filled symbols) and rejection rate of various solutes (represented by open symbols) for the polyLLC membrane. 186

Figure 5-9. Schematic illustration of thermos- and pH-responsiveness mechanism of the polyLLC membrane. 187

Figure 6-1. (a) The average pore size and thickness-normalized flux (at 30 psi) values of the membranes created via synergistic LLC templating using different LLC structures, as reported by Gin et al.,[34,93,118–120] Osuji et al.,[31,125,297] and the present study. (b) Selectivity/permeability trade-off for the synergistic LLC-templated membranes. 1/pore size has been used as the separation factor representing the membrane selectivity. Hagen–Poiseuille equation has been used to estimate the theoretical permeability for membranes having different tortuosity (τ) values (τ=1 for an ideal membrane with straight capillary tube pores across the membrane and τ=1.5-2.5 as the typical tortuosity range reported for different membranes[296]). Notably, the membranes produced in the current research exhibit the ability to alter their pore size and thus selectivity/permeability in response to temperature change from 25 to 45 °C. The red and blue arrows depicted in the figure denote the heating and cooling cycles, respectively. The membrane having 2.2 nm at 25 °C shows pH-responsiveness in addition to thermoresponsiveness, changing its selectivity towards ionic species with a change in pH. 193

List of Tables

Table 1-1. Characteristics of LLC structures used is LLC templating. 17

Table 1-2. Summary of the reported results for synergistic LLC templating. 33

Table 1-3. Summary of the reported results for transcriptive LLC templating. 43

Table 1-4. The differences and advantages/disadvantages of synergistic and transcriptive LLC templating methods in summary. 52

Table 2-1. Calculated parameters for different LLC structures before and after polymerization. 79

Table 2-2. Overall monomer conversion and maximum polymerization rate for different initiation systems and theoretical average values for APS+AIBN and APS+BPO mixtures. 86

Table 2-3. Calculated overall kinetics rate coefficient at different temperatures and overall activation energy of the polymerization in lamellar and hexagonal structures using different initiators. 94

Table 4-1. Calculated structural parameters for different species based on SAXS data.....143

Table 5-1. Calculated structural parameters for different species based on SAXS data.....171

CHAPTER 1: INTRODUCTION[1]

1.1 Self-assembled surfactant phases

Nanostructured materials have attracted the attention of scientific communities as well as industries world-wide because of their unique properties which make them applicable in a variety of technical fields including biomedical devices,[1,2] light scattering,[3] membranes,[4,5] energy storage devices,[6] and so forth. Precise control of the structure in the nanometer scale is the key to improve the functionality of such materials and thus to guarantee their applicability in each field. Process-ability and chemical functionality of the components are other important factors when it comes to the large scale production of nanostructured substances.[7] As an example, inorganic materials such as zeolites that are widely used for separation in molecular scale suffer from challenging process-ability as well as limited range of chemistry (e.g., chemical functionality), resulting in restricted application as highly selective membranes.[7]

The "bottom-up" approach, which works based on self-arrangement in the atomic, molecular or colloidal scales, is the common method used in nanotechnology for the fabrication of precisely designed nanostructures.[8] Amongst the huge diversity of materials employed in this technique, the components that form liquid crystalline structures (LCs) through a molecular self-assembly process (supramolecular chemistry) have received a great deal of attention.[8] LCs have both ordered and disordered regions in their structures. These structures, also called mesophases, offer some of the properties of liquids and solid simultaneously (e.g., fluidity coupled with optical anisotropy). Many organic compounds show LC behavior under certain conditions. LC behavior can be

[1] Reprinted with permission from Journal of Materials Chemistry A, 2021, 9, 21607-21658 with some modifications.

observed in the molten state (thermotropic LCs), or in the presence of a solvent as in lyotropic LCs (LLCs).[9] In both cases, molecular self-assembly, liquidity and diverse chemistry not only provide an opportunity to precisely control the nanostructure, but also result in the ease of processing as well as a wide range of chemical functionality.[7]

Amphiphilic molecules, which have lipophilic tail(s) and hydrophilic head(s), are used to form LLCs in the presence of solvent(s). Water has been the common solvent in most of the formulations, though assembly in non-aqueous phases has also been studied[10–13]. Molecular self-assembly of these substances results in several LLC nanostructures such as normal (oil-in-water) micelles (L_1), normal discontinuous cubic (I_1), normal hexagonal (H_1), lamellar (L_α), normal bicontinuous cubic (Q_1), reverse (water-in-oil) bicontinuous cubic (Q_2), reverse hexagonal (H_2), reverse discontinuous cubic (I_2), and reverse micelles (L_2), which all are shown schematically in Figure 1-1. Herein we have assigned I_α, H_α, and Q_α as the general signs for discontinuous cubic, hexagonal and bicontinuous cubic phases regardless of the type of each structure. Temperature, pressure, light, and magnetic field are some of the external factors which can affect the phase structure of LLCs. In addition, there are other factors including concentration, chemistry and shape of the amphiphilic molecules, water content, and additives (e.g., in the oil phase) that can influence the formation of a particular nanostructure. The LLC structural transitions, which are controlled by aforementioned parameters, are explained via the critical packing parameter (CPP). CPP is defined as:

$$CPP = \frac{V}{al} \tag{1-1}$$

Where *V*, *a*, and *l* represent the lipophilic tail volume, 'effective' cross-sectional area of the hydrophilic head group, and extended lipophilic chain length, respectively. Although the

parameter *a* is sometimes interpreted in LLC literature as a measure of the physical/geometric cross-sectional area of the surfactant head group, it is in fact an effective thermodynamic quantity,[14] which encapsulates various conditions, such as charge, solvent ionic strength, temperature, and additives.[15] Free energy minimum models for calculating *a* have been developed at various levels of complexity. However, examples exist in literature where simply estimating a_e as the geometrical cross-sectional area[16] of the charged head group still leads to excellent matching between theory and experiment.

As shown in Figure 1-1, when the cross-sectional area of hydrophilic group is larger than that of lipophilic tails (CPP < 1), mean curvature is positive, resulting in the formation of normal phases. When CPP > 1, negative mean curvature is present, resulting in inverted nanostructures (inverse phase). Lamellar structures are obtained when the mean curvature is zero (CPP = 1), meaning that the cross-sectional area of the polar head group and the tail are almost equal. Therefore, the CPP concept is a powerful semi-quantitative lens for understanding type and stability of LLC phases of amphiphiles. The solvent(s) content is the leading factor which can induce a transition in the structure as schematically shown in Figure 1-1. Common techniques used for the characterization of LLC structures include Cross Polarized Light Microscopy (CPLM), Small-Angle X-ray Scattering (SAXS), X-ray Diffraction (XRD), and Nuclear Magnetic Resonance (NMR). Among commonly encountered LLC structures, only the lamellar and hexagonal phases are optically birefringent. H_α mesophases typically show a fan-like texture in CPLM, while L_α typically exhibit oily-streak textures. Figure 1-2a shows examples of these typical textures. Cubic systems lack birefringence due to the isometric nature of the system, and therefore appear dark in CPLM. This includes I_α and Q_α, e.g. body-centered cubic (*BCC*) or face-centered cubic (*FCC*) packings of micelles, and the gyroid, double diamond, and primitive bicontinuous

cubic mesophases. Likewise, disordered micellar systems (L_1 and L_2) are also optically isotropic and appear dark in CPLM. In conjunction with CPLM, the relative position of Bragg peaks obtained from XRD or SAXS measurements is the most common method to identify the phase of LLCs.[17] The typically observed X-ray crystallographic features of each structure, presented in Figure 1-2, will be discussed in section 1-2.

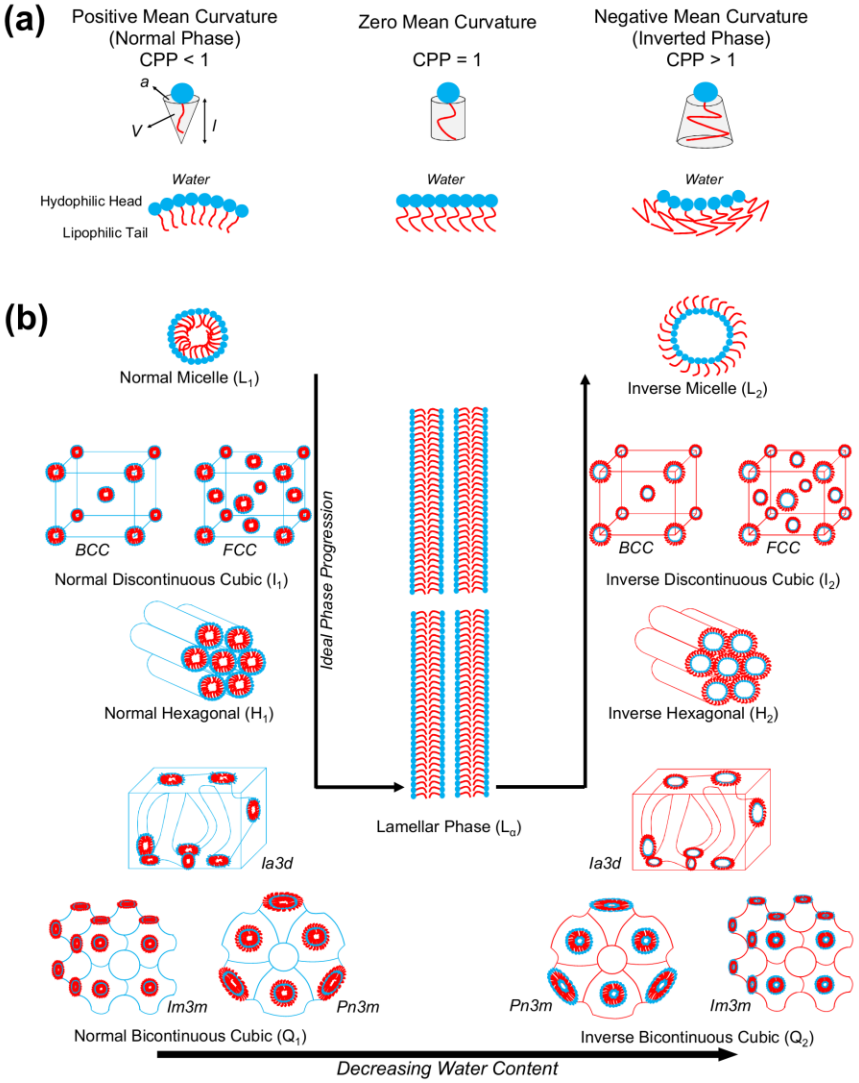

Figure 1-1. (a) The schematic representation of CPP and its corresponding favorable structure. (b) Schematic diagram of common LLC structures.[9,17–19] Addition/removal of solvents, such as decreasing water content can drive the phase transition.

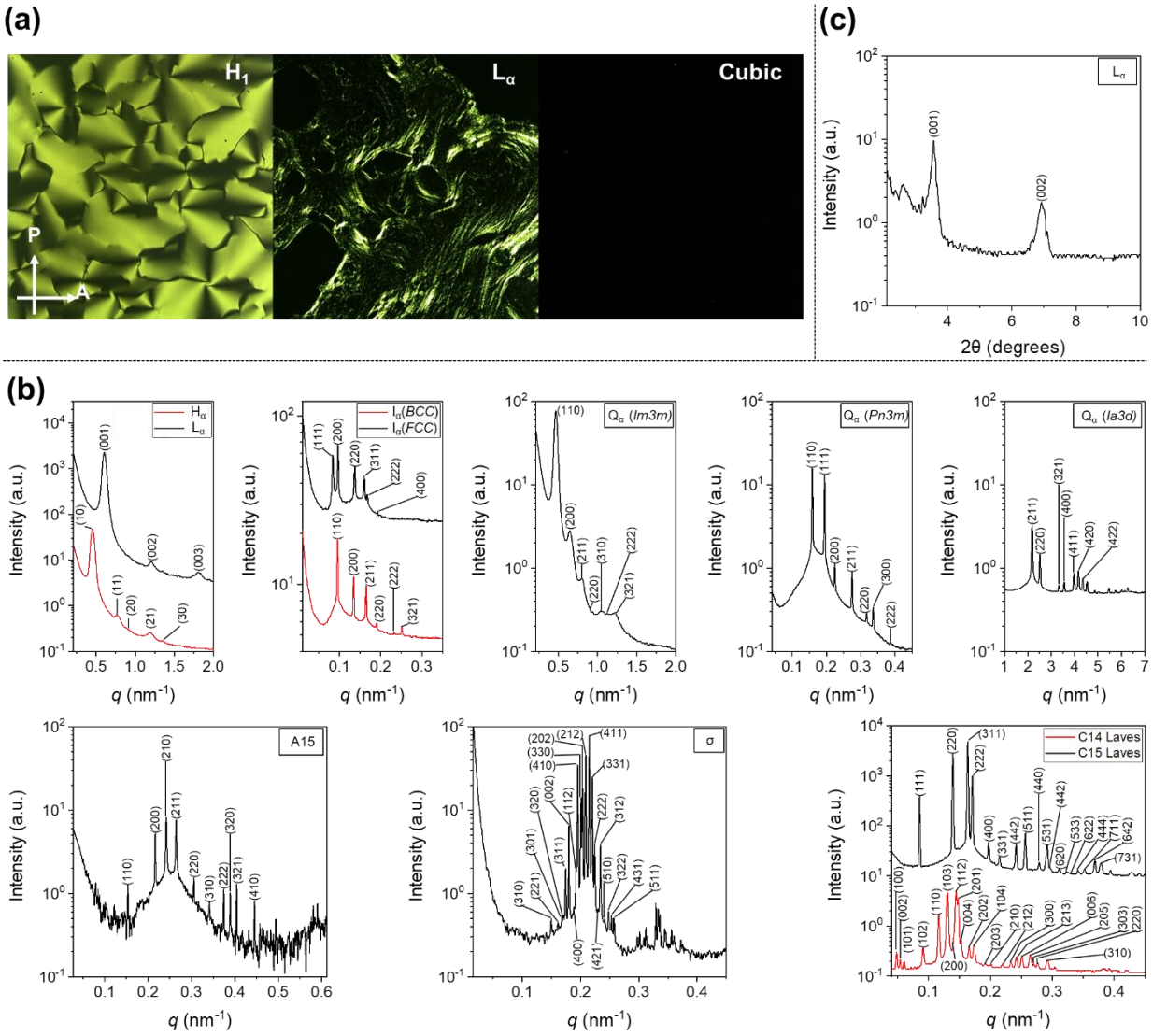

Figure 1-2. (a) Typical CPLM Textures for LLC Mesophases – Representative micrographs for various LLC mesophases when samples are observed in a light microscope with a 90º difference in the Polarizer (P) and Analyzer (A) directions. Birefringent 'fan-like' and 'oily-streak' textures are observed for the normal cylinder (H_1) and lamellar sheet L_α) mesophases. No birefringence is observed for any of the cubic phases i.e. *Im3m*, *Pn3m*, *Ia3d*, *BCC*, and *FCC*. (b) Typical 1D SAXS profiles and corresponding assigned diffraction planes observed for L_α,[20] H_α,[20] I_α (*FCC*[21] and *BCC*[21]), Q_α (*Im3m*,[20], *Pn3m*,[22] and *Ia3d*[23]) and Frank-Kasper phases (A15,[24] σ,[24] C14 Laves,[22] and C15 Laves[22]). (c) Representative example of results acquired from XRD for an L_α LLCs.[25]

Even though LLC phases offer several advantages as previously mentioned, they still suffer from poor mechanical and thermal properties which reduce their suitability in many applications.

The predominant method to circumvent these limitations is to use LLCs as a template to synthesize polymers known as polyLLCs, with the desired nanostructure and chemical properties. Such templating is approached via two common routes: synergistic and transcriptive templating. In the former method, the organic component forming the LLC is polymerized, resulting in a cured template. In the transcriptive approach, the desired material is formed (e.g., via polymerization) in the nano-confinement of the LLC template, resulting in the formation of a one-to-one replica. The main challenge in the transcriptive method is to preserve the parental template nanostructure. If the structure is not retained, the method is instead referred to as reconstructive templating and the final product may have a higher or lower order compared to the parent LLC, as shown schematically for the H_2 phase in Figure 1-3. Having a precisely controlled structure has led almost all of the studies to focus on high-fidelity retention of the parental nanostructure, which is considered successful LLC templating.[26] There are several reports on using LLC templating for fabrication of organic (e.g., polymers),[27] inorganic (e.g., silica and mesoporous metal and alloys),[28] and organic/inorganic hybrid[29,30] nanostructures. However, LLC templating through the polymerization of organic compounds is the focus of this research since the templating of inorganic species is usually carried out to fabricate nanostructured inorganic materials[28] rather than improving the properties of LLC templated materials.

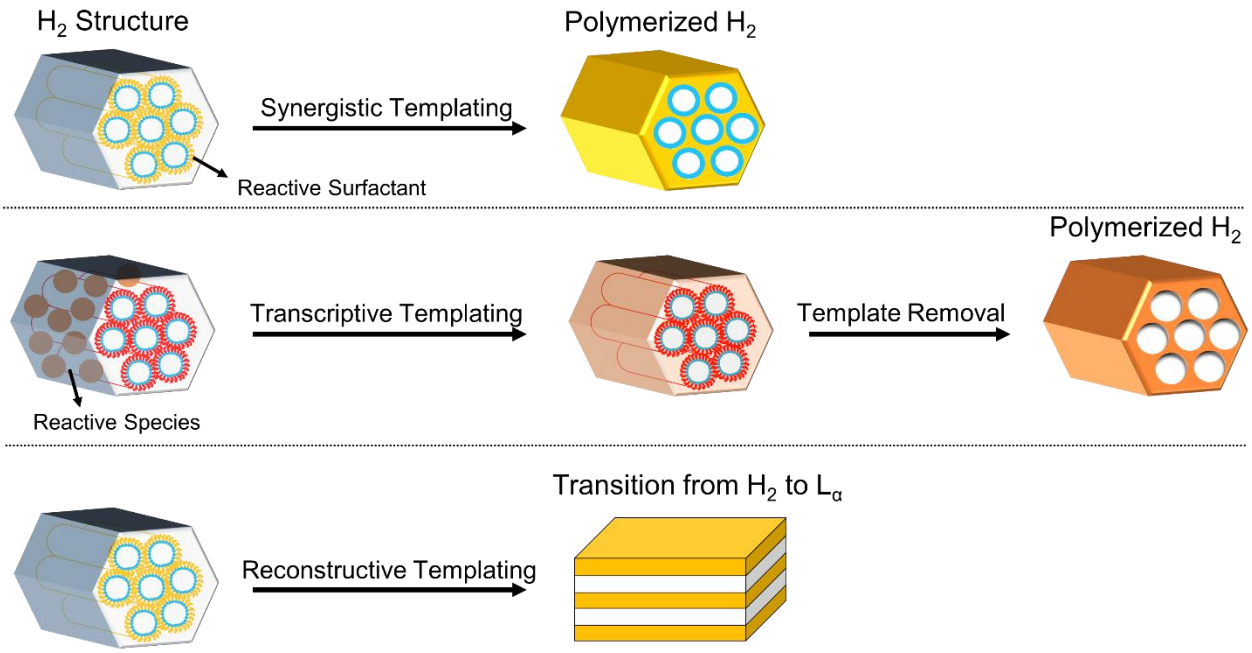

Figure 1-3. Schematic illustration of typical synergistic, transcriptive, and reconstructive LLC templating using H_2 structure. The reconstructive templating may lead to various structures and the lamellar structure shown here is just one example of the phase transition possible in this method.

Thanks to the diversity in nanostructures with 1-10 nm length scale, the fabricated polyLLCs not only are applicable in a wide variety of technical applications, but also can provide enhanced properties compared to common materials. For instance, the membranes obtained from polyLLC technology show an enhanced permeability, selectivity, and fouling resistance compared to the current industry standard.[31–35] Furthermore, the LLC-templated hydrogels offer an excellent balance of water uptake, swelling/de-swelling rate, and mechanical properties while preserving key characteristics including biocompatibility, biodegradability, and stimuli-responsiveness.[36–46] For body motion sensors, LLC templating has provided an opportunity to fabricate conductive materials with improved mechanical properties over non-LLC counterparts.[13,47,48] Additionally, distinctive catalytic activity/selectivity compared to commercially used catalysts has been reported for the catalytic systems fabricated through LLC templating approach.[29,49] Unique light emitting

properties are another advantage of LLC-templated products over non-LLC materials.[50,51] There are many other potential applications (e.g., energy storage devices[52]) for polyLLCs which will be further discussed in section 1-7.

The interesting properties of polyLLCs have promoted the LLC templating approach for a variety of organic compounds since the first trials of synergistic templating by Luzzati and coworkers in the 1960s.[53] In-lab synthesized reactive surfactants have been used in almost all of the synergistic templating studies. For the case of transcriptive templating, there have been several reports concerning the polymerization of widely available (co)monomers and/or cross-linkers in LLC structures created by the solution self-assembly of commercially produced non-reactive surfactant molecules. In the latter case, the cross-linker is used to prevent structure loss during polymerization by kinetically trapping the formed polymer chains and therefore avoiding phase separation/inversion.[54,55] The chemistry, polarity, shape, and concentration of LLC components are not only key factors for preserving the structure, but also determine the reaction kinetics as well as the properties of the final nano-structure.[27] Hence, a wide variety of reactive amphiphiles and different combinations of non-reactive surfactants/(co)monomers have been used to perform successful synergistic and transcriptive LLC templating as listed in Figure 1-4 and Figure 1-5, respectively.

Formation of polymer and thus increasing the molecular weight of the monomer phase results in an increase in the thermodynamic penalty of mixing. Additionally, surface energy of the polymerizing phase changes upon the synthesis of polymer chains. Furthermore, the density increases (shrinkage of polymerizing phase takes place) due to the formation of polymer network. The combination of these phenomena can result in a change in the domain size and even phase separation/inversion, and thus loss of the structure.[32] Therefore, in addition to the surfactant,

(co)monomer and cross-linker, the polymerization initiation system has an important role on retention of the structure since it affects the polymerization kinetics and therefore controls the formation rate of cross-linked network. According to literature reports, fast polymerization rate increases the chance of structure retention due to the rapid cross-linking of polymer network. As a rule of thumb, when the reaction rate is faster than the time scale required for demixing of growing polymer chains, the structure will most probably be preserved.[27] In addition, polymerization near room temperature decreases the risk of structure disturbance.[27,56] Therefore, photoinitiated polymerization, which typically delivers a fast polymerization rate at room temperature, has been the top choice in most of the studies.[27] A variety of photoinitiators have been employed for LLC templating, as listed in Figure 1-6. Nevertheless, there are some studies which have successfully carried out templating by using other initiation systems (e.g., thermal[57] and redox[58]), as presented in Figure 1-6. For enhancing readability and simplifying chemical references throughout the paper for readers, we have coded the large variety of key components used in LLC templating (as seen in Figure 1-4 to 1-6), with the names or chemical formulae of the component tabulated in Table B1, Appendix B.

Following the above introduction on the basic concepts of LLC templating, the remainder of this chapter is outlined as follows. First, characteristics of common LLC structures used in LLC templating will be presented. Then, the available literature on synergistic templating will be reviewed based on the structure of the LLC template. A similar survey will be presented for transcriptive templating afterward. In each section, the efficiency of the templated products will be analyzed in the application(s) they are designed for (e.g., membranes, hydrogels, energy storage devices, light emitting components, catalyst support, tissue engineering scaffolds, and compatibilizers of immiscible monomers). These sections will be followed by a summary of

polymerization kinetics in nanostructured LLCs as well as a concise comparison between synergistic and transcriptive templating techniques. The outlook of the field and available opportunities will be summarized at the end of the chapter.

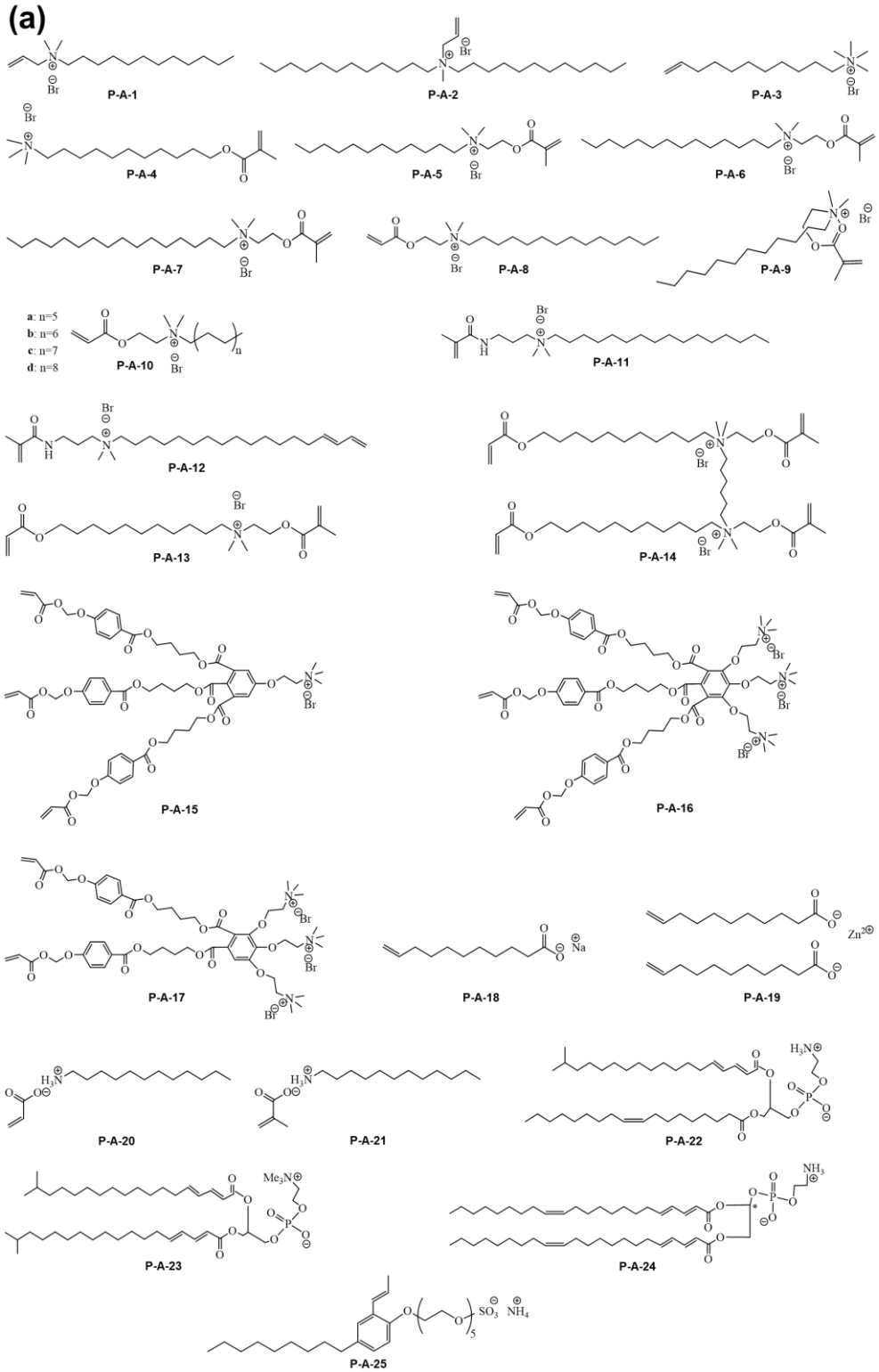

Figure 1-4. Chemical structure of (a and b) polymerizable ionic, (c) polymerizable non-ionic and (d) non-polymerizable amphiphiles used for LLC templating.

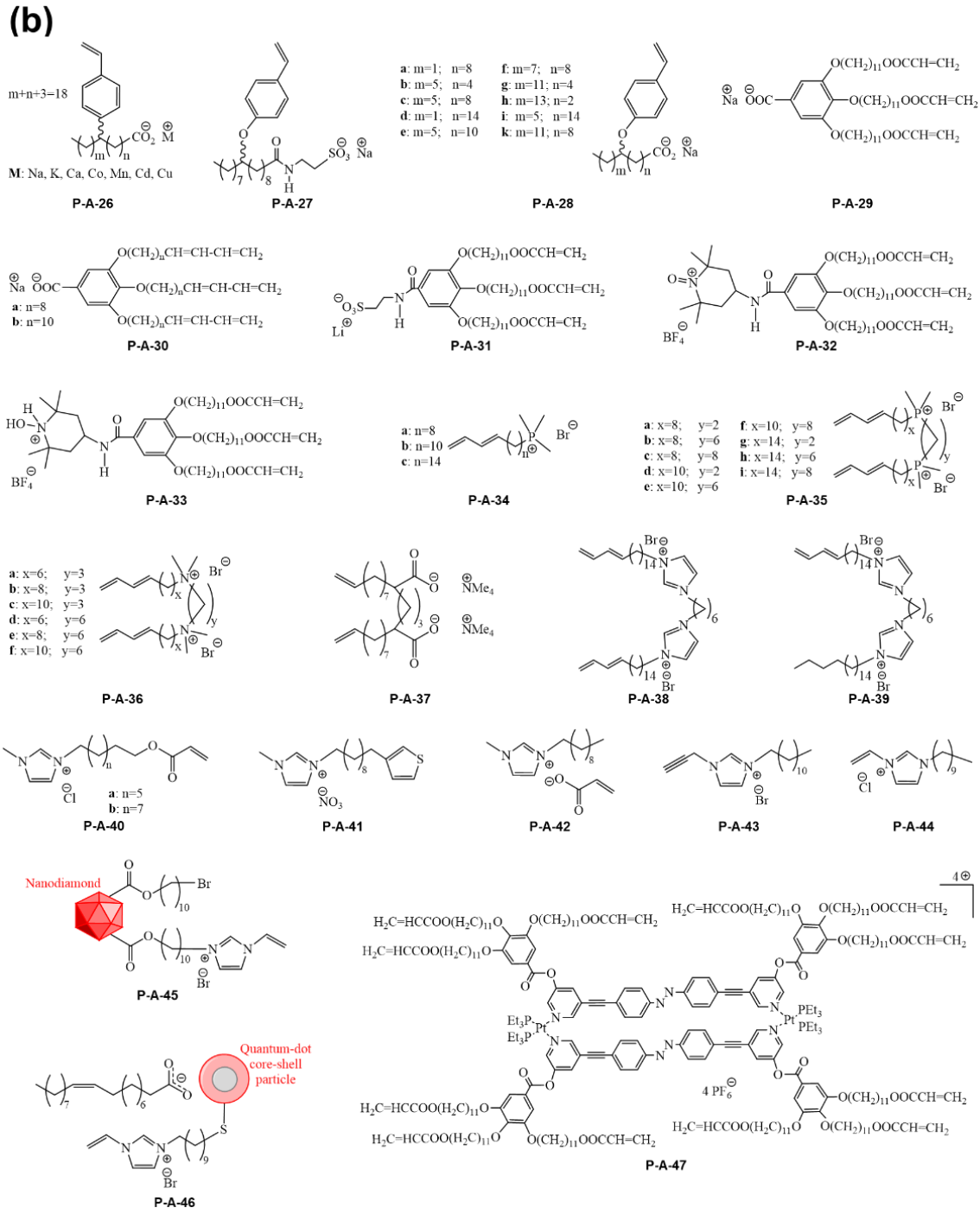

Figure 1-4. *(Contd.)*

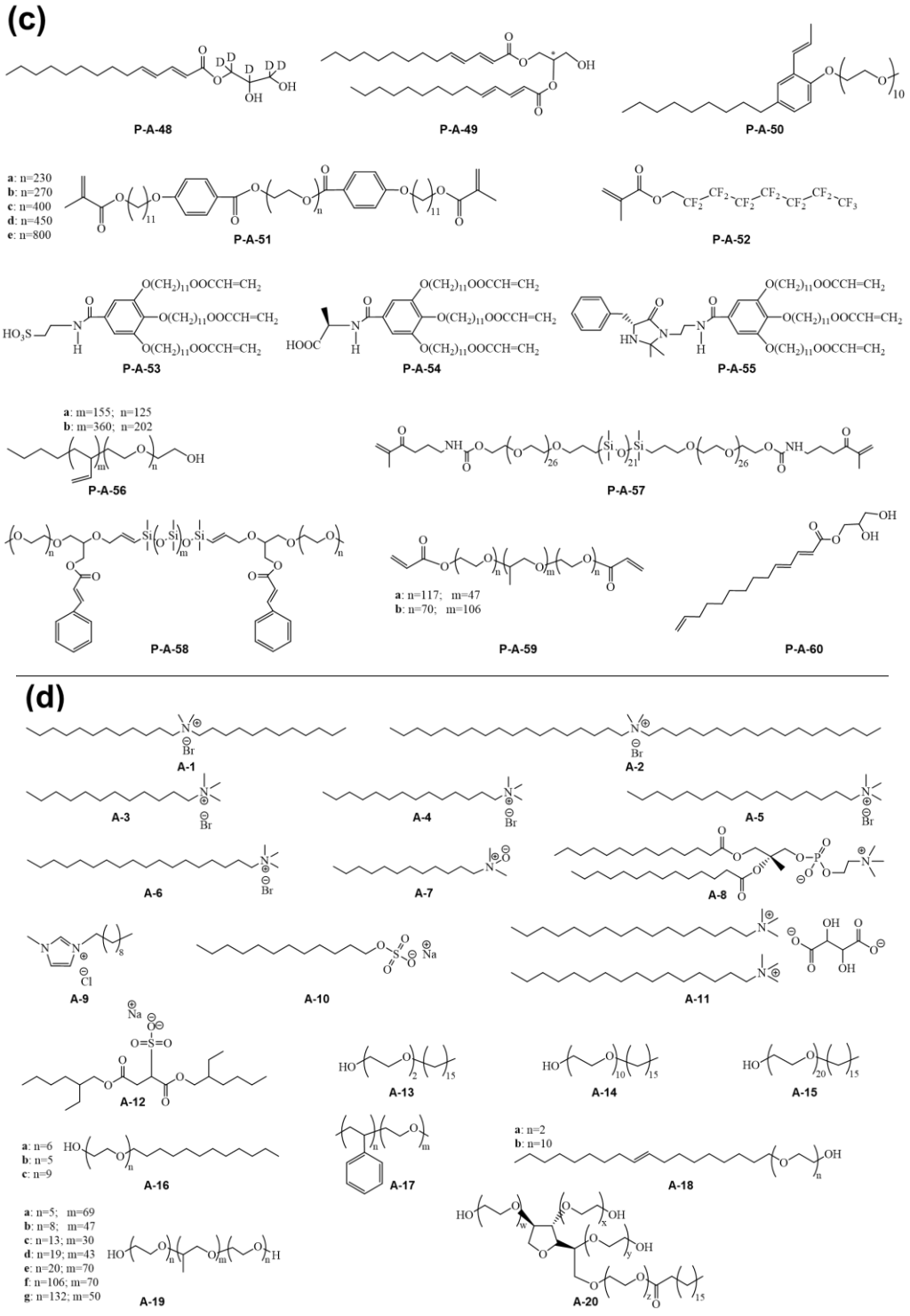

Figure 1-4. *(Contd.)*

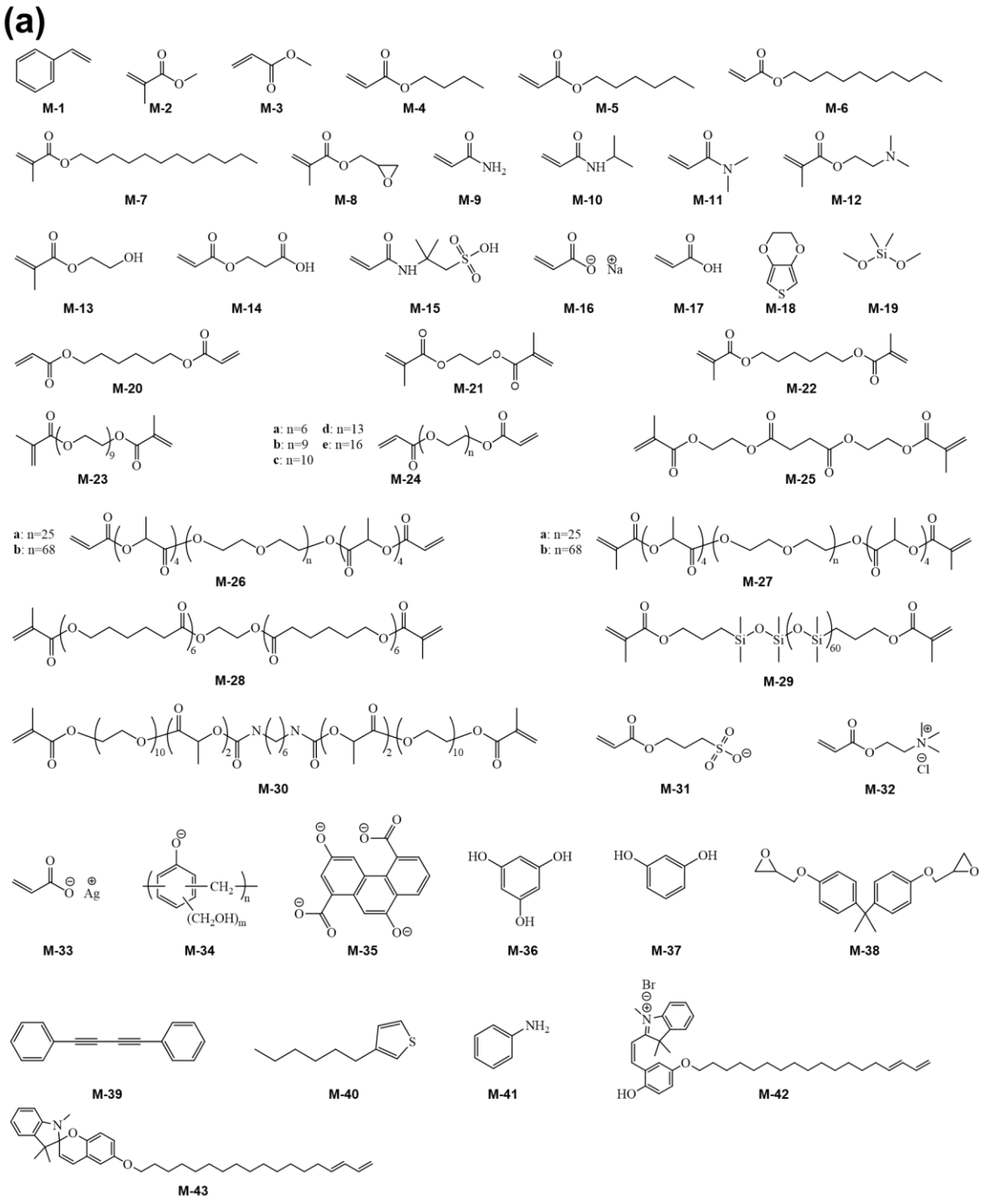

Figure 1-5. Chemical structure of (a) (co)monomers and (b) cross-linkers used for LLC templating.

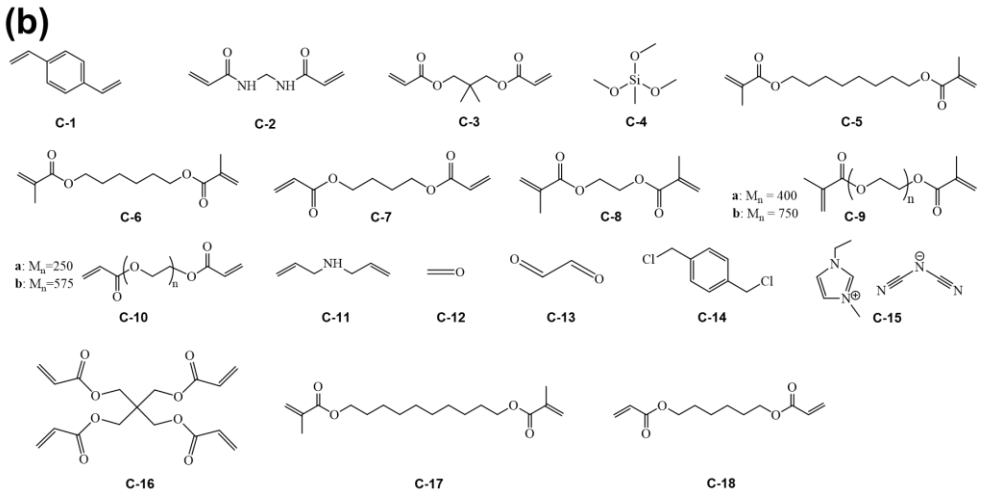

Figure 1-5. *(Contd.)*

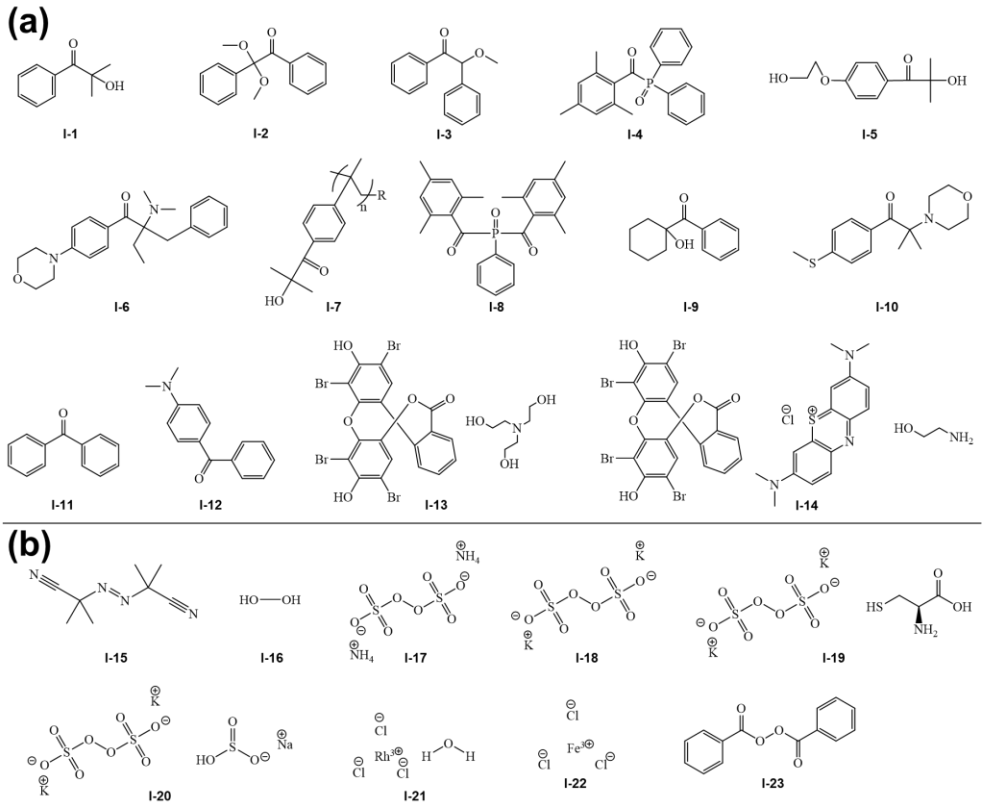

Figure 1-6. Chemical structure of the polymerization initiators used for LLC templating: (a) photoinitiators and (b) other (i.e. thermal and ionic) commonly used initiator.

1.2 Characteristics of LLC structures

As shown in Figure 1-1, a variety of LLC nanostructured phases can be obtained from LLC templating processes. Hence, methods for distinguishing different phases/structures are central to verifying a successful templating. X-ray crystallographic studies are the primary tool of choice for LLC structure characterization. In this section, we discuss key geometric characteristics of different LLC structures, which can be revealed via X-ray crystallographic studies. The characteristic period for commonly studied LLC mesophases (~2-5 nm) is amenable to study by X-ray scattering. Both SAXS and conventional XRD are used for this purpose, though the latter is typically better suited for elucidating structures at even smaller length scales. A summary of LLC structural characteristics is presented in Table 1-1.

1.2.1 Hexagonal (H_α)

The hexagonal columnar structure is one of the most studied phases in LLC templating. H_α consists of closely packed cylindrical micelles arranged in a hexagonal lattice. Depending on the curvature, the hydrophilic head of the surfactant is located on the external or internal surface of the micelles to be in contact with water in H_1 or H_2 structure, respectively. As shown in Figure 1-7, there are multiple parameters of interest in the hexagonal phase structure: *d* is the distance between the planes passing by two adjacent rows of cylinders or *d*-spacing, *a* is the center to center distance of two adjacent cylinders or lattice parameter, R_m is the radius of micelle, R_c is the radius of confined phase in micelle, D_m is the intermicellar distance, and $R_{h,max}$ is the radius of the largest circle trapped between the micelles.[56] Bragg peaks with relative positions at the ratios of $1:\sqrt{3}:2:\sqrt{7}:3:\sqrt{12}:\sqrt{13}\ldots$ (corresponding to the d_{10}, d_{11}, d_{20}, d_{21}, d_{30}, … diffraction planes) are the characteristic signature of the hexagonal structure in X-ray measurements (see Figure 1-2b).[18] The

d is calculated from Eq. (1-2) by using the position of the first Bragg peak from SAXS measurement, q_{10} or q^*. The lattice parameter can be calculated from Eq. (1-3) based on the obtained value of d.[18]

Table 1-1. Characteristics of LLC structures used is LLC templating.

LLC structure	**CPLM**	**X-ray Bragg Peak Ratios**	**Lattice parameter**
Hexagonal	Fan-like texture	1:√3:2:√7:3:√12:√13…	$a = \frac{2}{\sqrt{3}} d$, $d = \frac{2\pi}{q^*}$
Lamellar	Oily-streak texture	1:2:3:4:5:6…	$d = \frac{2\pi}{q^*}$
Bicontinuous cubic	Not birefringent	*Im3m*: √2:√4:√6:√8:√10… *Pn3m*: √2:√3:√4:√6:√8:√9… *Ia3d*: √6:√8:√14:√16:√18:√20…	$1/a$ = Slope of $1/d_{hkl}$ vs $(h^2 + k^2 + l^2)^{1/2}$
Discontinuous cubic	Not birefringent	*BCC*: 1:√2:√4:√6:√8:√10… *FCC*: 1:√3:√4:√8:√11:√12…	$1/a$ = Slope of $1/d_{hkl}$ vs $(h^2 + k^2 + l^2)^{1/2}$
Frank-Kasper phases	Not birefringent	A15:1:√2:√4:√5:√6:√8:√10:√12… C15:1:√3:√8:√11:√12:√16:√19…	$1/a$ = Slope of $1/d_{hkl}$ vs $(h^2 + k^2 + l^2)^{1/2}$

$$d = \frac{2\pi}{q^*} \tag{1-2}$$

$$a = \frac{2}{\sqrt{3}} d \tag{1-3}$$

To calculate R_c, the following equation is used. In this equation, ϕ is the volume fraction of the dispersed phase (i.e., the phase confined in the cylindrical micelles).[18]

$$R_c = a\left(\frac{\sqrt{3}}{2\pi}\phi\right)^{1/2} \tag{1-4}$$

The radius of micelle R_m is calculated using Eq. (1-5). Here, ϕ_t is the volume fraction of the confined phase plus the volume fraction of the surfactant.

$$R_m = a\left(\frac{\sqrt{3}}{2\pi}\phi_t\right)^{1/2} \tag{1-5}$$

The intermicellar distance for H_2 phase D_m, is obtained using Eq. (1-6). Moreover, the size of the nanoconfinement cavity between micelles can be estimated from the radius of the biggest circle trapped between the micelles $R_{h,max}$. Eq. (1-7) and (1-8) can be used for this estimation.

$$D_m = a - 2R_m \tag{1-6}$$

$$R_{h,\max} = \sqrt{\frac{A_h}{\pi}} \tag{1-7}$$

$$A_h = a^2\frac{\sqrt{3}}{4} - \pi\frac{(R_m)^2}{2} \tag{1-8}$$

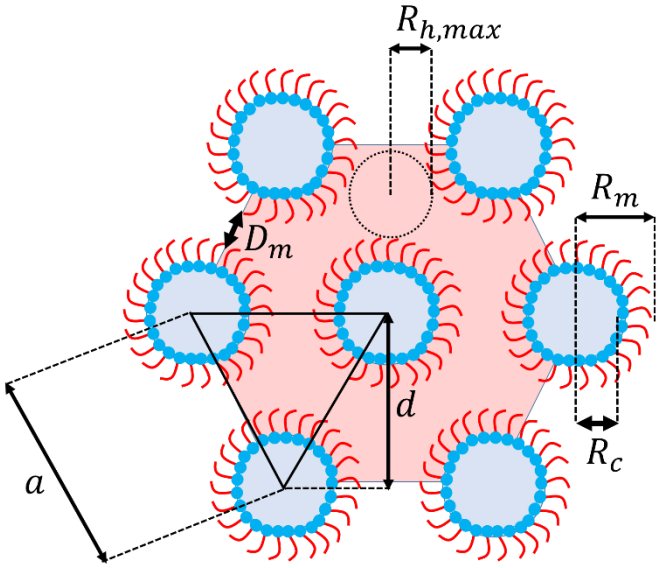

Figure 1-7. Typical schematic of H_2 structure with *d*-spacing (d), lattice parameter (a), radius of micelle (R_m), radius of confined phase in micelle (R_c), intermicellar distance (D_m), and radius of the biggest circle

trapped between the micelles ($R_{h,max}$). In this case, ϕ is the volume fraction of the polar phase. In the case of H_1 structure, ϕ is the volume fraction of the apolar phase.

In the broader mesophase literature, other columnar mesophases have been studied which exhibit non-circular cross-sections and/or non-hexagonal packing of the columns. These LLC phases are sometimes termed 'ribbon' phases, and include lattices of rectangularly or obliquely packed mesogen columns.[59] However, they have generally not been studied in the polyLLC context. There are studies of rectangular columnar phases for thermotropic LCs,[60] but for lyotropic LCs hexagonal columns are the predominantly observed and studied columnar mesophase.

1.2.2 Lamellar (L_α)

The lamellar phase is formed under zero mean curvature. The hydrophilic heads of the amphiphile molecules assemble toward the water, while lipophilic tails remain away from water. As shown in Figure 1-8, L_α has various characteristic dimensions; d is the repeating distance of bilayers or lattice parameter, δ_1 is the thickness of the apolar domain, δ_2 is the thickness of the polar domain, D_1 is the intermicellar distance in apolar phase, D_2 is the intermicellar distance in polar domain, and $R_{1,max}$ and $R_{2,max}$ are the radii of the largest circles trapped between the micelles in apolar and polar domains, respectively.[56] As shown in Figure 1-2b,The lamellar structure shows a sequence of Bragg peaks in integer ratios of 1:2:3:4:5:6…[18] (corresponding to the d_{001}, d_{002}, d_{003}, d_{004}, d_{005}, d_{006}, … diffraction planes) in X-ray crystallographic studies. The position of the first Bragg peak in SAXS measurement (q_1 or q^*) is used to calculate d, δ_1 and δ_2 via the following equations, respectively. In these equations, ϕ_1 and ϕ_2 are the volume fraction of the apolar and polar domains, respectively. In other words, ϕ_1 is the volume fraction of oil phase plus surfactant hydrophobic moiety, whereas ϕ_2 is the volume fraction of aqueous phase plus the surfactant hydrophilic segment.

$$d = \frac{2\pi}{q*} \tag{1-9}$$

$$\delta_1 = d\phi_1 \tag{1-10}$$

$$\delta_2 = d\phi_2 \tag{1-11}$$

To calculate D_1 and D_2, Eq. (1-12) and (1-13) can be used. The average intermicellar distance in lamellar structure D_L is obtained via Eq. (1-14). In these equations, ϕ' and ϕ'' are the volume fraction of the phases confined in the apolar and polar domains, respectively

$$D_1 = d\phi' \tag{1-12}$$

$$D_1 = d\phi'' \tag{1-13}$$

$$\frac{1}{D_L^3} = \frac{1}{D_1^3} + \frac{1}{D_2^3} \tag{1-14}$$

$R_{1,max}$ and $R_{2,max}$ are obtained using Eq. (1-15) and (1-16).

$$R_{1,\max} = \frac{D_1}{2} \tag{1-15}$$

$$R_{2,\max} = \frac{D_2}{2} \tag{1-16}$$

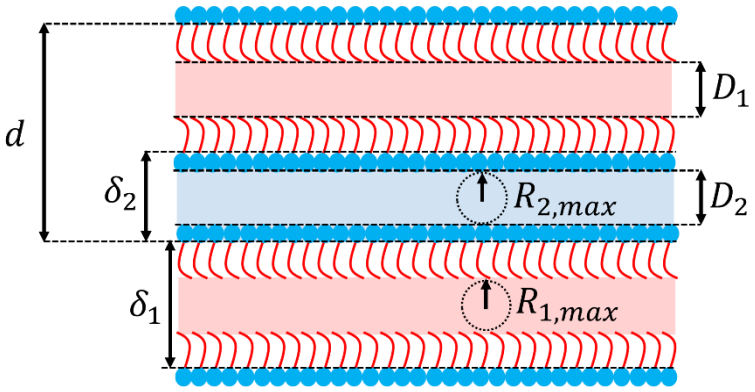

Figure 1-8. Typical schematic of L_α structure showing lattice parameter d, δ_1 is the thickness of the apolar domain, δ_2 is the thickness of the polar domain, D_1 is the intermicellar distance in apolar phase, D_2 is the intermicellar distance in polar domain, and $R_{1,max}$ and $R_{2,max}$ are the radii of the biggest circles trapped between the micelles in apolar and polar domains, respectively.

1.2.3 Bicontinuous cubic (Q_α)

Bicontinuous cubic phases are some of the more interesting but uncommon LLC structures which have been studied for LLC templating. These structures, which are usually obtained by using precisely designed amphiphiles in typically very narrow amphiphile/water weight ratio ranges, consist of continuous but non-intersecting nanochannels separated by a curved bicontinuous layer. Depending on the mean curvature, the bicontinuous bilayer can be hydrophobic tail or polar head (see Figure 1-1).[17] Interconnected pores make these structures perfect candidates for a variety of applications, particularly molecular separations because the pores/channels do not require structural alignment. X-ray crystallographic studies typically encounter Q_α structures of three main types, namely the primitive lattice (*Im3m*, Q_{229}), the double-diamond lattice (*Pn3m*, Q_{224}) and the gyroid lattice (*Ia3d*, Q_{230}), as schematically shown in Figure 1-1.[9,17,19] The important dimensional parameters of the primitive type are presented schematically in Figure 1-9. $2l$ represents the thickness of the apolar domain (including the surfactant tail), $2t_{polar}$ is the polar domain thickness (including the surfactant headgroup), and a is the lattice parameter.[9]

In X-ray crystallographic studies, the peak ratios for *Im3m*, *Pn3m* and *Ia3d* are √2:√4:√6:√8:√10… (corresponding to the d_{110}, d_{200}, d_{211}, d_{220}, d_{310}, … diffraction planes),[61] √2:√3:√4:√6:√8:√9… (corresponding to the d_{110}, d_{111}, d_{200}, d_{211}, d_{220}, d_{221} (or d_{300}), … diffraction planes),[61] and √6:√8:√14:√16:√18:√20… (corresponding to the d_{211}, d_{220}, d_{321}, d_{400}, d_{411} (or d_{330}), d_{420}, … diffraction planes),[61] respectively.[9,17] Typical SAXS profiles for different Q_α structures are shown in Figure 1-2b. Calculation of these parameters for Q_α structure from X-ray studies is not as simple as for H_α and L_α. To calculate the lattice parameter a, the reciprocal spacings, $1/d_{hkl}$, of the peaks in the X-ray measurement are plotted versus the sum of the Miller indices, $(h^2 + k^2 + l^2)^{1/2}$.[18] The $1/a$ is equal to the slope of the line passing through the data points.

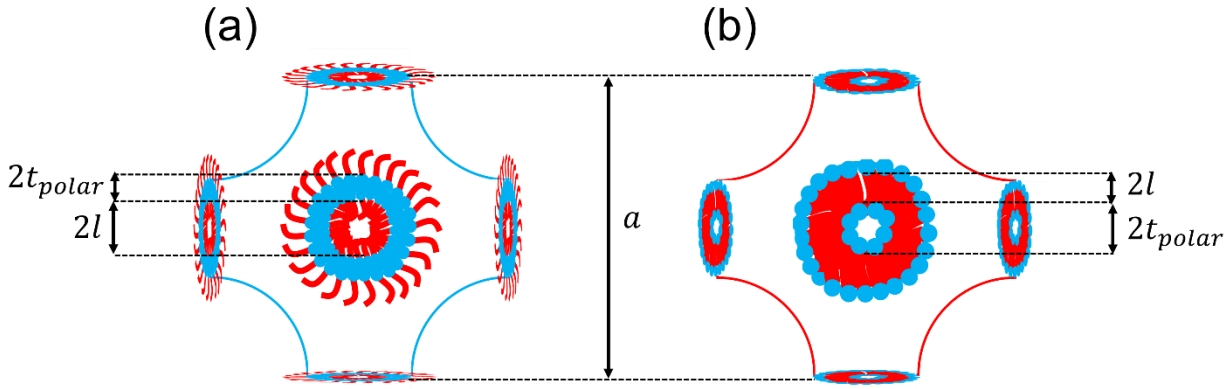

Figure 1-9. Typical schematic of (a) normal and (b) reverse primitive Q_α structure with lattice parameter (a) and the thickness of the polar ($2t_{polar}$) and apolar domains ($2l$).

1.2.4 Discontinuous cubic (I_α)

The discontinuous cubic phases, which are also called micellar cubic, consist of micelles arranged in a cubic lattice. There are two types of cubic lattices for this structure, body-centered cubic (*BCC*) and face-centered cubic (*FCC*), as presented in Figure 1-1. In the X-ray measurements, the characteristic peak ratio for BCC and FCC phases are 1:√2:√4:√6:√8:√10… (corresponding to the d_{100}, d_{110}, d_{200}, d_{211}, d_{220}, d_{310},… diffraction planes)[62] and

1:√3:√4:√8:√11:√12… (corresponding to the d_{100}, d_{111}, d_{200}, d_{220}, d_{311}, d_{222},… diffraction planes),[62] respectively (see Figure 1-2b).[9] To calculate the lattice parameter (see Figure 1-10), a procedure similar to the one for bicontinuous cubic structures is used.[62] Polar domain size α_1 and apolar domain size α_2 of *BCC* lattice can be estimated via Eq. (1-17) and Eq. (1-18), respectively.[63] In these equations, R_c is the radius of the spherical micelles and ϕ, which is obtained by Eq. (1-19), is the volume fraction of continuous domain.

$$\alpha_1 = 2R_c \tag{1-17}$$

$$\alpha_2 = 2a\left(\frac{3\phi}{8\pi}\right)^{\frac{1}{3}} \tag{1-18}$$

$$\phi = 1 - 2\frac{\frac{4}{3}\pi R_c^{\,3}}{a^3} \tag{1-19}$$

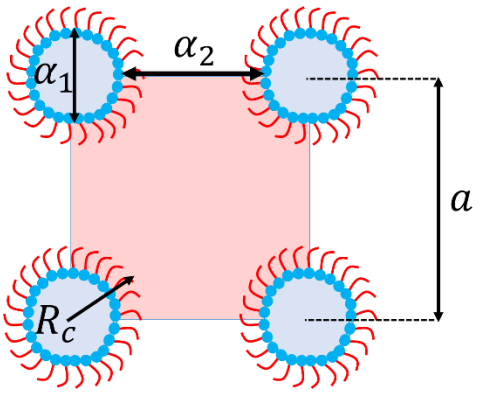

Figure 1-10. Typical schematic of inverse *BCC* discontinuous cubic structure with lattice parameter (a), radius of spherical micelles (R_c), polar domain size (α_1) and apolar domain size (α_2).

1.2.5 Other LLC structures

So far, we have discussed the LLC structures which are commonly observed in different LLC formulations. However, quasi-crystal structures, such as Frank-Kasper (F-K) phases, are also reported for lyotropic systems.[21,22,24,64] F-K phases, which exhibit tetrahedrally close-packed

structures, were discovered for metal alloys more than 50 years ago.[65,66] Since then, more than twenty different types of F-K phases have been experimentally observed in metal alloys. Amongst such variety, A15, Laves, σ, μ, M, P, R, and Z phases are the most common ones.[67] In the case of LLCs, formation of A15,[21,24,64] Laves (e.g., C14 and C15)[22] and σ[24,64] phases have been reported in the literature. The LLC with A15 structure contains 8 quasispherical micelles per unit cell with two different types of coordination environments.[21,24,64] The C15 Laves phase includes eight quasispherical micelles located at the positions of a cubic diamond lattice and tetrahedral groupings of smaller micelles fill the remaining tetrahedral interstitial sites.[22] In the case of C14 Laves phase, the micelles are located on the sites of the hexagonal diamond structure.[22] The lyotropic σ mesophase consists of a primitive tetragonal unit cell with 30 quasispherical micelles which belong to five different symmetry-equivalent classes.[24,64] The common F-K phase reported for LLCs are schematically shown in Figure 1-11. As with other mesophases, X-ray analysis is used to characterize these structures. Accordingly, as presented in Figure 1-2b, the characteristic peak ratio of 1:√2:√4:√5:√6:√8:√10:√12… (corresponding to the d_{100}, d_{110}, d_{200}, d_{210}, d_{211}, d_{220}, d_{310}, d_{222},… diffraction planes) and 1:√3:√8:√11:√12:√16:√19… (corresponding to the d_{100}, d_{111}, d_{220}, d_{311}, d_{222}, d_{400}, d_{331}, … diffraction planes) is observed for A15[21,24,64] and C15[22] Laves phases, respectively. In the case of C14 Laves[22] and σ[24,64] phases, Bragg peaks corresponding to the d_{100}, d_{002}, d_{101}, d_{102}, d_{110}, d_{103}, d_{200}, d_{112}, d_{201}, d_{004},… and the d_{310}, d_{221}, d_{301}, d_{320}, d_{311}, d_{002}, d_{400}, d_{112} or d_{321}, d_{410}, d_{330},…diffraction planes have been reported, respectively. Although these LLC phases have not yet been applied in LLC templating, they seem to have excellent potential in fabrication of nanostructured species with unique properties (see the discussion in section 1.3.4).

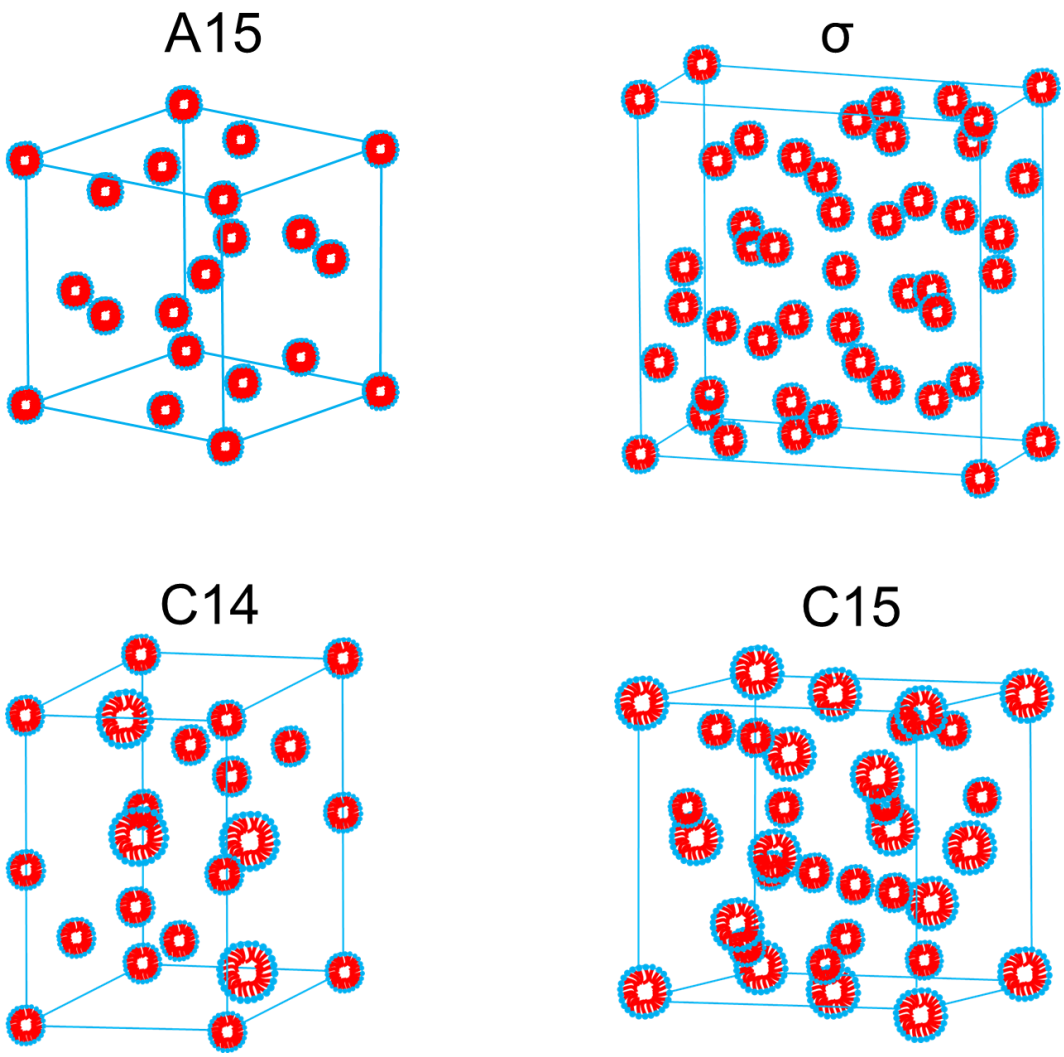

Figure 1-11. Typical schematics of different F-K phases observed for LLCs including A15, C14 and C15 Laves, and σ phases.

For the sake of completeness, it should be mentioned that there are other occasionally observed LLC structures which are variously described as 'intermediate', 'transition' or 'irregular' mesophases. One such mesophase is the L_3 'sponge' phase, which has an overall lamellar structural motif, but the spacing of solvent domains is irregular. This polydispersity in feature spacing manifests itself as a broad primary peak in L_3 X-ray diffractograms.[68,69] Another example are the 'ribbon' phases, which are transition/intermediate structures typically observed between hexagonal and lamellar phases.[70] As the focus of this work, and of polyLLC focused research

efforts in general, is to obtain regular and well-ordered nanofeatures, these miscellaneous mesophases are understudied in polyLLC literature, likely because they lack any immediately apparent utility because of their non-uniform order and/or transitory nature.

1.3 Synergistic LLC templating

Since the first works on synergistic LLC templating in 1960s,[53] there have been several successful LLC templating efforts. Early studies suffered from the inability to retain the parent LLC structures after polymerization and/or rather low extents of polymerization/conversion.[57,71–76] These issues were partly resolved by the introduction of novel reactive amphiphiles, employing highly efficient polymerization initiation systems, and developing new LLC formulations.[7,27] However, the major concern was still to expand the available variety of LLC nanostructures accessible for a successful templating. The performance of different polyLLCs in desired applications is highly dependent on the structures. For instance, in molecular separation applications (e.g., water filtration), permeability, selectivity, and fouling resistance have to be optimized simultaneously.[4] While Q_2 structures offer such opportunity, they are not easily accessible. Moreover, due to the high tortuosity of this structure, cleaning the nanochannels blocked by foulants is highly challenging. On the other hand, H_2 and L_α phases, while easily achievable LLC structures, need further processing steps (e.g., pore/channel alignment by magnetic field) to decrease the tortuosity, thus optimizing the aforementioned membrane characteristics.[31] Similar examples concerning the differences among LLC structures and obtained polyLLCs provide the motivation to classify the following discussion based on the LLC nanostructures.

1.3.1 Hexagonal (H_α)

A summary of reports in the current literature on synergistic templating of H_α structures is listed in Table 1-2. As shown in the table, the lattice parameter reported for this structure typically ranges from ~ 3 to ~ 11 nm. The lattice parameter is controlled by the geometric characteristics of the employed reactive amphiphile such as the molecular size and shape, ionic charge, the position of the polymerizable group, and so forth. As an example, P-A-16 which has a 3-head/3-tail structure, results in a larger lattice parameter compared to P-A-15 and P-A-17 with 1-head/3-tail and 3-head/2-tail structures, respectively.[77] P-A-29 is another example for which the *d*-spacing decreases when the hydrophilic head contains trivalent lanthanide salts instead of sodium ion.[78] In addition to the lattice parameter, the accessibility of H_α is also determined by the type of the surfactant. For instance, to form LLC from the mixture of P-A-32 and P-A-33 in water, addition of P-A-54 is crucial.[79] Moreover, specific compositions of amphiphiles in mixture are required to obtain the intended structure. Change in the lattice parameter after polymerization is another important result in most of the studied cases. If the structure is retained, dimensional changes due to the formation of the polymer network[42,56] and formation of a hexagonal structure with different *d*-spacing are believed to be the main reasons for changes in the lattice parameter.

Enhanced thermal stability,[58,61,73,80–88] swelling behavior,[58,76,86–90] and mechanical properties[81,87,90,91] of polyLLC are the common outcomes of a successful synergistic templating process. However, as listed in Table 1-2, there are some reports on the enhanced properties of polyLLCs in particular applications such as molecular separation membrane,[31,92–94] catalysis,[49,79,95] and light emitting materials.[50,78] As described by Osuji and co-workers, synergistic LLC templating by polymerization of H_1 structure has outstanding potential as membranes in water purification application because such polyLLC membranes offer low tortuosity without requiring

any structural alignment. According to their results,[31] it is possible to fabricate a membrane with an excellent permeability coupled with proper selectivity and biofouling resistance by polymerizing H_1 template created from self-assembly of P-A-6 in water. Using one oil- and one water-soluble cross-linker simultaneously in the mesophase formulation is one promising technique for creating an interconnected network among nanocylinders and therefore fabricating a mechanically robust membrane.

Gin and co-workers have focused on the preparation of molecular separation membranes (e.g., for water purification and gas separation) based on synergistic LLC templating with H_2 structure.[92–94] Although they have obtained promising results demonstrating the higher efficiency of the polyLLC specimens over non-LLC ones, there are still some modifications required (e.g., alignment of the nanochannels) due to the performance mismatch between permeability and selectivity metrics. In addition to the membrane applications, polyLLCs from synergistic H_2 templating have been used as catalyst support in reactions, such as alcohol oxidation[79] and esterification.[95] The reported results show that polyLLC-based catalysts exhibit an improved selectivity and activity comparable to the industrially used catalysts.[49,79,95] In another application, a H_2 template has been used to fabricate a nanocomposite containing poly(*p*-phenylenevinylene) (PPV) inside the nanochannels, resulting in a durable material with higher light emission capabilities compared to pure PPV.[50,78]

1.3.2 Lamellar (L_α)

As summarized in Table 1-2, several studies have used L_α structures in synergistic templating. Depending on the amphiphile(s) and LLC formulation, lattice parameters in the range of ~3 to ~12 nm have been obtained. In addition, in most of the cases, L_α is obtained at relatively high surfactant concentrations (~ >70 wt%).[51,73,81,96–102] Similar to the hexagonal structure, changes in the lattice dimension are typically observed after polymerization, attributed to the formation of a polymer

network as well as the production of L_α structures with different *d*-spacings. Another notable point here is the formation of a unique structure called hexagonal perforated lamellar (HPL) which is a hybrid lamellar-hexagonal structure made from sheets that have in-plane aqueous perforations arranged on a hexagonal lattice. HPL is formed when structural changes from L_α to Q_α takes place during LLC formation or after the polymerization. HPL has been commonly observed in LLCs based on amphiphilic imidazolium-based ionic liquids.[103] HPL is considered to be a necessary kinetic pathway for the existence of Q_α phase.[104]

As mentioned in section 1.1, improving the thermal, mechanical, and physical properties of nanostructured polymers are the primary goals of polymerization of LLC phases. Therefore, the majority of the reported works on synergistic templating of the L_α phase have focused on proving this concept in addition to studying the polymerization kinetics, which will be discussed in a later section.[58,61,73,80,81,86,87,101,103,105,106] As an example, Firestone *et al.* have performed several studies to cure L_α and HPL structures made by reactive amphiphilic imidazolium-based ionic liquids to produce a robust ion gels without sacrificing the conductivity of the parent LLC phases.[86,87,103,105]

1.3.3 Bicontinuous cubic (Q_α)

LLCs with Q_α structures having lattice parameters of ~5 to ~13.5 nm have been used in synergistic templating efforts (see Table 1-2). The accessibility of Q_α phase before polymerization is the most important challenge in templating process. Due to the relative scarcity of Q_α phases, researchers have generally focused their efforts in synthesizing new reactive amphiphiles and formulations design and optimizations.[107] For instance, the formation of Q_α phases is less challenging in binary phases rather than in ternary ones.[107] On the other hand, the shape of the amphiphilic monomer (e.g., the volume of the lipophilic tail, the 'effective' area of the hydrophilic head, and the extended lipophilic chain length) dictates the type of the LLC structure. As an

example, monomers with small hydrophilic head and a broad flattened hydrophobic tail (tapered shape) tend to form H_2 structure, whereas amphiphilic monomers with cylindrical shape tend to form lamellar phase.[83] O'Brian and co-workers were pioneers in designing reactive surfactants that form Q_2 structure.[58,82,108–111] The Gin group have added a considerable body of knowledge on synergistic templating of Q_α structures. Among other contributions, they have shown that Gemini-structured reactive amphiphiles which have low critical micelle concentration (CMC) are reliable species for obtaining Q_1 structures.[33,34,52,112–121]

Efforts by the Gin group are not limited to design and synthesis of new monomers for LLC templating in bicontinuous cubic structures, but also include investigations of the efficiency of the polymerized LLCs in different applications. In one trial, they have shown that polymerized Q_2 structure of P-A-31/Li salt solution of propylene carbonate shows a conductivity similar to the liquid-like electrolytes while maintaining high flexibility even at temperatures as low as -35 °C.[116] In another series of works, they have used Q_1 phases obtained from P-A-35 to fabricate membranes with different applications. As breathable barrier materials for chemical agent protection, the produced butyl rubber (BR) incorporated membranes (LLC/BR composite) with Q_1 structure show improved water vapor permeability/selectivity over LLC/BR composite membranes with H_2 structure.[115] On the other hand, the water filtration performance of the membranes fabricated with the Q_1 LLC lies in between that of conventional nanofiltration (NF) and reverse osmosis (RO) membranes.[34,119] They have also shown the possibility to modify/reduce the pore size of the final product by atomic layer deposition (ALD) and therefore to increase the efficiency of light gas separations.[117] In another effort, Gin and co-workers decreased the production cost of Q_1-based water filtration membranes by using P-A-36 instead of P-A-35 while maintaining the same efficiency.[118] To further examine the performance of this structure, the team has used a mixture of

P-A-38 in glycerol to obtain Q_1-based membranes having a thin active layer (< 0.1 micrometer) as a thin film composite (TFC). The generated membranes show a water flux comparable to the industrially used NF and RO membranes, salt rejection in between of them, and higher fouling resistance and flux recovery.[33,114,120,121] Furthermore, the fabricated membranes exhibit an improved water/chemical agent molar vapor selectivity over Q_1 LLC/BR membranes created by P-A-35 while requiring lower production costs.[112] Modification of ion sorption and pore transport properties via polymerization of an ionic monomer inside the membrane pores has also been explored to modify the performance of the Q_1-based membranes.[113] Finally, they have reported a higher dehydration and resistivity of the Q_1-based anion exchange membrane (AEM) in dilute $FeCl_3$ solutions compared to amorphous AEMs thanks to closer spacing of ion exchange sites.[52]

1.3.4 Discontinuous cubic (I_α)

Discontinuous cubic phases have mainly been used in synergistic templating to study the polymerization kinetics in LLCs,[98,122] which will be discussed later. However, Lopez-Barron *et al.* have used a P-A-59 directed FCC type discontinuous cubic structure to fabricate a cross-linked ion gel with lattice parameter spanning from 15 to 30 nm. Partially deuterated ionic liquid (ethylammonium nitrate) has been used instead of water to fabricate the LLC. By controlling the LLC composition, they have been able to fabricate ion gels having highly viscoelastic or elastomeric behavior with excellent mechanical properties, conductivity, and mechanoelectrical responses.[13,47] They have also shown that the produced ultrastretchable iono-elastomers can be used as a motion sensor as well as a temperature sensor with sufficient sensitivity and accuracy. Impressive mechanical properties of such discontinuous cubic structures, in which discrete micelles (spheres) are cross-linked, can indicate opportunities in other technical fields (e.g., membrane application) which require robust materials.[48] The mentioned properties can possibly

be further improved if the F-K phases are employed in the synergistic templating instead of common discontinues cubic structures.

Table 1-2. Summary of the reported results for synergistic LLC templating.

Amphiphile	Cross-linker	Initiation system	Amphiphile concentration [wt%] and structure before reaction	Structure after polymerization	Lattice parameter before reaction [nm]	Lattice parameter after reaction [nm]	Remarks	Ref.
P-A-1	-	I-15 or UV	48 - 83 (H_1) 83 - 92 (Q_1) > 94 (L_α)	Retention of the structures	4 (H_1), 7.21 (Q_1), 3.02 (L_α)	4.08 (H_1), 7.57 (Q_1), 2.95 (L_α)	• Monomer conversion of ~ 30% • 20 °C higher thermal stability of the cured LLC	73
P-A-2	-	I-15 or UV	>75 (L_α)	-	2.5 - 2.97	-	• Unsuccessful Polymerization	73
P-A-3	-	I-15 or UV	50 - 60 (L_1) 63 - 80 (H_1)	Retention of the structures	3.57 (H_1)	3.57 (H_1)	• Monomer conversion of ~ 45% • No difference in thermal stability after templating	75
P-A-4	-	γ-ray radiation	58 – 65 (H_1)	Retention of the structures	3.98	-	• Higher reaction rate than non-LLC sample but lower conversions than P-A-5 (conversion of ~ 60%) • Swelling with polar and nonpolar solvents	76
	-	I-2 or I-5	60 - 79 (H_1) > 82 (L_α)	Complete structure lose with I-5 and limited retention of H_1 with I-2	4.157 (H_1), 3.05 (L_α)	-	• Polymerization rate: $L_\alpha < H_1 <$ non-LLC • Higher polymerization rate with I-2 and lower reaction rate compared to P-A-5	96
P-A-5	-	γ-ray radiation	50 - 60 (L_1) 60 - 83 (H_1) 83 - 90 (Q_1)	Retention of the structures	3.56 (H_1), 7.3 ± 0.7 (Q_1)	3.83 (H_1)	• Polymerization rate: non-LLC < $Q_1 < L_1 < H_1$ • Higher toluene uptake for H_1 over Q_1 • Higher water uptake for Q_1 over H_1 • The order of the structures were changed by swelling	76
	-	I-5	60 - 80 (H_1) 80 - 90 (Q_1) > 90 (L_α)	Retention of the structures	3.71 (H_1), 3.03 (Q_1)*	3.71 (H_1), 3.3 (Q_1)*	• Polymerization rate: $H_1 < Q_1 < Q_1 + L_\alpha < L_\alpha$	97
	-	I-5	50 (I_1) 60 - 78 (H_1) > 90 (L_α)	H_1 changed to L_α L_α is retained	3.55 (H_1)	3.7 (H_1)	• Polymerization rate: I_1 = mixed phase of I_1 and $H_1 < H_1 < L_\alpha$ • H_1 structure was highly prone to phase transition	98
	-	I-2 or I-5	60 - 79 (H_1) 79 - 82 (Q_1) > 82 (L_α)	structure retention in higher reaction rates	3.84 (H_1), 3.2 (Q_1)*, 3.07 (L_α)	3.88 (H_1)	• Polymerization rate: non-LLC < $H_1 = Q_1 < L_\alpha$ • Higher polymerization rate with I-2	96
P-A-6	-	I-5	50 (I_1) 60 - 78 (H_1) > 90 (L_α)	H_1 changed to L_α L_α is retained	4.32 (H_1)	4.18 (H_1)	• Polymerization rate: I_1 < mixed phase of I_1 and $H_1 < H_1 < L_\alpha$ • The polymerization rate of P-A-6 was lower than P-A-5	98
	C-6	I-5	70 (H_1)	H_1 is retained when more than 5.9% C-6 is used	4.32 - 4.1 (at 0 - 8.34% of C-6)	-	• Polymerization rate was the highest when H_1 changed to L_α (C-6 content of less than 3.5%) • Higher water uptakes at higher cross-linker contents was in contrary with the behavior of the non-LLC samples	89
	C-8 / C-9-b	I-3	55-80 (H_1)	Retention of the structure	4.16	4.16	• Membrane with a thickness-normalized permeability of ~10 liters m^{-2} $hour^{-1}$ bar^{-1} μm,and molecular weight cut off of ~350 Da was obtained • Antifouling and antimicrobial properties due to the presence of quatemary ammonium groups	31
P-A-7	-	I-5	50 (I_1) 60 - 78 (H_1)	H_1 changes to L_α	4.8 (H_1)	4.64 (H_1)	• Polymerization rate: I_1 < mixed phase of I_1 and $H_1 < H_1$	98
P-A-8	C-18	I-3	65 (H_1)	Retention of the structure	4.16	4.04	• Membrane with ~200 nm thickness, ~ 10 L m^{-2} h^{-1} bar^{-1} permeability and ~300 Da molecular weight cut off was obtained	123
P-A-9	-	I-15 or UV	40 - 57 (L_1) 70 - 73 (H_2) 80.7 (Q_1)	-	-	-	• P-A-9 formed H_1, Q_1 and L_α, but polymerization was not successful for these structures	124
P-A-10	C-16 or C-18	I-3	50 - 76 (H_1)	Retention of the structure	3 - 4	3 - 4	• Organic solvent–stable membranes were obtained with well-defined pores at ~1 nm scale • Membranes pore size can be tuned through changing the length of lipophilic tail of P-A-10	125
P-A-11 / P-A-12	C-17	I-2 or I-5	87.5 (Q_1)	Retention of the structure	8.74	8.55	• Simple single-head/single-tail surfactants were used to create polymerizable Q_1 phase • pH- and light-responsive polyLLCs can be produced by incorporation of M-42 and M-43.	126, 127
P-A-13 or P-A-14	C-3	I-2	-	-	-	-	• The presence of methacrylate at the hydrophilic head group and low cross-linker content resulted in phase transition • Water contents of around 40% can be tolerated with the transparent polymers	128
P-A-15	C-3	I-2	81 (H_1)	Retention of H_2 at 10 wt% C-3	6.53	7.1	• The structure cannot be retained at 30 wt% C-3	77
P-A-16	C-3	I-2	28 (I_1) 54 (H_2)	Disordered structure at 30 and 12 wt% C-3 for H_2 and I_1, respectively	8.65 (H_2)	9.62 (H_2)	• Incomplete conversion due to the chains mobility restriction in cross-linked network	

Table 1-2. *(Contd.)*

Amphiphile	Cross-linker	Initiation system	Amphiphile concentration [wt%] and structure before reaction	Structure after polymerization	Lattice parameter before reaction [nm]	Lattice parameter after reaction [nm]	Remarks	Ref.
P-A-17	C-3	I-2	54 (H_1)	Structure Retention at 30 wt% C-3	7.61	7.82	-	77
P-A-18	-	I-17	47 – 59 (H_1)	Disordered structure at high temperature	4.192 (H_1)	2.883 (L_α)	• After polymerization, L_α was seen when the temperature was decreased to 20 °C	57,71
	-	γ-ray radiation	40 – 60 (H_1)	Probable change to L_α	-	-	• Monomer conversion of ~20 - 40% • The highest polymerization rate happened in LLC structure	72
	-	I-15 or UV	< 38 (L_1) 42 - 55 (H_1)	Retention of the structures	4.5 (H_1)	3.7 (H_1)	• Monomer conversion of less than 30% • Monomer conversion in non-LLC phase was ~80%	74
P-A-19	-	γ-ray radiation	-	-	-	-	• Monomer conversion of less than 30% • This mixture can form L_α at temperatures more than 100 °C	72
P-A-20	C-1	I-3	80 (L_α)	Retention of the structure	3.56	3.62	• Almost complete monomer conversion • Insolubility of polyLLC in water and organic solvents even without cross-linker	106
P-A-21	C-1	I-3	20 (Q_1) 80 (L_α)	L_α was retained but Q_1 changed to L_α	2.58 (L_α), 10.47 - 11.59 (Q_1)*	2.93 (L_α), 3.33-3.45 (Q_1)*	• Q_1 changed to L_α with or without using C-1 • Insolubility of polyLLC in water and organic solvents even without cross-linker	106
P-A-22 / P-A-23	-	I-20	2.5 – 50 (H_2, L_α, Q_2)	Retention of H_2	5.5 (L_α), 6.5 (H_2)	6.75 (H_2)	• Monomer conversion of more than 80% • H_2 and L_α were seen at temperatures higher and lower than 60 °C, respectively • Q_2 structure was obtained via low concentrations of P-A-22/P-A-23 in water (25 - 100 mg/ml) • PolyLLC showed an improved thermal stability and insolubility in organic solvents	58
P-A-24	-	I-16 or I-19	50 (H_2)	Retention of the structure	7.26	7.06	• Monomer conversion of more than 90% • The presence of H_2 + Q_2 phase was detected for the LLC before polymerization when the temperature was less than 40 °C • Improved thermal stability	82
P-A-25	This reactive surfactant has been used for transcriptive templating. See Table 1-3/M-4 section.							
P-A-26	C-1	I-1	87 (H_2, L_α)	Retention of the structures	3.2 - 4.24 (H_2), 3.82 (L_α)	3.24 - 4.12 (H_2), 3.82 (L_α)	• L_α was obtained when the metal ion was potassium • *d*-spacing depends on the type of metal ion incorporated in the structure of P-A-26 • This structure can also be used for in-situ synthesis of ~ 2 wt% silica in the pores	51,100
P-A-27	C-1	I-1	86 (H_2)	Retention of the structure	4.71	4.35	• The structure underwent a slight distortion due to Sc(III) ion exchange • The formed catalyst afforded condensation products with consistent syn/anti diastereoselectivity ratios of ~ 2/1 in Mukaiyama aldol and Mannich reactions in water	49
P-A-28	-	I-1	82 (H_2)	Retention of the structure	2.87 - 5.33	2.92 - 5.35	• Monomer conversion of ~ 80% • High water content can change H_2 to L_α • Higher thermal stability	83
P-A-29	-	I-1	80 (H_2)	Retention of the structure	4.04	3.98	• PPV was in-situ formed as a filler in the pores of H_2 structure • Higher light emission of the nanocomposite compared to pure PPV • Longer stability of PPV in polymerized LLC due to the isolation from oxygen	50
	-	I-1	85 (H_2)	Retention of the structure	3.62 - 4.3	3.49 - 4.13	• Same metal ion charge resulted in same *d*-spacings • Trivalent lanthanide salts showed lower spacings • When PPV was incorporated in trivalent Eu containing polyLLC, a new intense emission band appeared compared to sodium ion	78
	-	I-1	88 (H_2)	Retention of the structure	4.25	4.18	-	84
	-	I-1	80 (H_2)	Retention of the structure	4.04	3.98	• Monomer conversion of less than 30% in air and almost complete conversion under nitrogen atmosphere • To prepare the membrane, a solution of LLC in methanol was used for roll-casting • Membrane with water flux of 0.3 ± 0.1 L m^{-2} h^{-1} at 50 psi and average pore size of ~1.2 nm was obtained	93
	-	I-1	25 - 73.5 (H_2)	Retention of the structure	4.22 (at 13.8 wt% BR)	4.1	• H_2 structure was achieved when up to 75 wt% BR was used • BR solution in *n*-hexane was used for blending • The obtained membrane of polyLLC/BR composite resulted in water vapor flux of 438 g m^{-2} day • Additional BR phase vulcanization step was used to improve CEES rejection	92
	-	I-1	80 (H_2)	Retention of the structure	-	4.03	• The membrane of the polymerized LLC significantly influenced the solubility of CO_2 and retarded the diffusion for all gases	94
	-	I-4	88.5 (H_2)	Retention of the structure	-	-	• Magnetic field was used to successfully align the nano-channels before polymerization • 8 wt% of M-4 was also used as the oil phase in LLC	129

Table 1-2. *(Contd.)*

Amphiphile	Cross-linker	Initiation system	Amphiphile concentration [wt%] and structure before reaction	Structure after polymerization	Lattice parameter before reaction [nm]	Lattice parameter after reaction [nm]	Remarks	Ref.
P-A-30	-	I-1	86 (H_2)	Retention of the structure	3.84 (P-A-30a) 4.14 (P-A-30b)	3.77 (P-A-30a) 3.98 (P-A-30b)	• *n*-Dodecane initiator solution was used in LLC preparation • Improved thermal stability upon polymerization	84
P-A-31	-	I-1	84 (Q_2)	Retention of the structure	8.87	8.29	• Li salt solution of the liquid electrolyte, propylene carbonate was used instead of water to prepare LLC • The polymerized LLC showed a conductivity similar to the liquid-like electrolytes while maintaining high flexibility even at temperatures as low as -35 °C	116
P-A-32 / P-A-33	-	UV	95 (H_2)	Retention of the structure	4.91	4.85	• 19 wt% of amphiphile was a mixture of P-A-32 and P-A-33 and the remaining 76 wt% was P-A-54 • The polyLLC-based catalyst showed higher activity compared to industrially available TEMPO-based catalysts • Lower catalyst activity toward alcohols with bigger molecules • The catalyst can be reused without major loss of activity	79
P-A-34	C-1	I-2	50 - 75 (H_1) 75 - 85 (Q_2) 85 - 95 (L_α)	Retention of the H_1 structure (only H_1 was polymerized)	4.57	4.5	• It was possible to retain the structure without using a cross-linker but improved thermal stability was observed for the sample containing C-1	85
P-A-35	-	I-2	45 - 85 (H_1) 80 - 90 (Q_1) 50 - 98 (L_α)	Retention of the structures	3.44 - 4.91 (H_1) 2.92 - 4.41 (L_α) 7.92 (Q_1)	3.39 - 4.88 (H_1) 3.03 - 4.53 (L_α) 7.67 (Q_1)	• Monomer conversion of ~23 - 71% • LLC formulation and structure characteristics depend on x and y of P-A-35 • Excellent thermal stability in air	61
	-	I-1	80 (Q_1)	Retention of the structure	-	7.23	• P-A-35e was used in this study • Membrane showed a thickness-normalized water permeability of ~ 0.089 liters m^{-2} $hour^{-1}$ bar^{-1} µm, full water flux recovery (> 95%) and less than 15% water flux loss after contact with salty water and a pore size of 0.75 nm	34
	-	I-1	73.9 (Q_1)	Retention of the structure	8.86 (at 8.2 wt% BR)	8.52	• P-A-35e was used in this study • Broader Q_1 range in phase diagram in the presence of BR (44.7 - 76.4 wt% P-A-35e) • Membrane showed higher water vapor permeability compared to the membrane with H_2 structure prepared via P-A-29 while maintaining proper CEES rejection	115
	-	I-1	80 (Q_1)	Retention of the structure	-	8.73 before ALD ~ 8.52 after 5 cycles ALD ~ 6.21 after 10 cycles ALD	• P-A-35e was used in this study • ALD of alumina was carried out to modify/reduce the pore size • After 10 cycles of ALD, the gas selectivity of hydrogen/nitrogen increased from 12 to 65 while gas permeability decreased ~ 40%	117
	-	I-1	80 (Q_1)	Retention of the structure	-	-	• P-A-35e was used in this study • Membrane exhibited a water filtration performance in between that of conventional NF and RO membranes and excellent resistance against chlorine degradation	119
P-A-36	-	I-1	84.2 (Q_1)	Retention of the structure	4.95 - 6.73	7.35 - 9.46	• Only P-A-36c and P-A-36f can produce Q_1 structure • P-A-36 is cheaper than P-A-35 to be produced • The synthesized membrane showed water flux and permeability comparable to the membrane prepared by P-A-35	118
P-A-37	This reactive surfactant has been used for transcriptive templating. See Table 1-3/M-22 section.							
P-A-38 / P-A-39	-	I-1	79.7 (Q_1)	Retention of the structure	8.71	9.34	• Membrane with a thickness-normalized water permeability of ~ 0.066 liters m^{-2} $hour^{-1}$ bar^{-1} µm was obtained which is comparable to the industrially used NF and RO membranes • The membrane showed a salt rejection in between of NF and RO • Partial ion exchange can reversibly change water flux but does not change *d*-spacing of the structure • Unique selectivity toward TDS and DOC under different FW pH • Higher fouling resistance and flux recovery compared to industrially used membranes	33,114,120,121
	-	I-1	79.4 (Q_1)	Retention of the structure	-	4.03 *	• The prepared membrane was cheaper than the BR/LLC system in same application • The membrane did not have appropriate selectivity toward water over CEES without addition of a PDA layer on the surface of the membrane • Higher water/CEES and water/DMMP molar vapor selectivity compared to previously reported LLC based membranes • Mechanical properties of the polyLLC can be tuned by addition of P-A-39 without losing selectivity	112,130
	-	I-1	79.4 (Q_1)	Retention of the structure	-	-	• The internal surface of the pores was modified by polymerization of M-31 inside the pores • Eternal presence of anionic polymer inside the pores resulted in significant changes in ion sorption and pore transport properties	113
	-	I-1	79.4 (Q_1)	Retention of the structure	-	10.57	• Higher dehydration and resistivity of Q_1 anion exchange membrane in dilute $FeCl_3$ solutions compared to amorphous AEMs thanks to closer spacing of ion exchange sites	52

Table 1-2. *(Contd.)*

Amphiphile	Cross-linker	Initiation system	Amphiphile concentration [wt%] and structure before reaction	Structure after polymerization	Lattice parameter before reaction [nm]	Lattice parameter after reaction [nm]	Remarks	Ref.
P-A-40a	-	UV	78 ± 3 (no structure)	Formation of L_α	-	2.8	• Proper thermal stability and high swelling capacity via water and polar hydrogen-bonding solvents	86,87
P-A-40b	-	UV and I-1	60 - 70 (H_2)	Formation of Q_α at low water contents and retention of H_2	3.23 (H_2)	3.78 (H_2) 4.3 - 7.97 (Q_α)	• Mechanically robust gel was obtained through production of IPN via swelling the polymerized LLC by M-33 and then photopolymerization initiated by I-1 • The structure changed to L_α after formation of the IPN (lattice parameter of 3.3 nm) • Enhanced mechanical properties and insolubility in a variety of solvents were the key characteristics of the obtained compatible IPN	87,90
P-A-41	-	ChO	> 85 (H_2)	Disordered structure	3.41	-	• Anion-exchange to a divalent anion (sulfate and sulfite) and difficulty of controlling the regio-regularity during the polymerization of thiophene were the reason of losing the structure after polymerization	131
P-A-42	C-10b	I-1	87.9 (H_2)	Formation of HPL structure	3.12	-	• Relatively low T_g, high thermal stability, and high resistance toward swelling by organic solvents and water were the important features of the synthesized polyLLC	88
P-A-43	-	I-21	50 ± 5 (HPL)	HPL changed to a hybrid of H_2 and L_α	3.74 *	3.38 *	• Enhanced conductivity of the polyLLC thin film over non-LLC sample	103
P-A-44	C-10b	I-13 and UV	~15.25 (H_2)	H_2 changed to HPL and was retained by post-UV curing	4.6	3.92 (for the retained Hα)	• Disruption of the structure was observed at C-10 contents of higher and lower than 20 w% • Proper structure stability toward swelling and de-swelling by ethanol	91
P-A-44 / P-A-45	-	UV	~80 (no structure)	Formation of H_2	-	3.2	• A mixture of 17 wt% DMSO and 3 wt% water was used as the solvent • Enhanced thermal stability due to the presence of covalently bound nanodiamond	80
P-A-44 / P-A-46	-	UV	70 ± 2 (H_2)	H_2 changed to HPL	3.29	-	• Pairs of quantum-dot core-shell particles were confined within the center of mesoscale cylinders • Minor structure variations via limited swelling with water	132
P-A-47	-	I-15	50 (H_2)	Loss of some long-range order	6.14	5.1	• Photopolymerization resulted in loss of structure due to isomer changes before cross-linking • The cross-linked network showed photo-responsive behavior	133
P-A-48 / P-A-49	-	I-16	25 (Q_2)	Retention of the structure	12.3	13.5	• The polymerized LLC was soluble in organic solvents due to incomplete cross-linking but it showed higher thermal stability compared to non-polymerized LLC	108
P-A-50	This reactive surfactant has been used for transcriptive templating. See Table 1-3/M-4 section.							
P-A-51	This reactive surfactant has been used for transcriptive templating. See Table 1-3/M-7 section.							
P-A-52	-	I-5	10 – 50 (I_1, L_α)	Structure retention at high reaction rates	-	-	• The LLC structure was altered with changing pH at a fixed amphiphile content • L_α had the highest polymerization rate	122
P-A-53	-	I-1	93 (H_2)	Retention of the structure	4.81	4.56	• Similar activity and 10 times higher selectivity compared to industrially available catalysts for esterification reaction	134
P-A-54	This reactive surfactant was discussed in P-A-32/P-A-33 and P-A-53 sections							
P-A-55	-	I-1	90 (H_2)	Retention of the structure	4.7 - 5.7	4.83 - 5.67	• LLC structure depends on the nature of the acid used for LLC formation • No enhancement of enantio- or diastereo-selectivity by polyLLC	135
P-A-56	-	γ-ray radiation	a: 25 - 75 (H_1) > 66 (L_α) b: 45 - 75 (H_1) > 85 (L_α)	Retention of the structures	5.1 (H_1)	4.83	• The gel morphology was stable against temperature changes, extraction, drying, and reswelling with polar or nonpolar solvents	101
P-A-57	-	I-1	55 - 65 (H_1) 75 - 80 (L_α)	Retention of the structures	6.01 - 6.59 (H_1) 5.46 - 5.54 (L_α)	6.14 - 6.72 (H_1) 5.61 - 5.68 (L_α)	• P-A-57 cannot form LLC, but it can in combination with A-18b • Enhanced mechanical and thermal stability of the polyLLC when P-A-57 is used	81
P-A-58	-	UV	50 (H_1) 73 (L_α)	Retention of the structures	10.95 (H_1) 8.34 (L_α)	10.17 (H_1) 8.03 (L_α)	• The polymerized structure was destroyed when swelled by an organic solvent, but after drying and swelling with water, the original structure was retained	102
P-A-59a / A-7 / A-8	C-10b	I-1	~26.5 (L_α)	Retention of the structure	12.2	11.7	• Enhanced mechanical properties and preserving the structure after swelling even by organic solvents were the main characteristics of the obtained hydrogel	105
P-A-59	C-10b	I-1	22.8 (L_α + L_1)	Packed hard sphere structure	19.5	26.5	• P-A-59a was used in this study	105
	-	I-3 or I-9	5 - 24 (I_1 with FCC lattice)	Retention of the structure	~15 - 30	~15 - 30	• PolyLLC showed excellent mechanical properties, conductivity, and mechanoelectrical response • PolyLLC can be used as a motion and temperature sensor with sufficient sensitivity and accuracy	13,47, 48
P-A-60	C-1	I-12 or I-20	25 (Q_2)	Retention of the structure	-	-	• The LLC was used to prepare and polymerize nanoparticles with Q_2 structure (stabilized cubosomes)	110

* Calculated d-spacing for the primary reflection in the SAXS profile; TDS: Total dissolved solid; DOC: Dissolved organic carbon; FW: Flow back water; PDA: Polydopamine; CEES: 2-Chloroethyl ethyl sulfide; DMMP: Dimethyl methylphosphonate; DOP: Dioctyl phthalate; ChO: Chemical oxidation

1.4 Transcriptive LLC templating

Although synergistic templating is in many cases sufficient for obtaining polymerized LLCs with a variety of nanostructures for different applications, the tedious in-lab synthesis of many reactive amphiphiles can be a drawback. While some recent works have used commercially available formulation additives in conjunction with surfactants obtained from one-pot synthesis,[31] the synthesis of many reactive amphiphiles can be more involved (e.g. Gemini surfactants for cubic bicontinuous mesophases). This issue is also an obstacle in rapid industrial adoption of polyLLCs. Therefore, there have been several efforts to use a combination of commercially available surfactants and monomers instead. In this approach, a non-polymerizable surfactant is usually used to direct the LLC formation followed by the polymerization of the monomer. At the end of this process, which is called transcriptive templating, a polymer having the structure of the parent LLC is formed. Both ternary mixtures of water/hydrophobic monomer/surfactant and binary mixtures of hydrophilic monomer + water/surfactant are common in this templating approach. Despite the advantages obtained from easy sourcing of commercially available materials, preserving the structure of LLC template during polymerization is more challenging in transcriptive templating compared to synergistic templating. Because the formed polymer is not chemically bond to the surfactant, polymerization-induced phase separation/inversion becomes highly probable, reducing the chances of successful transcriptive templating. This issue has been addressed by addition of cross-linkers in the mesophase formulation, using reactive (co)surfactants, and employing block copolymer (BCP) surfactants. The first two approaches are centered around the formation of a kinetically trapped cross-linked network and the last one makes phase-separation/inversion process kinetically slow, enhancing the retention of the structure.[32] Transcriptive templating is very flexible since different monomers can be polymerized with the same surfactant system

without the need for synthesis of new chemicals. Moreover, copolymerization can also be used in the process to add chemical functionality to the final product.[136] As such, a wide variety of surfactants, (co)monomers, and cross-linkers have been used in transcriptive LLC templating, as shown in Figure 1-4 and Figure 1-5. A summary of the reported results for each monomer is presented in Table 1-3. Similar to synergistic templating, we will discuss the results of transcriptive templating for each type of LLC structure separately in the following sections.

1.4.1 Hexagonal (H_α)

Transcriptive templating of a variety of monomers has been reported for the hexagonal phase structure. Based on the employed surfactants and LLC formulations, lattice parameters of ~2.7 to ~14 nm have been obtained for the templated products, a range which is quite similar to that obtained for synergistic templating with H_α. As stated previously, the retention of structure in transcriptive templating is a major concern, especially after removal of the template. While most of the studies have used the three approaches mentioned above, Zhang *et al.* have also tried an additional step to preserve the H_1 structure directed by A-3 or A-14 surfactants after polymerization of M-24c and removal of the template.[137] They have reported that when the drying step is carried out under zero surface tension (by replacing water with CO_2) it is possible to retain the structure.[137] In another effort, they were able to retain the parent structure using a regular drying method via reinforcing the polymerized LLC by an in-situ formed silica network.[138] They have also shown that the required silica content for the structure retention can be reduced from 50 to 10 wt% with respect to the total monomer content if low surface tension solvents (e.g., mixture of hexane and ethanol) are used for the template extraction.[139] It is noteworthy to point out that the silica present in the polymerized domains of the obtained composite material not only participates

in the structure preservation, but also imparts relatively higher thermal stability[139] and enhanced hydrophilicity to the final product.[138]

There have been several efforts to utilize transcriptive templating of H_α structures in different applications. For instance, Guymon and co-workers have used this approach to prepare hydrogels that possess a proper balance of water uptake, swelling/de-swelling rate, and mechanical properties without compromising other properties such as stimuli-responsiveness and biodegradability.[36–46] They have also used transcriptive templating for compatibilization of immiscible monomers. To do so, hydrophilic M-24c and hydrophobic M-20 are mixed with the aqueous solution of A-14, resulting in the formation of a LLC with H_1 structure. The polymerization of these two monomers in the LLC template results in a semi-interpenetrating polymer network (IPN) structure having excellent polymer compatibility.[140]

Templating with H_2 structure has also been applied for the fabrication of water filtration membranes. In one such effort, Osuji and co-workers magnetically aligned the nanochannels of a H_2 phase before polymerization to decrease the tortuosity of the produced membrane. Although they were able to successfully retain the aligned structure after polymerization, the study did not extend to filtration membrane fabrication.[141] Qavi *et al.* have successfully utilized LLC templating of H_2 structures to fabricate ultrafiltration (UF) membranes that show excellent permeability as well as higher fouling resistance over commercially available UF membranes.[32] Successful production of antimicrobial UF membranes has also been reported by polymerization of M-32 in the same LLC structure.[142]

Fabrication of ordered mesoporous carbon (OMC) material is another application of transcriptive templating of H_1 structures. Polycondensation and cross-linking of monomers such as M-34, M-35, M-36 and M-37 results in a nanostructured thermoset polymer such as phenol-

formaldehyde. Subsequently, calcination and carbonization of the polymerized LLC at high temperature (e.g., above 600 °C) is carried out to obtain OMC species.[20,55,143–146] In the reported results, OMC materials obtained via this technique show extremely high thermal stability,[20,146] excellent mechanical properties,[20,55] enhanced electrochemical performance,[145] and promising CO_2 capture properties.[55]

1.4.2 Lamellar (L_α)

The Lamellar phases are easily accessible structures in most LLC formulations (especially in ternary systems). Several studies performed on transcriptive templating of L_α structure have reported lattice parameters between ~2.8 to ~10.5 nm. In most such studies, the focus has been on the investigation of fundamental/mechanistic underpinnings of retention of the L_α structure during templating as well as the polymerization kinetics in nanoconfinement. However, there are also studies which primarily focus on the templated products in particular application scenarios. As an illustration, Qavi *et al.* fabricated UF membranes with transcriptive templating of M-4 in lamellar structure directed by A-19c. According to the obtained results, L_α-based membranes not only show higher permeability and fouling resistance over commercially available UF membranes, but also exhibited slightly higher water flux compared to H_2-based membranes described earlier.[32] Antimicrobial membranes with lamellar structure have also been successfully fabricated.[142] In a recent trial, Bandegi *et al.* have produced a robust ion gel with decent ion conductivity by LLC templating in the presence of ionic liquids.[147,148] In other demonstrations of important applications of transcriptive templating in the lamellar phase, Guymon's team performed compatibilization of immiscible monomers[149] and synthesis of hydrogels which have a good balance of water uptake, swelling/de-swelling rate, and mechanical properties without changing the chemistry or sacrificing the general biocompatibility of the biopolymers.[46,89,150]

1.4.3 Bicontinuous cubic (Q_α)

The Q_α phases have been studied less than H_α and L_α for transcriptive templating due to the limited accessibility of bicontinuous cubic phase in LLC systems and difficulties in structure retention after polymerization. As shown in Table 1-3, lattice parameters of ~6 to ~23.5 nm have been reported so far for the Q_α structures used for the templating. In addition to the fundamental studies on the transcriptive templating process with this structure,[54,151–154] a handful of works have also investigated the applicability of the final product. For instance, Guymon's group has been able to produce a hydrogel with an improved water uptake and de-swelling rate while keeping the mechanical properties intact by taking the advantages of structural interconnectivity in Q_1 phase created by a mixture of A-13 and M-10.[155] They have also used bicontinuous cubic structure directed by A-15 to polymerize M-9 and produce a hydrogel with a faster swelling rate, higher swelling capacity, and higher compressive modulus over non-LLC product.[44] In another trial, they have employed P-A-37, a Gemini surfactant, to make Q_1 phase easily accessible. Although the retention of the structure after the template removal was not possible, they observed an enhanced swelling of the polyLLC in water and 2-propanol.[23] Generation of a Q_1 structured OMC material with excellent thermal stability and mechanical properties is another notable application of transcriptive templating via bicontinuous cubic mesophase.[20]

1.4.4 Discontinuous cubic (I_α)

The discontinuous cubic phases are the least studied structure for transcriptive templating. Almost all of the studies on these mesophases, which have been conducted by Guymon and co-workers, have focused on revealing the differences among LLC structures in terms of polymerization kinetics[36,37,39,40,43,44,99,156,157]. However, the observed higher water uptake in prepared hydrogels with micellar cubic structure over ones with H_1 structure[40], as well as the

impressive properties of the ion gels obtained from synergistic templating within discontinuous cubic structure[13,47,48] indicate that there may be plenty of opportunities in transcriptive templating of such structures to fabricate materials with exceptional properties.

Table 1-3. Summary of the reported results for transcriptive LLC templating.

Monomer	Amphiphile	Cross-linker	Initiation system	Amphiphile / monomer [w/w] and structure before reaction	Structure after polymerization	Lattice parameter before reaction [nm]	Lattice parameter after reaction [nm]	Remarks	Ref.
M-1	A-1	C-1	I-15	44.9 / 7 (Q_α)	-	-	-	• Uniform microporous materials of arbitrary size and shape was produced	151
	A-1	-	I-15 / UV	42.66-64.32 / 7.23-19.81 (Q_α)	Retention of the structure	6.01 - 10.017	Remained almost unchanged	• C-1 was also used as monomer instead of M-1 to increase the cross-linking density • Q_α structure was obtained in surfactant/oil ratio of 30.43 / 4.99 for C-1	54
	A-2	-	I-15	19.4 - 37.5 / 3.2 - 6.2 (Q_α)	Q_α changed to L_α	9.4 - 18.8	8.4 - 14.2	• Phase separation was observed between polymer and the template	152
	A-17	-	-	50 / 33 (H_1) 63 / 16 (L_α)	H_1 changed to L_α Disordered L_α	-	-	-	158
	A-19f	C-1	I-15	45 - 65 / 10 - 30	H_α or L_α having some disordered domains	-	-	• 1-Ethyl-3-methylimidazolium tetrafluoroborate ionic liquid was used as polar phase • Polymerization of M-1 was used to enhance the mechanical properties of the ion gel • High mechanical properties while maintaining proper ion conductivity was the main feature of the product	147
M-2	A-1	-	I-15	55 / 10 (Q_α)	Retention of the structure	-	11.8	-	151
M-3	A-3	-	I-2	35 / 25 (L_1) 40 / 25 (Q_1) 45 / 25 (H_1) 65 / 25 (L_α)	Retention of H_1	4.28 (H_1)	4.31 (H_2)	• Polymerization rate: $L_1 <<< Q_1 < H_1 < L_\alpha$ • Relative water solubility of M-3 resulted in polymerization in the polar domains of the self-assembled molecules and therefore encapsulation of the surfactant aggregates	159
	A-3	-	I-2	30 / 10 (L_1) 50 / 10 (H_1) 70 / 10 (Q_1) 75 / 10 (L_α)	-	-	-	• Polymerization rate: $L_1 <<< H_1 < Q_1 < L_\alpha$ • Higher reaction rate resulted in higher MW of the produced polymer	99
M-4	P-A-25 / P-A-50	C-7	I-18	63.2 / 19 (H_α)	Retention of the structure	5.37	5.5	• To be able to preserve the structure, 6.3 wt% cyclohexane was added to the mixture as a non-reactive oil phase • Nano-channels alignment was carried out via 5 - 6 T magnetic field before polymerization	141
	A-19	C-8	I-9 / I-15	55 - 60 / 25 - 30 (H_2) 50 - 60 / 10 - 15 (L_α)	Retention of the structures	10.2 - 10.4 (H_2) 7.4 - 8.5 (L_α)	10.4 - 10.7 (H_2) 7.8 - 9.2 (L_α)	• A-19c was used • The synthesized membrane showed excellent permeability as well as higher fouling resistance over a commercially used UF membrane	32
	A-19	C-8	I-15	40 - 55 / 25 (H_2) 57 - 60 / 25 (L_α)	Retention of the structures	6.6 - 7.4 (H_2) 6 - 10 (L_α)	7.32 - 7.41 (H_2) 6 - 10.18 (L_α)	• Polymerization rate: $L_\alpha < H_2 <<<$ non-LLC • A-19a, A-19c, and A-19d were used	56
M-5	A-3	-	I-2	50 / 25 (H_1)	Disordered structure	-	-	-	159
	A-3	-	I-2	30 / 10 (L_1) 50 / 10 (H_1) 80 / 10 (L_α)	Disordered structure for H_1	4.92 (H_1)	4.46 (H_1)	• Polymerization rate: $L_\alpha < H_1 < L_1 <$ mixed phase of L_1 and H_1 • Higher reaction rate resulted in higher MW of the produced polymer • Phase separation was seen for LLC and polymer for H_1 structure	99
M-6	A-3	-	I-2/I-5	35 / 10 (L_1) 40 / 10 (I_1) 55 / 10 (H_1) > 60 / 10 (L_α)	-	-	-	• Polymerization rate: $L_\alpha < H_1 < I_1 < L_1$	43
	A-3	-	I-2	40 / 25 (Q_1) 50 / 25 (H_1) 60 / 25 (L_α)	Disordered structure for H_1	5.52 (H_1)	4.25	• Polymerization rate: $L_\alpha < H_1 < Q_1$ • M-6 tends to be present at nonpolar domains, so the formed polymer framework was weak, resulting in structure disruption	159
	A-3	-	I-2	30 / 10 (L_1) 40 / 10 (I_1) 55 / 10 (H_1) 75 / 10 (L_α)	-	-	-	• Polymerization rate: $L_1 < L_\alpha < I_1 < H_1$ • The MW of the produced polymer increased from micellar to H_1 and then decreased in L_α structure	99
M-7	P-A-51 / A-16b	C-5	-	21.6 / 20 (L_α)	Retention of the structure	-	7.2	• 3.8 wt% P-A-51 was used in this study • The structure was retained even after removal of the template • 2 T magnetic field was used for the alignment of the structure before polymerization • Anisotropic increase of the dimensions through swelling with water	160
M-8	A-15 or A-20	C-8	I-18	7 -9 / 20 -37 for A-15 30 / 7.6 for A-20	-	-	-	• The produced copolymer showed continuous gel structures of high connectivity, where the gel is composed of polymer strings, resembling the morphology of a marine sponge • The type of surfactant had only a marginal influence on the final gel structure	136

Table 1-3. *(Contd.)*

Monomer	Amphiphile	Cross-linker	Initiation system	Amphiphile / monomer [w/w] and structure before reaction	Structure after polymerization	Lattice parameter before reaction [nm]	Lattice parameter after reaction [nm]	Remarks	Ref.
M-9	A-1 or A-16a	C-2	I-16 / UV	24.3 / 10 for A-1 (Q_α) 69.7 / 6.05 for A-16a (Q_α)	Retention of the structure	-	9.3 for A-16a	• n-Decane was also used in preparation of LLC with A-1	151,153
	A-10 or A-12	C-2	I-14	47.7 / 10 for A-10 (H_1) 50 / 10 for A-12 (Q_α and L_α)	Retention of the structures	4.53 (H_1) 3.81 (L_α)	4.69 (H_1) 3.69 (L_α)	• Q_α was obtained from ternary system of water/A-12/decanol	154
	A-5 or A-11	C-2	I-18	43 - 48 / 26 (H_1)	H_1 changed to L_α with A-11	-	-	• The structures can be destroyed with the removal of the template • The prepared gels can be chemically functionalized by incorporation of M-17, M-15, M-12, M-14 and M-13/M-21 • Enhanced mechanical stability of water-swollen gels obtained from templating	158,161
	A-14	C-2	I-18	6 -28 / 23 - 30	-	-	-	• Continuous gel structures of high mechanical strength was obtained due to the presence of a structure having connected spherical gel particles of ~ 500 nm diameter • The prepared gel showed a reduction of the moduli by only 10 - 40%	136
	A-15	C-2	I-5 or I-15	30 / 25 (L_1) 40 - 60 / 25 (Q_2) 70 / 25 (L_2)	Retention of Q_2	6.1 (Q_2) *	Remained almost unchanged	• Polymerization rate: non-LLC <<< $L_1 = L_2 < Q_2$ • Q_2 changed to L_α when I-15 was used to carry out the reaction at 60 °C • Faster swelling rate, higher swelling capacity and higher compressive modulus of the structured gel compared to non-LLC one	36,37,44,162
	A-14	C-2	I-5, I-6 or I-15	40 / 25 (I_1) 50 - 60 / 25 (H_1) 70 / 25 (L_2)	Retention of the structures when I-5 was used Disruption of the structures when I-15 was used for thermal polymerization	-	-	• Polymerization rate with I-5: non-LLC <<< $L_2 < I_1 < H_1$ • Polymerization rate with I-6: non-LLC <<< $I_1 \leq H_1 \leq L_2$ • Photoinitiation resulted in much faster polymerization rate compared to thermal initiation • Higher temperature resulted in lower reaction rate by changing structure to micellar • Slow reaction rate was the reason of structure lose after polymerization by I-15 • Anisotropic increase of the dimensions through swelling with water in the case of the LLCs polymerized via I-15 and I-5 at high temperatures • Higher water uptake for the polymerized Dis. Cube structure compared to H_1	36,37,39,40
	A-5 / P-A-10	C-2	I-2	50 / 20 (H_1)	No structure retention without A-5 Addition of 10-15 wt% P-A-10 to retain structure	4.53 - 4.68	5.58 - 6.04	• The polymerization rate increased with an increase in the content of P-A-10 due to the structure retention • Higher water swelling rate was seen for the hydrogel having H_1 structure • The water uptake decreased with an increase in hydrophobic P-A-10 content • The hydrogel with H_1 structure showed improved release properties • Higher compressive modulus was seen in dehydrated state for polyLLC compared to non-LLC sample	41
M-10	A-14	C-2	I-18	10 - 24 / 24 - 30	-	-	-	• A "cauliflower" morphology was obtained • The moduli of the formed gels strongly depend on the frequency and the gels have a low absolute strength	136
	A-13	C-2	I-2	50 / 20 (Q_1)	Retention of the structure	-	-	• 400% more water uptake in the temperatures less than 33 °C, similar compressive modulus despite of higher water uptake and higher de-swelling rate of templated hydrogel compared to non-LLC sample	155
	A-13	C-2	I-1	50 / 40 (H_1)	Retention of the structure	7.18 - 7.65	7.04 - 7.18	• M-29 was incorporated in the LLC (6.7 - 50 wt% with respect to the total monomer content) to improve the mechanical properties of the produced hydrogel without compromising other properties • Relatively lower water uptake, intact thermoresponsive behavior, high de-swelling rate and appropriate mechanical properties when M-29 was incorporated in LLC	42
	A-13	C-2	I-2	40 / 20 (Q_1)	Retention of Q_1 at low M-16 contents Q_1 changed to H_1 at 4 wt% M-16 content	-	8.24 (H_1)	• M-16 was incorporated in the structure of the LLC (up to 4 wt% with respect to the total monomer content) to improve water uptake while preserving other properties • Dramatic increase in water uptake, shifting the thermoresponsive behavior to higher temperatures and lower de-swelling rate by incorporation of M-16 in the LLC structure	38
M-11	A-14 or A-20	C-2	I-18	24 / 24 for A-14 28 / 14 for A-20	-	-	-	• Continuous gel structures of high mechanical strength was obtained • The prepared gel showed a reduction of the moduli by only 10 - 40%, a weak frequency dependence and low mechanical loss	136

Table 1-3. *(Contd.)*

Monomer	Amphiphile	Cross-linker	Initiation system	Amphiphile / monomer [w/w] and structure before reaction	Structure after polymerization	Lattice parameter before reaction [nm]	Lattice parameter after reaction [nm]	Remarks	Ref.
M-12	This monomer was discussed in M-9 section								
M-13	A-14 or A-20	C-8	I-18	24 / 24 for A-14 28 / 14 for A-20	-	-	-	• The obtained gel showed a morphology consisting of porous sheets • The prepared gels had a low absolute modulus and a very high mechanical loss	136
	A-3	C-9	I-2 / I-5	40 - 45 / 20 (I_1) 50 - 55 / 20 (H_1) 60 - 65 / 20 (L_α)	Disordered H_1 and L_α	4.2 (H_1) 2.96 (L_α)	4.4 (H_1) 3.22 (L_α)	• Polymerization rate: non-LLC < H_1 = I_1 < L_α • Lower water uptake, slower swelling rate and lower compressive modulus compared to non-LLC sample	43,44
	A-3	C-9	I-4	47.5 / 19 (H_1)	Retention of the structure	3.7	3.81	• The hydrophobic tails of the surfactant adsorbed to the hydrophobic SWNTs, resulting in the confinement of the nanoparticles inside the pores of H_1 structure • 5 T magnetic field was used to align the structure before polymerization	30
M-14	This monomer was discussed in M-9 section								
M-15	This monomer was discussed in M-9 section								
M-16	This monomer was discussed in M-10 section								
M-17	This monomer was discussed in M-8 and M-9 sections								
M-18	A-18b	-	EP	35 - 60 / 0.25 M (H_1)	Retention of the structure even after removal of the template	6.65	-	• LLC templating eliminated the need for post-polymerization methods (e.g., stretching and rubbing) to align the conductive film layer • Higher conductivity, and anisotropic absorption and conductivity of the templated film compared to the non-templated sample	163,164
	A-5	-	I-22	Up to 0.3 M monomer was used (H_1)	Limited retention of the structure	-	40 (thickness of spindle like nanostructures)	• Good thermal stability (up to 200℃) of the obtained nanostructures • Higher electrical conductivity of the produced nanostructures compared to non-templated products	165
M-19	A-18	C-4	PC	50 - 70 / ~8 (H1, L_α)	Formation of rod and sheet particles from H_1 and L_α, respectively after about 5 days	6.37 (H_1)	6.62 (H_1) after 5 days	• LLC structures were preserved after reaction.However, the structure of produced polymer changed from polyLLC to polymeric particles after ~ 5 days • Slow condensation and cross-linking kinetics, gradual build-up of molecular weight, and the nonlinear architecture of the polysiloxane molecules seemed to be the reason of the particles formation • The particles were thermally stable while the polymerized LLCs were not	166
M-20	A-3	-	I-2, I-5, I-6 or I-8	40 / 10 (I_1) 50 - 60 / 10 (H_1) 70 - 80 / 10 (L_α)	Retention of H_1	2.69 - 3.9 (H_1) 3.17 (L_α)	-	• Polymerization rate with I-2: $L_\alpha \leq H_1 < I_1$ • Polymerization rate with I-5: $L_\alpha < H_1 < I_1$ • Polymerization rate with I-6: $H_1 < L_\alpha < I_1$ • Polymerization rate with I-8: $L_\alpha = H_1 < I_1$ • MW of the produced polymer depends on the extinction efficiency of the initiator, monomer segregation, and LLC-dependent initiation efficiency	39,43,156, 157,167
	A-19b	-	I-10	18 / 10 (L_1) 40 / 10 H_1) 58 / 10 (Q_1) 78 / 10 (H_2) 82 / 10 (L_2)	Retention of H_1 and H_2	7.27 (H_1) 10.22 (H_2)	7.33 (H_1) 9.95 (H_2)	• Polymerization rate: $L_2 = H_2 < H_1 < Q_1 < L_1$ • Higher thermal stability of the templated sample in H_2 structure compared to H_1	45
	A-14	-	I-5	40 / 40 (H_1)	Retention of the structure	-	-	• 25 - 100 wt% M-24c was used with respect to the total monomer content along with M-20 • The water uptake decreased, and compressible modulus and Tg increased linearly with an increase in M-20 content approving the compatibility of two polymers via LLC templating	140
	A-14	-	I-2	30 - 40 / 20 (H_1) 50 - 60 / 20 (L_α)	Disordered L_α	6.16 (L_α)	-	• Polymerization rate: non-LLC < L_α < H_1	157
M-21	This monomer was discussed in M-9 section								
M-22	P-A-37	-	I-2	29 / 25 (H_1) 59 / 14 (Q_1) 64 / 25 (L_α)	Retention of Q_1 H_1 and L_α changed to Q_1	4.7 (H_1) 8.3 (Q_1) 2.8 (L_α)	6.5 - 6.8 (Q_1)	• Retention of the structure after surfactant removal was not possible • Higher 2-propanol swelling capacity of Q_1-structured sample compared to others • Water-swollen polymerized LLCs showed lower compressive modulus over less hydrated non-LLC one	23
M-23	A-3	-	I-2, I-5, I-6, I-7 or I-8	40 / 20 (I_1) 50 - 60 / 20 (H_1) 65 - 70 / 20 (L_α)	Retention of H_1 and L_α	-	-	• Polymerization rate with I-2, I-5, I-7 • Polymerization rate with I-8: $I_1 < H_1 < L_\alpha$ • Polymerization rate with I-6: $I_1 \leq H_1 << L_\alpha$	39,43,156, 167
	A-3	-	I-5	50 / 10 - 30 (H_1)	Retention of the structure with some structural changes at high M-23 contents	3.96 (10 wt% M-23) 3.6 (30 wt% M-23)	4 (10 wt% M-23) 3.82 (30 wt% M-23)	• Rod-like morphology was seen in SEM images at 30% M-23	168

Table 1-3. *(Contd.)*

Monomer	Amphiphile	Cross-linker	Initiation system	Amphiphile / monomer [w/w] and structure before reaction	Structure after polymerization	Lattice parameter before reaction [nm]	Lattice parameter after reaction [nm]	Remarks	Ref.
M-24	A-3	-	I-1	36.7 / 35.6 (H_1)	Retention of the structure after surfactant removal under certain conditions	3.87	3.82	• M-24c was used in this work • The retention of the structure was not possible after removal of the surfactant and drying under vacuum or via air drying • When drying was carried out by CO_2, it was possible to retain the structure thanks to maintaining zero surface tension	137
	A-3	-	I-1	36.7 / 35.6 (H_1)	Retention of the structure	3.6 (0% TEOS) 3.68 (10% TEOS) 3.98 (30% TEOS) 4.61(50% TEOS)	3.9 (0% TEOS) 3.6 (10% TEOS) 3.46 (30% TEOS) 3.41 (50% TEOS)	• M-24c was used in this work • A polymerized LLC reinforced by an in-situ formed silica network was produced The presence of silica network resulted in the retention of the structure even after the surfactant removal and drying under vacuum • Enhanced hydrophilicity of the product by incorporation of a silica network	138
	A-14	-	I-1	40 / 35 (H_1)	Retention of the structure	8.37 (0% TEOS) 8.88 (10% TEOS) 9.04 (30% TEOS) 9.39 (50% TEOS)	8.7 (0% TEOS) 8.35 (10% TEOS) 8.02 (30% TEOS) 7.5 (50% TEOS)	• M-24c was used in this work • A polymerized LLC reinforced by an in-situ formed silica network was produced • A mixture of hexane and ethanol was used as the low surface tension solvent to first extract the surfactant and then dry the samples • Drying via the low surface tension solvent mixture, reduced the content of the silica which is required for the retention of the structure • Relatively enhanced thermal stability of the product having silica network	139
	A-19b	-	I-5	20 / 10 (L_1) 44 / 10 H_1) 58 / 10 (Q_1) 81 / 10 (L_2)	Retention of H_1	7.33 (H_1)	7.27 (H_1)	• M-24b was used in this study • Polymerization rate: $L_1 < H_1 < L_2 < Q_1$ • Enhanced thermal stability and compressive modulus of the templated gel	45
	A-14	-	I-9	3 - 33 / 40 (L_1+ I_1) 33 - 38 / 40 (H_1) 38 - 42 / 40 (Q_1) 42 - 60 / 40 (L_α)	Retention of the structures	-	-	• M-24c was used in this study • Enhanced water uptake, rate of swelling and rate of diffusion for the obtained hydrogel with a change in structure from L_1 to lamellar	169
	A-14	-	I-2	40 - 50 / 20 (H_1) 60 - 70 / 20 (L_α)	Disordered H_1	6.27 (H_1)	7.6 (H_1)	• M-24a was used in this study • Polymerization rate: non-LLC < H_1 (50% A-14) <L_α (70%) < L_α (60%) < H_1 (40%)	157
	A-3	-	I-5	30 / 20 (L_1) 50 - 60 / 20 (H_1) 70 / 20 (L_α)	Retention of H_1 structure for M-24a Loss of order of H_1 for M-24e	For M-24a: 3.72 (H_1) For M-24e: 3.6 (H_1)	For M-24a: 3.7 (H_1) For M-24e: 3.8	• M-24a, d and e were used in this study • Polymerization rate: $L_\alpha < H_1 < L_1$ • Higher reaction rate at L_1 was more pronounced in the case of M-24e • Polymerization rate for M-24a was higher than M-24e in H_1 structure	168
	A-9	-	I-1	83.3 / 9.34 (Q_α)	Formation of HPL structure	-	-	• M-24b was used in this study • Due to the absence of a dense cross-linked network, almost 80% of ionic liquid amphiphile washed off with ethanol • Relatively low Tg, high thermal stability, and high resistance toward swelling in organic solvents and water were the important features of the product	88
	This monomer was also discussed in M-20 section								
M-25	A-14	-	I-9	45 / 40 (L_α)	Retention of the structure after surfactant removal	-	-	• The immiscible polymers of hydrophilic M-27a and hydrophobic M-25 was blended through LLC templating • Linear decrease of water uptake and linear increase of compressive modulus and Tg with an increase in M-25 content approved the compatibility of two polymers via LLC templating	149
M-26	A-14	-	I-9	40 / 40 (L_α)	Retention of the structure after surfactant removal	-	-	• The polymerization rate in LLC was faster than non-LLC phase	150
M-27	A-14	-	I-9	40 / 40 (L_α)	Retention of the structure	6.3	6.35	• Higher water uptake, permeability and degradation rate over non-LLC sample without changing the chemistry or general biocompatibility of the biopolymer	150
	A-14	-	I-9	35 / 40 (L_α)	Retention of the structure after surfactant removal	-	-	• Higher water uptake, rate of swelling and rate of degradation while having lower compressive modulus compared to non-LLC sample	46
	This monomer was also discussed in M-25 and M-28 sections								

Table 1-3. *(Contd.)*

Monomer	Amphiphile	Cross-linker	Initiation system	Amphiphile / monomer [w/w] and structure before reaction	Structure after polymerization	Lattice parameter before reaction [nm]	Lattice parameter after reaction [nm]	Remarks	Ref.
M-28	A-14	-	I-9	45 / 40 (L_α)	Retention of the structure	-	-	• The immiscible polymers of hydrophilic M-27a and hydrophobic M-28 formed interpenetrating polymer network through LLC templating • The water uptake decreased linearly with an increase in M-28 content	149
M-29	This monomer was discussed in M-10 section								
M-30	A-14	-	I-9	Specific contents of A-14 and 40 wt% M-30 (H_1, L_α)	-	-	-	• Enhanced water uptake of the gel obtained from the parent LLC with H_1 structure while maintaining high compressive modulus • The obtained gel from H_1 LLC structure seemed to be a perfect candidate for tissue engineering scaffolds	46
M-31	This monomer was discussed in synergistic templating. See Table 1-2/P-A-38 section								
M-32	A-19c	C-8, C-10a or C-11	I-18	50 / 17.5 (H_2) 50 / 25 (L_α)	Retention of the structures	9.3 (H_2) 6.9 - 7.4 (L_α)	9.5 (H_2) 7.3 - 7.5 (L_α)	• A mixture of M-4 and C-8 was also used as oil phase to enhance the mechanical properties of the polymerized LLC • No bacterial colony growth on the surface of the prepared membrane	142
M-33	This monomer was discussed in synergistic templating. See Table 1-2/P-A-10b section								
M-34	A-4, A-5 or A-6	-	-	1 / 1 - 6 molar ratio (H_1 and L_α)	Disordered structure at high M-34 contents	-	2.9 for A-4 * 3.5 for A-5 * 3.7 for A-6 *	• A base or acid was used to catalyze the condensation reaction • No porous carbon was obtained via LLC templating due to improper thermal stability of the structure	25
	A-19	-	-	1 / 0.5 - 2.5 (H_1, Q_1 and L_α)	Retention of the structures	-	9.8 - 14 (H_1) 12.6 - 23.5 (Q_1) 10.5 (L_α)	• A-19e, A-19f, and A-19g were used in this study • Ultrahigh thermal stability up to 1400 °C, mechanical stability up to 500 Mpa and proper high reverse electronic capacity was observed for the obtained mesoporous carbon material	20
M-35	A-5	-	-	2.1 / 1.2 (H_1)	Limited structure retention	-	3.7 - 4.2 *	• Ordered mesoporous carbon material was not obtained after removal of the template	170
M-36	A-19f	C-12	-	1 / 1 (H_1)	Retention of the structure	-	-	• Polymerization of M-36 was much faster than M-34 • Highly ordered H_1 structure was achieved by controlled solvent evaporation or a shear force	143
	A-19f	C-13	I-11	2 / 1 (H_1)	Retention of the structure	-	9.9 - 11.8	• Polymerization was faster in the presence of I-11 compared to the sample without initiator • Highly organized H_1 structure was obtained at high contents of I-11	144
	A-19f	C-13	-	2 / 1 (H_1)	Retention of the structure	-	9.5 - 12	• The product of bio-based material showed better electrochemical performance due to the presence of a more suitable/accessible porous structure	145
	A-19f	C-12 / C-14	-	2 / 1 (H_1)	Retention of the structure	-	-	• The product had a robust organic framework while maintaining a promising CO_2 capture property	55
M-37	A-19f	C-12	-	1 / 1 (H_1)	Retention of the structure	-	12.24	• The obtained highly ordered carbon material showed extremely high thermal stability and could be graphitized at 2400 - 2600°	146
M-38	A-19e	C-15	-	10 - 80 / 80 - 20 (L_1) 30 - 50 / 0 - 30 (L_α) 70 - 90 / 0 - 25 (H_1)	Order-order and order-disorder changes were observed	9 - 22 *	12.4 – 19 *	• C-15 also acts as structure directing agent instead of water • The structural changes continue even after completion of the polymerization	171
M-39	A-10	-	I-3 and γ-ray radiation	Up to 20 wt% monomer was used (H_1)	Retention of the structure when γ-ray radiation is used	7.5 *	18.4 *	• Micron-sized spherical particles were obtained by photo-polymerization • Nanofibers were obtained by γ-ray radiation • Conductivity of 10^{-1} S/cm was obtained for the obtained nanofibers which was higher than the reported values in the literature	172
M-40	A-5	-	I-22	Up to 0.1 M monomer can be used (H_1)	Retention of the structure	27 (diameter of the oil domain)	30 (diameter of the obtained nanowires)	• The optical band gap (estimated from the absorption edge, at 550 nm) of 2.25 eV was observed for the templated product • Strong absorption in the visible region was observed	173
M-41	A-10	-	I-17	Up to 20 vol% monomer content (H_1)	Limited retention of the structure under slow agitation of the mixture	-	100 – 200 (diameter of nanorods)	• Nanospheres were produced under vortex mixing • Nanorods were obtained under slow agitation of the mixture	174
M-42 / M-43	These monomers were discussed in synergistic templating. See Table 1-2/P-A-11 section								

* Calculated d-spacing for the primary reflection in the SAXS profile; SWNT: Single-walled carbon nanotube; EP: Electropolymerization; PC: Polycondensation

1.5 Kinetics of polymerization in LLC templates

Studying the polymerization kinetics in nanoconfinements of LLC templates is an attractive research ground not only due to the dramatic changes of the polymerization reaction rates in LLC templates, but also due to the important role of kinetics in ensuring structure retention during polymerization. As a rule of thumb, for both synergistic and transcriptive templating approaches, the faster the polymerization rate, the higher the probability of structure retention. When the reaction rate is high, the kinetically trapped cross-linked network forms rapidly, decreasing the chances of phase separation/inversion. This is why photopolymerization, which can often be completed in a few minutes, has been the first choice in most of the studies. The self-assembly of amphiphiles is temperature dependent.[73–75,124] In addition, the polymerization reaction is exothermic. Therefore, the change in temperature during non-isothermal reactions due to the heat of reaction may induce mesophase transition.[56] However, rapid formation of cross-linked polymer network can inhibit such phase separation/inversion.

Polymerization kinetics in different LLC structures have mainly been studied by Guymon and co-workers. They have shown that reactive sites segregation (e.g., double bond) and diffusion limitations are the main factors that determine the differences in the radical reaction rate among different mesophases.[27] The effect of the mentioned parameters will be discussed for the two types of LLC templating approaches separately in the following sections.

1.5.1 Synergistic LLC templating

In synergistic templating, the location of polymerizable group on the reactive amphiphile and the length of lipophilic chain are the main parameters that control the polymerization kinetics (see Figure 1-12).[27] The impact of polymerizable group placement on the kinetics has been demonstrated by comparing the reaction rates between P-A-4 and P-A-5 in which the reactive

groups are located on the lipophilic tail and hydrophilic head, respectively. Based on the reported results, the polymerization rate for P-A-4 increases when the LLC structure changes from lamellar to micellar cubic, whereas an opposite trend is seen for P-A-5. With a change in the structure from micellar cubic to lamellar, the proximity of the double bonds decreases for P-A-4, resulting in fewer propagation reactions and therefore a lower polymerization rate.[96–98] It is worth noting that the effect of the initiation system cannot be neglected in this comparison since applying γ-ray radiation on a similar templating formulation with P-A-5 results in a slightly different trend compared to photoinitiation method (see Table 1-2).[76] To evaluate the effect of lipophilic chain length on the reaction rate, one can compare P-A-5, P-A-6, and P-A-7 in synergistic templating. Under the same conditions (e.g., surfactant content), the reaction becomes slower with an increase in the chain length. The formation of LLC structures that offer lower local double bond concentration (e.g., micellar cubic) is the reason why slower polymerization rates are observed when lengthy surfactants are used.[89,98]

1.5.2 Transcriptive LLC templating

Studies on transcriptive templating have shown that monomer and initiator polarity are the key parameters controlling the polymerization kinetics, as schematically demonstrated in Figure 1-13. Hydrophilic monomers tend to be present at the interface of water/surfactant. Such arrangements inhibit termination reactions by limiting the mobility and diffusion of the propagating polymer chains. In addition, when the LLC structure changes from micellar to lamellar, the local concentration of monomer increases in the continuous polar domain, resulting in higher radical propagation rates. When the limited mobility of the propagating chains and higher local concentration of the monomer exist simultaneously, a dramatic increase in polymerization rate is

observed.[27] Hydrophilic monomers such as M-9,[36,37,39–41,44,162] M-13,[43,44] and M-23[39,43,156,167] have experimentally shown this behavior (see Table 1-3).

Hydrophobic monomers show the opposite behavior i.e. the polymerization rate decreases with a change in LLC structure from micellar to lamellar. The concentration of surfactant increases with a change in LLC structure from micellar to lamellar, resulting in an augment of the apolar domains' volume fraction. The local monomer concentration diminishes at higher apolar domain sizes which results in a lowering of polymerization rates.[27] Monomers such as M-4,[56] M-5,[99] M-6,[43,99,159] and M-20[39,43,45,156,157,167] are some of the hydrophobic species exhibiting lowered polymerization rates at high surfactant content, as shown in Table 1-3. A slightly different trend is seen for some of the monomers presented in Table 1-3. This is believed to be due to phase separation, which alters the local concentration, segregation, and diffusional behavior of the monomers. It is worth mentioning that M-3 exhibits unique behavior among hydrophobic monomers. As shown in Table 1-3, this monomer shows higher reaction rates when the LLC structure changes from micellar to lamellar, a behavior similar to the hydrophilic species. This observation is attributed to the partial water solubility of this monomer, which results in polymerization in the polar domains of the self-assembled molecules.[99,159] In addition to the monomer partitioning and mobility of the propagating chains, the effect of nanoconfinement on the polymerization rates cannot be underestimated. Qavi and co-workers have shown that the probability of termination steps increases when the reaction is carried out in nanoconfinement, with smaller domain sizes of polymerizing phase resulting in slower polymerization rates.[56]

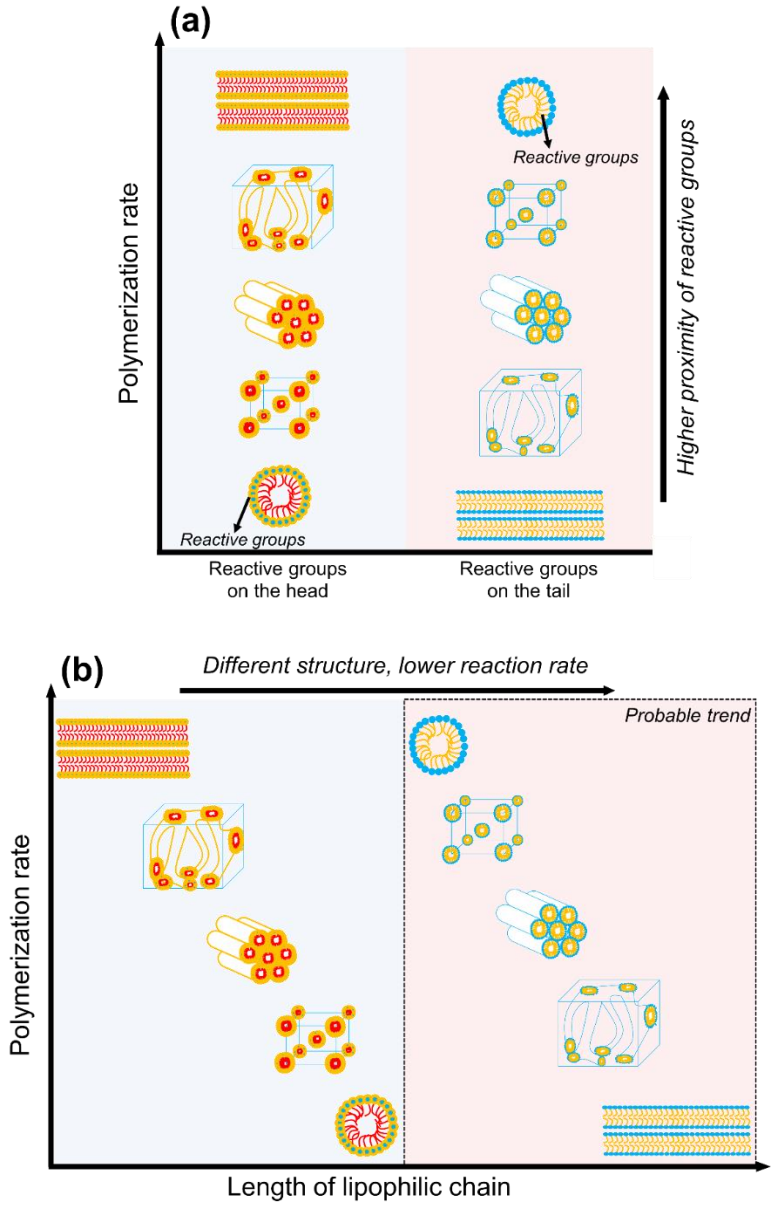

Figure 1-12. The relative effect of (a) polymerizable group placement on the reactive amphiphile and (b) the lipophilic chain length on the polymerization rate in synergistic templating. Different structures are obtained with an increase in the length of lipophilic chain, resulting in lower reaction rate. Higher proximity of the reactive groups enables higher reaction rates.[27]

The effect of the photoinitiator polarity on the reaction rate is another parameter that has been examined in the templating of M-20 and M-23 by Guymon and co-workers. [39,156,167] Generally, the initiation efficiency of the initiator is a measure of this effect. Higher initiator efficiency leads to

higher polymerization rates. The obtained results show that the efficiency of hydrophilic initiators (e.g., I-5) decreases as the structure changes from micellar to lamellar. The volume fraction of polar domains diminishes for this change in the structure, resulting in higher proximity of the molecules of the water-soluble initiator. When the free radicals are formed, radical recombination due to the cage effect occurs, usually producing nonreactive components which in turn result in lower initiator efficiency. On the other hand, hydrophobic initiators (e.g., I-6) are partitioned in the opposite way, resulting in lower probability of cage effects and thus higher initiation efficiency.[27]

1.6 Synergistic versus transcriptive LLC templating: a summary

So far, we have discussed the two types of LLC templating approaches in detail. As a summary of our discussion in previous sections, Table 4 lists the differences and advantages/disadvantages of the mentioned techniques.

Table 1-4. The differences and advantages/disadvantages of synergistic and transcriptive LLC templating methods in summary.

	Synergistic	Transcriptive
Differences	Reactive surfactant(s) is the polymerizable species	Reactive monomer(s) is the polymerizable species
Advantages	Chemically bonding the surfactant to the structure, and thus, a higher chance of structural retention	The commercial availability of the employed components (e.g., monomers and surfactants)
Disadvantages	Unavailability of commercial reactive surfactants, and thus, requiring multi-step synthesis methods to prepare surfactants	Physically bonding the surfactant to the structure and thus lower chance of structural retention

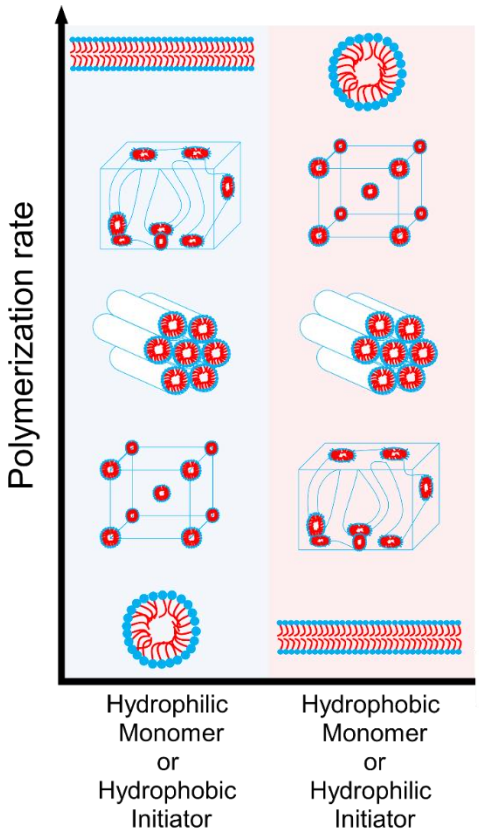

Figure 1-13. The relative effect of monomer and initiator polarity on the polymerization rate in transcriptive templating.[27]

1.7 Advanced functional materials: opportunities, challenges, and outlook

LLC templating is an efficient "bottom-up" approach to fabricate nanostructured polymers that can be applicable in a wide variety of applications, as shown in Figure 1-14. The membranes developed from the polyLLCs show enhanced permeability, selectivity, and fouling resistance compared to the current industry standard.[31–35] For instance, NF membranes having a thickness of 100 nm with effective pore sizes in the 1 nm range, MWCO ~300 Da, and permeability of ~20 liters m^{-2} $hour^{-1}$ bar^{-1} have been fabricated via polyLLC technology.[31,123] These membranes have better performance than the commercially available NF membranes like Dow FILMTEC NF90-400 which have typical permeabilities in the range of 10 to 15 liters m^{-2} $hour^{-1}$ bar^{-1}. The mentioned

polyLLC membranes have also an intrinsic degree of biofouling resistance thanks to the presence of water-facing quaternary ammonium groups available in the structure of the employed reactive surfactant (P-A-6). In another effort, NF membranes with Q_1 structure have been fabricated, which outperform the commercial NF90 (Dow Filmtec) membrane in the treatment of hydraulic fracturing produced water. These PolyLLC membranes show a thickness-normalized flux of ~2.9 liters m^{-2} $hour^{-1}$ µm (about 8 times of the commercial membrane) with much higher stability against fouling compared to NF90.[114] Additionally, the Q_1 membranes are able to recover up to 22% dissolved organic carbon while rejecting 75% of the salt which is a unique selectivity feature of these advanced materials over commercial opponents.[33] PolyLLC membranes have also proven advantages in breathable barrier materials for chemical agent protection. Dense polymers such as cross-linked BR, which are the common components used in such application, can cause heat and fatigue for the wearer as they are impermeable to water vapor. However, a proper water vapor permeability (~500 g m^{-2} day^{-1}) can be achieved without compromising the selectivity when BR incorporated polyLLC membranes are employed.[112]

The hydrogels prepared thorough the templating processes offer a proper balance of water uptake, swelling/de-swelling rate, and mechanical properties without compromising other key characteristics such as biocompatibility, biodegradability, and stimuli-responsiveness.[36–46] As an example, transcriptive templating has been used to fabricate nanostructured biodegradable hydrogel made of M-26 monomer, exhibiting 80% increase in network swelling and around 230% increase in diffusivity compared to the corresponding non-LLC polymer without changing the biocompatibility of the material.[150] Polyacrylamide hydrogels have been synthesized in LLC templates with ~ 10% higher water uptake and almost two times faster swelling rate than non-LLC analogous with no change in compressive modulus.[44] In another effort,[38] LLC templated poly(N-

isopropylacrylamide) (PNIPAM) hydrogels have been prepared, which not only show twice the equilibrium swelling of analogous non-LLC counterparts but also exhibit 5 times greater dynamic range between the swollen and deswollen state. In other words, the nanostructured hydrogels possess faster deswelling rates at temperatures above the lowest critical solution temperature (LCST) for PNIPAM. These important properties have further been improved via the incorporation of about 2 wt% M-16 in the polyLLC structure. [38]

The templating process can also result in conductive components with excellent mechanical properties compared to non-LLC materials.[13,47,48] The work done by Lopez-Barron *et al.* [13,47] is one of the best examples in this field. They have created *FCC* lattice by combining P-A-59 and a partially deuterated ionic liquid (ethylammonium nitrate) to fabricate a cross-linked ion gel having a highly elastomeric behavior with excellent mechanical properties, conductivity, and mechanoelectrical responses. The produced highly stretchable iono-elastomers (exhibiting a maximum elongation of 340%) are accurately and reliably sensitive to small motion as they show a linear strain-resistance response. Additionally, they have a large temperature-dependent conductivity (3.24 %/°C @ 30 °C) which is more than twice that of the most sensitive reported materials.[48] Therefore, they have been employed as thermo-mechanical sensors to capture the simultaneous/real-time strain and temperature of the human body during anaerobic exercise. This tough nanostructured material can resist external damages such as rubbing, pinching, and directional cutting while maintaining its functionality over 1000 cycles. Thus, it can potentially be used in sports training, prosthetic, personable healthcare, and robotics applications.[48]

It has also been shown that the nanostructured catalytic components obtained from mesophase templating exhibit unique catalytic activity/selectivity over commercially used catalysts.[29,49] For example, Gin *et al.* have shown that a polyLLC of P-A-26 with H_2 structure can be used as an

effective heterogeneous base catalyst for the Knoevenagel condensation of ethyl cyanoacetate with benzaldehyde while maintaining faster reaction compared to basic versions of zeolite-Y and MCM-41 mesoporous sieves.[29] In another study, heterogeneous polyLLC-based catalyst with the application in aerobic oxidation of alcohols has shown higher activity (~93% versus ~72% benzyl alcohol conversion) and selectivity (~4.2 versus ~1.9 benzyl alcohol/ 3,5-bis(*tert*-butyldiphenylsilyloxy)benzyl alcohol) over the industrially available TEMPO-based catalysts (e.g., Silicat® brand).[79]

The distinctive light emitting behavior of LLC templated products is another advantage of such materials over non-LLC ones.[50,51] PPV-incorporated polyLLCs with H_2 structure are the best example in this application. Photoluminescence quantum efficiency of about 80% has been reported for such nanostructured materials, which is much higher than 5 - 27% yields reported for the pure PPV. Additionally, the stability of PPV against oxidation can be improved by chain isolation/protection inside the polyLLC pores.[50] Polarized photoluminescence behavior can also be obtained by shear-aligning the PPV containing H_2 phase.[29] Moreover, metal-based luminescence can be introduced into this system by using transition-metal and lanthanide cations as the counterions.[78]

Although there have been plenty of studies on the advancement of LLC templating, some challenges still exist in the field. Scalability of the templating process is perhaps the most challenging hurdle to making polyLLCs fabrication applicable on larger scales. Synergistic templating requires reactive surfactants which are currently not commercially available and are usually synthesized through relatively complicated and expensive chemistries. This issue has been addressed by Gin's groups to a limited extent through the introduction of polymerizable species synthesized via cheaper raw materials (e.g., P-A-36).[118] The alternative approach is transcriptive

templating, although it requires a large amount of non-reactive components (i.e., surfactant) which are not chemically integrated in the polymerized phase.

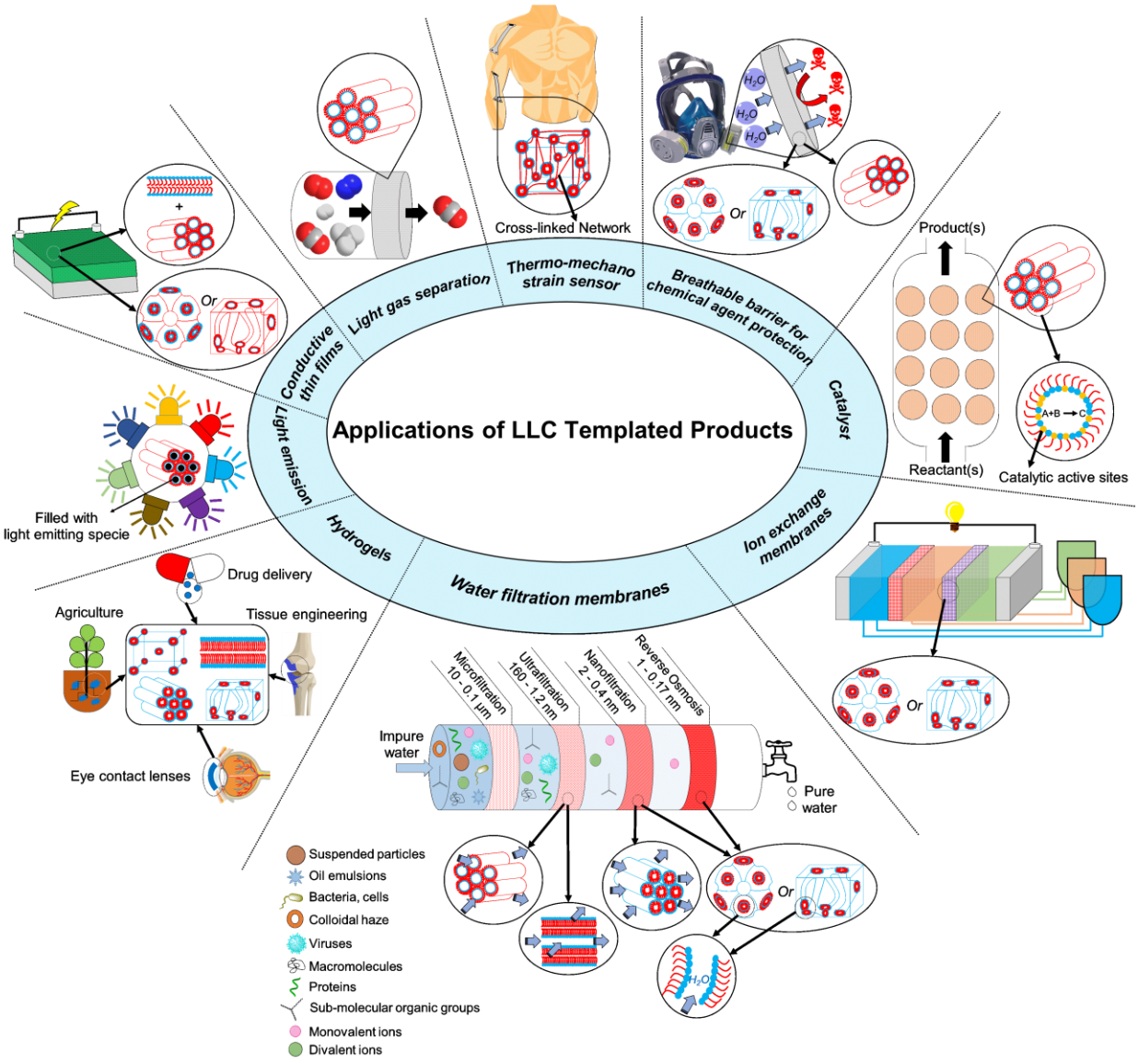

Figure 1-14. Potential applications of LLC templated products

For membrane applications, H_2 and L_α phases that are easily accessible suffer from improper alignment of the nanochannels and need additional pre-polymerization steps (e.g., magnetic alignment),[30] which are complicated and/or costly. On the other hand, no alignment is required for Q_α structure, but stable polyLLC structures are not easily achieved via commercially available

amphiphiles. This challenge can be resolved to a large extent by using easily accessible H_1 structures which do not need any alignment, as recently shown by Osuji and co-workers, using a synergistic templating approach.[31] The accessibility of the H_1 mesophase makes it a feasible structure for developing a broad range of membranes tailored for different uses, including ion transport,[31,123] and organic solvent nanofiltration.[125] Recent work by the same group[123] has demonstrated a solution-based process for rapid fabrication of ~100 - 200 nm thick membrane selective layers over large areas using H_1 mesophases. The permeability and rejection characteristics are on par with several commercial NF membranes, with effective pore sizes in the 1 nm range, MWCO ~300 Da and permeabilities ~2 liters m^{-2} $hour^{-1}$ bar^{-1} μm. At thicknesses of 100 nm, this corresponds to a permeance of ~20 liters m^{-2} $hour^{-1}$ bar^{-1}.

In the general liquid crystal literature, there are a plethora of studies on the influence of surface conditions to aid the anchoring/alignment of liquid crystalline molecules or phases. In commercial display devices based on nematic phases, surface modification by lecithin surfactant coatings or microgrooves[175] is used to order the nematic phases. For thermotropic mesophases, Osuji *et al.*, among others, have demonstrated the uniform homeotropic alignment of hexagonal cylindrical pores by confined annealing of the pre-polymerization phase between compatible substrates such as glass and Polydimethylsiloxane (PDMS).[176] There are also examples in literature utilizing surface anchoring techniques to align lyotropic chromonic liquid crystal phases.[177] It stands to reason that surface anchoring-based alignment techniques can be utilized to resolve the alignment issues for H_2 and L_α LLC structures. Foudazi et. al. have also shown that it is possible to induce the alignment in LLCs simply via applying large amplitude oscillatory shear, although further studies are still required.[148,178]

The typical molecular weight range of the amphiphiles (<2 kDa) discussed in this chapter necessarily limits the feature sizes of their lyotropic mesophases to the sub-10-nm, and more typically the sub-5-nm regime. Recent advances in block-copolymer self-assembly have enabled BCP systems which exhibit self-assembled features in the 5-10 nm range. Therefore, a continuous spectrum of options is provided for fabrication of self-assembled materials with features in the 1-5 nm range templated by polyLLC, and features larger than 5 nm enabled by BCP micro-phase segregation. However, there are at least two approaches based on lyotropic liquid-crystalline materials to obtain features sizes near- and beyond-10 nm.

The first of these approaches relies on so-called 'giant surfactants' or 'shape amphiphiles', which are higher molecular weight analogues of small-molecule amphiphiles. As summarized by Yue et al,[179] giant surfactant analogous can be synthesized to mirror their lower-MW polyLLC counterparts in terms of architecture i.e. single-headgroup single-tail, single-headgroup multiple tail, bolaform architecture, gemini architecture and beyond. Typically, the headgroup consists of a large 'cage' like structure, sometimes termed a molecular nanoparticle (MNP). MNP headgroups in giant surfactant literature[180] are most often fullerene or functionalized polyhedral oligomeric silsesquioxane (POSS) derivatives, although globular proteins[181] can also be incorporated as the hydrophilic head-groups . The most commonly studied tails in the literature are polystyrene tails. Work by Yu et al[182] has demonstrated that with appropriately designed chemical structures, POSS-PS giant surfactants can display most of the phases (micellar, lamellar, hexagonal, cubic) found in LLCs with 2 or 3 times larger periodicities i.e. 7 - 20 nm. Given the longer tail lengths and larger headgroup radii of giant surfactants compared to typical surfactants, the former provides many more atomic sites for targeted/localized synthetic modifications to increase functionality for advanced applications such as protein/biomolecular sensing platforms, although with the trade-off

of increased synthetic and purification complexity. In principle, the additional functional sites afforded by the larger molecular size could be utilized to incorporate unsaturated bonds/cross-linking sites in giant surfactant molecules. In one case,[183] a methacrylate cross-linker based on the giant surfactant headgroup (M-POSS) was utilized for phase preservation in a small-molecule amphiphile mesophase. However, in general, there is very little work focusing on synergistic or transcriptive templating for giant surfactant mesophases currently.

A second approach relies upon swelling of lyotropic bicontinuous cubic mesophases unit cell sizes by addition of charged lipids. Angelov et al[184] reported a 50% swelling in unit cell dimensions of a Diamond-type cubic bicontinuous phase consisting of an aqueous Monoolein cubic phase swelled with a small amount of octyl-glucoside, resulting in a lattice parameter of 15.3 nm. Work by the Brooks group has shown that increasing the formulation complexity of similar swollen mesophases of ternary lipid mixtures and beyond can yield even larger unit cell sizes and provide additional handles for controlling the unit cell spacing. Barriga and Tyler et al[185] have shown that addition of cholesterol and charged lipids to monoolein-water bicontinuous phase swell the primitive cubic unit cell spacing from ~10 nm to nearly 50 nm, while also enabling pressure and temperature sensitivity in the phase to tune the unit cell parameter. In a follow up work,[186] they further elucidate the importance of the electrostatic stability imparted to the swelled cubic bicontinuous phase by the added anionic lipid in the ternary mixture. This additional stability allows the mesophase to surpass the theoretically expected limit[187] of ~30 nm lattice parameter due to the effect of thermal oscillations. Recent work from Leal's group has demonstrated even larger lattice cell parameters. In glycerol monooleate based mesophases,[188] doped with charged lipids and poly(ethylene glycol) (PEG)-lipids, a gyroid phase with unit cell parameter 64.4 nm was obtained, corresponding to an estimated water channel diameter of 38 nm. Further work[189] on this

composition identified the role of the PEG-lipid composition as a reliable handle to switch the mesophase between diamond, gyroid and primitive cubic bicontinuous morphology. The larger water channels of the swollen lipidic mesophases reduce much of their suitability for selective separations such as filtration, but in turn enable their use in emerging biotechnology applications such as platforms for protein crystallization processes.[190]

Most of the existing literature on the aforementioned two approaches focuses on the chemical synthesis or formulation stability of the larger lattice parameter lyotropic mesophases. Neither approach has been extensively studied for phase and feature preservation after polymerization, thus presenting opportunities for future researchers to combine synergistic or transcriptive templating approaches to preserve large unit cell self-assembled mesophases of giant surfactants or swelled LLC phases.

The optimization of transcriptive templating recipes seems necessary to decrease the required concentration of surfactant and thus to improve the thermal and mechanical properties of the final products. Using specific types of amphiphiles which have very low CMCs (such as sodium alkoxy sulfate reported by Chen *et al.*[191]) might be helpful in resolving this issue. Furthermore, the high porosity of polymerized LLCs after extraction/drying of non-reactive component(s) results in poor mechanical properties. Although the random alignment of the nanostructures overshadows this effect to some extent, incorporation of nanoparticles (e.g., carbon nanotubes) in LLC structures might be a proper approach to overcome this challenge if the structure retention is not affected by the presence of nanoparticles.[80] Nanoparticles may induce heterogeneity in the structure or direct the self-assembly toward formation of a different LLC structure.

In addition to the discussed challenges, there are still some relatively unexplored application-oriented opportunities available in the field. For instance, production of stimuli-responsive (e.g.,

thermoresponsive and pH-responsive) membranes through LLC templating needs further attention. To the best of our knowledge, except for the reported works on LLC templated thermo-responsive hydrogels (hydrophilic polymers),[38,42] there is a handful of reports exploring the possibility of having dynamic pore sizes in stimuli-responsive polyLLCs.[126,133] According to the literature, stimuli-responsive membranes that possess inherent pore size tuneability exhibit higher water flux recovery and variable permeability/selectivity.[5,192] Application of LLC templating in the production of ion gels is another fertile research ground. The combination of BCPs and ionic liquids is the common approach to fabricate ion gels.[193–199] While this method works perfectly, in some cases, to preserve the conductivity of the obtained polymer electrolyte, a relatively high amount of ionic liquid is required which results in deterioration of the mechanical properties over time. To address this issue, a limited number of reports have used LLC templating to fabricate robust ion gels having proper conductivity.[13,47,48,147,148] Nevertheless, expanding the available formulations and using different structures are still required to improve the mechanical properties beyond those offered by the current polymer electrolytes.

There has been a great deal of interest toward commercialization of energy conversion devices in fuel cells and solar cells.[200] Therefore, it can be a great opportunity to employ polyLLCs with different nanostructures to improve the efficiency of such materials and thus facilitate the commercialization process. PolyLLCs and LLC templating methods offer several advantages over the materials and methods currently used in this field. For instance, microemulsion-templated products usually do not have anisotropic structure as L_α , H_1 and H_2 LLCs do.[200] Moreover, LLC templating is much more straightforward than multi-step gas bubble templating approach employed to create porous structures.[201] Additionally, templating with soft LLCs is simpler and

safer than employing hard templates which not only is a complex technique, but also is not safe as harmful chemicals are used for the template removal.[202]

Successful production of inorganic nanostructures (e.g., Pt, Pd and bimetallic) in LLC templates has already been documented. According to the experimental results, the obtained nanomaterials exhibit remarkable electrocatalytic activity, high conductivity and chemical stability, and low cost of production.[200] Nevertheless, there are still limited works on LLC templating of organic species. In one work, Hulvat *et al.* used M-18 in normal hexagonal structure to fabricate nanostructured conductive materials. The obtained products have shown higher conductivity compared to the non-templated formulation.[163,164] Similar increase in conductivity has been reported for the products obtained from LLC templating of M-18 by Ghosh *et al.*[165] In another effort, M-39 has been polymerized in H_1 structure, resulting in nanofibers with a conductivity higher than the values reported in the literature for same polymer.[172] M-40 has been used in LLC templating to fabricate nanostructured semiconductors with the optical band gap of 2.25 eV and strong absorption in the visible region, applicable in electronic devices or solar light harvesting applications.[173] Furthermore, there are some works in the literature showing that the properties of LLC-templated conductive polymers can be further enhanced by incorporation of inorganic nanoparticles in the LLC structure.[200] These appealing results confirm the potential of polyLLCs in this field.

Another area of opportunity lies in the use of polymerized LLCs to control the synthesis and organization of inorganic nanomaterials. The use of LLCs to template synthesis of nanostructured inorganic materials is well-known and is the basis for the production of mesoporous molecular sieves such as SBA-15[203] and MCM-41[204]. These siliceous materials are valued as catalyst supports[204,205]. The opportunity exists for templated synthesis of inorganic materials in the aqueous

channels of polymerized LLCs. A simple route for example is the formation of nanoparticles by reduction of precursor species (e.g., metal ions). The resulting nanomaterial-containing nanostructured polymer membranes are of potential utility as catalytic membranes. Early work by Gin *et al.*,[206] highlighted this potential with the formation of Pd nanoparticles in polymerized hexagonal mesophases derived from a wedge-shaped amphiphile. The concept of nanostructured catalytic polymer membranes is a compelling one. In some cases, rather than relying on the synthesis of a second phase material, the chemistry of the polar headgroup itself can be used, as demonstrated by Gin *et al.*, for Lewis[49] and Bronsted[95] acid catalysis. In total however, well-controlled nanomaterial synthesis in polymerized LLCs can be challenging due to the difficulties in controlling the polymerization, as identified in this chapter.

1.8 Overview of thesis research: goal and objectives

As we discussed in section 1.7, there are a plenty of research opportunities for LLC templating. The goal of this work is to synthesize stimuli-responsive membranes through transcriptive and synergistic LLC templating using thermoresponsive poly(ethylene oxide)-poly(propylene oxide)-poly(ethylene oxide) (PEO-PPO-PEO) triblock copolymer surfactants (known as Pluronics or Poloxamers). Pluronic block copolymers (see A-19 amphiphile in Figure 1-4 for chemical structure) come in a diverse array of types, each featuring a unique combination of molecular weight for the PPO block and weight percentage for the PEO block, as shown in Figure 1-15. Each Pluronic block copolymer is denoted with a letter that corresponds to its physical form. Specifically, the notation for each Pluronic begins with one of three letters: L for liquid, P for paste, or F for flakes. After the initial letter, there is a numerical code that indicates both the molecular weight of the PPO block and the weight percentage of the PEO block. As an example, consider Pluronic P84 and F88, which share the same molecular weight for their PPO block.

However, Pluronic P84 has a weight percentage of 40% for its PEO block, while Pluronic F88 contains 80% PEO by weight. As shown by Alexandridis *et al.*,[207–212] Pluronics can create LLCs with a variety structures upon mixing with water or in ternary systems with water and oil. Figure 1-16 exhibits phase diagram for Pluronic L64, Pluronic F127 and Pluronic P84, which have been used in this research.

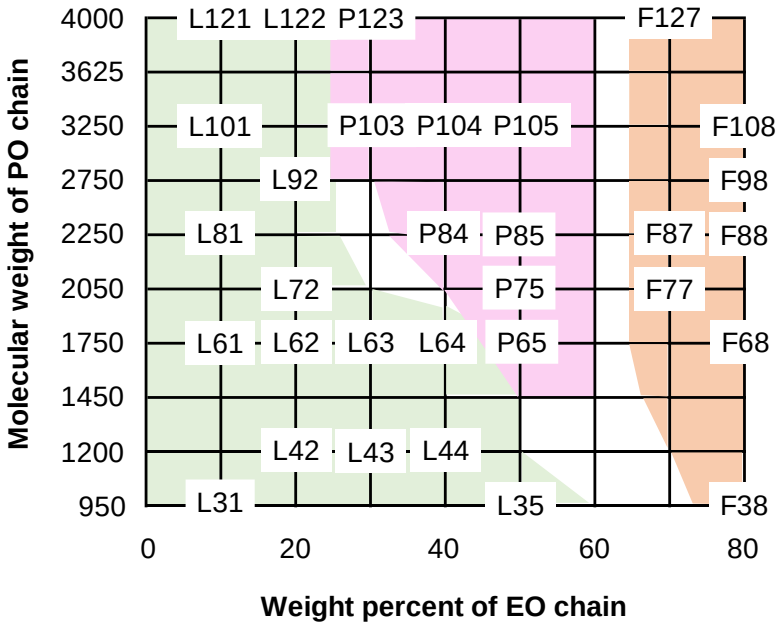

Figure 1-15. The Pluronic block copolymer chart displaying different types of the copolymer based on the PPO molecular weight and the weight percentage of PEO.[142]

Stimuli-responsive membranes can be synthesized in LLC templates directed by Pluronic block copolymers, which can alter their surface properties and pore structure via an external stimulus, such as temperature[192] and pH.[213] This behavior not only results in a tunable pore size and thus dynamic selectivity, but also improves the cleaning efficiency of the membrane after contamination with foulants. Using LLC templating will also address the challenges (e.g., little or no control over the size of pores, limited surface porosity and employing large quantities of organic

solvent) involved with non-solvent induced phase separation (NIPS), as the common method used to prepare such membranes.

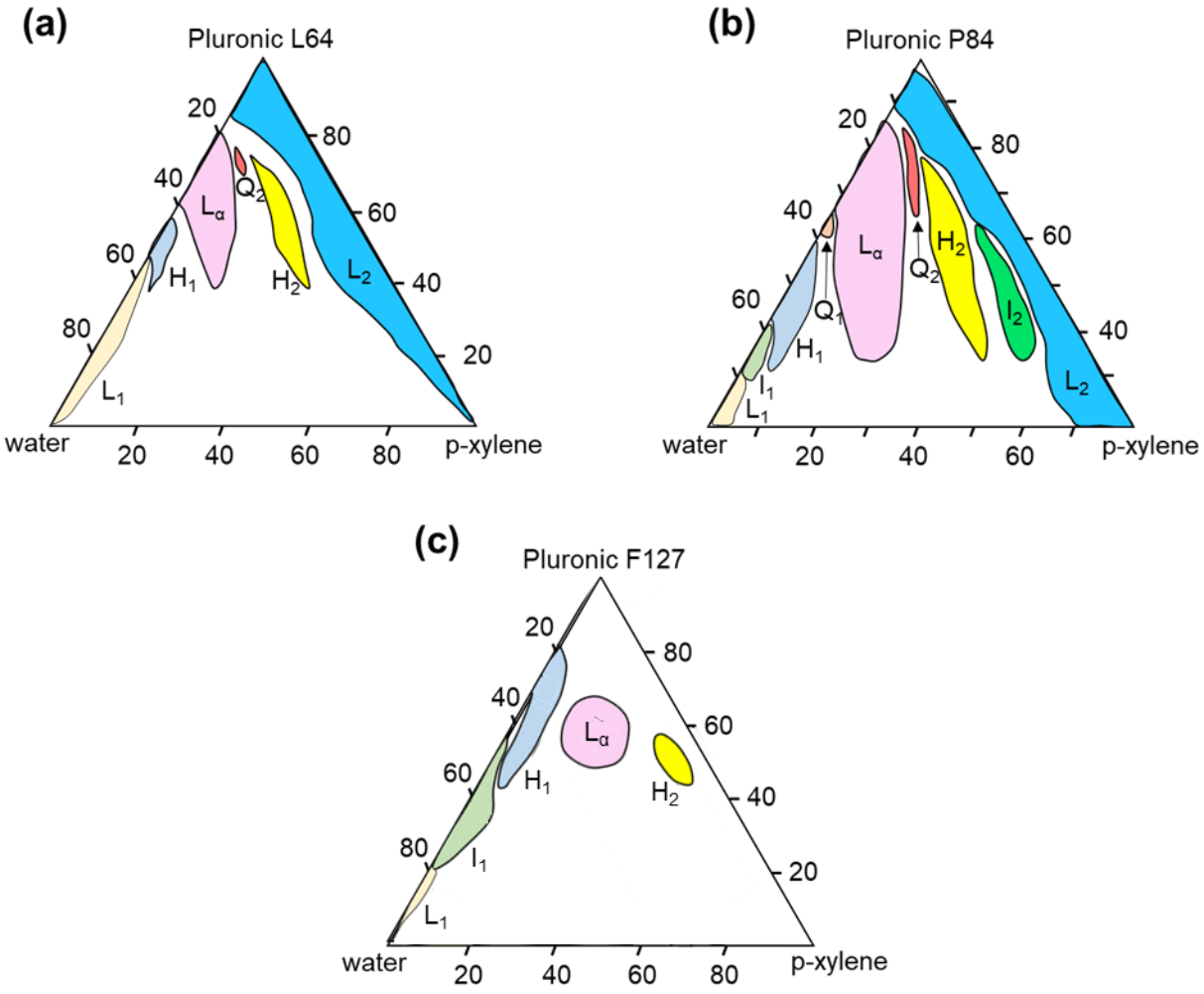

Figure 1-16. Ternary phase diagram of (a) Pluronic L64,[207] (b) Pluronic P84[212] and (c) Pluronic F127[209] in the presence of water and p-xylene. The concentrations are in wt%.

Throughout this dissertation, we are trying to answer following research questions to fulfill our goal:

I. How the polymerization kinetics, mesophase stability and mechanical properties of polyLLCs obtained from transcriptive templating can be controlled through changing the loci of initiation step of thermal polymerization?

II. To what degree can membrane created through transcriptive LLC templating employing a thermoresponsive surfactant adjust its pore size, permeability, and selectivity in response to temperature alteration? Additionally, how does the performance efficiency of this membrane in terms of permeability, selectivity, and fouling resistance compare to that of existing commercial alternatives?

III. What is the achievable pore size for UF membrane synthesized via synergistic LLC templating utilizing a reactive thermoresponsive surfactant? To what extent do changes in temperature induce variations in membrane pore size, permeability, and selectivity? How effectively does the synthesized membrane perform in terms of resistance to fouling caused by various ionic and nonionic species?

IV. What pore size can be achieved for NF membrane generated through synergistic LLC templating by employing a reactive thermoresponsive surfactant and an ionic monomer? How does the resulting membrane perform in terms of rejecting salts containing monovalent, divalent, and trivalent anions? To what degree do changes in temperature and pH affect the selectivity and permeability of the membrane?

Based on the mentioned research questions, the following objectives can be defined:

Objective 1: investigate how loci of initiation step of thermal polymerization affects the reaction kinetics, mesophase stability, and mechanical properties of polyLLCs formed using transcriptive LLC templating. The main objective is to identify a highly efficient initiation system for thermal polymerization that can retain the LLC structure during transcriptive templating. The findings of this investigation will be presented in Chapter 2.

Objective 2: assess the thermoresponsiveness of PolyLLCs produced through transcriptive LLC templating, utilizing a thermo-responsive surfactant. Additionally, the performance of these

PolyLLCs as a UF membrane will be evaluated. The results of this investigation will be documented in CHAPTER 3.

Objective 3: examine the thermoresponsiveness of polyLLCs produced through synergistic LLC templating utilizing a polymerizable Pluronic. Moreover, the performance of these polyLLCs as a UF membrane will also be evaluated. The results and conclusions of this investigation will be presented in Chapter 4.

Objective 4: assess the thermo- and pH-responsiveness of NF membranes produced through synergistic LLC templating using a polymerizable Pluronic. The findings of this investigation will be detailed in Chapter 5.

The conclusion of our research and outlook for future work are provided in Chapter 6.

CHAPTER 2: INITIATOR-DEPENDENT KINETICS OF LYOTROPIC LIQUID CRYSTAL-TEMPLATED THERMAL POLYMERIZATION[1]

2.1 Introduction

As we discussed in Chapter 1, the most important challenge in transcriptive LLC templating is preservation of the nanostructure during polymerization, which can be altered due to the phase-separation/inversion.[54,55] While cross-linking the polymer chains[31–35] and using block copolymer surfactants[45,143–145] are the main approaches to overcome this challenge, maintaining a fast polymerization rate can be a complementary method to kinetically trap the chains and thus retain the nanostructure. Furthermore, the polymerization kinetics can be used as a tool to predict any probable structural changes during templating since any discontinuities in the profile of the reaction rate can be a sign of structural alterations.[27]

Due to the importance of polymerization kinetics during LLC templating, Guymon and coworkers studied the kinetics of photopolymerization in LLCs for a variety of LLC formulations which we discussed in further details in section 1.5. Even though photopolymerization is frequently used in LLC templating, thermal polymerization is an alternative approach that is more favorable for industrial scale synthesis of polymers. However, there are few systematic works on evaluating the thermal polymerization in LLC templating. DePierro *et al.* have reported that it is challenging to preserve the LLC structure during thermal polymerization of acrylamide, possibly

[1] Reprinted with permission from Polymer Chemistry, 2021, 12, 2236-2252 with some modifications.

because of slow reaction rate.[40] However, Qavi and coworkers have shown the possibility to retain the structure (e.g., hexagonal and lamellar) when the thermal polymerization is used.[32,56] They have also found that the reaction is slower in nanoconfinements with lower domain size of polymerizing phase and attributed this observation to higher probability of termination reaction as well as free radicals recombination due to the cage effect.[56]

In this study, we use Pluronic L64, as the model Pluronic surfactant, in combination with water and oil phases to create inverse hexagonal (H_2) and lamellar (L_α) structures. The oil phase contains n-butyl acrylate (nBA) as monomer and ethylene glycol dimethacrylate (EGDMA) as cross-linker. Two types of thermal initiation system are used to polymerize the oil phase: initiation from water (IFW) by using ammonium persulfate (APS) and initiation from oil (IFO) by employing azobisisobutyronitrile (AIBN) or benzoyl peroxide (BPO). Despite the fact that monomer and crosslinker form the oil phase, we show that the polymerization rate is much faster in the case of IFW compared to IFO. Faster polymerization rate has already been reported for APS over AIBN in an inverse emulsion polymerization of acrylamide.[214] In such polymerization system, free radicals generated by oil-soluble AIBN diffuse into hydrophilic polymer particles as monomer-rich loci, resulting in slower reaction rate. In contrast, even though free radicals of water-soluble APS migrate into the monomer-rich oil phase in the current study, the reaction is still faster for APS compared to AIBN. Furthermore, our experiments reveal that in similar monomer conversions, the templated product using IFW system exhibits enhanced mechanical properties than the samples obtained from IFO approach. Both observations make the current study unique in terms of the effect of initiation system on polymerization kinetics as well as the mechanical properties of final products. We also study the effect of initiator concentration and the temperature on the polymerization kinetics.

2.2 Experimental

2.2.1 Materials

Pluronic L64 (PEO_{13}-PPO_{30}-PEO_{13}) with the polydispersity index of 1.1[215] was kindly provided by BASF. nBA, EGDMA, APS, AIBN and BPO were purchased from Sigma-Aldrich and used as received. Deionized water (0.055 μS/cm, EMD Millipore Direct-Q3) was used as the aqueous phase. The reaction scheme and chemical structures of the employed materials are shown in Figure 2-1a-e.

2.2.2 Preparation of mesophase samples

Pluronic/water/oil weight ratios of 50/35/15 and 55/15/30 were used to produce lamellar and hexagonal structures, respectively.[32] To prepare the mesophases, the components were mixed using centrifugation at 10000 rpm for 10 min. The centrifugation was repeated until a transparent gel was obtained. EGDMA concentration in the oil phase was adjusted on 30 wt% with respect to nBA content. For all of the initiators, 5 mol% concentration was used with respect to the total monomer content (nBA + EGDMA). To incorporate the initiators, APS was dissolved in water and the oil soluble initiators were dissolved in the monomer phase before mixing and centrifugation. To evaluate the effect of combining IFO and IFW systems on the polymerization kinetics, some samples were prepared with 2.5 mol% APS in water phase and 2.5 mol% AIBN or BPO in oil phase.

2.2.3 Structural characterization

A cross-polarized light microscope (model BX60, Olympus) was used to characterize the structure of mesophases before and after the polymerization to assess any structural changes upon reaction. A small amount of non-polymerized, mesophase sample was placed on a glass slide and covered with a glass cover slip. Cross-polarized images of samples were taken using a microscope-

mounted digital camera. SAXS was employed to further characterize the structure of LLCs before and after the reaction. The mesophase samples were loaded into quartz capillaries with a nominal diameter of 1.5 mm (Charles Supper Company, Natick, MA) by centrifugation, followed by sealing with critoseal and epoxy glue. The samples were then cured in the capillaries at 65 °C for 24 hours to study the structure after the polymerization. A Bruker Nanostar X-ray scattering system equipped with a monochromated Cu Kα radiation source was used for SAXS measurement. One dimensional (1D) scattering profiles were generated via azimuthal integration of the two-dimensional (2D) scattering patterns.

2.2.4 Polymerization kinetics

Isothermal differential scanning calorimetry (DSC) was performed using Q2000 (TA Instruments, New Castle, DE). Approximately 10 mg of mesophase sample was placed in a Tzero aluminum pan and sealed with a Tzero hermetic lid. The polymerization kinetics at 65 °C (± 0.1 °C) was studied under nitrogen atmosphere. To evaluate the effect of the reaction temperature on the reaction kinetics, some experiments were also performed at 55 and 75 °C. To determine the rate of polymerization (normalized to the total reactive concentration), the procedure developed by Guymon *et al.* was employed.[39,43,99,157] Having the heat flow, $Q(t)$, the polymerization rate, R_p, was calculated using Eq. (2-1):[56]

$$\frac{R_p(t)}{[M]_0} = \frac{Q(t)}{\left[Q_{monomer} + Q_{crosslinker}\right]} \tag{2-1}$$

Where $Q_{monomer}$ and $Q_{crosslinker}$ are the theoretical heat of reaction of monomer and crosslinker (in J), respectively. Eq. (1-2) can be written as following equation:

$$\frac{R_p(t)}{[M]_0} = \frac{Q(t)}{\left[\left(\frac{n\Delta H_p m}{M}\right)_{monomer} + \left(\frac{n\Delta H_p m}{M}\right)_{crosslinker}\right]} \quad (2\text{-}2)$$

where M, $[M]_0$, ΔH_p, n, and m are molar mass, initial concentration, reaction enthalpy (86,200 J/mol for acrylates and 56,000 J/mol for methacrylates),[216] functionality, and the total mass of corresponding species (i.e., monomer or crosslinker), respectively.[99,168] The degree of monomer conversion was calculated by integrating the area under the $R_p(t)/[M]_0$ versus time curve since $R_p(t)/[M]_0 = -\frac{dp}{dt}$ with p being the monomer conversion.[41] Schematic of the polymerization process in different LLC structures is shown in Figure 2-1f.

2.2.5 Chemorheology and mechanical properties

A stress-controlled rheometer DHR-3 (TA Instruments, New Castle, DE) was used to study the chemorheology and the mechanical properties of the polymerized samples.[56] A 40 mm sand blasted parallel plate geometry with 1 mm gap was employed in all of the experiments to suppress the wall-slip, which was confirmed to be indeed negligible in uncured and cured mesophases (Figure C1 in Appendix C) in agreement with previous study.[178] A solvent trap filled with deionized water was used to minimize any probable monomers or water loss during the reaction at 65 °C under the rheometer. In the case of chemorheology, the tests were performed in the linear viscoelastic region (0.1% strain, confirmed from amplitude sweep tests). The evolution of dynamic moduli with time at 65 °C was considered for determining the polymerization kinetics.[217] To evaluate the mechanical properties of polymerized LLCs, after curing the sample under rheometer, the temperature was decreased to 25 °C and then dynamic frequency sweep test was carried out in the frequency range of 0.1 to 400 rad/s.

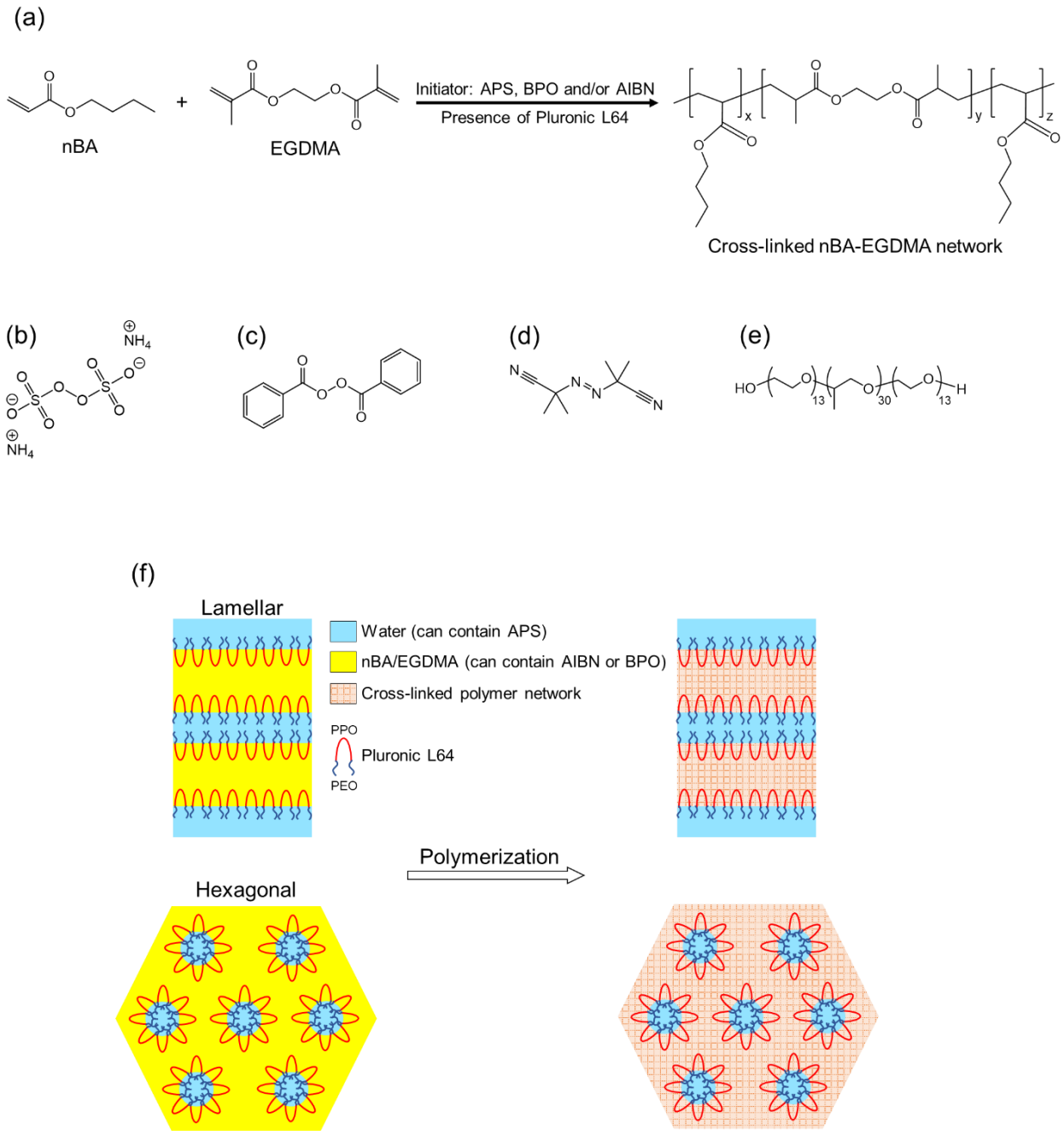

Figure 2-1. (a) Monomers and reaction scheme of their polymerization process in this study; (b-e) Chemical structures of initiators and surfactant: (b) APS, (c) BPO, (d) AIBN, and (e) Pluronic L64; (f) Schematic of polymerization process in lamellar and hexagonal structures.

2.3 Results and discussion

2.3.1 Cross-polarized light microscopy (CPLM)

Qavi *et al.* previously showed that Pluronic L64/water/oil systems with weight ratios of 50/35/15 and 55/15/30 have lamellar and hexagonal structures, respectively.[32] To confirm the preservation of these LLC structures after polymerization, cross-polarized light microscopy studies were carried out on the LLC samples before and after polymerization. The obtained results are shown in Figure 2-2. All of the formulations are birefringent before polymerization regardless of the applied initiation system as some textures are observed under CPLM. The absence of extinction (a dark image) in the CPLM photograph of polymerized species indicates that the structure remains birefringent after the polymerization using IFW or IFO systems.

2.3.2 Small angle X-ray scattering (SAXS)

To confirm the results of CPLM and study the structure of LLCs quantitatively, we performed SAXS analysis. The SAXS results for lamellar and hexagonal systems before and after curing with different initiators are shown in Figure 2-3. As expected, Bragg peaks with ratios of 1:2 and 1:$\sqrt{3}$ are observed for lamellar and hexagonal structures, respectively, before polymerization. The peaks with similar ratios are obtained after polymerization via different initiators for both lamellar and hexagonal phases. The only notable point here is the change in positions of the peaks after polymerization which is a sign of change in *d*-spacing of the structures after polymerization. Such structural changes have commonly been reported in the literature for polymerization of LLCs.[32,42,56,133]

Using the obtained data for the principal scattering vector, q^*, we can calculate the lattice parameter and nanoconfinement radius ($R_{h,max}$ and $R_{1,max}$ for hexagonal and lamellar, respectively)

for both structures using the equations presented in section 1.2.1 and 1.2.2 and following equations:

$$R_{1,\max} = \frac{\phi_{Oil} d}{2} \tag{2-3}$$

$$R_{h,\max} = a\left[\frac{\sqrt{3}}{4\pi}\left(1-\phi_{Pluronic}-\phi_{Water}\right)\right]^{\frac{1}{2}} \tag{2-4}$$

where ϕ_{Oil}, $\phi_{Pluronic}$, ϕ_{Water} are volume fraction of oil, Pluronic, and water, respectively.

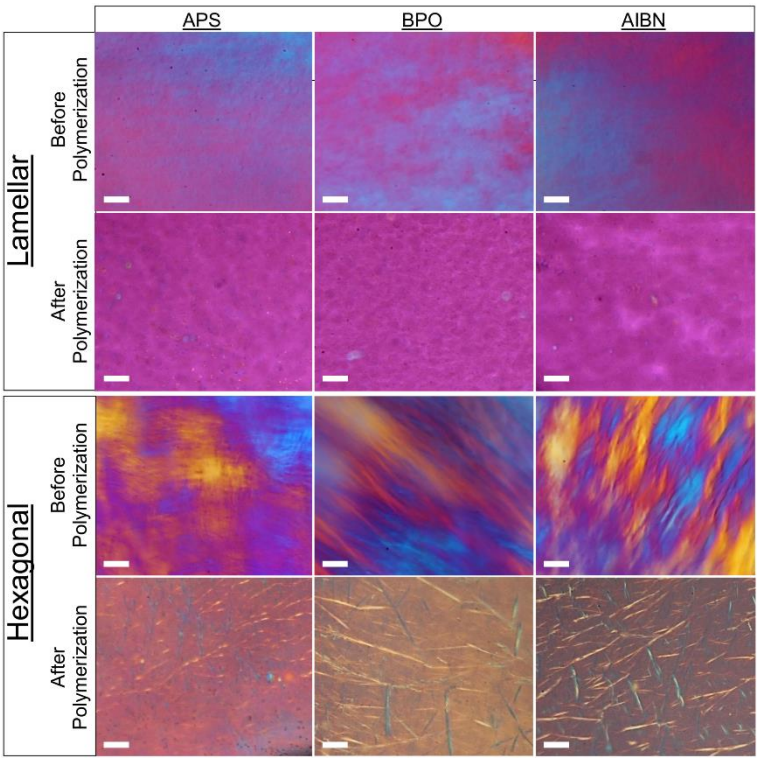

Figure 2-2. CPLM images of LLCs with lamellar and hexagonal structures before and after thermal polymerization by IFW and IFO systems. Scale bar: 50μm.

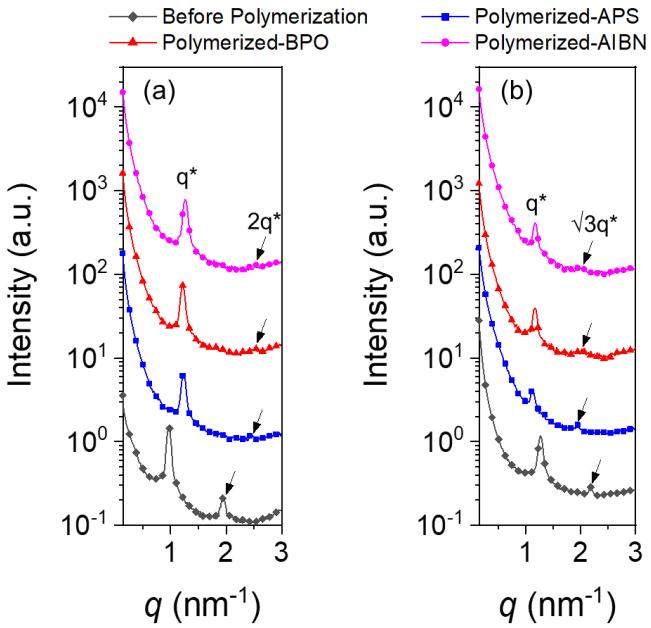

Figure 2-3. 1D SAXS data for (a) lamellar and (b) hexagonal phases before and after polymerization with different initiators. The plots are vertically shifted for clarity.

It should be mentioned that in these calculations, the volume fraction of apolar domain was defined as the volume fraction of the oil phase and PPO block. Additionally, the volume fraction of PEO chains and water was considered as the volume fraction of polar domain. To calculate the mentioned volume fractions, we followed the assumptions and procedures proposed earlier.[32] Briefly, by considering the complete segregation of the water, PEO, PPO, and monomer phases and thus using their bulk density, the volume fractions are calculated. The radius of gyration (R_g) for Pluronic P85 (PEO_{25}-PPO_{40}-PEO_{25}) is 1.7 nm.[218] Pluronic P85 has a higher polymerization degree than Pluronic L64, thus, the latter has even smaller R_g. Therefore, as discussed by Qavi *et al.*,[62] there is hardly any bridging between polar/apolar domains by Pluronic chains in this system.

Table 2-1 shows the results of the aforementioned calculations. The confinement size almost remains unchanged regardless of the employed initiation system. Additionally, the confinement size is bigger for hexagonal structure compared to lamellar one, which can significantly affect the

polymerization kinetics, as previously reported in the literature[56] and will be discussed in the following sections. It is also noteworthy that the lattice parameter changes upon polymerization for both structures, which is a common phenomenon in polymerization of LLCs that happens due to the formation of polymer network and thus the competition between thermodynamics and kinetics.[42] In terms of thermodynamics, the thermodynamic penalty of mixing increases by increasing the molecular weight of the oil phase. Such increase in the thermodynamic penalty coupled with the change in surface energy of the polymerizing phase can induce phase separation, resulting in the domain size increase. On the other hand, the density increases due to the formation of polymer network (shrinkage of the polymerizing phase) which can result in smaller domain sizes. Due to the suppression of the chains mobility by the cross-linking, the phase separation and thus complete loss of nanostructure is avoided, but yet the domain size is controlled by the competition between demixing and shrinkage.[32,219] In the case of lamellar structure, ~20% decrease in lattice parameter is seen after polymerization for all of the initiators which is higher than the changes typically reported for similar systems.[32] Formation of lamellar structure with smaller lattice parameter due to the probable phase separation during reaction, decreasing the density and water loss (water expulsion form the polar domain and/or water evaporation during reaction) can be responsible for such observation. For the hexagonal phase, there is an approximate 10% increase in the lattice parameter, indicating a probable demixing during the reaction.

Table 2-1. Calculated parameters for different LLC structures before and after polymerization.

Sample	LLC structure	Lattice parameter (nm)	ϕ_{Oil}	$\phi_{Pluronic}$	ϕ_{Water}	Confinement size (nm)
Unpolymerized	L_α	6.40	0.16	0.49	0.36	~0.5
	H_2	5.75	0.31	0.54	0.15	~1.2
APS-initiated	L_α	5.06	0.16	0.49	0.36	~0.4
	H_2	6.47	0.31	0.54	0.15	~1.3
AIBN-initiated	L_α	4.98	0.16	0.49	0.36	~0.4
	H_2	6.25	0.31	0.54	0.15	~1.3
BPO-initiated	L_α	5.15	0.16	0.49	0.36	~0.4
	H_2	6.25	0.31	0.54	0.15	~1.3

2.3.3 Thermal polymerization kinetics

DSC was utilized to study the thermal polymerization kinetics in LLC nanoconfinements dependent on initiators. The calculated normalized polymerization rate and overall monomer conversion for LLC structures are shown in Figure 2-4. It is noteworthy that for all of the initiation systems, the absence of any fluctuation and/or discontinuities in DSC results (see Figure C2 in Appendix C for typical raw DSC data) confirms that no structural changes happen during polymerization of LLCs.[27] This conclusion agrees with SAXS results, proving the retention of structure during polymerization of studied samples.

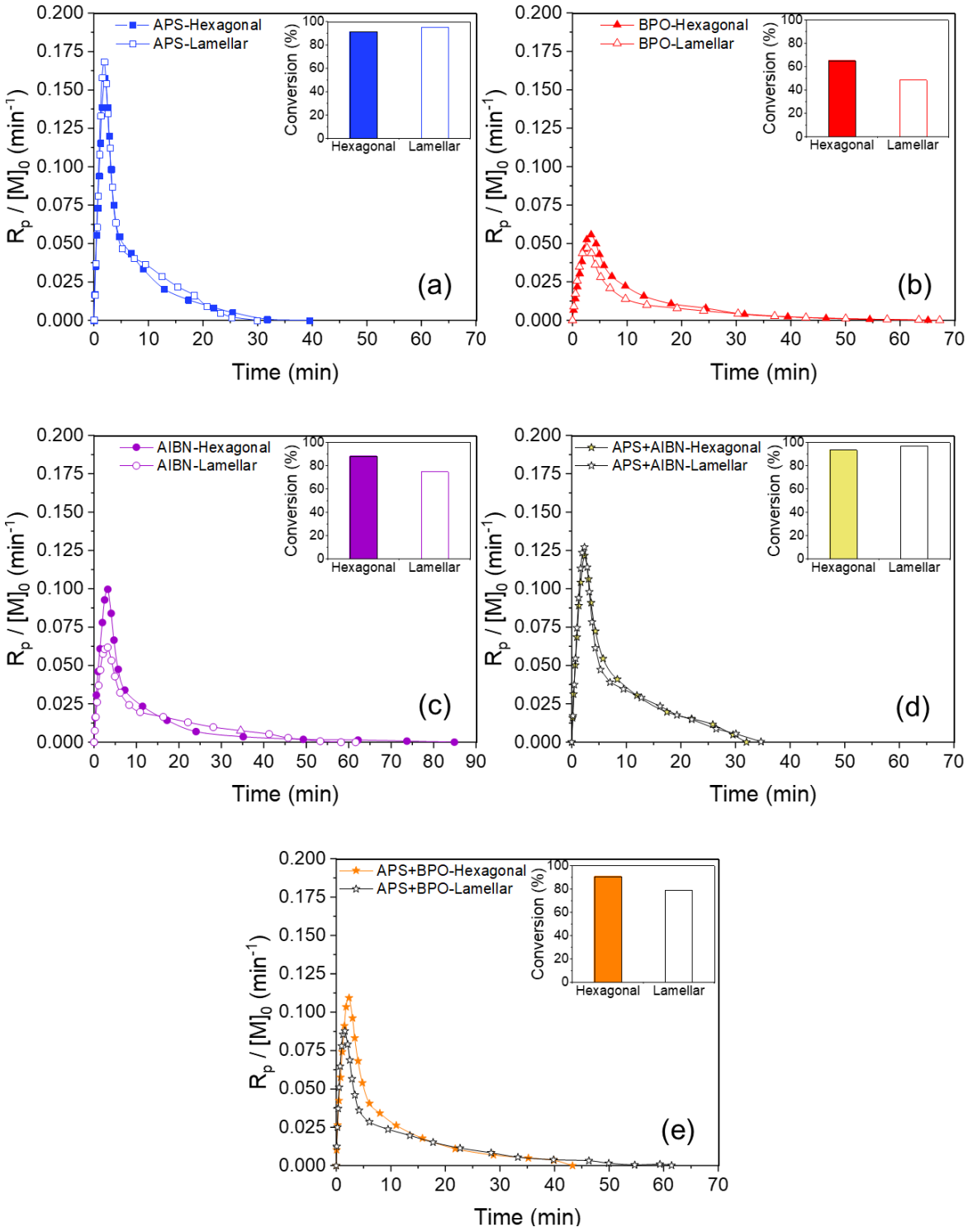

Figure 2-4. Normalized polymerization rate versus time and overall monomer conversion obtained from thermal polymerization in hexagonal and lamellar structures using different initiation systems: (a) APS, (b) BPO, (c) AIBN, (d) APS+AIBN and (e) APS+BPO. For all samples, the total initiator concentration of 5 mol% was used with respect to the total monomer content.

Unexpectedly, APS-initiated thermal polymerization (IFW) shows much faster polymerization rate compared to the IFO reactions initiated by AIBN and BPO. The maximum polymerization rate for IFW system is ~2.5-3 times higher than for IFO ones. Furthermore, the overall monomer conversion is more than 90% for IFW, whereas less than 75% conversion is achieved with IFO approach. One might argue that such difference is due to the different free radical concentrations generated by different initiators. To examine this hypothesis, we calculated and plotted the theoretical concentration of free radicals (normalized with the initiator efficiency) produced by different thermal initiators over time at 55, 65, and 75 °C and initial initiator concentration of 5 mol% with respect to the total monomer content. The calculation and results are presented in Appendix C (the text and Figure C3). AIBN has the highest free radical generation capability and the concentration of the free radicals generated by APS is in between of AIBN and BPO. Therefore, the free radical concentration is not the only factor determining the reaction rates for different initiation systems.

To further evaluate IFW and IFO, we polymerized the oil phase in the same structure using a combination of IFW and IFO systems (APS+AIBN and APS+BPO). We used 2.5 mol% of each initiator to adjust the total initiator content to 5 mol% with respect to the total monomer concentration. The acquired results show that the reaction kinetics for IFW+IFO fits in between of IFW and IFO systems. Additionally, the maximum polymerization rate is almost doubled for both AIBN and BPO when combined with APS. Furthermore, the overall monomer conversion enhanced from ~75% to ~97% and from ~50% to ~80% for AIBN+APS and BPO+APS, respectively. These results become interesting when we compare the free radical concentration trend for the mixed initiation systems with those for separate initiators (see Figure C3). The concentration of active sites decreases when we combine 2.5 mol% APS with 2.5 mol% AIBN,

but the reaction rate as well as monomer conversion increases compared to 5 mol% AIBN alone. In contrast, the free radical content of 2.5 mol% BPO combined with 2.5 mol% APS is higher than that of 5 mol% BPO and still the polymerization rate and monomer conversion improve. Based on these observations, one may suggest that there is another important factor controlling the polymerization kinetics in the nanoconfinements of the LLCs. To determine the controlling parameter, we performed the same experiments with hexagonal LLC structure to investigate if the same trend is observed for polymerization kinetics.

As shown in Figure 2-4, the reaction kinetics in the hexagonal LLC changes in a fashion similar to what is observed for lamellar phase, i.e., the fastest polymerization rate is observed when APS is used. The maximum reaction rate for APS is ~1.6 and ~2.7 times higher than that for AIBN and BPO-initiated samples, respectively. The monomer conversion of about 90% is achieved for APS and AIBN, whereas the conversion of 65% is seen for BPO. Furthermore, similar to the polymerization in lamellar structure, an improvement in the polymerization rate as well as monomer conversion is seen for AIBN+APS and BPO+APS.

Although the overall trends of polymerization kinetics are similar in lamellar and hexagonal structures, some noticeable differences exist in terms of the values of polymerization rates and monomer conversions. Therefore, it seems crucial to have a comparison between the results for lamellar and hexagonal phases. Since we have normalized the polymerization rate to the monomer concentration, we can compare the polymerization kinetics irrespective of monomer concentration difference between these two LLC structures. Analysis of SAXS data revealed that the nanoconfinement size of 0.5 and 1.2 nm is obtained for lamellar and hexagonal LLCs, respectively. Qavi *et al.* have shown that as the size of confinement decreases, the local concentration of radicals and macroradicals increases, enhancing the termination reaction as well as free radicals

recombination due to the cage effect and thus slowing down the polymerization in LLCs.[56] These findings can be explained via overall rate of polymerization formula shown as Eq. (2-5) which can be derived under steady state conditions (the rate of initiation is equal to the rate of termination). In this equation, k_d, k_p, k_t, *[M]*, *[I]*, and *f* are kinetics rate constant of initiator decomposition, the propagation rate constant, the termination rate constant, monomer concentration, initiator concentration, and initiator efficiency, respectively. Based on this equation, any phenomenon that results in slower termination rate (lower k_t) can enhance the overall rate of polymerization. Trommsdorff or Norish-Smith effect, which is also known as autoacceleration, is the best example of such phenomenon. Autoacceleration occurs when viscosity of the reaction medium significantly increases due to reaching a specific monomer conversion and polymer molecular weight. According to Norrish and Smith, and Trommsdorff,[216] under these conditions, the probability of collisions between growing chains decreases due to the diffusion limitations, leading to limited termination of the reaction. As a result, the ratio of k_p^2/k_t increases significantly (up to a hundredfold), leading to a significant increase in the polymerization rate. Under nanoconfinement, however, the likelihood of chain termination rises as a consequence of the proximity of the growing chains to one another, resulting in slower rate of polymerization. The confinement can also elevate the possibility of free radical recombination because of the cage effect, leading to a decrease in initiator efficiency (*f*) and ultimately resulting in a slower polymerization rate. Evaluation of the molecular weight of the produced polymer at the same initiator content is an approach to determine whether the polymerization rate is governed by the rate of termination. Slower reaction rates that lead to lower molecular weights are indicative of an increase in termination reactions.[99] In the current study, conducting this experiment seems unfeasible due to the crosslinking of the polymer phase, which is implemented to mitigate phase separation during the reaction.

$$R_p(t) = k_p \left(\frac{f k_d}{k_t} \right)^{\frac{1}{2}} [I]^{\frac{1}{2}} [M] \qquad (2\text{-}5)$$

Similar to the results of Qavi *et al.*,[56] lower reaction rate and monomer conversion is observed for lamellar structure for BPO- and AIBN-initiated reactions. In APS-initiated systems, however, the polymerization rate and overall monomer conversion is slightly higher for lamellar structure compared to hexagonal counterpart. We hypothesize that since the free radicals of APS are generated in the non-reactive phase and then migrate into the monomer phase, the local concentration of radicals/macroradicals gradually rises in the monomer phase. This phenomenon lowers the chance of the termination reactions. In addition, the higher contents of active species near the walls in IFW system can have a similar effect on the polymerization rate as reported for the polymerization in hard templates,[220] in which the template surface acts as a catalyst for initiation, resulting in higher polymerization rate at early stages. When comparing lamellar and hexagonal structures, we note that the different trend in APS initiated system is caused by the competition between (i) gradual increase in radicals/macroradicals initiated from interface and (ii) enhancement of the termination reactions due to confinement. In AIBN and BPO initiated systems, only the latter phenomenon is dominant.

Combined APS and AIBN initiators show an improvement in the polymerization rate and monomer conversion in hexagonal structure similar to lamellar phase. The reason for such improvement is that the concentration of free radicals generated by AIBN decreased in half and the other half is gradually provided by APS, resulting in lower termination rate in oil phase. Thus, the chain propagation rate increases in AIBN+APS system. The same improvement is also noticeable for the combination of APS and BPO over IFO polymerization with BPO. Nevertheless, for both BPO and APS+BPO cases, hexagonal structure still exhibits faster polymerization rate as

well as higher monomer conversion than the lamellar one. Given the fact that BPO generates less free radicals compared to APS and AIBN (see Figure C3), enhanced termination reaction is not the only factor affecting the polymerization kinetics initiated by BPO. One phenomenon that might predominate in BPO-initiated system is the recombination of free radicals due to the cage effect in the nanoconfinements of lamellar structure. In other words, under nanoconfinement, the initiator efficiency (*f* in Eq. 2-5) is much lower for BPO in comparison to other initiators. Bigger size of radicals generated by BPO compared to those by APS and AIBN can be the reason of such difference. Relative immobility of radicals under nanoconfinement increases the chance of their recombination. Similar observation has been reported by Guymon and coworkers for polymerization of LLCs using different photoinitiators.[39] To prove this hypothesis, further tests were required to shed lights on this point.

We evaluate if combining IFO and IFW systems has a synergistic effect on the polymerization rate in LLCs. Table 2-2 lists the average values of maximum polymerization rate and overall monomer conversion for different initiation system. It also contains the theoretical average values of IFO and IFW systems and compare them with the experimental results for IFW+IFO system. Synergistic effect is evident for the monomer conversion for both lamellar and hexagonal structures as the IFW+IFO systems show higher conversion than the average value of their corresponding single initiation systems. Having a good balance between propagation rate and terminate rate may be the reason why the synergistic effect is observed. In the case of maximum polymerization rate, the synergistic effect is detected only for the combination of APS and AIBN in the lamellar structure.

Based on the obtained results, the gradual increase of propagating chains in monomer phase and thus suppressed termination rate is the main reason why the polymerization rate is faster for

IFW than IFO system. To further confirm this hypothesis, we run the same experiments in both LLC structures using initiator concentration of 2.5 mol% with respect to the total monomer content. The results for lamellar phase are presented in Figure 2-5a-c. In the unconfined free radical polymerization (e.g., bulk polymerization), the rate of polymerization is proportional to the square root of initiator concentration (see Eq. 2-5), meaning that the extent of polymerization (e.g., overall monomer conversion) decreases with a decrease in initiator content.[216] In contrary, we observe an increase in the monomer conversion for all of the initiation systems when the initiator content is reduced to half. This outcome shows that the lower local concentration of macroradicals due to the reduced initiator content is the key factor which determines the rate of termination and thus the extent of the polymerization in LLC nanoconfinements.

Table 2-2. Overall monomer conversion and maximum polymerization rate for different initiation systems and theoretical average values for APS+AIBN and APS+BPO mixtures.

Initiation system	Hexagonal		Lamellar	
	Conversion (%)	$\{R_p / [M]_0\}_{max}$ (min^{-1})	Conversion (%)	$\{R_p / [M]_0\}_{max}$ (min^{-1})
APS	91.4	0.160	95.4	0.170
AIBN	88.1	0.100	74.8	0.062
BPO	65.1	0.056	48.9	0.047
APS+AIBN	93.6	0.122	97.1	0.127
Average of APS and AIBN	89.7	0.130	85.1	0.116
APS+BPO	90.7	0.110	79.2	0.090
Average of APS and BPO	78.2	0.108	72.1	0.108

Another important result here is that the maximum reaction rate slightly decreases with a decrease in the initiator content for APS and AIBN, whereas it increases for BPO. At a fixed initiator concentration, the higher the efficiency, the higher the maximum reaction rate will be. Recombination reaction of the free radicals that usually produces nonreactive components is one of the main phenomena that lowers the initiator efficiency. It seems that a portion of free radicals generated by BPO are deactivated through this reaction at high initiator contents due to the relative

immobility of radicals. With a decrease in BPO concentration, the proximity of generated free radicals decreases, resulting in lower chance of recombination reactions and therefore higher initiator efficiency. The enhanced initiator efficiency can improve the maximum reaction rate if the number of total initiation sites is increased. This phenomenon is evident only for BPO possibly since it generates fewer free radicals at a given time compared to AIBN (see Figure C3). Even if we assume that both AIBN and BPO can undergo the recombination of free radicals under confinement in a same fashion, the polymerization rate with BPO will be affected more intensely since it is already vulnerable due to the relative immobility of its radicals. This observation approves our speculation concerning different polymerization kinetics with BPO initiator in LLC structures compared to APS and AIBN.

Similar trend in polymerization rate and monomer conversion is observed in hexagonal structure when the initiator content is decreased to half (Figure 2-5d-f). The monomer conversion increases for all of the initiators and the maximum polymerization rate increases for BPO-initiated system, whereas it decreases for AIBN and APS. As discussed for lamellar structure, lower active site concentration due to the decreased initiator content reduces the termination reaction, resulting in higher monomer conversion. The reduced termination rate is evident in the reaction kinetics curves either in the form of an extended time of reaction and/or gradual decrease of the polymerization rate after the peak of the reaction rate as indicated by the arrows in Figure 2-5. As mentioned earlier, in the theory of free radical polymerization, the reaction rate scales with the square root of initial initiator concentration, i.e., $R_p \propto ([I]_0)^{0.5}$.[216] The maximum polymerization rate of APS-initiated system in hexagonal structure follows this scaling (Figure C4 in Appendix C), suggesting that other factor(s) (e.g., enhanced recombination of free radicals due to confinement) has negligible effect on the polymerization reaction. Nevertheless, for other cases

(e.g., polymerization in lamellar structure with different initiators and reaction in hexagonal phase using AIBN and BPO), this relation is not valid probably due to the occurrence of nanoconfinement-related phenomena such as the recombination of free radicals, diffusion limitations of free radicals, and free radicals concentration gradient in the confinements.

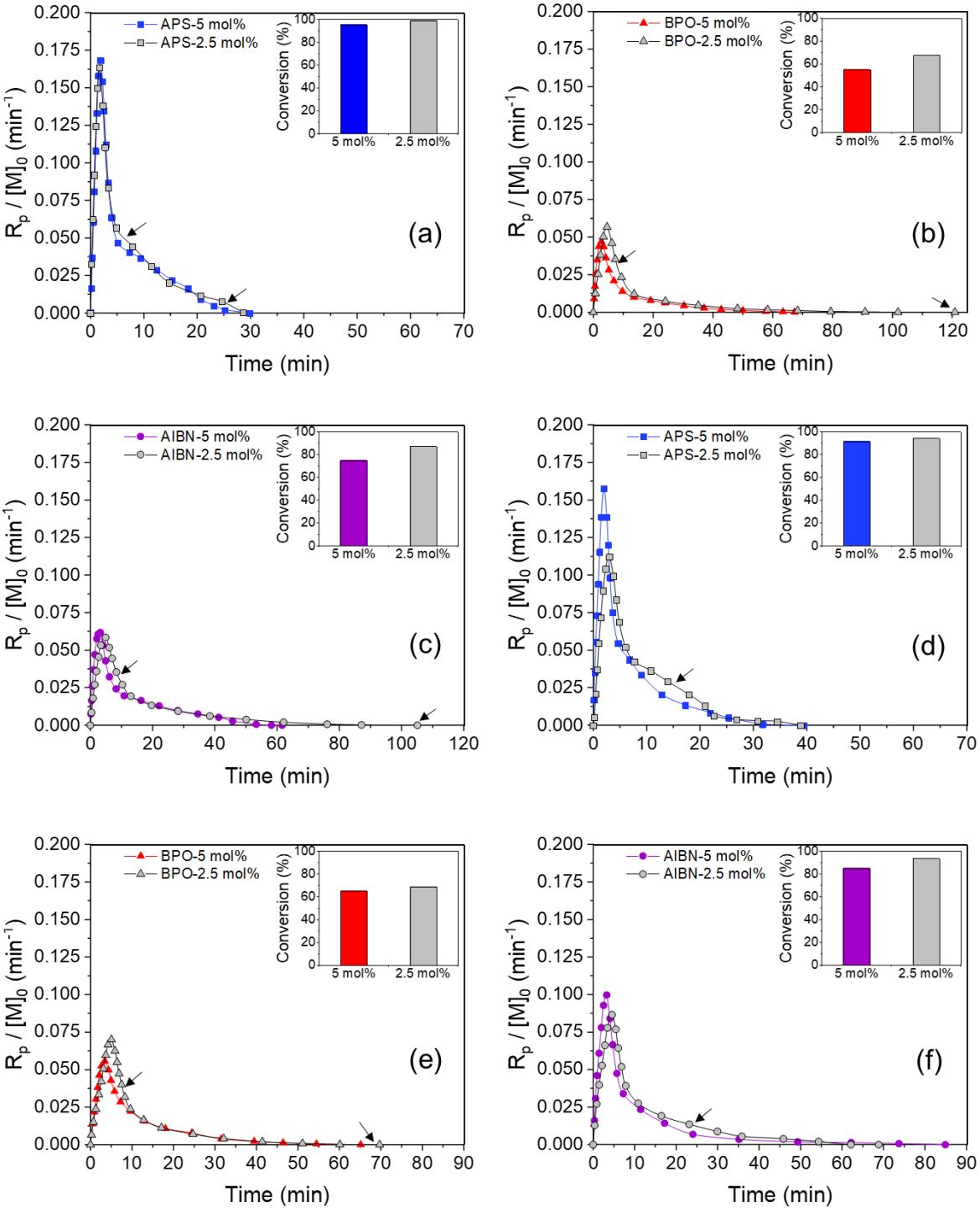

Figure 2-5. Normalized polymerization rate versus time and overall monomer conversion obtained from thermal polymerization in (a-c) lamellar and (d-f) hexagonal structures using different initiation systems having varied initiator contents. Arrows denote the time points that show the evidence of reduced termination rate (see main text).

The polymerization temperature is an important factor controlling the reaction kinetics. The kinetics for different initiators were studied using lamellar and hexagonal structures at 55, 65, and 75 °C (Figure 2-6). As expected, the maximum polymerization rate increased for all of the initiators when temperature increased. However, the trend of monomer conversion with temperature change was not anticipated. The overall monomer conversion decreases for APS and AIBN-initiated systems when the temperature increases from 65 to 75 °C, which can be due to two main factors. First, the faster kinetics of cross-linking chains at higher temperatures can expedite the formation of polymer network and thus suppress the mobility of macroradicals. Such effect has already been reported in the literature for the polymerization in LLC structures.[77] Second, the concentration of propagating chains increases sharply in a short period of time with an increase in the temperature, which results in higher local concentration of macroradicals and therefore enhanced termination rate. The simultaneous presence of these two factors reduces the monomer conversion. Nevertheless, the conversion for BPO-initiated polymerization slightly increases with temperature from 65 to 75 °C. The limited local concentration of macroradicals due to the lower free radical concentration generated by BPO (Figure C3) compared to the other initiators is likely the reason why its monomer conversion does not change in similar fashion to AIBN and APS initiated polymerizations when the temperature increases to 75 °C. In other words, nanoconfinement has less effect on the termination rate at high temperatures in the case of BPO compared to AIBN and APS due to the limited number of free radicals and macroradicals generated by BPO. In addition, BPO is subjected to the cage effect at low polymerization temperatures. Thus, the diminishing cage effect at higher temperatures can be another reason for the difference between BPO and the other initiators. Overall, the results show that the rate of

termination reaction and free radical recombination in LLC nanoconfinement control the polymerization rate and monomer conversion.

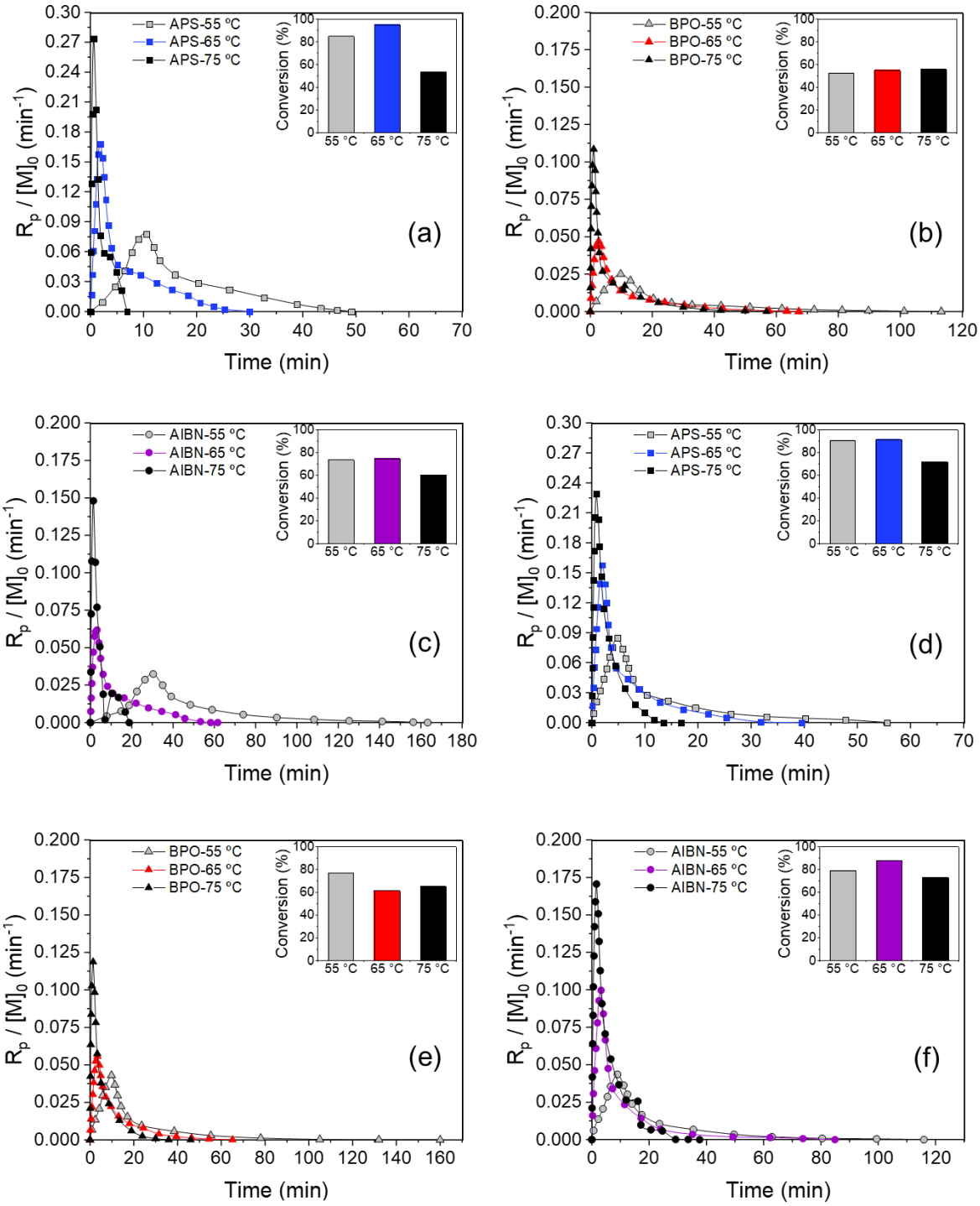

Figure 2-6. Normalized polymerization rate versus time and overall monomer conversion obtained from thermal polymerization in (a-c) lamellar and (d-f) hexagonal structures using different initiation systems at varied reaction temperatures. For all samples, the total initiator concentration of 5 mol% was used with respect to the total monomer content.

For IFW system, the polymerization is faster in lamellar structure than hexagonal one (although it has smaller confinement) and opposite behavior is observed for IFO systems at three different temperatures. Similar trend is also seen when different contents of initiators are employed. As a conclusion, for IFW system, polymerization rate is always faster for studied lamellar structure, whereas the reaction rate has higher pace in hexagonal phase for IFO systems. Therefore, the reaction rate in soft nanoconfinement not only depends on the confinement size, but also the loci of polymerization reaction.

To quantify the drawn conclusion, we calculated the overall kinetics rate coefficient, *K′*, and the overall activation energy of the polymerization, *E*. By considering the steady-state hypothesis for the free radical polymerization, normalized polymerization rate can be written as a function of the monomer conversion, *X*:[221]

$$\frac{R_p(t)}{[M]} = \frac{dX}{dt} = k_p \left(\frac{f k_d}{k_t} \right)^{\frac{1}{2}} [I]^{\frac{1}{2}} (1 - X) \cong K'(1 - X) \tag{2-6}$$

$$K' = k_p \left(\frac{f k_d}{k_t} \right)^{\frac{1}{2}} [I]^{\frac{1}{2}} \tag{2-7}$$

For low degrees of monomer conversion (1% to 10% in the current systems), it is possible to have an expression which directly correlates double bound conversion to the overall polymerization rate coefficient, *K′*:[221]

$$-\ln(1 - X) = K't \tag{2-8}$$

The slope of –ln(1 – *X*) versus *t* in conversion range of 1 to 10% gives *K′*.[221,222] Having the reaction kinetics data at different polymerization temperatures for APS, AIBN and BPO, we calculated the overall activation energy of the polymerization (in both lamellar and hexagonal

structures) by considering Arrhenius type dependency of reaction rate to temperature (Table 2-3). For APS initiator, higher values of K' at different temperatures (Figure C5) and lower activation energy in lamellar structure compared to hexagonal one confirm the higher reaction rate in lamellar phase. An opposite trend is observed for AIBN and BPO-initiated systems, implying that the reaction rate is higher in hexagonal structure for IFO systems. Additionally, APS shows the lowest activation energy as well as the highest K' values at different temperatures. These results reveal that, under nanoconfinement, APS is the most efficient initiator among the studied initiation systems in terms of polymerization kinetics.

Table 2-3. Calculated overall kinetics rate coefficient at different temperatures and overall activation energy of the polymerization in lamellar and hexagonal structures using different initiators.

Initiator	Structure	K' (10^{-3}/s) at 55 °C	K' (10^{-3}/s) at 65 °C	K' (10^{-3}/s) at 75 °C	Pre-exponential factor	E (kJ/mol)
APS	L_α	0.75	1.71	3.21	3.56×10^{-11}	69.3
	H_2	0.64	1.54	2.82	2.02×10^{-11}	70.2
AIBN	L_α	0.45	0.97	2.15	3.21×10^{-12}	74.3
	H_2	0.51	1.24	2.37	4.28×10^{-12}	73.8
BPO	L_α	0.29	0.76	1.67	2.12×10^{-13}	81.6
	H_2	0.38	0.83	1.73	7.95×10^{-13}	71.1

2.3.4 Chemorheology and mechanical properties

Although chemorheology has been used to study polymerization kinetics for many years,[217,223–225] there have been few reports applying this technique for the reaction in nanoconfinements.[81,226,227] Recently, Qavi *et al.* have employed this approach to thoroughly investigate the thermal polymerization kinetics during LLC templating.[56] They observed that the rheological properties of samples show three stages at elevated temperatures: induction, polymerization, and final curing. The polymerization rate obtained by DSC correlated well with

the rate of increase of dynamic moduli. Also, the mechanical properties of polymerized LLCs can be obtained from viscoelastic measurements after curing.[147]

Figure 2-7 shows the chemorheological behavior during polymerization of lamellar and hexagonal LLC structures by using different initiation systems. In the case of lamellar phase (Figure 2-7a-c), the dynamic moduli of the sample increase faster for APS compared to the other initiators, meaning that APS-initiated system has the fastest polymerization rate. Additionally, AIBN induces a higher polymerization rate over BPO. The reaction rate for IFW+IFO systems also lies in between the rates for IFW and IFO systems. The interesting result here is that the final values of the moduli for APS-cured sample is higher than other cases. To further examine such difference in mechanical properties, we run frequency sweep experiments on the polymerized samples in less than 2 min after reaching the final curing stage during chemorheological measurements (Figure 2-8a). The results indicate higher dynamic moduli for APS-cured sample. One may argue that this is due to the higher monomer conversion of APS initiated sample compared to IFO systems. Based on the DSC results, however, the monomer conversion for APS+AIBN system is almost equal to that for APS alone, but it has lower dynamic moduli than that of APS system. Therefore, there should be an additional parameter affecting the mechanical properties of the samples. Investigating the results gained for hexagonal structure can shed lights on this point.

Chemorheology study on hexagonal structure not only shows that the polymerization rate is faster for APS compared to other initiators, but also reveals an unexpected phenomenon in the development of dynamic moduli during reaction with APS (Figure 2-7d-f). When APS is used (in the pure form or in combination with other initiators), the storage (G') and loss moduli (G") increase sharply and then decrease to some extent followed by a partial recovery. Such change in

mechanical properties during polymerization, which is seen only for APS-initiated reactions, is probably due to the way that free radicals migrate from water to the monomer phase. In emulsion polymerization, as a generally accepted mechanism, the free radicals located in aqueous phase first react with monomer molecules dissolved (even in very low concentrations) in the aqueous phase to form surface active species (called *z*-mers) that subsequently enter the monomer droplets.[228,229] When APS is used in polymerization of LLCs, the *z*-mers probably form and either remain at the interface or enter the oil phase to react with the large reservoir of monomers. Since the oil/water interface is mechanically the weakest component in multiphase systems, the propagation of polymer chains at the interface results in a sharp increase in the moduli. However, detachment of growing *z*-mers from the interface and their entrance into the monomer phase may induce a decline in moduli. Further propagation and formation of polymer network results in a recovery of the mechanical properties to some extent. We speculate that the formation of a robust polar/apolar interface in IFW system is one of the reasons of higher mechanical strengths of the cured samples compared to IFO ones in different LLC structures, as shown in Figure 2-8. It is worth noting that we do not see the peak in dynamic moduli during the reaction in lamellar phase (see Figure 7a-c) in contrast to hexagonal structure. This can be due to the structure itself and/or lower monomer content in lamellar phase.

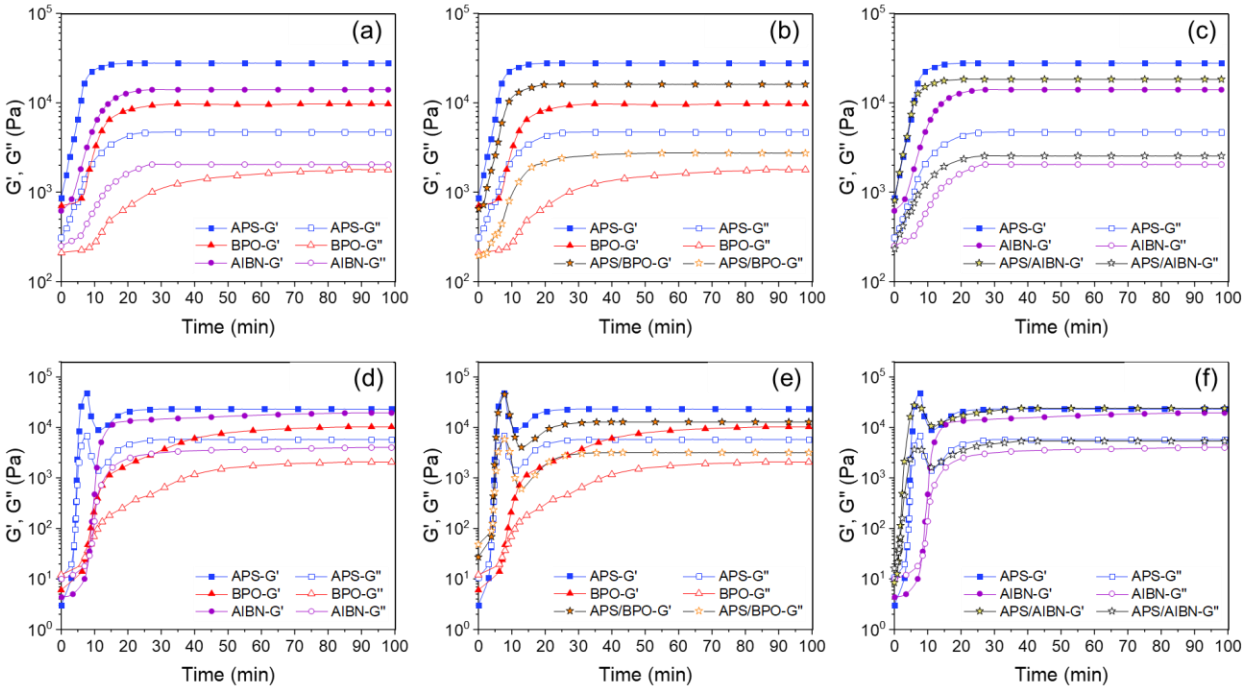

Figure 2-7. Evolution of dynamic moduli during LLC templating with (a-c) lamellar and (d-f) hexagonal structures using different initiation systems.

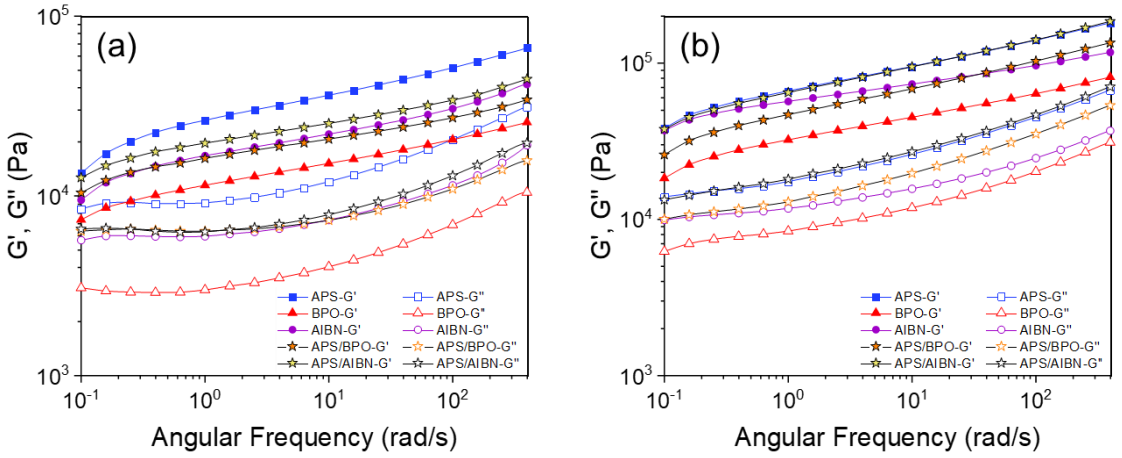

Figure 2-8. Frequency sweep curves of the samples obtained from polymerization in (a) lamellar and (b) hexagonal LLC structures using different initiation systems.

To further examine the effect of initiation system on the mechanical properties of the polymerized samples, we conduct rheological measurements on the LLCs containing 2.5 mol%

initiator content, which have less termination reaction than 5 mol% samples as discussed earlier. The samples containing 2.5 mol% APS and AIBN are used in this part as they show almost similar monomer conversion according to DSC analysis. The results are presented in Figure 2-9. For both initiation systems, the dynamic moduli of the polymerized samples having different nanostructures are enhanced with a decrease in the initiator content. Furthermore, APS-cured samples exhibit higher moduli over the samples cured with AIBN even under almost same monomer conversions. These observations confirm the considerable effect of the chains forming at the interface on the mechanical properties of polymerized LLCs. To further elaborate the effect of the chains formed at the water/oil interface, we have schematically presented the probable mechanism (as discussed above) in Figure 2-10. In summary, free radicals generated by the water-soluble initiator migrate to the polar/apolar interface and start the polymerization, resulting in the formation of *z*-mers. The growing *z*-mers can either continue the reaction at the interface or detach from the interface to continue the polymerization in the apolar domain. A robust polar/apolar interface is obtained at the end of the reaction due to the formation of polymer chains at the interface resulting in an enhanced mechanical properties. In the case of IFO system, however, the polymerization mainly takes place in monomer phase. Such polymerization behavior limits the reaction at the interface, resulting in the formation of less polymer chains in this location and thus acquiring weaker mechanical properties compared to IFW system.

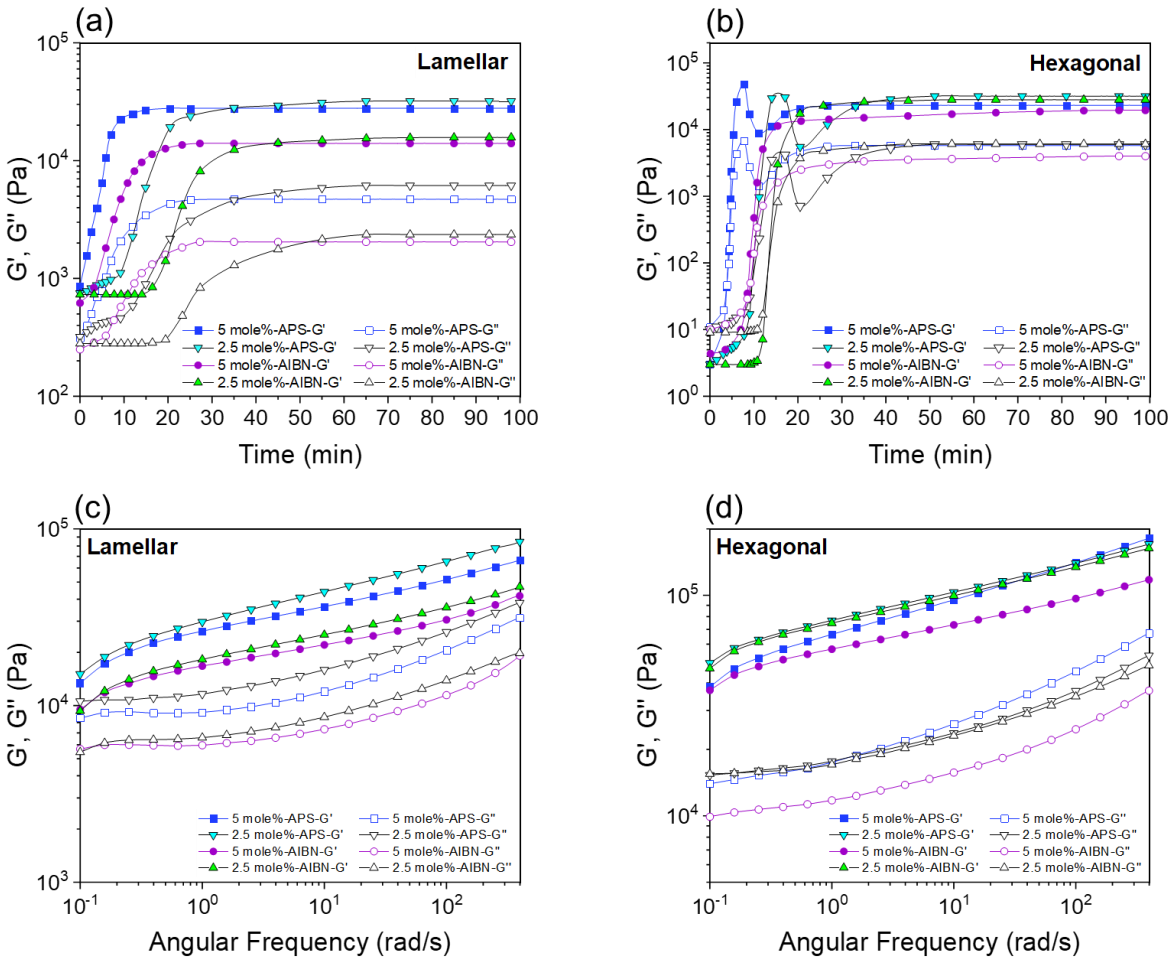

Figure 2-9. (a, b) Evolution of dynamic moduli during LLC templating and (c, d) frequency sweep curves of polymerized LLCs using different initiator contents.

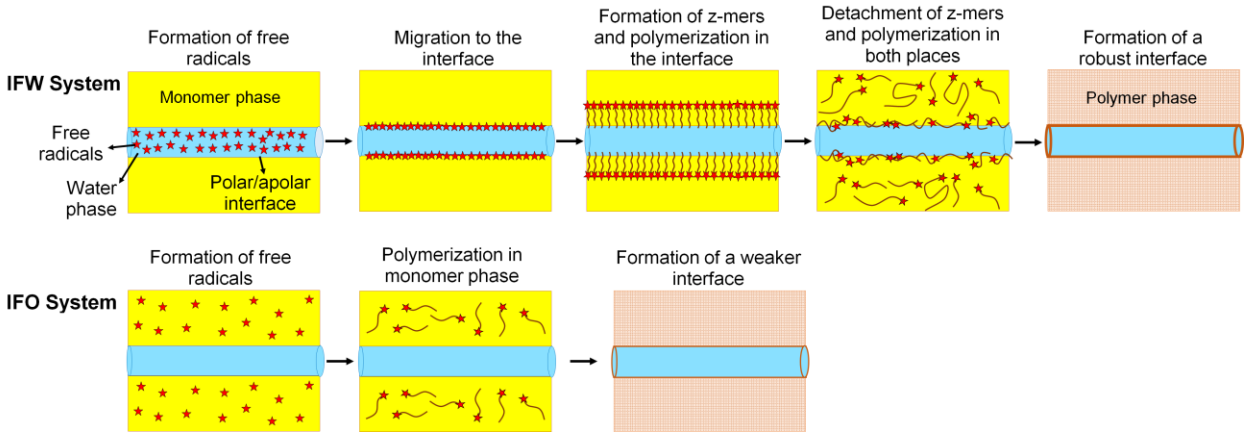

Figure 2-10. Schematic diagram of the polymerization mechanism in IFW and IFO systems and the consequent difference in the robustness of the polymerized LLCs.

2.4 Conclusion

Different thermal initiators were used to study the polymerization kinetics in lamellar and reverse hexagonal LLC structures through DSC analysis. The IFW system showed faster polymerization rates over IFO ones under any circumstances (e.g., different temperature, initiator concentration, and LLC structure). We attributed this behavior to the gradual increase of the propagating chains in the monomer phase which results in lower termination rate and thus higher overall polymerization rate. Higher initiator efficiency can be counted as another reason of higher polymerization rate for IFW system. Moreover, the experimental results showed that the polymerization rate in lamellar phase is faster than in hexagonal phase when IFW system is used, whereas an opposite trend is observed for IFO systems. Additionally, rheological measurements not only confirmed the DSC results concerning the faster reaction rates by IFW system, but also revealed that the samples cured by IFW system exhibit enhanced mechanical strength over other initiation systems even at similar monomer conversions. We attributed this observation to the polymerization at polar/apolar interface in IFW system.

CHAPTER 3: TWO-STEP THERMORESPONSIVE ULTRAFILTRATION MEMBRANE FROM POLYMERIZATION OF LYOTROPIC LIQUID CRYSTALS[1]

3.1 Introduction

Demand for clean water is continuously increasing with the growth of human population. Membrane technology is a highly efficient and versatile approach to purify different water resources (e.g., brackish water, seawater, and wastewater) for fulfilling this demand.[4,230] Microfiltration, UF, NF, and reverse osmosis are the main steps to purify water from different contaminants.[231] UF membranes have a key role in this process as they are used for the removal of suspended particles, viruses, bacteria, etc.[32] In addition to water filtration, UF membranes are vastly used in protein purification, pharmaceutical industries, and food processing.[232,233] However, there is a need for improving the membranes selectivity and permeability simultaneously. For instance, the feed of UF membranes usually contains solutes/particles with different sizes. Therefore, the separation of different components with one UF membrane will be limited. Having a UF membrane with a tunable pore size will address this challenge to a large extent.[234] Moreover, another crucial issue that must be tackled is the fouling of UF membranes, which can decrease the membrane efficiency over time.[5,235]

Stimuli-responsive membranes can address the aforementioned challenges and improve the performance of UF membranes.[5] The surface properties and pore structure of these membranes

[1] Reprinted with permission from ACS Applied Polymer Materials 2022, 4, 11, 8156–8165 with some modifications.

can be altered via an external stimulus, such as temperature,[236] pH,[213] light,[237] electrolyte,[238] and magnetic field.[239] This behavior not only results in a tunable pore size and thus dynamic selectivity, but also improves the cleaning efficiency of the membrane after contamination with foulants.[192]

Thermoresponsive membranes are of interest because not only implementation of thermal response has less complications in the synthesis, but also temperature changes has usually negligible effect on the chemistry of the feed stream.[5] Additionally, there are a variety of thermoresponsive polymers that can be used for the fabrication of membranes.[240] NIPS has been the main technique to produce thermoresponsive membranes. For example, Yu *et al.* used PNIPAM-grafted polyvinylidenefluoride (PVDF) copolymers and reported a dynamic permeability and selectivity of the membrane in response to the temperature changes.[241] By using NIPS process, Chen *et al.* fabricated membranes of PNIPAM microgels/PVDF blend, which show a similar dynamic behavior with temperature change.[242] Recently, Choi and coworkers used a mixture of polyethersulfone (PES) and in-lab synthesized poly(2-dimethylaminoethyl methacrylate)-block-poly(N-isopropylacrylamide) to form two-step thermoresponsive membranes capable of separating different proteins with temperature.[192] However, the NIPS method used for preparation of these membranes is environmentally questionable as large quantities of organic solvent, as high as 70% (in volume) is required.[243] Additionally, incorporation of in-lab synthesized thermoresponsive polymers in the final membrane makes the final product expensive and impractical for scaleup.[192]

LLC templating is an alternative approach to produce nanoporous membranes without using huge volumes of organic solvents.[4,31,93,120,244,245] There are some reports in the literature, in which surfactant or oil phase of LLCs is polymerized to fabricate porous membranes (mainly UF and NF).[31–33,118,176] Polymerization of aqueous phase of LLCs is also used to produce thermoresponsive

hydrogels.[38,42] However, there is no report in the literature on LLC templating process for fabrication of thermoresponsive membranes.

In this work, we present the first successful approach to create two-step thermoresponsive UF membranes from the polymerization of LLCs directed by commercially available F127 block copolymer surfactant, i.e., poly[(ethylene oxide)-block-(propylene oxide)-block-(ethylene oxide)] or PEO-PPO-PEO. F127 is commonly used in drug delivery systems thanks to its thermoresponsive behavior.[246] In combination with water and other components (e.g., acids), this commercially available copolymer, which possess FDA approval.[247] can form gels having LCST at about 25-37 °C.[248] Moreover, Holmqvist *et al.* showed that a mixture of F127, water, and *p*-xylene can create different LLC structures (e.g., lamellar and hexagonal).[209] Furthermore, Qavi *et al.* have recently shown the possibility of fabricating UF membranes though the polymerization of LLCs created by Pluronic copolymers. Their work has proved that the chains of Pluronic copolymer remain in the structure of the obtained polyLLC.[32] Inspired by the aforementioned studies, we prepared a polyLLC with lamellar structure from F127 for producing UF membranes with thermoresponsive behavior. The obtained polyLLC exhibited thermoresponsiveness at ~35 and ~50 °C thanks to the LCST of F127 and melting of the crystalline structure of PEO chains of the surfactant, respectively. The membrane obtained from the polyLLC showed dynamic permeability in response to the temperature with an excellent reversibility. Furthermore, taking the advantage of this thermal response, it was possible to increase the cleaning efficiency of the fouled membrane. The most important strengths of this work are the use of commercially available raw materials and employing a straightforward processing technique to create two-step thermoresponsive UF membranes.

3.2 Experimental

3.2.1 Materials

Pluronic F127 copolymer, PEO_{106}–PPO_{70}–PEO_{106}, with M_w of ~12,500 g/mol was kindly provided by BASF. *n*BA, EGDMA, APS, and AIBN were purchased from Sigma-Aldrich and used as received. DI water with a conductivity of 0.055 μs/cm (obtained from EMD Millipore Direct-Q3) was used in all experiments. Bovine serum albumin (BSA) was purchased from Sigma-Aldrich and used as a membrane foulant. For molecular weight cut-off (MWCO) measurements, we used PEO with different molecular weights (100, 200, 300, 400, 600 and 900 kDa) from Sigma-Aldrich. Nonwoven polyester sheets with 2 μm porosity (CraneMat® CU463) were kindly provided by Neenah Filtration and employed as a support layer for membrane fabrication. Moreover, a commercially available polyacrylonitrile (PAN) UF membrane with a rejection size of 400 kDa was purchased from Sterlitech Corporation (YMPX3001, Synder Flat Sheet Membrane) and used for comparison in this study.

3.2.2 Preparation of LLC

To prepare the lamellar mesophase, F127, water (containing APS) and oil (*n*BA and EGDMA) were mixed with weight ratio of F127/water/oil 50/20/30. EGDMA and APS concentration was 20 and 7 wt% with respect to *n*BA content, respectively. Briefly, all the components were mixed in a 50 ml centrifugal tube by hand mixing and centrifugation at 10,000 rpm for 30 min. Until obtaining a transparent gel, the hand mixing and centrifugation were repeated.

3.2.3 Characterization of LLC and polyLLC

3.2.3.1 Cross-polarized light microscopy (CPLM)

The birefringence of lamellar LLC structure was examined by a cross-polarized Nikon microscope (model LABOPHOT2-POL) equipped with a digital camera before and after polymerization. For sample preparation, about 0.2 gr of uncured LLC sample was sandwiched between a glass slide and a glass cover slip. In the case of polyLLC, the test was carried out after curing the LLC at 65℃ for 24 h.

3.2.3.2 Small angle X-ray scattering (SAXS)

SAXS[249] was used to confirm the structure of the LLC before and after polymerization. Centrifugation was used to load the LLC gel into quartz capillary with a nominal diameter of 1.5 mm (Charles Supper Company, Natick, MA) followed by sealing the capillary with epoxy glue. For SAXS analysis of polyLLC sample, the loaded LLC in the capillary tube was cured at 65 °C for 24 h. 2D scattering patterns were acquired from a Bruker Nanostar X-ray scattering system equipped with a monochromatic Cu Kα radiation source. Azimuthal integration of the 2D scattering patterns resulted in 1D scattering profiles.

3.2.3.3 Atomic force microscopy (AFM)

Morphological analysis of polyLLC was performed using AFM. To do so, a piece of polyLLC was placed in liquid nitrogen for 20 min. The frozen sample was broken into small flat pieces for the cross-section observation. AFM studies were carried out on the broken surfaces using the tapping mode of a Bruker Dimension FastScan AFM instrument.

3.2.3.4 Differential scanning calorimetry (DSC)

DSC was used to study the thermal behavior of pure F127, poly(*n*BA-co-EGDMA), and polyLLC. The poly(*n*BA-co-EGDMA) copolymer was synthesized through the bulk polymerization of the corresponding monomers at 65 °C using AIBN as the initiator and the composition used as the oil phase of LLC. DSC Q2000 (TA Instruments, New Castle, DE) was

employed for this study. Around 30 mg of the desired sample was loaded into a Tzero aluminum pan followed by sealing with a Tzero hermetic lid. The temperature sweep was performed from 0 to 60 °C (and vice versa for F127 and polyLLC) with 1 °C/min ramp. The cycle was repeated twice to erase the thermal history of samples. The results of the second cycle are presented in the paper.

3.2.4 Preparation of the polyLLC membrane

To polymerize LLC on the support layer (having ~5×5 cm2 surface area), about 0.8 g of the LLC was sandwiched between pre-cut Mylar films and smooth glass plates, which was subsequently cast under 5 ton pressure for more than 10 min. In the next step, the cast gel on the support was polymerized by heating in the oven at 65 °C for 24 h (see Figure D1 in Appendix D for schematic representation of the membrane fabrication process).

3.2.5 Characterization of the polyLLC membrane

3.2.5.1 Hydration capacity

The hydration capacity, which is the maximum water uptake per unit volume (mg/cm^3) of the membrane, was measured according to the available procedure in the literature.[192,236] Briefly, the weight of 5 membrane samples of size 2 cm ×2 cm was determined in dry state as well as in wet state at different temperatures. Then, the dry weight was subtracted from the wet weight, and the obtained number was divided by the volume of the membrane, resulting in the hydration capacity. Measurements were taken at various temperatures, and the mean value along with the corresponding standard deviation was reported (see Appendix G for the measurement uncertainty evaluations).

3.2.5.2 Water flux and permeability

We used Sterlitech HP4750 high pressure stirred cell with the effective area of ~ 14.6 cm^2 operating in dead-end filtration mode to measure the membrane flux (reported as $liter/m^2/h$) under

stirring at 750 rpm with a magnet stirrer. A nitrogen pressure of 30 psi (~ 2.07×10^5 Pa) was used for the flux measurements. To evaluate the thermoresponsiveness of the membrane, the flux test was carried out at different temperatures from 25 to 60 °C. To do so, the filtration setup containing the membrane was placed in a water bath maintained at the desired temperature with an accuracy of ±0.1 °C. Precise control of the temperature is necessary to have a constant temperature in the membrane level and thus avoid any reduction in the boundary layer due to the heat caused by shear, which can affect membrane performance (e.g., permeability, selectivity, and fouling resistance). The flux at elevated temperatures was measured after ensuring the isothermal condition and having a stable flux. It should be noted that all the measurements were repeated three times. The membrane permeability was calculated based on the obtained experimental results using Darcy's law [32]:

$$\frac{\kappa}{l}=\frac{Q\mu}{A\Delta P} \tag{3-1}$$

In this equation, Q, μ, A, ΔP, l, and κ are the flow rate, viscosity, membrane area, pressure difference across the membrane, membrane thickness, and Darcy's constant (intrinsic permeability), respectively. The intrinsic permeability was normalized to the membrane thickness to cancel out the effect of thickness variation in our comparisons. It is worth to point out that the following equation[250] was used to calculate the viscosity of water at different temperatures:

$$\mu_w=(1.002\times10^{-3})(10^B) \quad , \quad B=\frac{1.3272(20-T)-0.001053(T-20)^2}{T+105} \tag{3-2}$$

where μ_w is the kinetic viscosity of water and T is temperature in K.

3.2.5.3 Evaluation of fouling resistance and cleaning efficiency

The following experimental procedure was followed to determine the fouling resistance of and cleaning efficiency for the membrane:

1) The flux of the membrane was measured by passing DI water through the membrane for 30 min at 25 °C.
2) 1000 ppm aqueous solution of BSA (as the model foulant) was used as the feed stream and the flux was recorded at 25 °C until reaching steady state conditions.
3) The membrane was backwashed with DI water for 30 min at different temperatures: 25, 35, or 50 °C.
4) The fouling-cleaning cycle (i.e., steps 1-3) was repeated three times.

It should be mentioned that the backwashing steps were carried at different temperatures to examine the effect of membrane thermoresponsiveness on the cleaning efficiency.

The reversible (also called cleaning efficiency) and irreversible fouling of the membrane were calculated using the following equations, respectively:

$$Reversible\ fouling\ = \frac{(Flux\ of\ cleaned\ membrane\ -\ Flux\ of\ fouled\ membrane)}{(Initial\ flux\ of\ membrane)} \times 100 \qquad (3\text{-}3)$$

$$Irreversible\ fouling\ = \frac{(Initial\ flux\ of\ membrane - Flux\ of\ cleaned\ membrane)}{(Initial\ flux\ of\ membrane)} \times 100 \qquad (3\text{-}4)$$

3.2.5.4 Molecular weight cut-off measurements

The permeation of 1 mg/mL aqueous solutions of PEO with different molecular weights (100-900 kDa) was studied to determine the MWCO of the membrane. The concentration of PEO in the permeate stream was determined by the total organic carbon analyzer (TOC), Shimadzu (TOC-L series). The PEO rejection was determined by using following equation:

$$r = (1 - \frac{C_p}{C_f}) \times 100 \quad (3\text{-}5)$$

where r, C_p, and C_f are rejection, PEO concentrations in permeate, and PEO concentrations in feed, respectively. MWCO is defined as the molecular weight of the PEO that shows at least 90% rejection [251]. The TOC test was repeated 5 times and the average value is reported in the paper.

To examine the effect of thermoresponsiveness of the polyLLC membrane on the MWCO, the PEO solutions were passed through the membranes at different temperatures and the TOC measurements were performed on the permeates. To cancel out the effect of temperature on the hydrodynamic radius of PEO chains and thus have a precise MWCO results, dynamic light scattering (DLS) measurements on PEO solutions were done at different temperatures. To do so, a Malvern Zetasizer Nano ZS was used with a laser wavelength of 8324 Å and at a scattering angle of 90°. Solutions of PEO with different molecular weights at a concentration of about 0.1 wt% were used for DLS measurements using the procedure described in the literature [252].

3.3 Results and discussions

3.3.1 Characterization of LLC and polyLLC

As the first step, we needed to characterize the Pluronic/water/oil mixture to confirm the LLC and polyLLC structures created by F127. Structural analysis of the obtained LLC before and after polymerization via CPLM is shown in Figure 3-1a, b. The oily-streak texture reveals that the mesophase has the lamellar structure.[17] The absence of extinction (a dark image) in the CPLM photograph of polyLLC indicates that the structure remains birefringent, meaning that we have structure after polymerization. Then we characterized LLC and polyLLC with SAXS. According to the SAXS results (see Figure 3-1c), Bragg peaks with ratios of 1:2 is observed for LLC before reaction while only one peak is seen for polyLLC. Additionally, d-spacing of the structure ($d =$

$\frac{2\pi}{q*}$) increases from 11.6 to 20.18 nm after polymerization. The CPLM and SAXS observations reveal that even though we have a nanostructure with bigger domain sizes after polymerization, the parent lamellar structure has partially been retained. To further evaluate the polyLLC structure, AFM studies were carried out. The acquired results are shown in Figure 3-1d, e, f. As can be seen in the AFM images, the dried polyLLC sample (analysis of a dried sample seemed necessary to acquire proper image resolution) has a structure in the form of arranged stacks which confirms the presence of lamellar structure. However, the image analysis shows that we have a distribution of layers thicknesses with an average thickness of about 30 nm and standard deviation of 5.9 nm (the thickness of at least 50 lamellae was measured through image analysis followed by calculation of average and standard deviation of the measured thicknesses). Such variation in thickness of the layers confirms our observation in SAXS analysis (i.e., partially retaining the parent LLC structure). It should also be noted that the anisotropic shape of the two-dimensional lamellar structure can be another reason why the structural dimensions obtained from AFM is different than the d-spacing calculated from the SAXS measurement.

After making sure that the polyLLC has the desired nanostructure, we evaluated its thermoresponsiveness via DSC. We not only analyzed polyLLC, but also tested poly(*n*BA-co-EGDMA) and pure F127 to distinguish which component is responsible for probable thermal transitions in the temperature range of 25 to 60 °C. The obtained results are presented in Figure 3-2. As can be seen, there is not any thermal transition for poly(*n*BA-co-EGDMA) in this temperature range. However, F127 shows an endothermic peak at around 50-58 °C in the heating cycle, attributed to the melting of PEO crystalline regions. In addition, an exothermic peak is observed starting from 48 °C and ending at about 43 °C in the cooling cycle of F127. This peak can be attributed to the crystallization of PEO chains. In the case of as synthesized polyLLC (i.e.,

containing water), two endothermic peaks are observed in the heating cycle. The first peak at about 26-33 °C can be attributed to the LCST of F127, which is consistent with the reported LCST range of F127/water mixtures in the literature.[248] The second peak, observed at about 50 °C, belongs to the melting of PEO crystalline regions in accordance with the DSC of pristine F127. Having an exothermic peak in the cooling cycle also proves the presence of crystallinity in the obtained polyLLC, which can be melted down at 50 °C. The two thermal transitions provide the possibility to induce two-step thermo-responsiveness in the membrane.

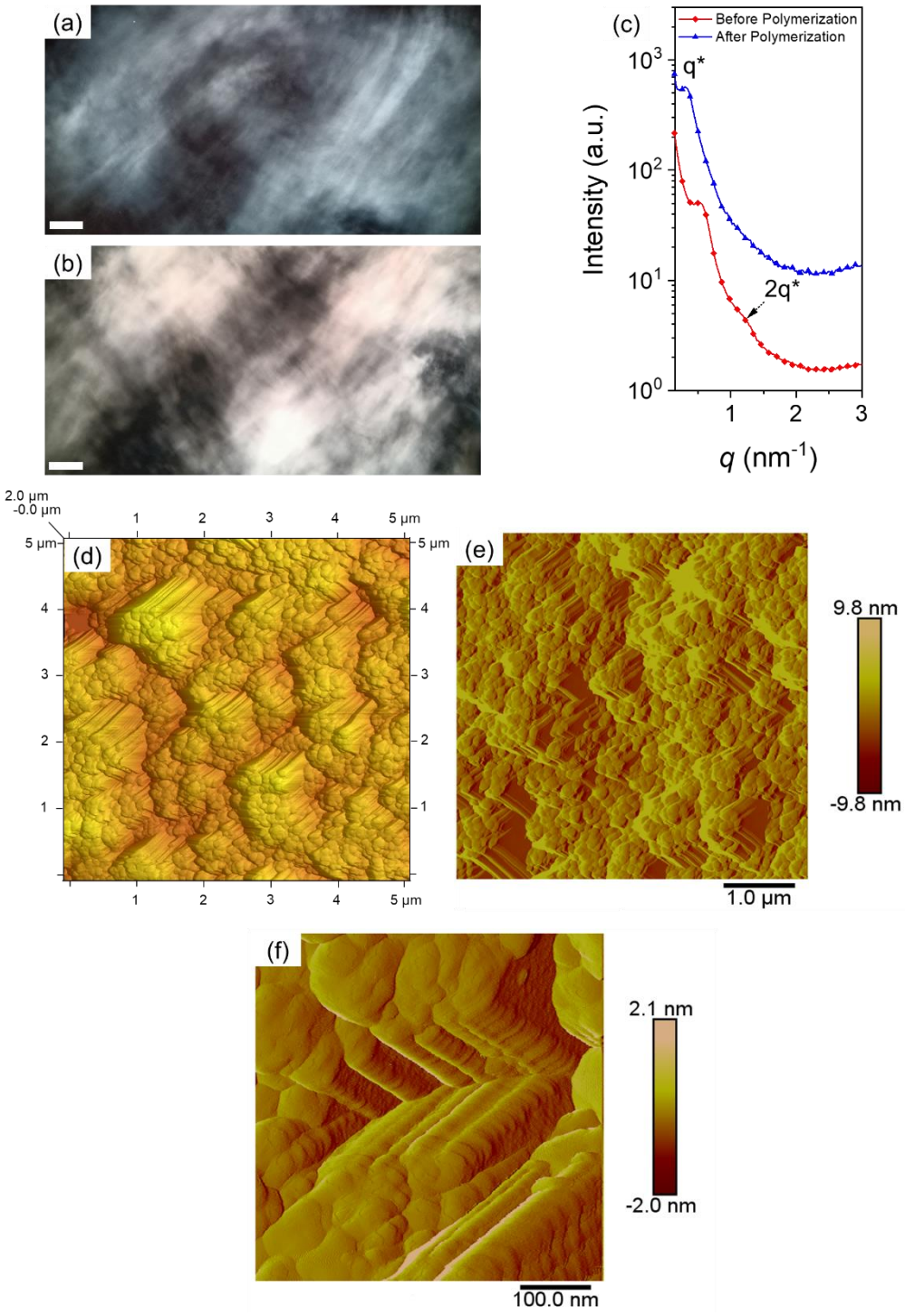

Figure 3-1. CPLM images of LLCs with lamellar structure: (a) before and (b) after thermal polymerization (scale bar: 50 µm). (c) 1D SAXS data for LLCs before and after reaction (the plots are vertically shifted for clarity). (d and e) AFM micrograph of the cross section of dried polyLLC in a $5\ \mu m \times 5 \mu m$ area; higher magnification is shown in (f).

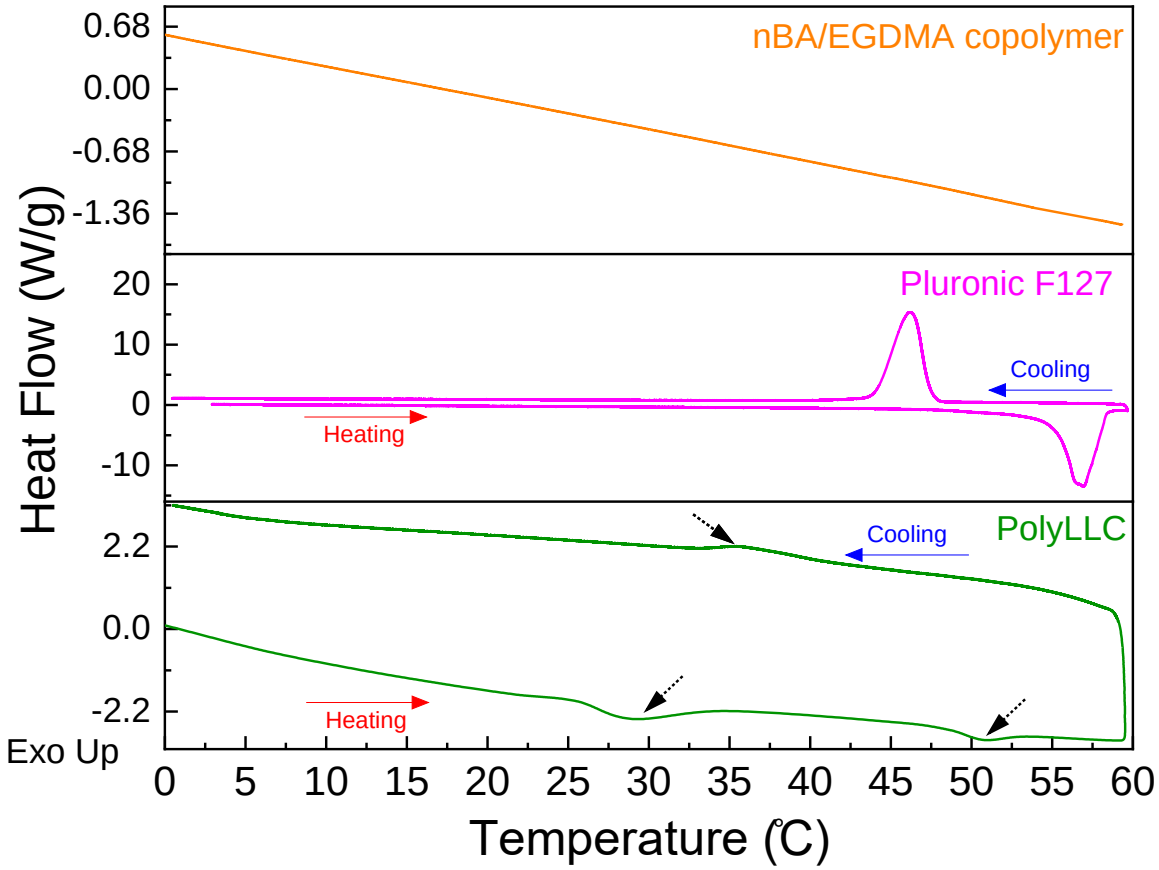

Figure 3-2. DSC measurement results for poly(nBA-co-EGDMA), F127, and polyLLC.

3.3.2 Characterization of membranes

As stated in the experimental section, a commercially available non-thermoresponsive PAN membrane was used to compare the results with the polyLLC membrane. The selected PAN membrane had a MWCO of 400 kDa, which is equal to the pore size of about 40 nm based on equation (6).[253]

$$a_{Stokes} = 10.44 \times 10^{-3} M_w^{0.587} \quad (3\text{-}6)$$

where a_{Stokes} and M_w are Stokes radius in nm and MWCO, respectively. The results of membranes performance evaluation will be discussed in the following sections.

3.3.2.1 Hydration capacity

Measuring the hydration capacity of a membrane at different temperatures is performed to confirm the thermoresponsiveness.[192] The membrane is called thermoresponsive if its hydration capacity changes by temperature. We measured the hydration capacity for PAN and polyLLC membranes at 25, 35, and 50 °C as shown in Figure 3-3. These temperatures were chosen based on the DSC results. While the hydration capacity remains constant for PAN membrane, it has an increasing trend for polyLLC sample. This means that the porosity of polyLLC membrane increases with an increase in temperature. This behavior happens in two steps, which is consistent with the thermal transitions observed in DSC analysis. It is worth noting that higher hydration capacity of PAN membrane compared to the polyLLC specie can be due to its higher porosity.

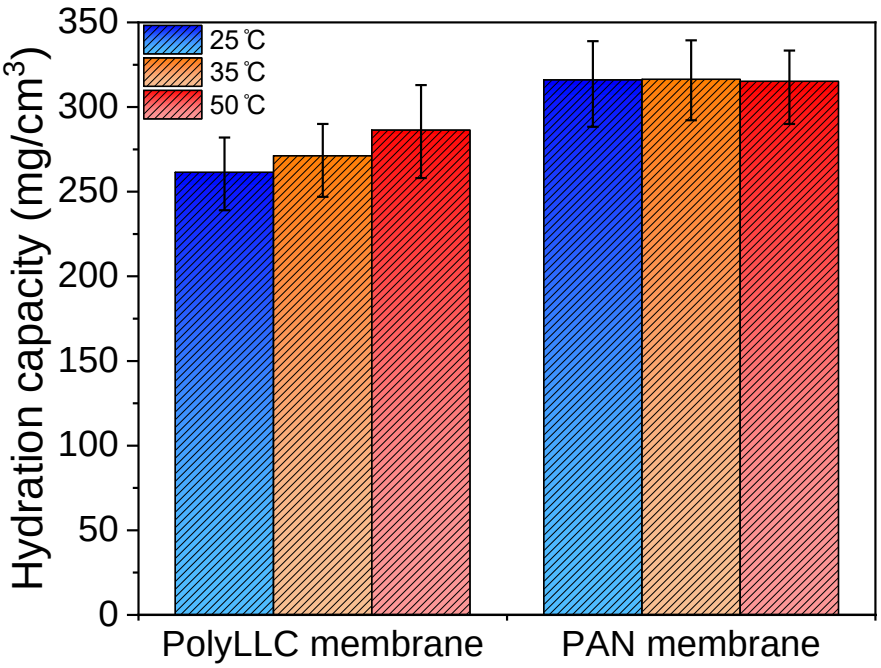

Figure 3-3. Changes in hydration capacity for PAN and polyLLC membranes based on the temperature variation.

3.3.2.2 Water flux and permeability

The water flux changes for PAN and polyLLC membranes versus temperature are shown in Figure 3-4a. Both of the membranes show an increasing trend in flux, but polyLLC one shows two steps of increase at 35 and 50 °C. To cancel out the effect of water viscosity decrease with temperature on the results, we also plotted permeability, κ/l, versus temperature (see Figure 3-4b). As can be clearly seen, the permeability of PAN membrane is almost constant at different temperatures, meaning that the reason of ascending water flux trend for PAN was the decrease in the water viscosity. However, the polyLLC membrane still maintains the two-step increase in the permeability. These transitions are in well agreement with the results of DSC analysis as well as the hydration capacity measurements. One important observation which must be considered here is that the second transition has more effect on the permeability (~ 14% increase) compared to the first transition (~8.5% increase). Therefore, the pore size increase is higher when the polyLLC loses its crystallinity rather than when the LCST transition of F127 takes place. In the following sections, we will elaborate the mechanism of two-step thermoresponsive behavior, where we will suggest that the crystallinity of the PEO blocks and rearrangement of F127 chains are its root causes. This conclusion can be further confirmed via MWCO measurements.

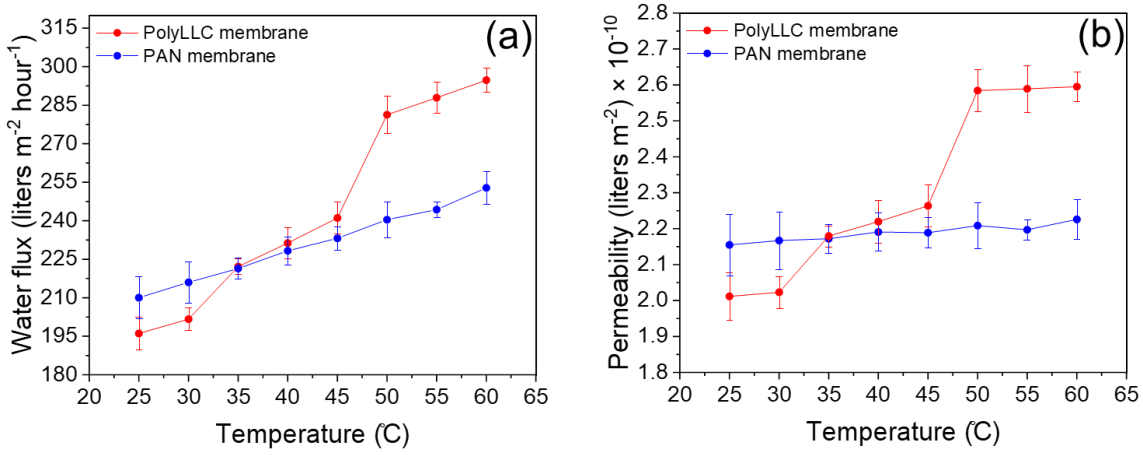

Figure 3-4. Changes in (a) water flux and (b) permeability for PAN and polyLLC membranes based on the temperature variation.

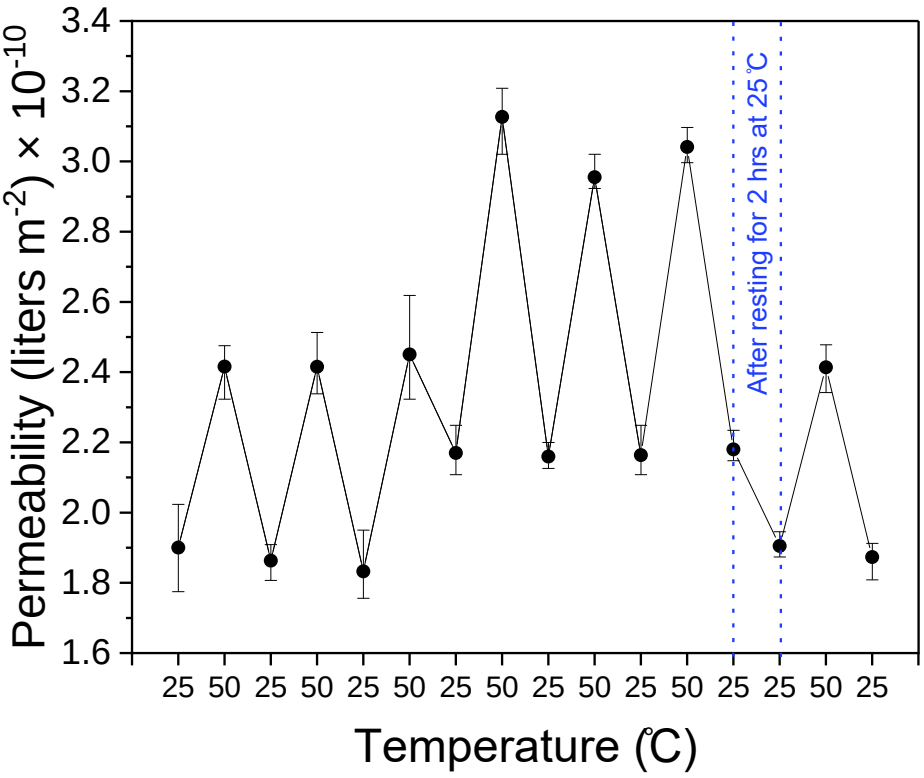

Figure 3-5. Reversibility of the water permeability of the polyLLC membrane under several heating-cooling cycles.

Reversibility of the response to an external stimulus is as important as stimuli-responsiveness since it determines the chemical and physical structural stability of the product after each response. In the next step, therefore, we evaluated the thermoreversibility behavior of polyLLC membrane. To do so, the water permeability of the membrane was measured at 25 and 50 °C repeatedly (under several heating-cooling cycles). The obtained results are shown in Figure 3-5. The membrane exhibits excellent reversible behavior under 3 heating-cooling cycles. However, after the third cycle, the permeability becomes higher at both 25 and 50 °C, which remains unchanged with continuing the test for consecutive cycles. Irreversible change of molecular structure (e.g., washing out of F127 from the membrane) was the first speculation. However, the permeate was tested using TOC measurement method and no sign of F127 was observed. Also, the permeability returned to the original values after giving 2 h rest to the membrane at 25 °C. Based on this observation, it appears that the change in molecular structure (melting and recrystallization of the PEO block) after several heating-cooling cycles is reversible yet time-consuming. It is noteworthy that the permeability of the polyLLC membrane remained unchanged at 25 and 50 °C after keeping the membrane at 50 °C for over 72 hrs, confirming the stability of the nanostructure at high temperatures.

3.3.2.3 Fouling resistance and cleaning efficiency

As stated in the introduction section, enhancing the reversible fouling over irreversible fouling (also called cleaning efficiency) is one of the important advantages of thermoresponsive membranes. Hence, we performed fouling-cleaning experiments (see the experimental section) on the polyLLC membrane and PAN membrane (as control sample). To evaluate the cleaning efficiency for the polyLLC membrane, the cleaning steps were carried out at 25, 35 and 50 °C (all the filtrations steps were performed on BSA feed solution at 25 °C). In the case of the PAN

membrane, we only did the cleaning at 25 and 50 °C. As shown in Figure 3-6, the normalized water flux, which is obtained through dividing the measured flux at any time by the primary flux of the fresh membrane, has also been evaluated in addition to the water flux itself. Based on the obtained trends, polyLLC membrane exhibits a higher fouling resistance compared to PAN membrane as the irreversible fouling is much lower for the former.

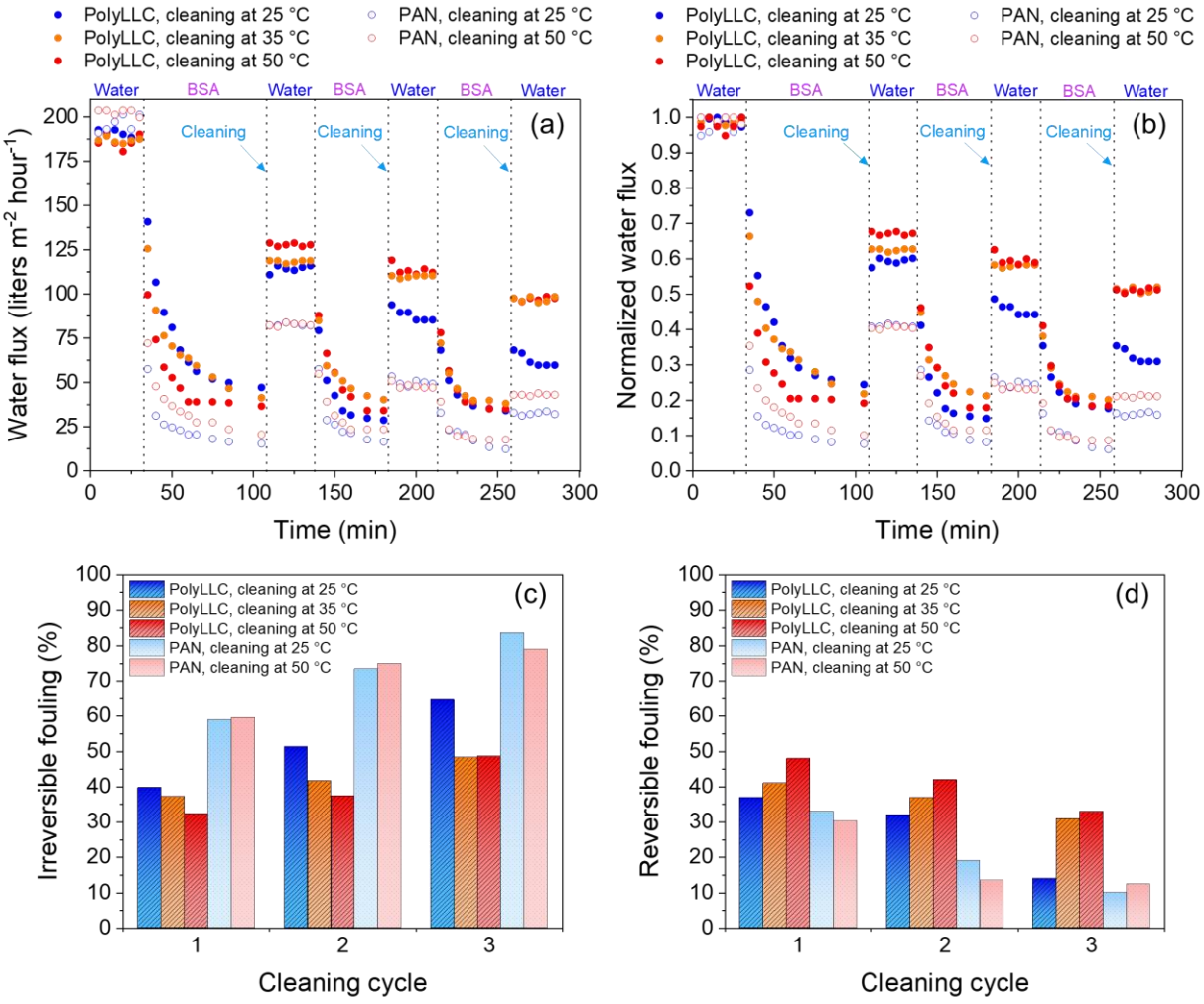

Figure 3-6. Change of (a) water flux, (b) normalized water flux, (c) irreversible fouling, and (d) reversible fouling for polyLLC and PAN membranes throughout fouling-cleaning experiment using different cleaning temperatures. The presented temperatures are cleaning temperature and filtrations steps were carried out at 25 °C.

According to the results presented in Figure 3-6, the reversible fouling for polyLLC membrane increases with an increase in the cleaning temperature, whereas there is no improvement for the PAN membrane. Such improvement happens due to an increase in the porosity of polyLLC membrane with temperature, which can enhance the foulant removal. Another noticeable observation here is the significant difference in the reversible fouling of polyLLC membrane in the third cycle in the case of cleaning at 25 °C compared to 35 and 50 °C. This result implies that utilizing the thermoresponsiveness of polyLLC membrane can increase the cleaning efficiency and decrease the irreversible attachment of foulants, thus, increasing membrane lifetime.

3.3.2.4 Molecular weight cut-off

Manipulation of the membrane selectivity through an external stimulus is one of the important advantages of stimuli-responsive membranes. Having this feature depends on changing the membrane pore size in response to a stimulus. MWCO measurement is the common method used for determining the pore size of membranes. Therefore, we used this approach to evaluate the extent of pore size change of the polyLLC membrane in response to temperature. PEO solutions having different molecular weights were employed to measure the MWCO at 25, 35 and 50 °C. The acquired results are shown in Figure 3-7. The MWCO of the membrane at room temperature is about 250 kDa from a sigmoidal fit on the rejection vs molecular weight data points in this figure. As presented in Eq. (3-7), Boltzmann sigmoidal equation has been used for the fitting MWCO behavior, where A_1, A_2, x_0, and m are initial value, final value, center, and slope, respectively:

$$y = A_2 + \frac{(A_1 - A_2)}{1 + e^{\frac{(x - x_0)}{m}}} \tag{3-7}$$

By using Eq. (3-6), a pore size of ~30.8 nm can be calculated for the membrane at room temperature. The MWCO of the membrane increases to around 336 and 570 kDa with an increase in the temperature to 35 and 50 °C, respectively. These MWCOs are equal to pore sizes of ~36.6 and ~50 nm, respectively. The results prove the possibility of the pore size manipulation for polyLLC membrane, and thus, its selectivity. It is also noteworthy to point out that melting of crystalline structure at 50 °C has stronger effect on the porosity compared to LCST transition at 35 °C, which is in good agreement with the results of hydration capacity, permeability, and fouling-cleaning experiments.

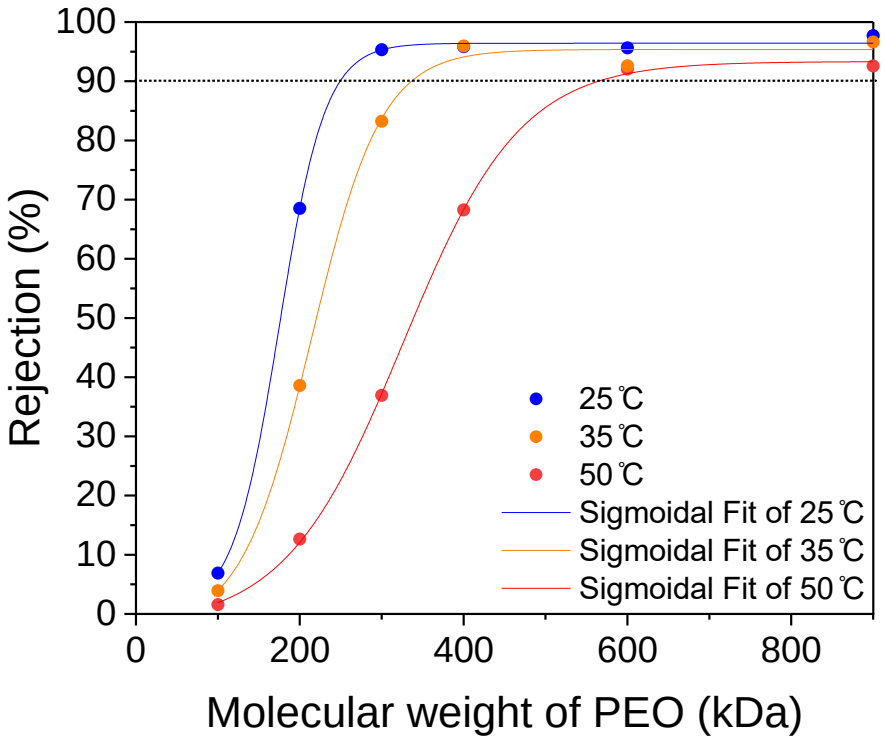

Figure 3-7. Temperature-dependent MWCO of polyLLC membrane.

The effect of temperature on the size of PEO chains has not been considered in the pore size calculations mentioned in the above paragraph. Therefore, we measured the hydrodynamic radius of PEO chains with different molecular weights at 25, 35 and 50 °C using DLS analysis. Figure 3-

8 represents the obtained results (PEO chains size distribution can be found in Figure D2). As can be seen, the size of PEO chains with different molecular weights slightly increases with an increase in the temperature. The same results have been reported by Hammouda *et al.* for PEG chains with molecular weight of 36.5 kDa using appropriate aqueous solution concentrations.[254] Using small-angle neutron scattering (SANS) and photon correlation spectroscopy (PCS), Branca *et al.* has also reported similar changes in hydrodynamic radius of PEO with molecular weight of 600 kDa with temperature.[255] It should also be noted that PEO has an LCST in water in 100-180 °C range (depending on molecular weight),[256] which is much higher than the temperature range used in our experiments. By interpolation of the obtained data, the pore size of the membrane can be calculated as 34.6 nm at room temperature which is in good agreement with the theoretical calculations. After correcting the pore size calculation with considering temperature effect, it appears that the pore size of polyLLC membrane increases to 45.7 and 59.6 nm at 35 and 50 °C, respectively.

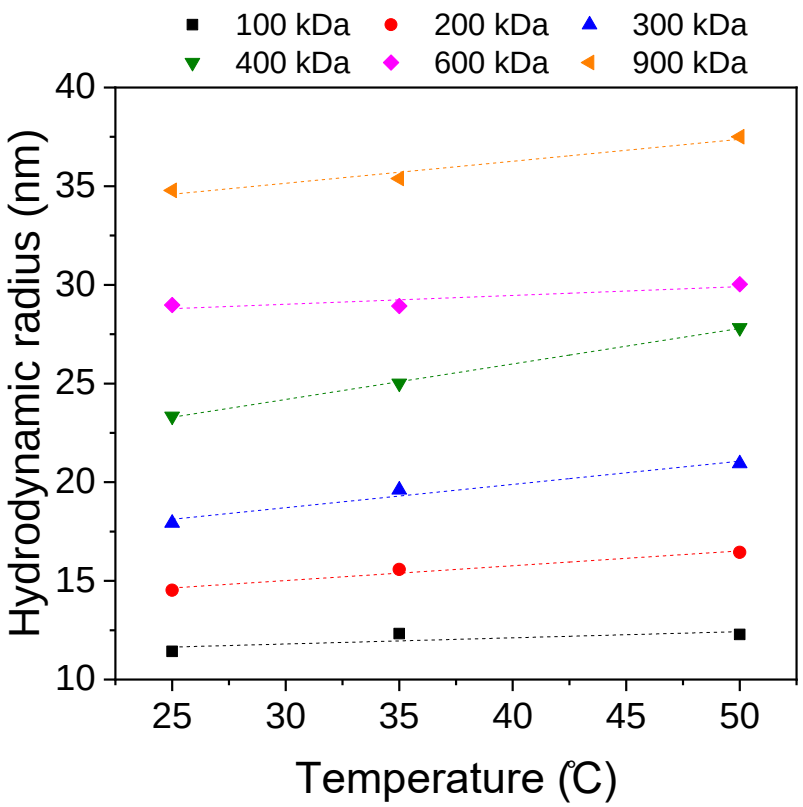

Figure 3-8. Temperature-dependent chain size for PEO having different molecular weights.

3.3.3 Thermoresponsiveness mechanism of polyLLC membrane

According to the presented results, the studied polyLLC exhibits a two-step response with temperature changes. While elaboration of the response at 50 ℃ is relatively simple, explanation of the response at about 35 ℃, which happens due to the LCST behavior of F127, is rather complicated. This observation can be attributed to the fact that the mechanism of LCST for PEO-PPO-PEO block copolymers is not fully understood in the molecular level.[257] Before starting the discussion regarding this behavior in LLC nanostructure, it is required to have an understanding about the LCST behavior of F127, which is observed as sol-gel transition in aqueous media.[258] When the temperature rises to 25-37 ℃, hydrophobicity of PPO block increases, which results in aggregation of PPO chains and thus formation of the core of the micelles. In addition, PEO chains

form a packed interconnected micelles corona, resulting in the formation of a gel. This transition can be reversed by cooling down the formed gel [258]. Therefore, PPO block is mainly responsible for the LCST behavior of F127 around 25-37 °C. In the reported works on LLCs and polyLLCs created by Pluronic surfactants, PPO block is suggested to be oriented towards the apolar domain [32,56,147,215]. It means that when the polymerization happens, PPO chains can be trapped inside the cross-linked polymer network near the interface. If the PPO block is responsible for the LCST behavior of the polyLLC studied in our work, having a dense cross-linked network can eliminate the first thermal transition observed in DSC diagrams by limiting the mobility of PPO chains. Additionally, as the LCST behavior takes place in the presence of water, the first thermal transition should not be detected via DSC when a dried polyLLC is examined. Based on these speculations, we carried out DSC on polyLLC samples containing 20, 50, 100, and 150 wt% EGDMA with respect to *n*BA content. Furthermore, we performed DSC on a dried polyLLC containing 20 wt% EGDMA with respect to nBA content. The obtained results are shown in Figure 3-9. As can be seen, the first thermal transition becomes weaker and then almost disappears as the cross-linker content is increased (area under the peak decreases from ~2.4 to ~0.5 J/g), while the second transition (PEO melting) remains intact (with an area under the peak of ~2.9 J/g). Moreover, there is no thermal transition around 30 °C for the dried polyLLC, whereas the transition at about 50 °C is stronger (area under the peak of ~42 J/g) for this sample compared to the wet one (area under the peak of ~2.9 J/g). This stronger peak can be attributed to the higher crystallinity of PEO blocks in the absence of water as the solvent. These results confirm our hypothesis that PPO block is responsible for the LCST behavior of F127 in polyLLC nanostructure, which is in agreement with the suggested mechanism of sol-gel transition at LCST for PEO-PPO-PEO block copolymers in the literature.[257]

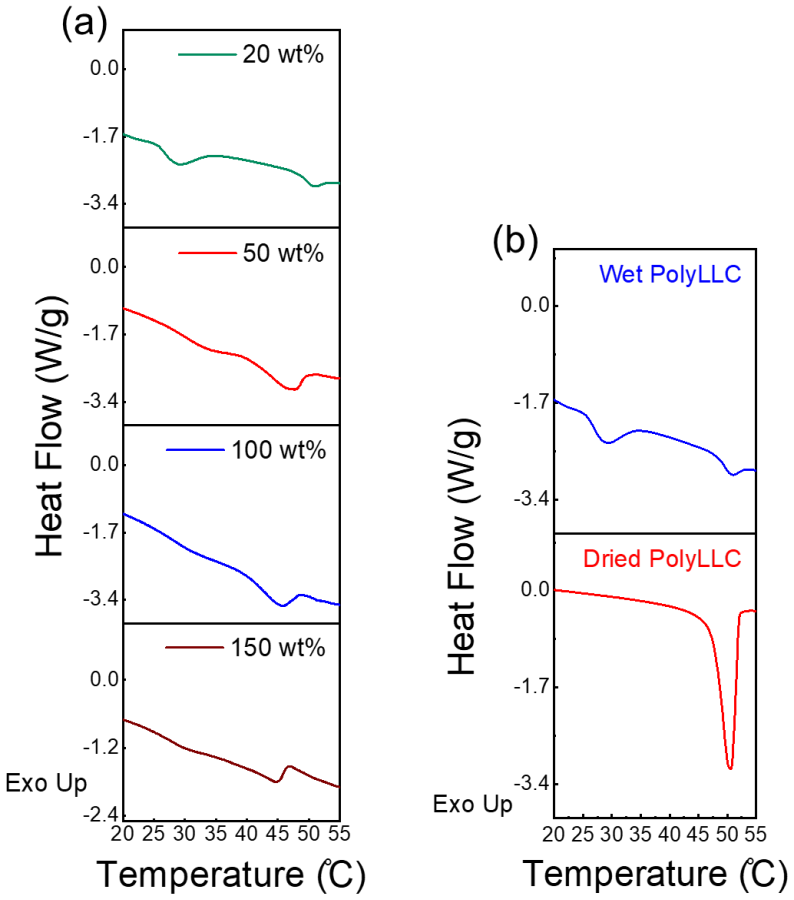

Figure 3-9. Results of DSC measurement for (a) polyLLCs containing different cross-linker contents and (b) wet and dried polyLLC containing 20 wt% cross-linker with respect to nBA content.

Change in the overall structure of the polyLLC (e.g., order-disorder transitions) can be another reason of having thermoresponsiveness. To examine this hypothesis, CPLM and SAXS analysis were performed on the polyLLC at 25, 35 and 50 °C. The obtained results (shown in Figure D3) reveal that the overall lamellar structure of the polyLLC remains intact when the temperature is increased, suggesting that the stimuli-responsiveness is not due to the mesoscale structural transitions but is rather because of change in molecular conformations. In other words, while the periodicity of lamellar structure remains the same upon increase in temperature, F127 at the interface of hydrophobic and water domains undergoes conformational and crystallization

transitions. Similar observations have also been reported for the polyLLCs swollen by water in which the SAXS and CPLM analysis show that the overall structure does not change while the molecular conformation does due to the swelling.[31]

According to the obtained results, the following thermoresponsiveness mechanism of the polyLLC membrane can be suggested. A mesophase with lamellar structure is obtained via mixing F127, water, and polymerizable oil phase. The PPO blocks arrange themselves towards the apolar domain and at apolar/polar domains interface (due to the partial hydrophilicity), while PEO blocks have a semi-crystalline structure in the water channels. The polymerization results in a cross-linked poly(nBA-co-EGDMA) network which holds PPO blocks at the interface of the polymer phase, thus, fixing F127 molecules in their position (negligible chance of their removal by water). With an increase in the temperature to 35 °C, PPO blocks start to rearrange themselves in a way to minimize their contact with water at the interface, resulting in dragging PEO blocks towards the water/polymer interface. Consequently, the membrane pore size increases. Further increasing the temperature to 50 °C melts down the crystalline structure of PEO block. Melting the crystalline regions can result in an increase in the volume of the freed PEO chains and thus decline in the membrane pore size. However, in the presence of water, the released PEO chains tend to adsorb to the water/polymer interface to minimize interfacial tension and get a conformation similar to the already free PEO chains, resulting in further increase in the pore size of the membrane. All of these transitions are reversible upon cooling the system to the room temperature. The explained mechanism is schematically shown in Figure 3-10.

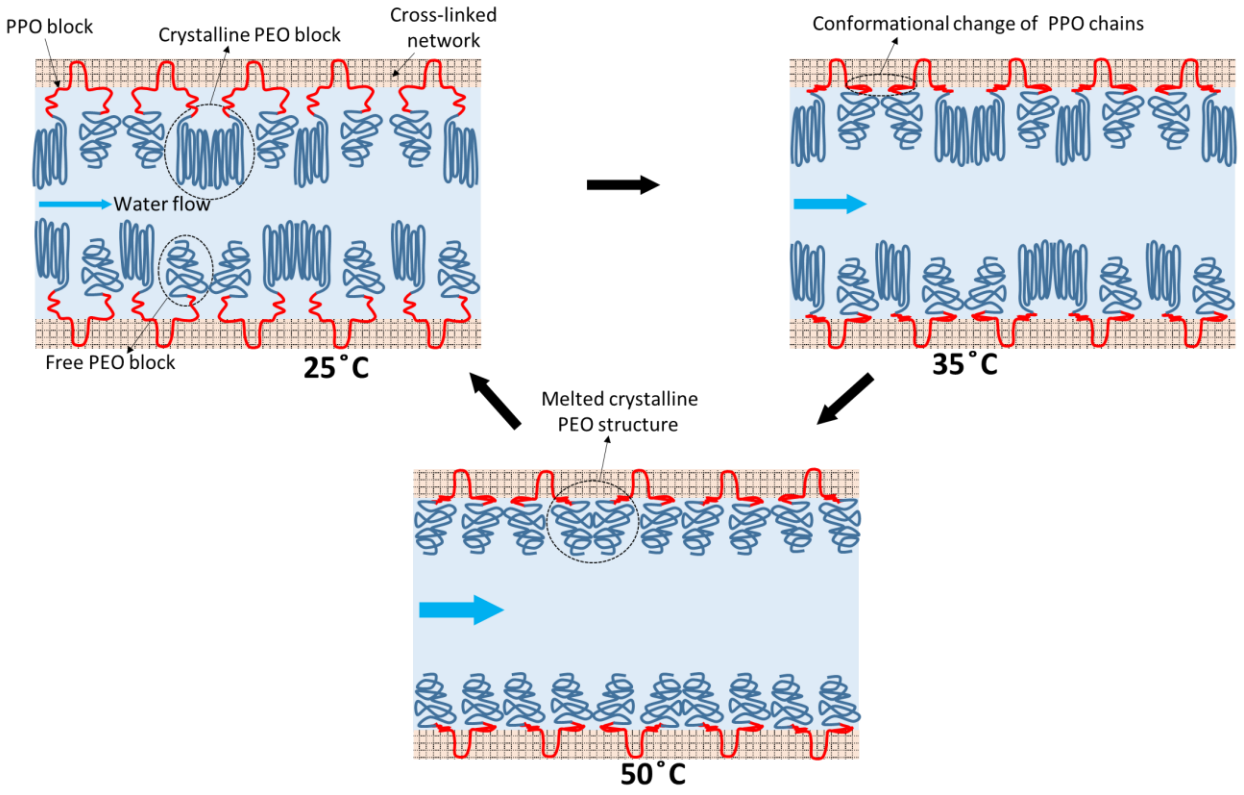

Figure 3-10. Formation and thermoresponsiveness mechanism of polyLLC membrane.

3.4 Conclusion

In this study, we reported a simple approach to fabricate two-step thermoresponsive UF membranes by polymerization of LLCs. Commercially available F127 with thermoresponsive property was used as an amphiphile to create lamellar structure in combination with water and hydrophobic monomers. After the polymerization, the formed cross-linked network fixed F127 molecules in their positions, preventing their removal by water. Hydration capacity, permeability, fouling resistance, cleaning efficiency, and MWCO of the fabricated membrane was evaluated. The experimental results revealed that the membrane exhibits two-step thermoresponsiveness at 35 °C due to the LCST of F127 and 50 °C thanks to the melting of PEO crystalline structure. Moreover, the MWCO measurements showed that the pore size of the membrane can be altered from 34.6 nm to 45.7 and 59.6 nm by increasing the temperature to 35 and 50 °C, respectively.

The cleaning efficiency and thus lifetime of the membrane can be enhanced by cleaning the contaminated membrane at high temperatures due to the porosity change in response to the temperature.

CHAPTER 4: THERMORESPONSIVE ANTIFOULING ULTRAFILTRATION MEMBRANES FROM MESOPHASE TEMPLATING[1]

4.1 Introduction

Membrane separation, which can be considered as an energy-efficient and adoptable technique, is currently employed in a variety applications; e.g., treatment of different water resources,[4] protein purification,[259] vaccine filtration,[260] food processing,[261] and organic solvent filtration.[125] Despite all the offered advantages, there are still challenges involved in membrane technology. For instance, most of the membranes are only able to separate solutes with specific range of molecular sizes (i.e., fixed selectivity), resulting in their limited application.[192] Another significant challenge in membrane technology is membrane fouling, which is particularly prevalent in UF membranes. These membranes are utilized for separating species such as bacteria and viruses, which are prone to causing fouling issues.[262] Employing environmentally-questionable methods like NIPS, which consume large quantities of organic solvents to fabricate membranes in large scales, is the next notable problem in the field.[243] Creating stimuli-responsive membranes via an environmentally-friendly process can address these challenges. Such membranes can change their pore size in response to an external stimulus (e.g., temperature[192] and pH[235]), meaning that they exhibit a

[1] Reprinted with permission from Journal of Membrane Science 2023, 684, 121861 with some modifications.

dynamic permeability and selectivity.[5,213,236–238] Additionally, such changes in the porosity can improve cleaning efficiency of a fouled membrane.[192,263]

Synthesizing nanostructured polymers in LLC templates is an environmentally-friendly approach that can be used to create such functional membranes.[31,118,244] Normal hexagonal (H_1) [31,123,125], normal bicontinuous cubic (Q_1)[34,120,121,264], lamellar (L_α) [32,263], and reverse hexagonal (H_2) [32] structures are the common LLC structures employed for synthesis of NF and UF membranes. Q_1 and H_1 phases are preferred over H_2 and L_α as they offer 3D-continuous transport path and do not require any structural alignment. In contrast to Q_1, H_1 forms more frequently and in a wider range of compositions, which makes it ideal for membrane synthesis.[31] In a recent work, Osuji and coworkers have shown the possibility of fabricating H_1-structured NF membranes with effective pore sizes of about 1 nm, MWCO of ~300 Da, and permeability of ~20 liters m^{-2} $hour^{-1}$ bar^{-1}, which outperform the commercially available NF membranes like Dow FILMTEC NF90-400 with a typical permeability of 10 to 15 liters m^{-2} $hour^{-1}$ bar^{-1}.[123]

Despite the advantages of LLC templating, there are only a few reports available in the literature on synthesizing stimuli-responsive membranes via this technique. In one work,[263] as we discussed in Chapter 3, we were able to create a two-step thermoresponsive UF membrane with ~30 nm pore size from polymerization of L_α-structured LLCs directed by F127 self-assembly, which exhibited selectivity and permeability changes at 35 and 50 °C due to the LCST of F127 and melting of the crystalline structure of PEO block, respectively.. Li et al.[126] reported the synthesis of a pH- and light-responsive nanoporous polymer having Q_1 structure with a pore size of around 1 nm. According to the SAXS data, the pore size changes with altering pH. While these reports on responsive membranes show promising results, extending the pore size of LLC-templated

membranes is essential to broaden their applications. In addition, there is no report on synthesizing H_1-structured stimuli-responsive membranes.

In this Chapter, we report the first successful H_1-structued responsive membrane. H_1 LLC is obtained by mixing thermoresponsive Pluronic P84 diacrylate (P84DA) with 1-butyl-3-methylimidazolium tetrafluoroborate ([BMIM][BF_4]) and 1,6-hexanediol diacrylate (HDDA). PolyLLC is acquired through UV polymerization of the mesophase. After removal of the ionic liquid with water, water transport pores are created with a pore size of 2.5 nm at 25 °C, which can be increased to 3.2 nm upon heating the polyLLC to 45 °C. Such temperature-dependent change in the porosity can increase the thickness-normalized flux of the membrane from 28 to 68 liters m^{-2} $hour^{-1}$ µm. In addition, the membrane exhibits an outstanding fouling resistance. The achieved characteristics (e.g., range of pore size, tunable selectivity, and antifouling behavior) make this membrane an ideal candidate for a variety of applications (e.g., protein purification and removal of viruses and bacteria) without having to tune the structure or change the membrane entirely.

4.2 Experimental

4.2.1 Materials

All of the chemicals used in this work were purchased from Sigma-Aldrich and used as received unless stated otherwise. Pluronic P84 (P84) copolymer (PEO_{19}–PPO_{43}–PEO_{19}) with an average molecular weight of 4200 g/mol, anhydrous dichloromethane (DCM) with a purity of ≥99.8%, 99.8% pure anhydrous toluene, triethylamine having a purity of 99.5% and acryloyl chloride with a purity of 97% were used to synthesize P84DA as the polymerizable surfactant (as described in the next section). [BMIM][BF_4] with a purity of ≥98%, HDDA (obtained from Thermo Scientific Chemicals having a purity of 99%), and 99% pure 1-hydroxycyclohexyl phenyl ketone (HCPK) were used to create the desired LLC through mixing them with P84DA. DI water

with a conductivity of 0.055 μS/cm, which was acquired from EMD Millipore Direct-Q3, was used in all experiments.

Membranes performance (e.g., MWCO, protein and dye rejection, and fouling resistance) was evaluated through filtration of different solutes including PEG with different molecular weights (1, 2, 3, 4, 6, 8, and 10 kDa), lyophilized powder of BSA with a purity of ≥96%, direct red 23 (DR23) having a dye content of 30%, and direct red 80 (DR80) with 25% dye content. CraneMat® CU463 nonwoven polyester sheet with 2 μm porosity (supplied by Neenah Filtration) was employed as a support layer for membrane fabrication. Commercially available Ultracel® regenerated cellulose membrane with a nominal MWCO of 3 kDa (which is not thermoresponsive) was purchased from Millipore Sigma and used for thermoresponsiveness comparisons with membranes synthesized in this study.

4.2.2 Synthesis of P84DA

P84DA was synthesized through functionalization of P84 based on a well-established procedure available in the literature.[13,265] Briefly, 40 g of P84 was dissolved in a 150 mL mixture of DCM and toluene (DCM/toluene volume ratio of 80/20) under vacuum. Then, the mixture having a total volume of 190 mL was placed in an ice water bath followed by addition of triethylamine (2.5 mL). Subsequently, 1.2 mL acryloyl chloride was dissolved in 40 mL DCM and the obtained solution was added to the reaction mixture drop-wise in around 30 min to control the heat of reaction. The reaction medium was stirred for about 24 h under a static vacuum at room temperature. The precipitated triethylammonium chloride, which is the by-product of the reaction, was separated from the polymer solution using Büchner funnel vacuum filtration. At the next step, the functionalized polymer was precipitated in excess n-hexane having a temperature of about −18 °C. Subsequently, the obtained polymer was washed three times with n-hexane through addition

of excess amount of the *n*-hexane (about twice of the volume of the polymer) and stirring at 400 rpm with magnetic stirrer for 10 min and dried under vacuum for 3 days. Attenuated total reflectance-Fourier transform infrared spectroscopy (ATR-FTIR, Nicolet™ iS50 FTIR Spectrometer) and nuclear magnetic resonance (^{1}H NMR, Varian VNMRS-400 with Probe AutoX-DB-PFG) were used to evaluate the extent of the functionalization reaction (see Figure E1-2 and the corresponding text in Appendix E).

4.2.3 Mesophase preparation

The H_1-structured mesophase was prepared via mixing P84DA, [BMIM][BF4] (containing 1 wt% HCPK as UV initiator), and HDDA (containing 10 wt% HCPK) with a weight ratio of P84DA/[BMIM][BF4] /HDDA 48.6/48.6/2.8. Hand mixing and centrifugation at 11,000 rpm for 5 min in a 50 mL centrifugal tube were carried out repeatedly until a transparent gel was obtained. Figure 4-1 represents the chemical structure of the components used for mesophase preparation. Additionally, schematic of the created H_1 structure is presented in Figure 4-1e.

4.2.4 Characterization of LLC and polyLLC

4.2.4.1 Cross-polarized light microscopy (CPLM)

A cross-polarized Nikon microscope (model LABOPHOT2-POL) equipped with a digital camera was used to evaluate the birefringence of the H_1-structured sample before and after polymerization. Around 0.2 g of the mesophase gel was sandwiched between a glass slide and a glass cover slip for CPLM analysis. To polymerize LLC, the sandwiched sample was cured via UV radiation (using Uvitron Sunray 600 SM curing system equipped with a 600 W UV flood lamp) for 40 s. Structure of the polymerized LLC is schematically shown in Figure 4-1e.

4.2.4.2 Small angle X-ray scattering (SAXS)

SAXS was employed to further evaluate the mesophases of different samples. LLC gel was loaded into quartz capillary tubes with a nominal diameter of 1.5 mm (Charles Supper Company, Natick, MA) and sealed with epoxy glue. The loaded mesophase was cured under UV for 40 s to obtain the polyLLC for SAXS analysis. To analyze the water-swollen sample, the polyLLC was taken out of the capillary tube via breaking it and immersed in water for at least 72 h for the solvent exchange (exchange of water with the ionic liquid) and swelling. Then, the water-swollen sample was pushed into a capillary tube followed by sealing with epoxy glue. 1D scattering profiles were obtained from a Bruker Nanostar X-ray scattering system equipped with a monochromatic Cu Kα radiation source (X-ray wavelength of 1.541 Å) through azimuthal integration of 2D scattering patterns. SAXS analysis was also performed at different temperatures for LLC gels and water-swollen polyLLCs to assess any structural changes due to temperature alteration.

4.2.4.3 Differential scanning calorimetry (DSC)

Different species including pure P84DA, water-swollen polyLLC, and dried polyLLC (water-swollen polyLLC sample was dried under vacuum for at least 72 h) were analyzed by differential scanning calorimetry (DSC, Q2500, TA Instruments, New Castle, DE). About 10 mg of the desired sample was placed into an aluminum pan (PerkinElmer, Inc.) and sealed with a hermetic lid. The thermal analysis was carried out from 0 to 60 °C (and vice versa) with 1 °C/min ramp. The cycle was repeated twice and the second cycle was used for analysis (after erasing the thermal history of the samples).

4.2.4.4 Swelling behavior of the polyLLC

A film of polyLLC having a thickness of 500 µm was created between two glass plates followed by photopolymerization at room temperature. The obtained film was washed several

times with water and dried under vacuum, from which ca. 2 cm × 2 cm samples were cut for water uptake studies. Each sample was immersed in excess DI water maintained at the desired temperature (±0.1 °C) until reaching equilibrium swollen state. Then, the swollen samples were taken out of water followed by removing the excess water on the surface using paper towel. The swelling capacity (water uptake) was calculated using following equation by using the weight of the dry (W_0) and swollen (W_t) states:

$$Swelling\ Capacity = \frac{W_t - W_0}{W_0} \times 100 \qquad (4\text{-}1)$$

The kinetics of thermoresponsiveness was analyzed by transferring the swollen sample from a water bath at 25 °C to one maintained at 45 °C followed by measuring the water uptake in the new environment at different times. To demonstrate the reversibility of the response, the sequential change of the environment (e.g., transferring back and forth between 25 and 45 °C water baths) was performed for several cycles and the swelling capacity was measured upon each environmental change.

At least three samples were analyzed for water uptake measurements and the average value along with standard deviation is reported.

4.2.4.5 Rheo-mechanical studies

A strain-controlled rheometer ARES-G2 (TA Instruments, New Castle, DE) was employed to study the rheological behavior of the LLC and the mechanical properties of the polyLLCs at different states. The mesophase gel was placed in between of 25 mm sandblasted parallel plate geometry (to minimize the wall slip, although our previous work showed that the wall slip is negligible in LLCs [245,266]) with 1 mm gap. The viscosity was measured by sweeping temperature from 15 to 50 °C in rotational mode under constant shear rate of 0.1 s^{-1}. To make the polymerized

LLC and water-swollen polyLLC samples for rheological studies, the LLC was casted in between of two glass plates separated by 1 mm spacer plates. Then the cast gel was UV-polymerized for 40 s to obtain polyLLC sheet with 1 mm thickness. The polyLLC was then cut in circles having 25 mm diameter. The water-swollen samples were obtained through solvent exchange and swelling of the circular cut polyLLCs followed by trimming the swollen samples to fit the rheometer geometry. To analyze the acquired samples, dynamic frequency sweep test was carried out in the frequency range of 0.1 to 100 rad/s using 25 mm crosshatched geometry with 1 mm gap. The water-swollen samples were tested at 10, 25 and 45 °C. It should be mentioned that the dynamic frequency sweep test was performed in the linear viscoelastic regime (0.1% strain, confirmed from amplitude sweep tests).

4.2.5 Preparation of the polyLLC membrane

To fabricate membranes, first the mesophase was heated to 45 °C to lower its viscosity due to a reversible structural transitions (as confirmed by rheological studies, see Figure E3-4 and the corresponding text in Appendix E). Then, about 1.5 g of the mesophase was placed on a glass sheet followed by covering it with the polyester support layer. A doctor blade was subsequently used to coat the mesophase on the support sheet. The coated mesophase was let to equilibrate to room temperature for 20 min to recover its original H_1 structure. Finally, the LLC layer was cured via UV radiation for 40 s, resulting in the formation of the supported polyLLC membrane (Figure 4-1f shows the membrane preparation procedure schematically). Scanning electron microscope (SEM, ThermoFisher Quattro S field emission environmental SEM) was used to measure the thickness of the polyLLC coated layer.

To exchange the ionic liquid with water, all of the fabricated membranes were immersed in water for at least a week before use.

4.2.6 Characterization of the polyLLC membrane

4.2.6.1 Water flux and permeability

The performance of the membranes was evaluated using Sterlitech HP4750 high pressure stirred cell (dead-end filtration system) with the effective area of 14.6 cm^2 operated under stirring at 750 rpm with a magnetic stirrer and at a pressure of 30 psi (2.07×10^5 Pa). Thickness-normalized flux (reported as liters m^{-2} $hour^{-1}$ μm) of the membranes was measured at 25 and 45 °C. To measure the flux at elevated temperature, the filtration cell containing the membrane was placed in a water bath maintained at 45 ± 1 °C. The permeate collection was started after ensuring the isothermal conditions in membrane level and having a stable flux. All of the measurements were repeated for three membranes. Darcy's law[32] was used to calculate the membrane permeability (Eq. 3-1).

4.2.6.2 MWCO, protein and dyes rejection measurements

MWCO measurements were carried out through filtration of 1 mg/mL aqueous solutions of PEG with different molecular weights (1–10 kDa). At least 5 mL of permeate was collected for each analysis. 3 mL of a reagent [267] made of potassium iodide (2 g), iodine (1.27 g), and water (100 mL) was added to 0.3 mL of the collected permeate. Then, UV-Vis spectroscopy (Thermo Scientific™ GENESYS™ UV-Vis Spectrophotometer) was used within 15 min of sample preparation to determine the concentration of the PEG in the permeate. Eq. (3-5) was used to calculate PEG rejection.

The rejection capability of the membranes for protein and dyes were studied from filtration of BSA, DR23, and DR80 dispersions in water with 1, 0.5, and 0.5 mg/mL concentration, respectively. The concentration of the filtrated solutes in permeate was detected via UV-Vis spectroscopy. Eq. (3-5) was used to calculate the rejection.

To assess the thermoresponsiveness of the membranes, all of the experiments were performed at 25 and 45 °C. Additionally, the experiments were repeated for three membranes and the average value along with the calculated standard deviation is reported.

4.2.6.3 Contact angle and fouling resistance

Contact angle of the membranes was measured by using an optical tensiometer (Biolin Scientific). Fouling resistance of the membranes was tested through filtration of aqueous dispersions of PEG with molecular weight of 10 kDa, BSA, and DR80 at 1 mg/mL concentrations. The filtration cell was filled with about 250 mL of solution at the beginning of the experiment and 5–8 mL permeate was collected every 12 h. The test was continued for 60 h and the membrane flux and rejection were recorded in 12 h time intervals.

4.3 Results and discussions

4.3.1 Characterization of LLC and polyLLC

Combination of CPLM and SAXS was used to confirm the structure of the LLC as well as the synthesized polyLLC at different states. As shown in Figure 4-2a, CPLM confirms that the LLC is birefringent. The observed CPLM texture is the characteristic of hexagonal mesophases.[45] The birefringence remains intact after polymerization, implying that the polyLLC retains the parental structure. Furthermore, analysis of the water-swollen polyLLC at 25 °C indicates that the structure is preserved after the solvent exchange. SAXS analysis quantitatively confirms the CPLM results. As can be seen in Figure 4-2d, Bragg peaks with ratios (q/q^*) of $1:\sqrt{3}:2:\sqrt{7}$ are detected for the mesophase, where q is the scattering vector and q^* is the position of the principal peak in each curve. Therefore, a highly ordered H_1 structure is present in the samples. The peaks corresponding to H_1 structure (ratio of $1:\sqrt{3}$) is also seen for the polyLLC and water-swollen polyLLC. While higher peak ratios are not observed, having the characteristic birefringence of H_1 structure and the

first two peaks confirm that the structure is mostly retained after polymerization and solvent exchange. Similar observation has also been reported by Forney et al.[42] and Sievens-Figueroa et al.[96] for hexagonal structures, in which some of the SAXS peaks become weak after polymerization while the synthesized polymer still exhibits some other desired characteristic peaks. This behavior has been attributed to minor changes in the structure (e.g., adhering micelles to each other[31]) after polymerization.[42,96]

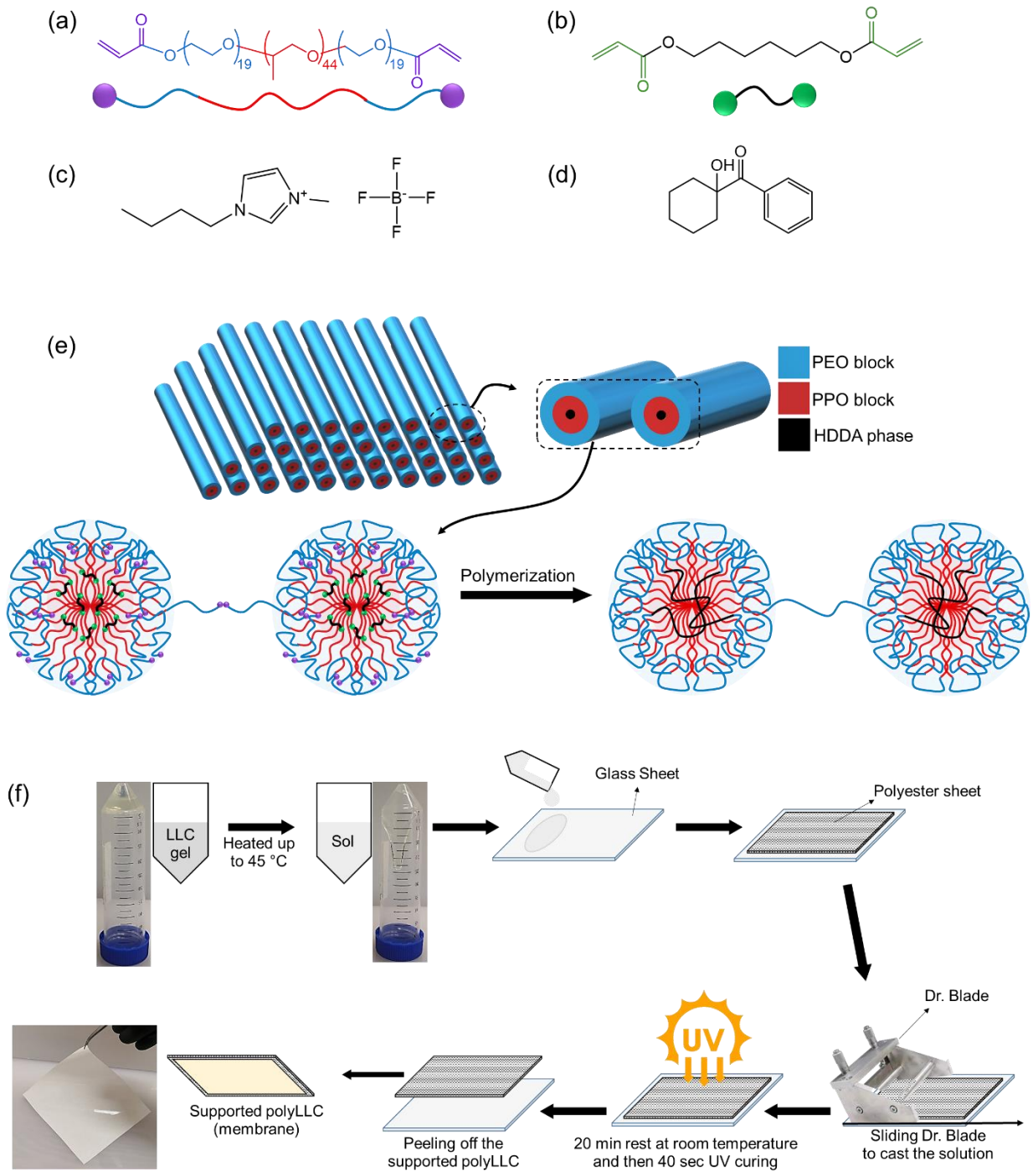

Figure 4-1. Molecular structure of (a) P84DA, (b) HDDA, (c) [BMIM][BF4] and (d) HCPK. Schematic representation of P84DA and HDDA have also been presented in panel a and b, respectively. (e) Schematic illustration of H1-structured mesophase which is obtained through mixing the components. The micelles are surrounded by [BMIM][BF4]. The apolar domain is made of PPO block and HDDA. Chemically-bonded polymer network is created through the reaction of acrylate groups of P84DA and

HDDA. The presence of intermicellar bridges, which form via the reaction of acrylate groups of extended PEO blocks, seems necessary to have an integrated H1-structured membrane.[31] (f) Schematic procedure for preparation of polyLLC membrane.

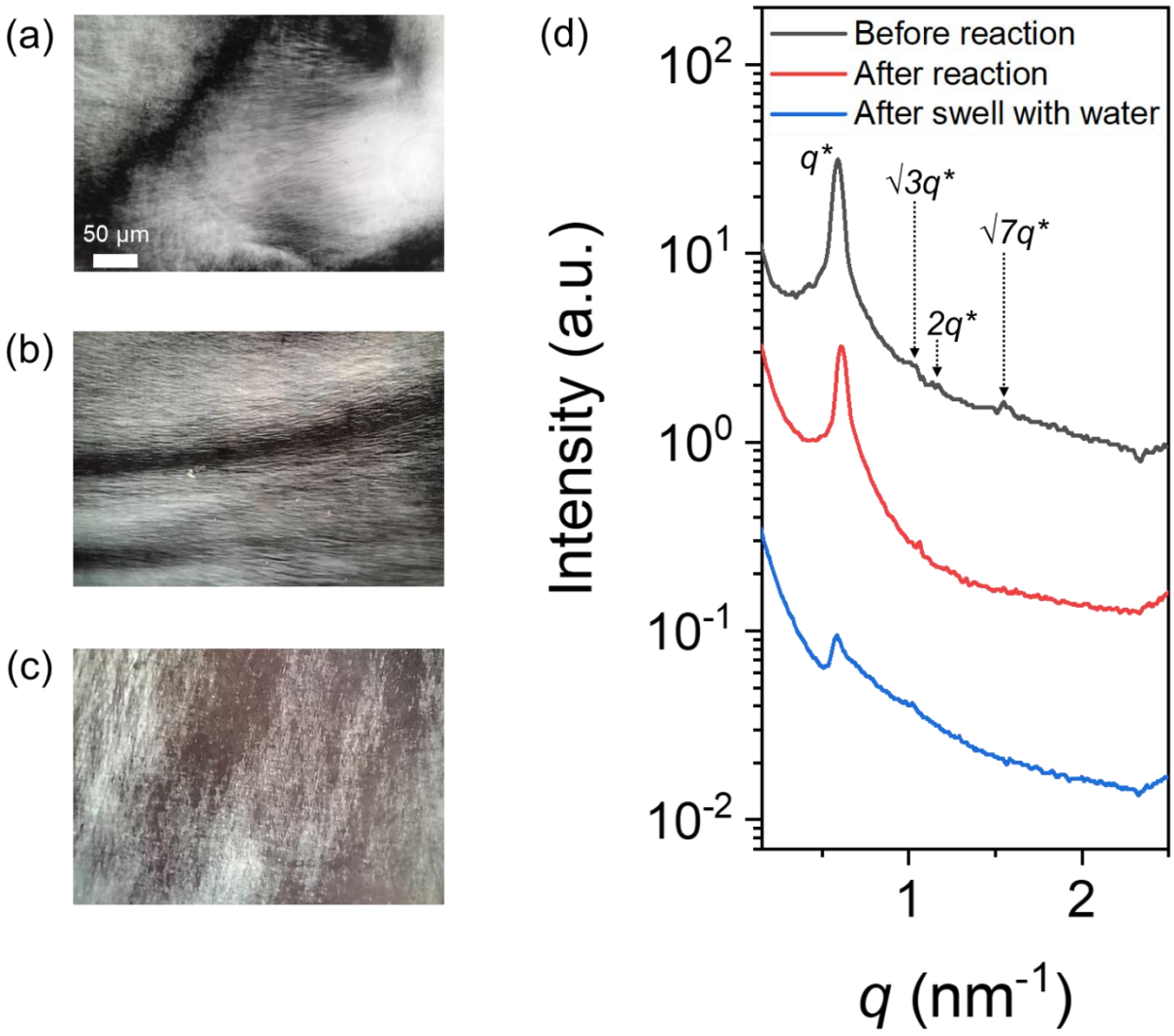

Figure 4-2. (a-c) CPLM images of samples: (a) before reaction, (b) after reaction, and (c) after swelling with water. (d) 1D SAXS scattering profile for samples (the plots are vertically shifted for clarity).

A variety of structural parameters including domain sizes of the synthesized polyLLC can be estimated from the SAXS data (see Figure 4-3 for schematic representation of the structural parameters). The lattice parameter (*a*) for hexagonal structure can be calculated as[210]:

$$a = \frac{4\pi}{\sqrt{3}q^*} \tag{4-2}$$

To simplify the calculations, we assume that the solvent ([BMIM][BF_4] or water), PEO, PPO and HDDA are fully segregated and each domain is characterized by its bulk density.[215] It should be noted that in the case of water-swollen samples, the polymer and water are not completely segregated since the polymer network can hold large amounts of water. Another important point is partitioning the PEO and PPO blocks in the solvent and HDDA phases which makes the calculations not to be rigorously accurate.[178] The size of ionic liquid or water domain can be assumed as the pore size of polyLLC membrane. We are aware that this assumption may not be valid in all cases and that is why we have also estimated the pore size of membranes from MWCO measurements which is closer to the real application. We also assume that HDDA and PPO block form the apolar domain with volume fraction of ϕ, whereas the solvent and PEO block form the polar domain that fills the rest of the volume ($1-\phi$). Therefore, the apolar domain size R_c is calculated as:[208,210]

$$R_c = a\sqrt{\frac{\sqrt{3}}{2\pi}\phi} \tag{4-3}$$

For deriving Eq. (4-3), it should be noted that a hexagonal lattice with a lattice parameter of a has three fully occupied cylinders with a radius of R_c. By dividing the volume of these cylinders by the volume of a single hexagon, we can obtain the volume fraction of the cylinders (apolar domain volume fraction, f) as:

$$f = \frac{3\pi R_c^2 L}{3\frac{\sqrt{3}}{2}a^2 L} \tag{4-4}$$

In this equation, the variable L represents the length of the lattice, which is equal to the length of the cylinders. By solving Eq. (4-4) for R_c, Eq. (4-3) is obtained.

By employing a similar approach utilized to derive the apolar domain size (α), we can define the micelle size, R_m as follows:[178]

$$R_m = a\sqrt{\frac{\sqrt{3}}{2\pi}(\phi_{Pluronic} + \phi_{HDDA})} \tag{4-5}$$

In this equation, $\phi_{Pluronic}$ and ϕ_{HDDA} are the volume fraction of the block copolymer and HDDA phase, respectively. In H_1 structure after polymerization, the shortest distance between micelles is the exclusion size of solutes, which is equal to the intermicellar distance D_m[178]:

$$D_m = a - 2R_m \tag{4-6}$$

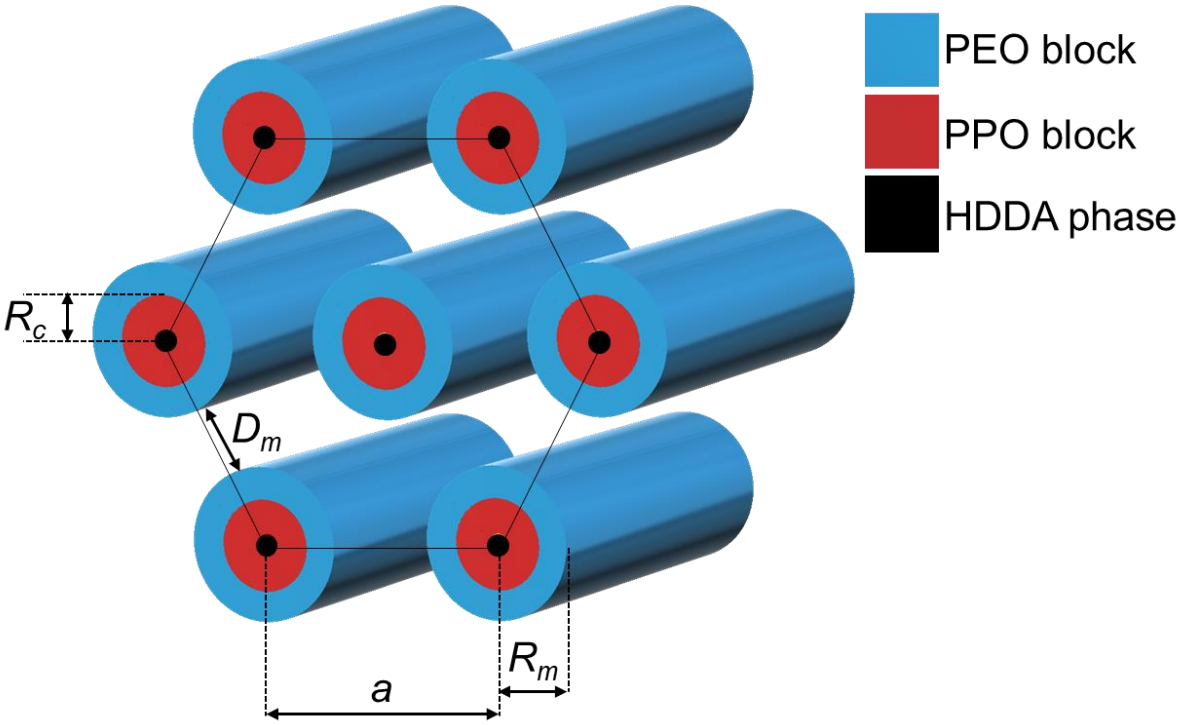

Figure 4-3. Schematic representation of structural parameters for H_1 structure.

Table 4-1 shows the calculated structural parameters. As can be seen, the estimated intermicellar distance (pore size) is about 2.6 nm for the LLC and polyLLC. However, this estimated value significantly increases to ~5.4 nm for the water-swollen sample at 25 °C. The more accurate pore size can be determined via the MWCO experiment, which will be discussed in section 4.3.2.2. In the upcoming sections, we will present the experimental results of the polyLLC membrane under testing conditions of 25 and 45 °C. To enhance the comparison of the calculated data obtained from SAXS, we have also included the data for water-swollen polyLLC at 45 °C in Table 4-1. The corresponding SAXS data for this particular sample can be seen in Figure 4-6. Section 4.3.2.2. will provide a detailed discussion on the calculated data.

Table 4-1. Calculated structural parameters for different species based on SAXS data.

Sample	q^* (nm^{-1})	ϕ_{PPO} [a]	ϕ_{HDDA}	$\phi_{Pluronic}$	ϕ	a (nm)	R_c (nm)	R_m (nm)	D_m (nm)
LLC	0.59	0.66	0.031	0.53	0.38	12.3	4.0	4.8	2.7
PolyLLC	0.60	0.66	0.031	0.53	0.38	12.1	3.9	4.7	2.6
Water-swollen polyLLC at 25 °C	0.59	0.66	0.016	0.27	0.20[b]	12.4	2.9	3.5	5.4
Water-swollen[c] polyLLC at 45 °C	0.59	0.66	0.026	0.446	0.32[b]	12.4	3.7	4.4	3.4

[a] ϕ_{PPO} is the volume fraction of PPO block in the Pluronic block copolymer.
[b] Volume fraction of the apolar domain for water-swollen polyLLC was calculated based on 220% and 120% swelling capacity of the polymer at 25 and 45 °C, respectively (see Figure 4-5c).
[c] SAXS data for water-swollen polyLLC at 45 °C is shown in Figure 4-6.

Thermoresponsiveness of the nanostructured polymer was evaluated with DSC, as shown in Figure 4-4. Control experiments were also carried out on pure P84DA and dried polyLLC to define responsible phenomena for thermal transition. The water-swollen polyLLC exhibits a thermal transition in 5–32 °C range, which is attributed to the LCST of Pluronic.[248,268] Hydrophilicity of the PPO block significantly decreases at LCST, reducing water solubility of the block copolymer.[258] Pure P84DA also shows a thermal transition in 20–47 °C range, which is due to the melting of crystalline regions made by PEO block.[269] In other words, since dried polyLLC has no thermal transition, we conclude that the formation of polyLLC suppresses the crystallization of PEO block and the observed thermal response of the water-swollen polyLLC is due to the LCST of the surfactant.

To further evaluate the thermoresponsive behavior, the swelling capacity was performed on polyLLC pieces having ca. 2 cm × 2 cm dimensions and a thickness of 500 μm (Figure 4-5a–b). Figure 4-5c shows that the swelling capacity of the polymer declines from ~600% to ~120% when the temperature increases from 5 to 45 °C. This change in the swelling capacity is in agreement with the DSC results, confirming that the polymer experiences an LCST transition in this range of temperature. Figure 4-5d reveals that this response is rapid and takes place within 5 min. Additionally, Figure 4-5e confirms the reversibility of the thermal response throughout several heating-cooling cycles.

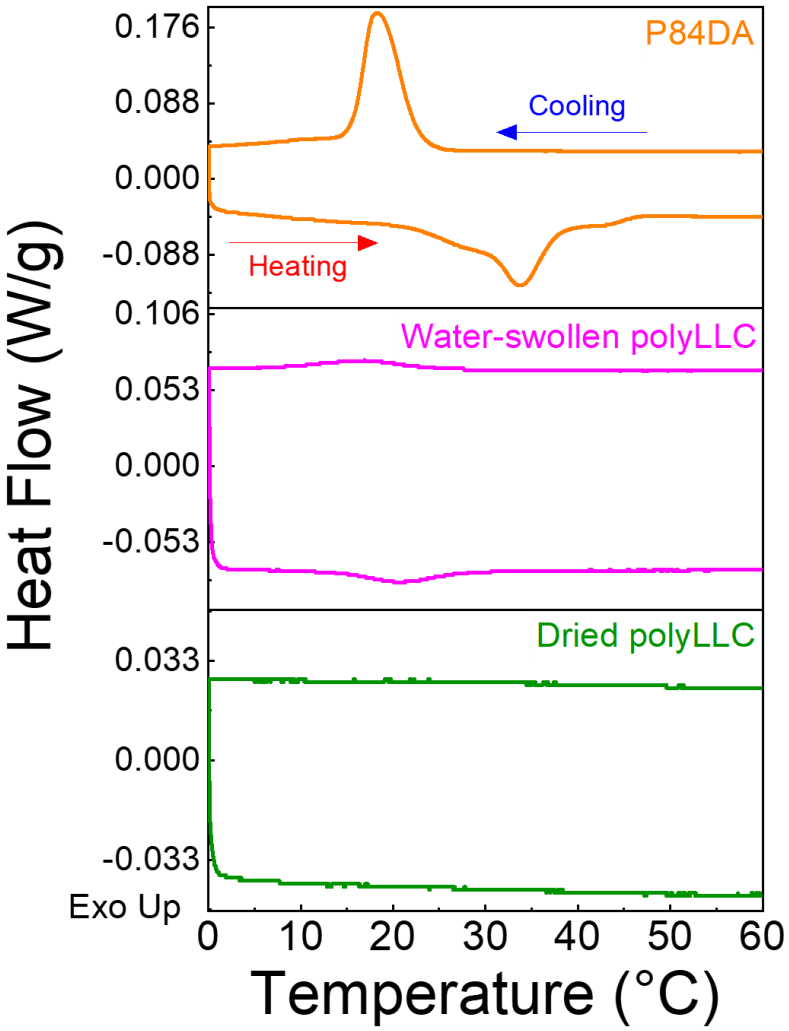

Figure 4-4. DSC results for pure P84DA, water-swollen polyLLC, and dried polyLLC.

We also performed rheo-mechanical experiments on the polyLLC at different states. The results in Figure 4-5f show that the polyLLC containing ionic liquid exhibits the best mechanical properties. The storage modulus, G', of water swollen polyLLC decreases with an increase in the swelling capacity of water-swollen samples as the temperature decreases from 45 to 10 °C. These results reveal that the mechanical properties of the obtained polyLLC is mainly affected by the solvent nature and content. In our previous study, we have shown that the elasticity of LLCs is controlled by intermicellar interactions, which change by the solvent type and intermicellar

distance.[62] The solvent content at 25°C increases from 48.6 wt% in the case of polyLLC containing ionic liquid (intermicellar distance of 2.6 nm) to ~70% (intermicellar distance of 5.4 nm) after exchange of ionic liquid with water. Therefore, the higher G' for polyLLC containing ionic liquid could be attributed to the lower contents of the solvent and/or stronger intermicellar interactions. When comparing water-swollen samples, G' decreases as the solvent content (i.e., intermicellar distance) increases from ~52% to ~70% and ~85 wt% by decreasing temperature from 45 °C to 25 °C and 10 °C, respectively. Similar changes in mechanical properties with variation of solvent content have been reported in the literature for solvent-swollen polyLLCs.[23]

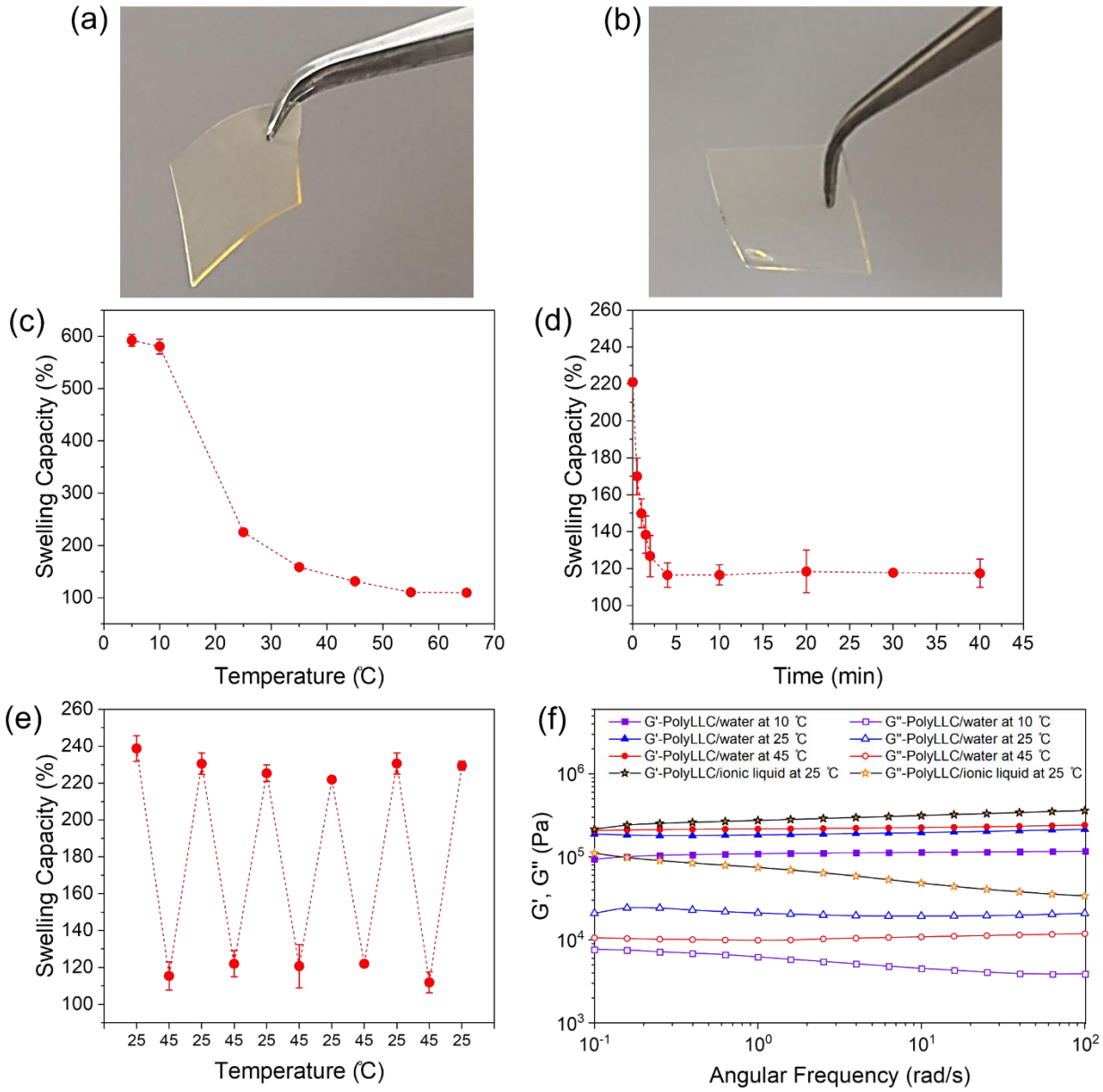

Figure 4-5. (a-b) PolyLLC sample (a) before and (b) after swelling with water. (c-f) Results of different experiments: (c) swelling capacity changes with temperature; (d) kinetics of thermal response when the temperature changes from 25 to 45 °C; (e) reversibility of the thermoresponsiveness; and (f) viscoelastic behavior of polyLLC film under different conditions.

Figure 4-6 shows the structural change of the water-swollen polymer with temperature, which was examined using CPLM and SAXS. The results suggest that the structure exhibits weak ordering at a temperature of 5 °C, as evidenced by the absence of texture in the CPLM image and

the presence of weak peaks in the SAXS profile. As mentioned before, PPO becomes hydrophilic at temperatures below LCST of the Pluronic[258,263], which will increase the miscibility of PEO and PPO blocks with water, leading to a substantial increase in the swelling of micelles with water. This is supported by the observation of an approximately threefold increase in the swelling capacity when the polyLLC is cooled to 5 °C (see Figure 4-5). Under these conditions, the segregation between the polymer chains and the water domain is disrupted. In other words, both PEO and PPO blocks will be swollen with no discernible structure. However, the structure can be restored by deswelling of the polymer through heating, due to the segregation of PEO and PPO blocks and LCST transition of PPO/water, and thanks to the presence of the chemically cross-linked polymer network preventing complete disruption of the structure. As such, as the temperature is increased from 5 to 65 °C, the texture and strong H_1 Bragg peaks appear in CPLM and SAXS profile, respectively. The change in the structure is reversible as the scattering profiles at 25 °C before and after carrying out the heating-cooling cycle are similar. When the temperature is increased from 25 to 45 °C, the H_1 structure remains intact with lattice parameter of 12.4 nm, whereas the swelling capacity decreases from ~230% to 120%. It should be noted that the intermicellar distance of 3.4 nm can be calculated for the deswollen sample at 45 °C which is in good agreement with 3.2 nm pore size obtained from MWCO measurement at 45 °C (see section 4.3.2.2). These results suggest that upon swelling-deswelling of the polymer network, the intermicellar distance changes due to change in the micelle size (R_m) while the overall structure remains intact (Figure 4-9 schematically shows the mechanism and section 4.3.3 provides further discussion).

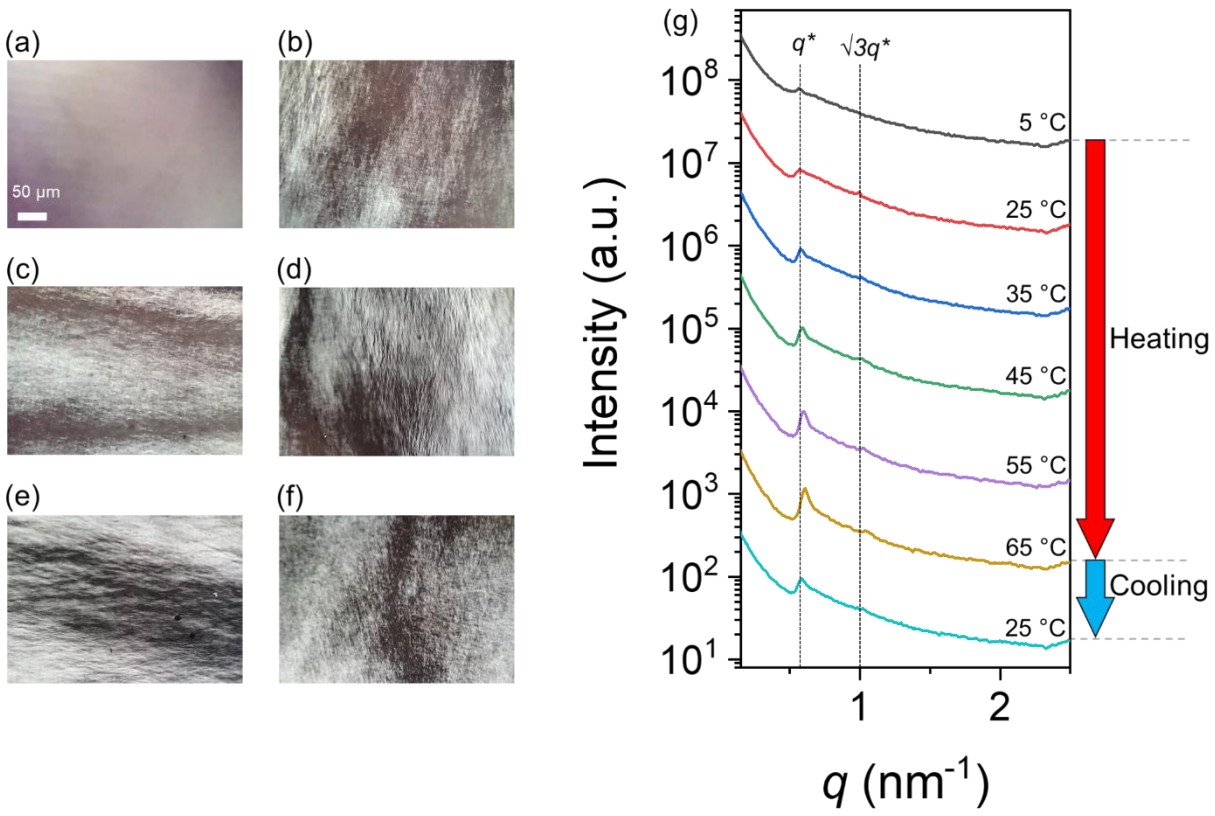

Figure 4-6. (a-f) CPLM images of water-swollen polyLLC at (a) 5, (b) 25, (c) 35, (d) 45, (e) 55, and (f) 65 °C. (g) 1D SAXS scattering profile of the water-swollen polyLLC upon heating and cooling experiment. The experiment starts by heating the sample from 5 to 65 °C and ends by cooling it to 25 °C. The plots are vertically shifted for clarity.

4.3.2 Characterization of membranes

LLCs have gel-like behavior,[62,266] which can make their casting as thin film challenging. As explained in Appendix E, the obtained LLC exhibits H_1 structure at room temperature, which undergo a reversible structural transition upon heating. We used this behavior to lower the viscosity of the Pluronic and ionic liquid mixture for coating on a polyester sheet with doctor blade. Then, the sample was let cool down to room temperature for about 20 min, followed by UV curing for 40 s. Figure 4-7a and b show a circular cut and a typical cross-sectional SEM image of the supported membrane, respectively. Image analysis revealed that the thickness of the membrane

ranges 20–60 µm with an average of 40 µm. Therefore, all the membrane flux data was normalized by this average thickness to liters m^{-2} $hour^{-1}$ µm unit. We also tested a non-thermoresponsive, commercially available UF membrane as control to confirm that the observed thermoresponsive behavior is originated by the membrane (see Appendix E). The following sections discuss the results for polyLLC membrane performance.

4.3.2.1 Water flux and permeability

Water flux and permeability of the membranes were measured at 25 and 45 °C in several heating-cooling cycles. As can be seen in Figure 4-7c and d, both flux and permeability increase when polyLLC membrane is heated up to 45 °C. The membrane performance returns to its original state as the temperature is decreased to 25 °C. In comparison, the commercial UF membrane does not show any changes in its permeability upon heating (Figure E5 in Appendix E). These results confirm that the pore size of the polyLLC membrane can be reversibly altered by changing temperature.

4.3.2.2 Rejection characteristics

The MWCO experiment was first carried out at 25 °C and then at 45 °C with the same membrane. To evaluate the reversibility of the thermal response, the membrane was cooled back to 25 °C and MWCO measurement was repeated. Boltzmann sigmoidal equation (Eq. 3-7) was also used to fit MWCO data. The reason for employing this fitting equation is that MWCO results typically exhibit a sigmoidal trend.[125] The obtained results are shown in Figure 4-7e. The MWCO is defined as the molecular weight that is 90% rejected by a membrane. The MWCO of the polyLLC membrane increases from 2200 to 3900 Da with an increase in temperature from 25 to 45 °C. The MWCO returns to 2200 Da after cooling the membrane back to 25 °C. The membrane pore size can be estimated from MWCO by using the following equation.[270] This equation has

been derived from the regression of molecular weight against the PEG hydrodynamic radius experimental data, as described by Hernández et al.[271]

$$Pore\,size = 0.12254 \times MWCO^{0.3931} \quad (4\text{-}7)$$

From this equation, the pore size changes from 2.5 to 3.2 nm upon heating the membrane from 25 to 45 ℃. It should be noted that the estimated pore size at room temperature is in agreement with intermicellar distance from SAXS results for the as-synthesized polyLLC containing the ionic liquid. However, pore size from MWCO measurment is smaller than the intermicellar size from SAXS analysis of the water-swollen polyLLC at 25 ℃. This discrepancy can be ascribed to the assumptions in our calculations based on SAXS data. In other words, the 5.4 nm pore size is calculated from SAXS data by assuming that water and the polymer are completely segregated (water only exists within the pores). However, a large portion of water is actually trapped between the polymer chains, which is partially released upon increase in temperature from 25 to 45 ℃ due to change in interaction parameters of PEO and PPO blocks with water. Nevertheless, the prediction from complete segregation assumption improves at higher temperatures, as evidenced by the close correspondence between the calculated intermicellar distance of 3.4 nm from SAXS data for the deswollen sample at 45 ℃ (see Table 4-1) and the results obtained from MWCO analysis at the same temperature. This agreement suggests that at 45 ℃, water primarily presents within the pores. Therefore, these results reveal that a considerable portion of water is trapped inside the polymer network (i.e., water and polymer are not segregated), which is released upon heating, resulting in the shrinkage of the polymer network and thus a larger pore size. The thermal response is perfectly reversible since the micelles are chemically cross-linked and do not disintegrate upon LCST transition.

Based on the MWCO analysis, it is observed that the pore size increases from 2.5 nm to 3.2 nm as the temperature is increased from 25 to 45 °C. Utilizing basic pore flow models such as the Hagen-Poiseuille equation,[32] this alteration in pore size can result in 2.7 times increase in membrane flux (since the flow rate is proportional to the fourth power of the pore size). Notably, this value closely corresponds to the observed 2.3 times increase in flux of our membrane when subjected to heating (see Figure 4-7). The minor variation observed between the experimental data and the predicted value can be attributed to the inherent complexities, such as non-tubular pore shape and possible change of pore tortuosity after expansion of the pores upon heating.

It is worthy to mention that the commercial UF membrane having a similar pore size shows negligible changes in MWCO by increasing temperature (Figure E5 in Appendix E). Furthermore, the hydrodynamic radius of PEG in the studied range of molecular weights (i.e., 1–10 KDa) exhibits negligible changes upon heating from 25 to 45 °C [272,273]. Accordingly, it can be concluded that the temperature-dependent MWCO of the polyLLC membrane is due to its thermoresponsiveness.

The rejection experiment was also carried out for BSA, DR23, and DR80 at 25 and 45 °C to further study the thermoresponsiveness of the polyLLC membrane. As shown in Figure 4-7f, the membrane can reject more than 90% of BSA protein. However, the rejection does not change at 45 °C. This observation is simply because of the fact that the average size of BSA molecules is ~7 nm,[274] which is much larger than the membrane pore size at 45 °C.

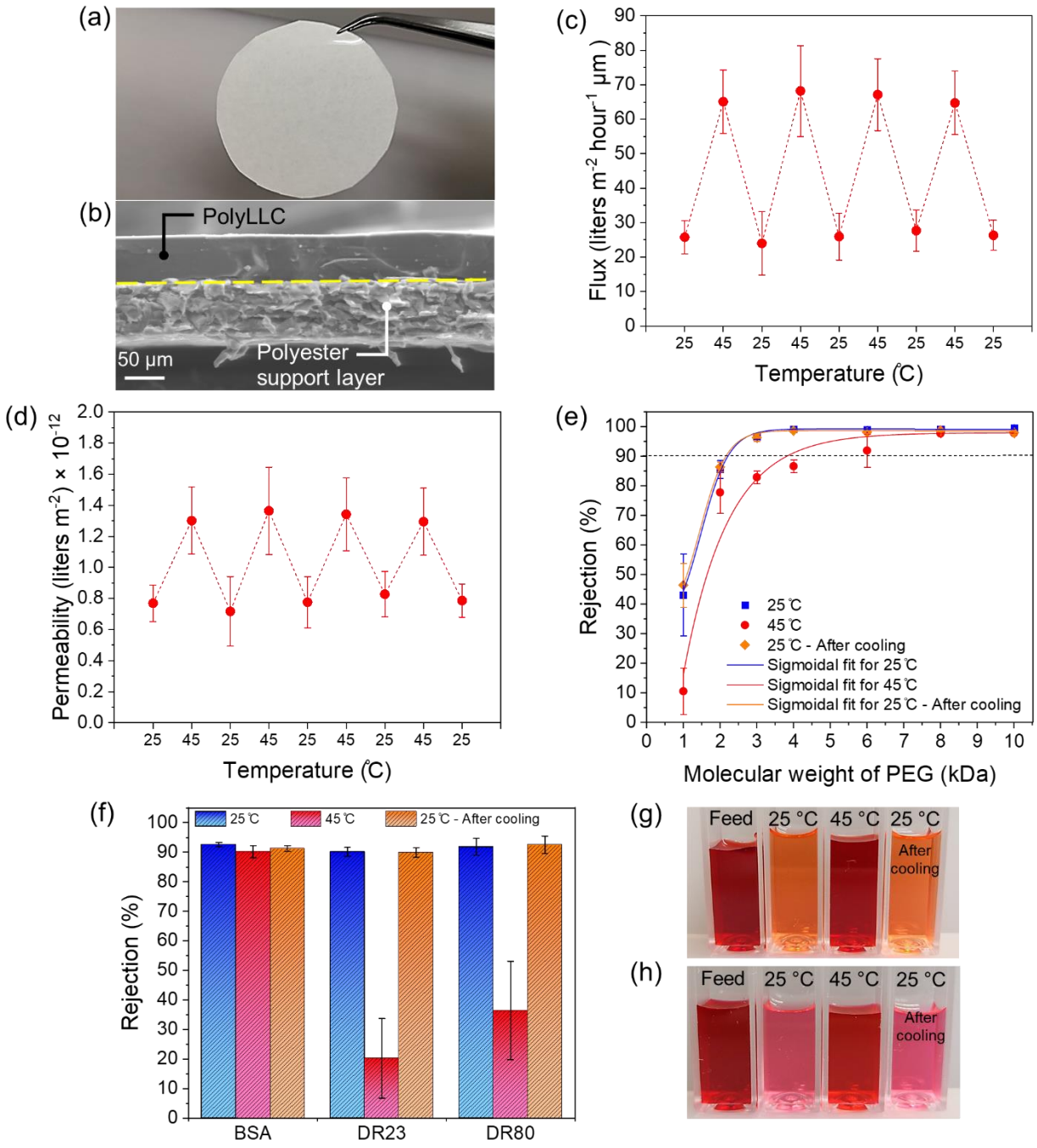

Figure 4-7. (a) Circular cut supported polyLLC membrane and (b) typical cross-sectional SEM image of the membrane. (c-d) Variation of (c) thickness-normalized flux and (d) permeability with cyclic change of temperature. (e) MWCO and (f) BSA protein and red dyes rejection at 25 °C, after increasing temperature to 45 °C, and after cooling down back to 25 °C. (g-h) Photos of feed and collected permeates at different temperatures (at 25 °C, after increasing temperature to 45 °C, and after cooling down back to 25 °C) for (g) DR23 and (h) DR80.

While the membrane rejects around 90% of DR23 and DR80 at room temperature, the rejection of DR23 and DR80 significantly declines to <35% and <55%, respectively. In comparison, the commercial UF membrane does not show any changes in its rejection towards these two dyes upon heating (Figure E5 in Appendix E). As it has been described in the literature,[275] these dyes have a molecular size of ~1 nm, but can form clusters larger than 1 nm in water. That is why both the polyLLC and commercial membranes can efficiently reject them at 25 °C. Additionally, unlike the commercial membrane, the thermoresponsive polyLLC membrane can enlarge its pore size at 45 °C, resulting in passage of dye clusters and thus the lower rejection rates. Figure 4-7g and h show that the change in dye rejection is reversible.

We also studied the adsorption of PEG and dyes by water-swollen polyLLC to make sure that the rejection is not affected by the adsorption phenomenon. To do so, the polyLLC was added to the solutions of PEG (10 kDa molecular weight), BSA, DR23, and DR80 in such a way that the polyLLC content is 0.3 g/L (amount of polyLLC on the supported membrane in contact with the feed solution during filtration experiments). The concentration of PEG, BSA, and DR80 solutions was adjusted to 1, 1, and 0.5 mg/mL, respectively. After 48 h contact time at 25 and 45 °C, UV-Vis spectroscopy was utilized to evaluate the change in concentration of solutes. As shown in Figure E6, none of the solutes show a considerable change in concertation, meaning that the adsorption has negligible effect on the rejection performance of the membrane.

It is worth considering that we chose 45 °C temperature to test the thermal response of our membrane based on several observations. Firstly, the swelling capacity of the polyLLC changes negligibly after reaching 45 °C, as depicted in Figure 4-5. Secondly, as shown in Figure 4-6, there is a similar preliminary peak position in the SAXS data of the water-swollen sample at both 25 and 45 °C. Lastly, our preliminary rejection experiments with PEG molecules of 2 and 3 kDa

demonstrated slight differences in the rejection rates at temperatures below 40 °C when compared to the values obtained at 25 °C. In contrast, the differences depicted in Figure 4-7 were significant at 45 °C.

Additionally, it is important to address the kinetics of the membrane thermal response, which explains the observed changes in its transport properties. Our observations indicate that the membrane performance undergoes changes at a rate comparable to the alteration in the swelling capacity of the polyLLC (see Figure 4-5d) when the system reaches the isothermal conditions at 45 °C.

4.3.2.3 Contact angle and fouling resistance

Fouling is one of the important challenges involved in membrane separation as it can reduce the performance and thus lifetime of the membrane. Fouling is more pronounced for UF membranes as they are used in pretreatment and filtration of large species (e.g., proteins, bacteria, and viruses) that cause severe fouling.[4] Increasing the surface hydrophilicity can be counted as the most important approach to limit membrane fouling.[276] Measurement of water contact angle is a simple way to examine the surface hydrophilicity of membranes.[276] Therefore, we performed this measurement on the water-swollen polyLLC membrane, and the obtained results are shown in Figure 4-8a. The results present an average contact angle of 36° and 39° for the polyLLC swollen at 25 and 45 °C, respectively. This test confirms that the polyLLC membrane has highly hydrophilic surface, which can significantly enhance its fouling resistance.

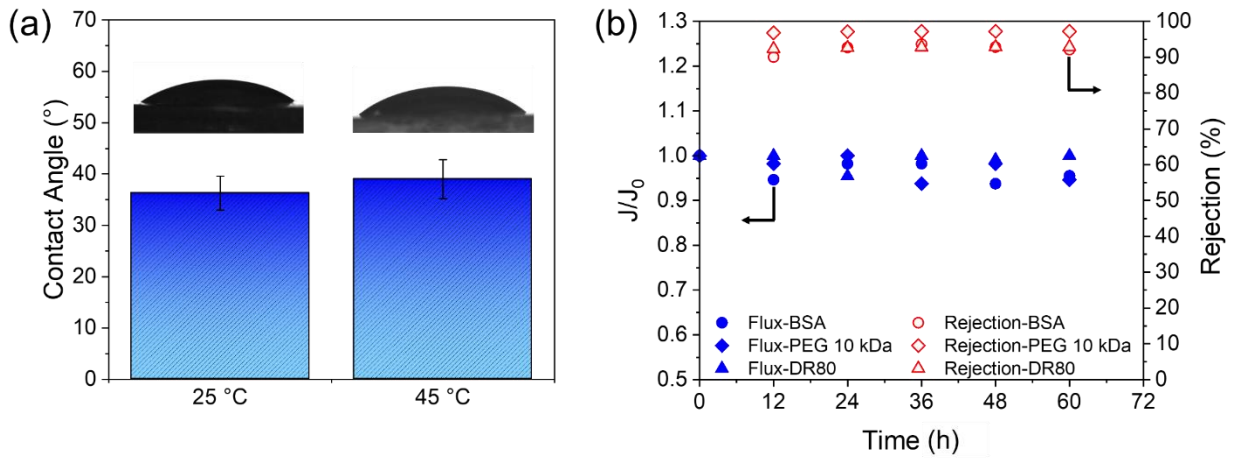

Figure 4-8. (a) Contact angle of the polyLLC membrane swelled with water at 25 and 45 °C. (b) Ratio of membrane flux at a given time (J) to preliminary flux with DI water (J_0) (filled symbols) and rejection rate of different solutes (open symbols) for the polyLLC membrane.

To evaluate the fouling resistance, we passed the solution of three different species through the membrane maintained at 25 °C over the course of 60 h. The rejection rate was monitored in addition to the membrane flux to ensure that the reported rejection results are for steady-state conditions rather than transient state which might occur because of dead spots (fluid stagnation points) in the filtration cell, adsorption of the solute, membrane compaction, or probable leaching of materials from the system. The results presented in Figure 4-8b reveal that a ≤6% membrane flux decline is seen after 60 h during filtration of different species. This super-fouling resistance behavior was expected as the polyLLC membrane has highly hydrophilic surface. It should also be noted that this performance is observed under dead-end filtration operation, which can induce severe fouling. Therefore, an even better performance (less than 6% flux decline) is expected under a crossflow filtration condition. The results for the rejection of different solutes confirm that the membrane rejection performance remains almost unchanged throughout the 60-h filtration period.

It is worth noting that despite the increased hydrophobicity of the PPO block at 45 °C, the measured contact angle at this temperature only shows a negligible change compared to the value

observed at 25 °C (39° versus 36°). Therefore, the alteration in the hydrophobicity of the PPO block does not significantly affect the surface hydrophilicity of the membrane, possibly due to the protective effect of the PEO component. Moreover, our previous research (see Chapter 3) has demonstrated that similar thermoresponsive membranes exhibit better performance against fouling at higher temperatures because pores will expand and result in a higher surface porosity when the membrane is heated up.[263] Therefore, it is not unexpected that this membrane demonstrates a similar antifouling performance at 25 and 45 °C.

4.3.3 Mechanism of thermal response

Based on the obtained experimental results, thermoresponsiveness mechanism of the polyLLC membrane can be defined as follow: a chemically cross-linked polymer network is swelled with water, resulting in the formation of an average pores of 2.5 nm. It should be noted that due to the partial hydrophilicity of PPO block at room temperature, it is partially present in the polar domain (PEO, PPO, and water do not form fully segregated domains[277]). The PPO block in the polymer network undergoes a major dehydration upon heating to 45 °C due to the LCST of the Pluronic copolymer, resulting in the shrinkage of polymer chains. The consequent conformational change increases the intermicellar distance and result in a larger pore size (Figure 4-9). This porosity alteration is perfectly reversible with rehydration of the PPO block when the system is cooled back to 25 °C. This hypothesis is in agreement with what we reported for the membranes synthesized via LLC templating using thermoresponsive F127 surfactant in Chapter 3.[263] Figure 4-9 represents the explained thermoresponsiveness mechanism schematically.

4.4 Conclusion

In this chapter, we reported the preparation of a mesophase-templated UF membrane with thermoresponsive and super-fouling resistant features. H_1-structured LLC directed by

thermoresponsive P84DA block copolymer was used to synthesize the membrane. By increasing the temperature from 25 to 45 °C, the thickness-normalized flux changes from 28 to 68 liters m^{-2} $hour^{-1}$ μm and MWCO changes from 2200 to 3900 Da, respectively. Additionally, highly hydrophilic surface (contact angle of 36–39°) makes these membranes antifouling as their permeability remains almost intact after 60 h of filtration of different charged and uncharged solutes. The remarkable characteristics of this membrane render it highly suitable for a diverse range of applications. For instance, the dynamic pore size of the membrane offers the ability to finely adjust the selectivity between two components, eliminating the necessity for structural alterations or complete membrane replacement. Other potential applications lie in protein purification and removal of viruses and bacteria. For protein purification or biopharmaceutical processing, however, the testing temperatures might not be raised to adjust the MWCO for separation. Nevertheless, we have shown in our previous publication that the thermoresponsive behavior can be used for cleaning membranes after probable fouling (see Chapter 3). The developed membrane also addresses the significant fouling challenges associated with such components, irrespective of being ionic or nonionic.

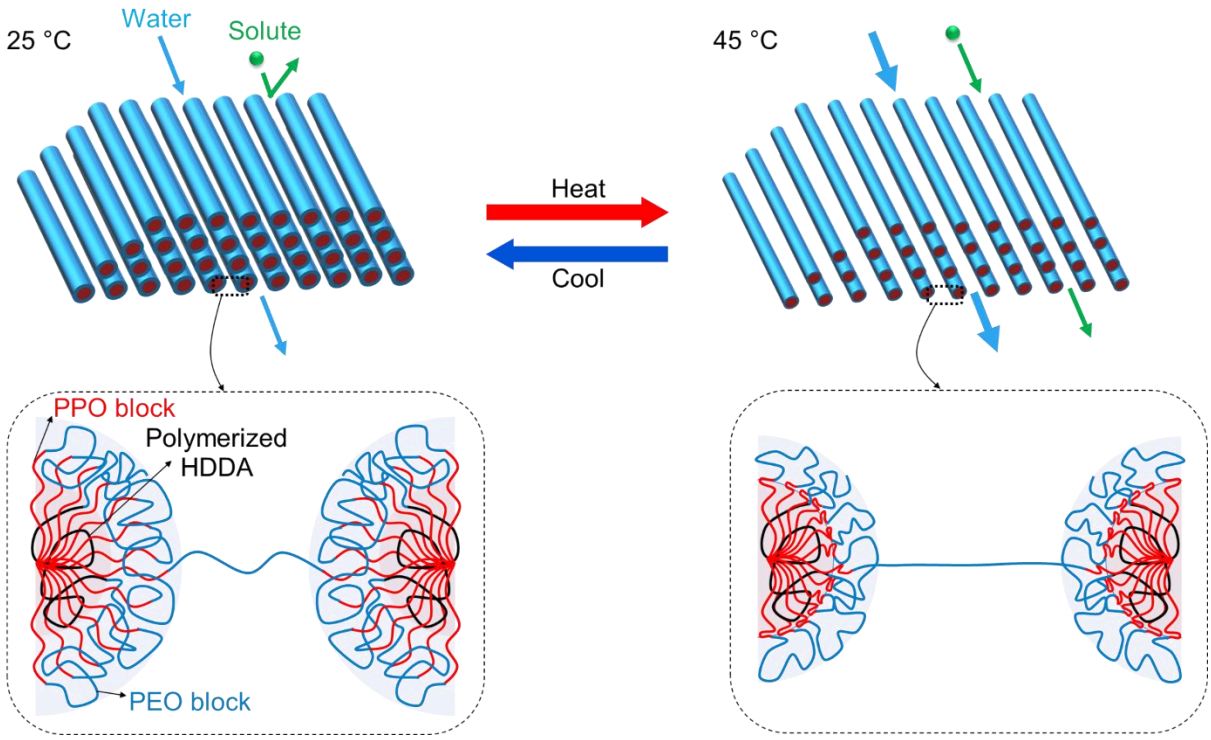

Figure 4-9. Schematic representation of thermoresponsiveness mechanism of the polyLLC membrane.

CHAPTER 5: THERMO- and pH-RESPONSIVE ANTIFOULING NANOFILTRATION MEMBRANES FROM LYOTROPIC LIQUID CRYSTAL TEMPLATING

5.1 Introduction

In today's world, the significance of NF membranes is rising due to their utilization in a variety of applications, including but not limited to water softening,[278] industrial wastewater remediation,[279] salt fractionation in water streams,[280,281] organic solvents nanofiltration,[125] and bio-separation.[282] Porous NF membranes facilitate the separation process through three mechanisms: size-exclusion, solution diffusion, and electrostatic interaction (also known as Donnan exclusion).[281] The common methods used to produce NF membranes with the ability to separate dissolved salts and molecular solutes at the 1 nm length scale are NIPS[283,284] and interfacial polymerization.[285–287] Although these methods offer certain benefits, they also come with some drawbacks. NIPS has limited control over membrane pore size distribution, and the process is also environmentally concerning due to the substantial amount of organic solvents required (up to 70% by volume).[243] The disadvantages of interfacial polymerization include limitations in the choice of monomers, variations in membrane properties (e.g., pore size, thickness, and surface morphology) due to the complex nature of the process, and susceptibility to fouling.[123,288]

LLC templating is an alternative approach which can address these challenges. Out of the various nanostructures available for LLCs, the most frequently utilized ones for synthesizing NF membranes are H_1[31,123,125] and Q_1.[34,120,121,264] Although both structures offer the desirable features of a 3D-continuous transport path without requiring structural alignment, H_1 is particularly attractive as it forms more frequently and is available in a wider range of compositions compared

to Q_1, making it a more ideal option for membrane applications.[31] A significant achievement in the field was demonstrated by Osuji and coworkers,[31,123,125] where they successfully synthesized H_1-structured NF membranes with an effective pore size of ~1 nm, MWCO of ~300 Da, and permeability of ~20 liters m^{-2} $hour^{-1}$ bar^{-1}. Notably, these membranes outperformed commercially available NF membranes like Dow FILMTEC NF90-400, which typically exhibit a permeability of 10 to 15 liters m^{-2} $hour^{-1}$ bar^{-1}.[123]

The incorporation of stimuli-responsiveness into membranes can offer new opportunities for applications by enabling dynamic selectivity and permeability,[192,213,235,237,238,263] and enhanced cleaning of a fouled membrane.[192,236,263] While there are a few reports on the production of stimuli-responsive UF membranes by using LLC templates,[263,289] there is currently no literature available on the synthesis of stimuli-responsive NF membranes from LLC templates. Li et al. published a report on the synthesis of a pH- and light-responsive nanoporous polymer with a pore size of about 1 nm, but the potential of the polymer as an NF membrane was not evaluated in their study.[126] In the current research, we present the first successful production of H_1-structured stimuli-responsive NF membrane via LLC templating. To create the membrane, we polymerize the LLC from mixture of P84DA, [BMIM][BF_4] ionic liquid (IL), acrylic acid (AAc), and HDDA by using UV light. After removing the IL through washing with water, the resulting polyLLC membrane exhibits a pore size of 2.2 nm. When the polyLLC membrane is heated to 45°C, the pore size increases to 2.6 nm, which leads to an increase in thickness-normalized flux and membrane MWCO from 16 to 31 liters m^{-2} $hour^{-1}$ μm and from 1600 to 2400 Da, respectively. The incorporation of AAc in the formulation incorporates charge on the pore wall, enabling the membrane to effectively reject dissolved salts containing trivalent and divalent anion at neutral and alkaline pH levels. Moreover, highly hydrophilic surface of membrane makes it resistant to fouling from various solutes.

5.2 Experimental

5.2.1 Materials

All the chemicals used in this study were purchased from Sigma-Aldrich and were used without any purification except when otherwise noted. The components employed in the synthesis of the polymerizable surfactant, P84DA, were Pluronic P84 (P84) copolymer (PEO_{19}−PPO_{43}−PEO_{19}) with an average molecular weight of 4200 g/mol, anhydrous DCM with a purity of ≥99.8%, anhydrous toluene with 99.8% purity, triethylamine having a purity of 99.5%, and acryloyl chloride with a purity of 97%. The desired LLC was produced by mixing P84DA with [BMIM][BF_4] with a purity of ≥98%, HDDA (obtained from Thermo Scientific Chemicals having a purity of 99%), AAc (99% pure), and 99% pure HCPK. For all the experiments, DI water with a conductivity of 0.055 μS/cm, which was acquired from EMD Millipore Direct-Q3, was employed.

The performance of the membrane, which includes MWCO, rejection of proteins, salts and dyes, and resistance to fouling, was assessed by filtering various solutes. These solutes comprised of PEG with molecular weights ranging from 1 to 10 kDa, BSA in the form of lyophilized powder with a purity of ≥96%, lysozyme from chicken egg white (lyophilized powder with a protein content of ≥90%), DR23 with 30% dye content, DR80 with 25% dye content, orange G (OG) containing 80% dye content, acid fuchsin (AF) having 70% dye content, acid red 1 (AR1, purchased from TCI America™), K_3PO_4, Na_3PO_4, Na_2HPO_4, Na_2SO_4, K_2SO_4, $MgSO_4$, Na_2CO_3, NaH_2PO_4, KNO_3, $MgCl_2$ (Thermo Scientific Chemicals), $CaCl_2$, NaCl (Thermo Scientific Chemicals), KCl, and LiCl (Thermo Scientific Chemicals). Sodium hydroxide (NaOH) and hydrochloric acid (HCl) were used for pH adjustments. The membrane support layer, which was a nonwoven polyester sheet with 2 μm porosity (CraneMat® CU463), was kindly provided by

Neenah Filtration. A commercially available Dow FILMTEC NF270-400 (NF270) with a MWCO of 400 Da was utilized to assess the pH-dependent rejection of ionic species and compare it with the membrane produced in this study.

5.2.2 Synthesis of P84DA

P84DA was acquired by performing a functionalization reaction on P84 following the procedure described in Chapter 4 and a commonly accepted protocol available in the literature.[13,265] The degree of functionalization reaction was evaluated using ATR-FTIR (Nicolet™ iS50 FTIR Spectrometer) and ^{1}H NMR (Varian VNMRS-400 with Probe AutoX-DB-PFG). Further details regarding this analysis can be found in Appendix F.

5.2.3 LLC preparation

To produce the H_1-structured LLC, a mixture of P84DA, [BMIM][BF_4] (containing 1 wt% HCPK with respect to [BMIM][BF_4] as UV initiator), AAc, and HDDA (containing 10 wt% HCPK with respect to HDDA) was prepared using a weight ratio of 48.8/48.8/0.5/1.9 for P84DA/[BMIM][BF_4]/AAc/HDDA. The mixture was repeatedly hand-mixed and centrifuged at 11,000 rpm for 5 minutes in a 50 mL centrifugal tube until a transparent gel was obtained. The chemical structure of the components utilized for mesophase preparation is depicted in Figure 5-1f, and a schematic of the H_1 structure is presented in Figure 5-1f.

5.2.4 LLC and polyLLC characterization

5.2.4.1 Cross-polarized light microscopy (CPLM)

To assess the birefringence of the H_1-structured sample before and after polymerization, a cross-polarized Nikon microscope (model LABOPHOT2-POL) equipped with a digital camera was utilized. For CPLM analysis, approximately 0.2 g of the mesophase gel was placed between a glass slide and a glass cover slip. To polymerize the LLC, the sandwiched sample was cured for

40 seconds using UV radiation (via the Uvitron Sunray 600 SM curing system equipped with a 600 W UV flood lamp having 15 cm distance from the sample). The structure of the polymerized LLC is illustrated schematically in Figure 5-1f.

5.2.4.2 Small angle X-ray scattering (SAXS)

SAXS was used to evaluate the structure of samples and obtain the formulation of desired structure. Quartz capillary tubes with a nominal diameter of 1.5 mm (Charles Supper Company, Natick, MA) were used for sample preparation following the procedure described in Chapter 4. Azimuthal integration of 2D scattering patterns using a Bruker Nanostar X-ray scattering system equipped with a monochromatic Cu Kα radiation source (X-ray wavelength of 1.541 Å) was used to obtain 1D scattering profiles. SAXS analysis was carried out at various temperatures for LLC gels and water-swollen polyLLCs to investigate any structural changes caused by temperature variation. Moreover, polyLLCs swollen by water at pH of 4, 6 and 9 were analyzed via SAXS to examine any probable structural changes with pH.

5.2.4.3 Differential scanning calorimetry (DSC)

DSC (Q2500, TA Instruments, New Castle, DE) was used to analyze various samples, including pure P84DA, water-swollen polyLLC, and dried polyLLC (the water-swollen polyLLC sample was dried under vacuum for at least 72 hours). Approximately, 10 mg of the desired sample was placed in an aluminum pan (PerkinElmer, Inc.) and sealed with a hermetic lid. Thermal analysis was performed with a 1 °C/min ramp from 0 to 60 °C (and vice versa). The cycle was repeated twice, and the second cycle was used for analysis after erasing the thermal history of the samples.

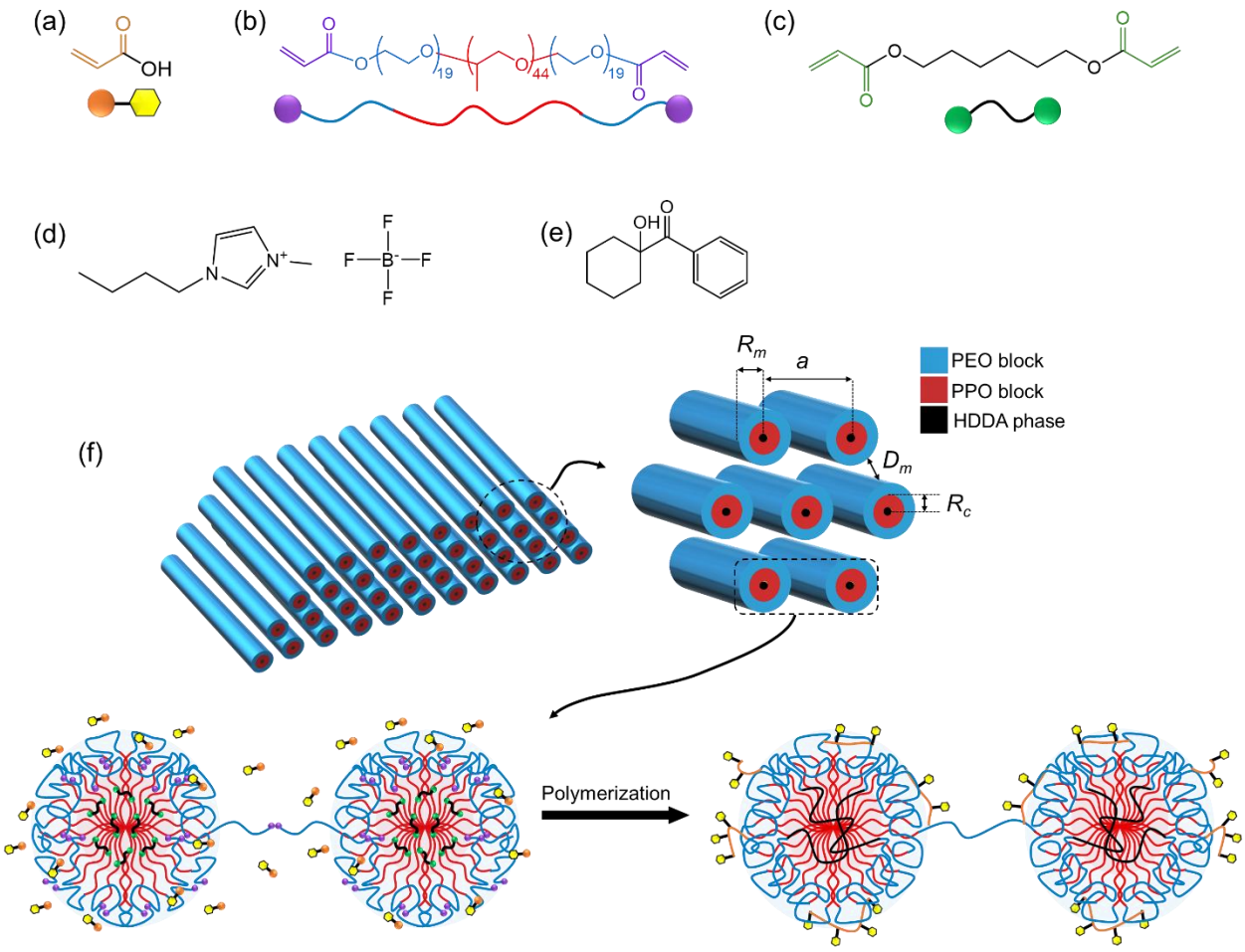

Figure 5-1. Molecular structure of (a) AAc, (b) P84DA, (c) HDDA, (d) [BMIM][BF_4] and (e) HCPK. Schematic illustration of AAc, P84DA and HDDA have also been shown in panel a, b and c, respectively. (f) A schematic depiction of an H_1-structured LLC obtained by blending various components, wherein the micelles are enveloped by a mixture of [BMIM][BF_4] and AAc. Important structural parameters have also been shown in the schematic. The apolar domain consists of PPO block and HDDA. A chemically bound polymer network is formed from reaction of acrylate groups of P84DA, HDDA, and AAc. To achieve a well-integrated H_1-structured membrane, it is crucial to have intermicellar bridges, which are formed from reaction of acrylate groups of extended PEO blocks.[31]

5.2.4.4 Swelling characteristics of the polyLLC

Temperature-dependent swelling capacity of the water-swollen polyLLC was evaluated using the procedure described in Chapter 1. To evaluate the salt-dependent swelling behavior of polyLLC, the polymer was swollen in aqueous solutions of K_2SO_4 at different ionic strengths (1,

5, 10, 50, and 100 mM) at 25 and 45 °C. Additionally, the swelling capacity of polyLLC was measured at different pH values ranging from 3 to 9 to investigate the effect of pH on the polymer's swelling behavior.

5.2.5 Manufacturing of the supported polyLLC membrane

Based on the findings from SAXS analysis, the obtained mesophase exhibits reversible structural transitions when heated to 45°C (refer to section Appendix F). As mentioned in Chapter 4, these transitions can reduce the mesophase viscosity, facilitating the use of knife coating to apply the mesophase onto a polyester support sheet, followed by UV polymerization to create the supported polyLLC membrane. Further information regarding the membrane fabrication process is available in Chapter 4. The thickness of the polyLLC coated layer was determined using a SEM (ThermoFisher Quattro S field emission environmental SEM).

To replace the IL with water, the manufactured membranes were submerged in water for a minimum of one week before being tested.

5.2.6 Analysis of the polyLLC membrane performance

5.2.6.1 Water flux and permeability

The Sterlitech HP4750 high-pressure stirred cell (a dead-end filtration system) was employed to assess the performance of the membranes, with an effective area of 14.6 cm^2, operating under stirring at 750 rpm using a magnetic stirrer and a pressure of 30 psi (2.07×10^5 Pa). The thickness-normalized flux of the membranes, reported as liters m^{-2} $hour^{-1}$ µm, was measured at both 25 and 45 °C. To measure the flux at an elevated temperature, the filtration cell containing the membrane was placed in a water bath set to 45 ± 0.1 °C. The permeate collection was initiated only after verifying the isothermal conditions at the membrane level and obtaining a stable flux. All

measurements were conducted on three separate membranes. Permeability of the membrane was calculated based on Darcy's law[32] (Eq. 3-1).

5.2.6.2 MWCO, protein, single salt and dye rejection measurements

To measure the MWCO, we filtered 1 mg/mL aqueous solutions of PEG with varying molecular weights (ranging from 1 to 10 kDa) using one membrane. For each analysis, we collected at least 5 mL of permeate. In 0.3 mL of the collected permeate, we added 3 mL of a reagent[267] consisting of potassium iodide (2 g), iodine (1.27 g), and water (100 mL). Within 15 minutes of sample preparation, we employed UV-Vis spectroscopy (Thermo Scientific™ GENESYS™ UV-Vis Spectrophotometer) to determine the concentration of PEG in the permeate. Eq. (3-5) was used to calculate PEG rejection.

The aqueous solutions of following components were used to evaluate the membrane performance in terms of the rejection of protein, dye, and single salt. A fresh membrane was employed for each experiment.

1) BSA and lysozyme proteins with a concentration of 1 mg/ml.
2) DR23, DR80, OG, AF, and AR1 dyes with a concentration of 0.5 mg/ml.
3) K_3PO_4, Na_3PO_4, Na_2HPO_4, Na_2SO_4, K_2SO_4, $MgSO_4$, Na_2CO_3, NaH_2PO_4, KNO_3, $MgCl_2$, $CaCl_2$, NaCl, KCl, and LiCl salts having different ionic strengths (1, 5, 10, 50 and 100 mM).

To determine the contents of proteins and dyes in the permeate, UV-Vis spectroscopy was utilized. The conductivity measurement via Fisherbrand™ accumet™ XL200 pH/conductivity meter was used to measure the salt concentration in the permeate. Eq. (3-5) was applied to calculate the rejection rate of various species.

Thermoresponsive properties of the membrane were evaluated at two different temperatures, 25 and 45 °C. To do so, the experiment was first performed at 25 °C and then at 45 °C with the same membrane. The reversibility of the thermoresponsiveness was evaluated by cooling the same membrane back to 25 °C and repeating the rejection experiment. To determine the selectivity of the membrane for ionic species as a function of pH, the rejection rate of Na_2SO_4, K_2SO_4, $MgSO_4$, OG, AF, and AR1 was measured at different pH values ranging from 3 to 9. For comparison purpose, we evaluated the pH-dependent rejection of OG using a commercially available NF270 membrane as well. The pH of the aqueous solutions was adjusted by HCl and NaOH having 0.1 M concentration.

All of the membrane performance experiments were conducted with three different membranes, and the reported results represent the average value and calculated standard deviation.

5.2.6.3 Contact angle and fouling resistance

The contact angle of the membranes was measured using an optical tensiometer from Biolin Scientific. The fouling resistance of the membranes was evaluated by filtering aqueous dispersions of PEG (10 kDa), BSA, and DR80 at a concentration of 1 mg/mL. The filtration cell was initially filled with approximately 250 mL of solution, and 5-8 mL of permeate was collected every 12 h. The test was conducted over 60 h, and the membrane flux and rejection were measured at 12-h time intervals.

5.3 Results and discussions

5.3.1 Characterization of LLC and polyLLC

The structural analysis of LLC and polyLLC was conducted through CPLM and SAXS techniques. After preparation and screening of several samples, LLC with P84DA/[BMIM][BF_4]/AAc/HDDA 48.8/48.8/0.5/1.9 w/w/w/w composition was selected since it

has the desired structure before and after polymerization as well as after exchange of IL with water. The CPLM results, depicted in Figure 5-2a-c, indicate that the LLC, polyLLC, and water-swollen polyLLC exhibit the birefringent characteristic of hexagonal mesophases.[45] This indicates that the original LLC structure remains intact even after polymerization and solvent exchange. Figure 5-2d displays the obtained 1D SAXS profiles, which support the findings from CPLM. The presence of Bragg peaks with $1{:}\sqrt{3}{:}\sqrt{7}$ q/q^* ratios for the LLC is observed in the data, where q represents the scattering vector and q^* represents the primary peak position in each curve. Thus, the LLC has an H_1 structure. Similar Brag peaks ratios have been reported for LLCs with H_1 structure.[31,123,125] Additionally, the presence of the typical birefringence associated with the H_1 structure and the retention of the distinct SAXS peaks confirm that the structure is preserved following polymerization and solvent exchange (i.e., exchange of IL with water in polyLLC).

From the SAXS data and using the equations presented in Chapter 4 (Eq. 4-2 to 4-6), structural parameters such as intermicellar distance (which determines the pore size), lattice parameter, apolar domain size, micelle size, and grain size can be estimated. A schematic representation of these parameters is shown in Figure 5-1f.

As discussed in Chapter 4,[56,289] it is assumed that the solvent (either [BMIM][BF_4]+AAc or water), PEO, PPO, and HDDA are completely segregated and each domain is characterized by a bulk density.[215] It is important to note, however, that in the case of water-swollen samples, the polymer and water are not entirely segregated, as the polymer network can absorb significant amounts of water. Furthermore, partitioning of the PEO and PPO blocks in the solvent and HDDA phases makes the calculations somewhat imprecise.[178] Nevertheless, we have shown that the this geometric calculation provides a good agreement with the pore size measured from MWCO.[32,289]

In this method, the size of the IL or water domain is assumed to be equal to the pore size of the polyLLC membrane.

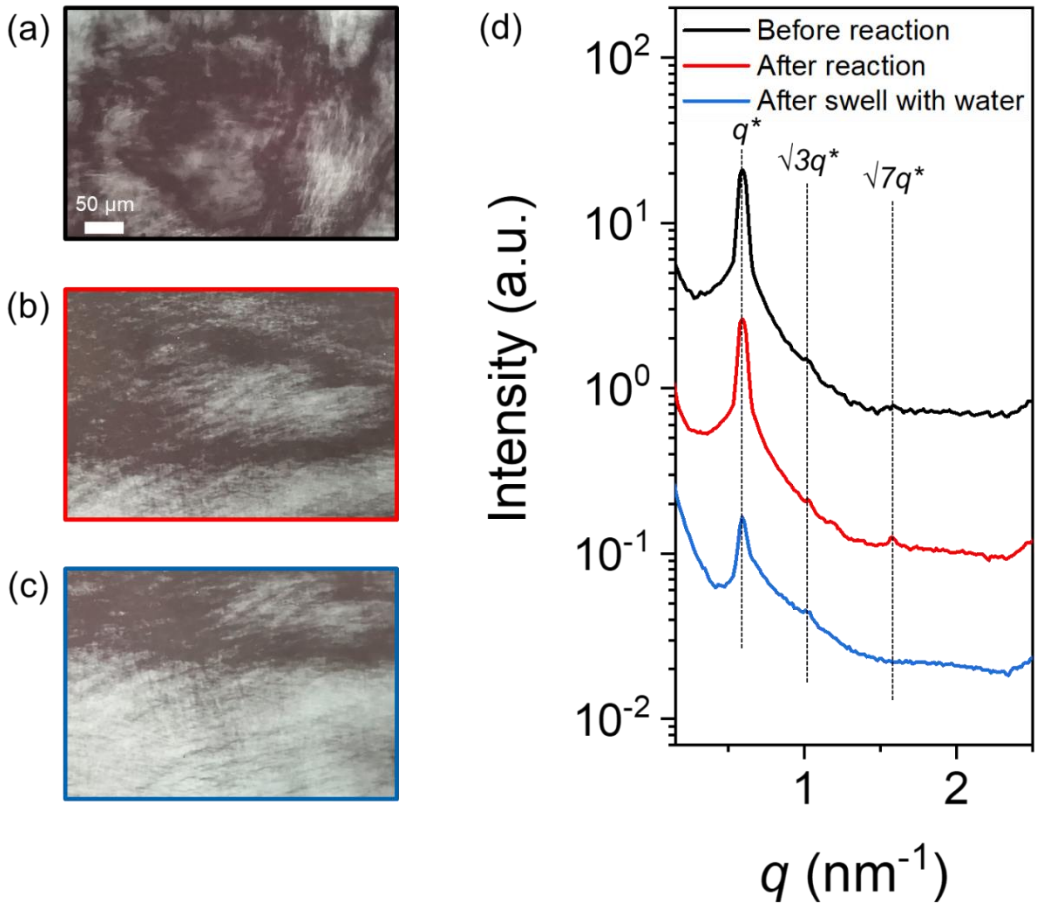

Figure 5-2. The images taken using CPLM display the samples in three different stages: (a) their original state (LLC), (b) after undergoing a reaction, and (c) after swelling with water. (d) 1D SAXS profile, in which plots are shifted vertically to enhance comparison.

The calculated structural parameters are presented in Table 5-1. It is evident that the estimated intermicellar distance (pore size) is approximately 2.7 nm for both the LLC and polyLLC samples. However, this value increases to around 4.2 nm for the water-swollen sample at 25 °C and pH of 6. The MWCO experiment can be utilized to achieve a more precise measurement of the pore size. Further details regarding the MWCO experiment will be provided in section 5.3.2.2. As control sample, we have included the calculated parameter for the water-swollen polyLLC at 45 °C and

pH of 6 in Table 5-1. Figure 5-5 displays the corresponding SAXS data for this specific sample. The calculated data for this particular sample will be discussed in detail in section 5.3.2.2.

Table 5-1. Calculated structural parameters for different species based on SAXS data.

Sample	q^* (nm^{-1})	ϕ_{PPO} [a]	ϕ_{HDDA}	$\phi_{Pluronic}$	ϕ	a (nm)	R_c (nm)	R_m (nm)	D_m (nm)
LLC	0.59	0.66	0.021	0.53	0.37	12.4	3.9	4.8	2.7
PolyLLC	0.58	0.66	0.021	0.53	0.37	12.5	4.0	4.9	2.7
Water-swollen polyLLC at 25 °C and pH of 6	0.60	0.66	0.014	0.37	0.26[b]	12.0	3.2	3.9	4.2
Water-swollen [c] polyLLC at 45 °C and pH of 6	0.60	0.66	0.019	0.48	0.33[b]	12.0	3.6	4.4	3.1

[a] The volume fraction of the PPO block in the Pluronic block copolymer is denoted as ϕ_{PPO}.
[b] The volume fraction of the apolar domain in the water-swollen polyLLC was determined by considering the swelling capacity of the polymer at 25 °C and 45 °C, which corresponded to 160% and 100% respectively, as shown in Fig. 4a.
[c] Figure 5-5 presents the SAXS data for the water-swollen polyLLC at temperature of 45 °C and pH of 6.

DSC was used to analyze the thermoresponsiveness of the water-swollen polyLLC in comparison to pure P84DA and dried polyLLC as control samples. The obtained results are shown in Figure 5-3. A thermal transition in 5–32 °C range is seen for the water-swollen polyLLC due to LCST of the Pluronic in water.[248,268] When the temperature reaches the LCST, the PPO block undergoes a significant increase in hydrophobicity, leading to a reduced water solubility of the block copolymer.[258] On the other hand, pure P84DA exhibits a melting point within the 20-47 °C range, which can be attributed to the melting of the crystalline regions created by the PEO block.[269] We can infer that the formation of polyLLC inhibits the crystallization of the PEO block since

dried polyLLC does not exhibit any thermal transition. Therefore, the thermal response observed in the water-swollen polyLLC can be attributed to the LCST of the block copolymer surfactant.

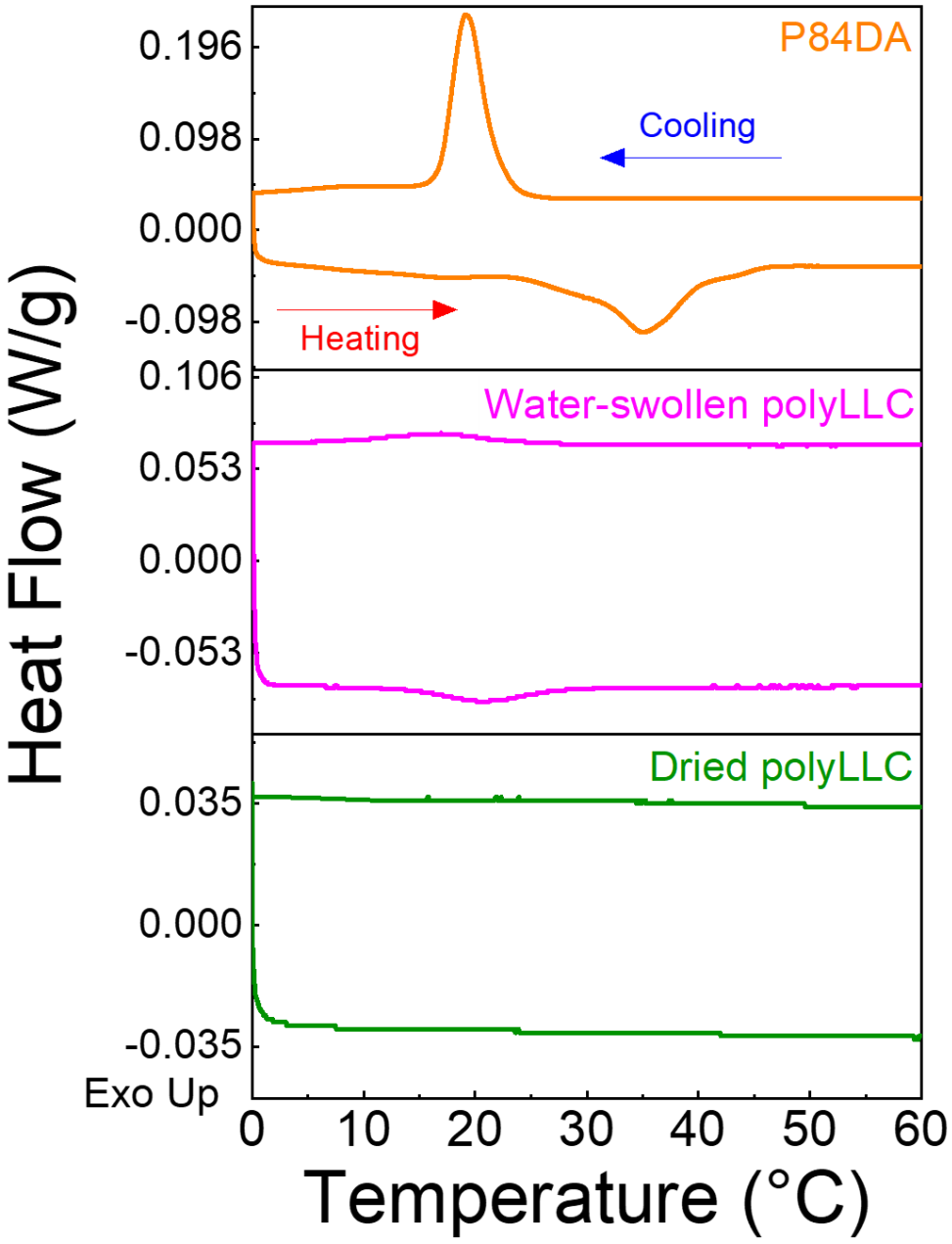

Figure 5-3. The DSC data for pure P84DA, water-swollen polyLLC, and dried polyLLC.

The swelling capacity analysis of the polyLLC sample (using pieces with dimensions of approximately 2 cm × 2 cm and a thickness of 500 µm) is shown in Figure 5-4. The swelling capacity decreases from around 390% to approximately 100% upon heating the samples from 5 to 45 °C as a result of the LCST of the polymer, in agreement with the DSC measurements. Moreover, our analysis indicates that the thermal response is rapid, occurring within 5 minutes, and fully reversible throughout several heating-cooling cycles. In our earlier study (Chapter 4),[289] we found that polyLLCs without AAc exhibited a swelling capacity of 600% at 5 °C, which decreased to 120% when the temperature was raised to 45 °C. The reduction in swelling capacity upon the addition of AAc to the formulation can be considered as a direct effect of inclusion of this specie in the chemically cross-linked polymer network.

We evaluated the swelling capacity at different pH values and ionic strengths. The ionic strength was altered by using different contents of K_2SO_4. Figure 5-4c demonstrates that the polyLLC still exhibits thermoresponsiveness, albeit with a slightly reduced swelling capacity and extent of thermal response (change in swelling capacity upon heating from 25 to 45 °C) at higher salt concentrations. This reduction in swelling capacity is a well-known phenomenon that has been observed in hydrogels when exposed to high salt concentrations. This is due to the high osmotic pressure in the saline water, which causes water to be desorbed from the hydrogel.[290] Additionally, Figure 5-4d reveals that there are no significant changes in swelling capacity at 25 °C when the pH is altered from 3 to 9.

As depicted in Figure 5-5, CPLM and SAXS were employed to investigate the impact of temperature and pH on the structural changes of the water-swollen polymer. The structure of the polymer remains unaffected by changes in pH, as evidenced by the consistent CPLM and SAXS results obtained at various pH values. However, irrespective of the pH values, the results indicate

that when the polymer is cooled to 10 °C, it exhibits a weakly ordered structure. This is evident from the absence of any discernible texture in CPLM and the presence of very weak peaks (or almost no peaks) in SAXS. This finding is aligned with our recently published research (Chapter 4)[289] and can be attributed to the disruption of PEO and PPO segregation within the water domain. This disruption occurs due to the increased miscibility of PEO and PPO with water, which is a result of PPO becoming hydrophilic at temperatures below LCST of the Pluronic.[258,263] Under such condition, the micelles adhere to each other because of significant swelling with water, leading to the formation of a weakly porous polymer that lacks any noticeable structure. Such structural alteration is reversible via deswelling the polymer upon heating it to 65 °C, as confirmed by the reappearance of texture in CPLM and the emergence of strong H_1 Bragg peaks in the SAXS profile.

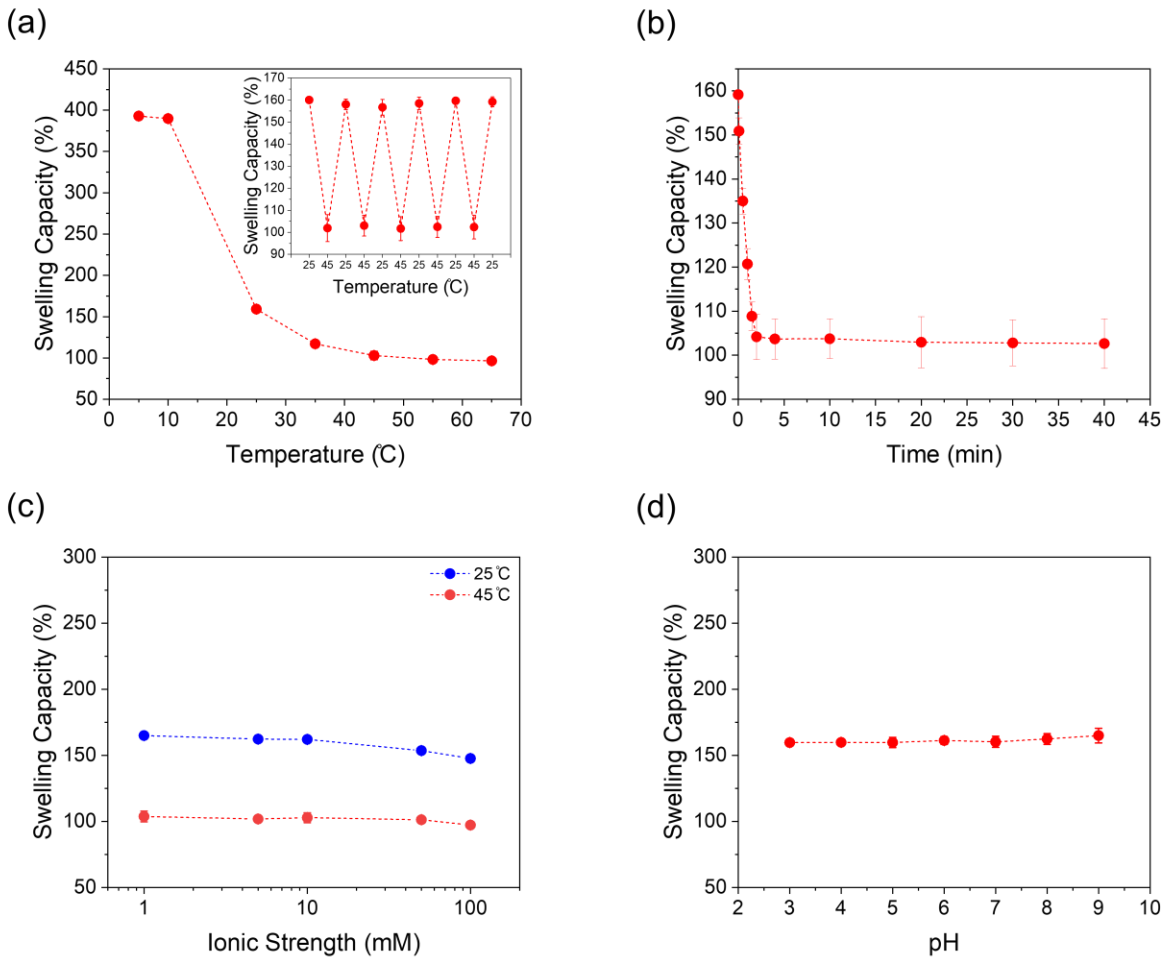

Figure 5-4. (a) Variation of polyLLC swelling capacity with temperature (reversibility of the polyLLC thermoresponsiveness is shown as inset). (b) Kinetics of thermal response when the temperature changes from 25 to 45 °C. (c) Changes in swelling capacity with ionic strength at 25 and 45 °C. (d) Variation of the swelling capacity with pH.

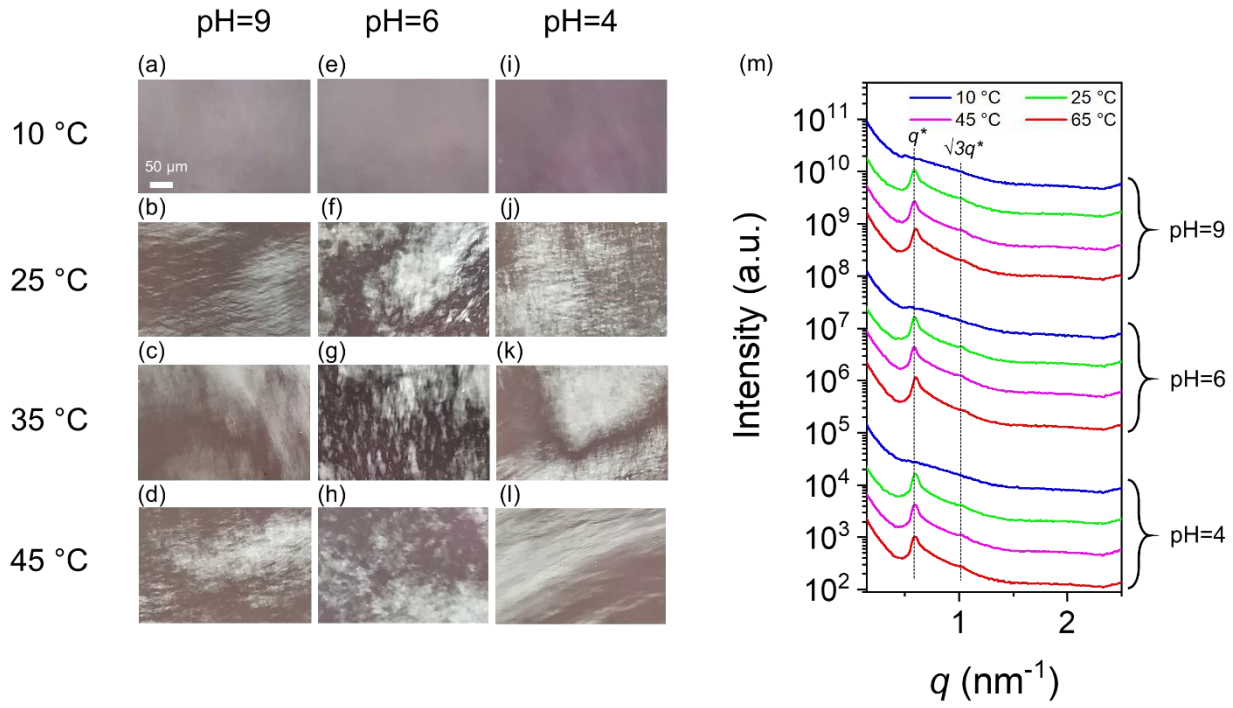

Figure 5-5. (a-l) CPLM images of water-swollen polyLLC at temperature of (a, e, i) 10, (b, f, j) 25, (c, g, k) 45, and (d, h, l) 65 °C and at pH of (a-d) 9, (e-h) 6, and (i-l) 4. (m) 1D SAXS profile of the water-swollen polyLLC at different temperatures and pH values. To enhance comparison, the plots have been vertically shifted.

5.3.2 Analysis of the polyLLC membrane performance

We have demonstrated the fabrication of H_1-structured membranes on a polyester support layer by applying a knife coating technique followed by UV curing (see Chapter 4)[289]. The same technique was employed to create the membranes discussed in the present study. The circular cut and typical cross-sectional SEM image of the supported membrane are depicted in Figure 5-6a and b, respectively. Based on image analysis, it can be determined that the membrane thickness is in 20-60 µm range with an average thickness of ~40 µm. Consequently, all membrane flux data are normalized by this average thickness to unit of liters m^{-2} $hour^{-1}$ µm. The performance of the polyLLC membrane is assessed through various tests, and the ensuing sections detail the findings obtained from these tests.

5.3.2.1 Water flux and permeability

Figure 5-6 illustrates the measurement of membrane flux and permeability in multiple heating-cooling cycles at 25 and 45 °C. The obtained results indicate that both parameters increase in a reversible manner with temperature rise. As shown in our previous work (Chapter 4),[289] commercially available membranes lack this behavior, which further confirms the thermoresponsiveness of the polyLLC membranes. Notably, the membrane containing AAc exhibit lower permeability than the one without AAc reported in our previous work,[289] suggesting smaller pore sizes due to the incorporation of this specie.

5.3.2.2 MWCO, protein, single salt, and dye rejection measurements

A fresh membrane was used to conduct the MWCO experiment at 25 °C, followed by conducting the same experiment at 45 °C using the same membrane. To assess the reversibility of the thermal response, the membrane was subsequently cooled down to 25 °C and the MWCO measurement was repeated. The MWCO data, which usually exhibits a sigmoidal trend, was fitted by using the Boltzmann sigmoidal equation, Eq. (3-7).

As depicted in Figure 5-6, the MWCO of the membrane can be altered reversibly from 1,600 to 2,400 Da by increasing the temperature from 25 to 45 °C. By considering the obtained MWCO values and using Eq. (4-7), therefore, the temperature increases from 25 to 45 °C results in a change in pore size from 2.2 to 2.6 nm. The obtained pore sizes are smaller than the ones obtained for polyLLC membranes without AAc in Chapter 4 (2.5 and 3.2 nm at 25 and 45 °C, respectively),[289] which correlates with the permeability results. As previously reported in Chapter 4,[289] non-thermoresponsive commercial UF membranes with comparable pore size does not show alterations in MWCO upon increasing temperature. Additionally, the hydrodynamic radius of PEG within the investigated range of molecular weights (1-10 kDa) displays insignificant changes upon being

heated from 25 to 45 °C.[272,273] Thus, the temperature-dependent MWCO of the polyLLC membrane can be attributed to its thermoresponsive nature.

The estimated pore size from MWCO analysis at 25 °C (2.2 nm) is smaller than the calculated intermicellar distance of 4.2 nm (see Table 5-1) determined from SAXS data of the water-swollen sample at the same temperature. A similar deviation is observed at 45 °C, with estimated pore sizes of 2.6 nm compared to the intermicellar distance of 3.1 nm. One reason for the difference is the assumptions made in our calculations based on SAXS data, especially complete segregation of water and the polymer, with water existing only within the pores. In other words, a significant portion of water is trapped between the polymer chains and is released when the membrane is heated, due to the LCST of the polymer. However, the role of this factor is not significant at 45 °C where most of the trapped water within polymer chains has already been released and water is mainly present in the pores. Therefore, there must be an additional factor contributing to this discrepancy. In our previous work presented in CHAPTER 4,[289] where we used a formulation without AAc, we observed that the discrepancies in pore size estimation based on MWCO and SAXS were resolved by heating the polymer to 45 °C. This suggests that the copolymerized AAc in the polymer network could be the other factor contributing to water holdup within polymer chains at 45 °C..

Figure 5-6 presents the rejection of BSA, lysozyme, DR23, and DR80 for further evaluation of the thermoresponsiveness of the produced membrane. A rejection of over ~85% is observed for BSA and lysozyme, with no significant variation in rejection upon changing temperature. This can be attributed to their large molecular size (~7 nm for BSA[274] and ~3.2 nm for lysozyme[31]), which surpasses the pore size of the membrane at various temperatures.

Figure 5-6 illustrates that the membrane rejects over 90% of DR23 and DR80 at 25 °C. It is well-known that these dyes, which have a molecular size of ~1 nm, can form clusters larger than 1 nm in water.[275] As such, the synthesized polyLLC membrane can efficiently reject them at 25 °C. Due to the passage of dye clusters upon increasing the temperature to 45 °C, the rejection of DR23 and DR80 decreases to less than 80% and 85%, respectively. The temperature-dependent changes in the rejection rate of these dyes are less significant compared to the membranes without AAc in its formulation (see Chapter 4),[289] which is attributed to the smaller pore size of the membranes containing AAc at 45 °C. The presence of electrostatic repulsions between the COO^- group on copolymerized AAc and the sulfate groups of the dyes may also contribute to the observed differences in rejection rates. Overall, the studied polyLLC membranes, both with and without AAc in formulation,[289] are capable of expanding their pores at higher temperatures, which allows the passage of dye clusters,[275] leading to lower rejection rates. The reversibility of the change in dye rejection can be observed in Figure 5-6.

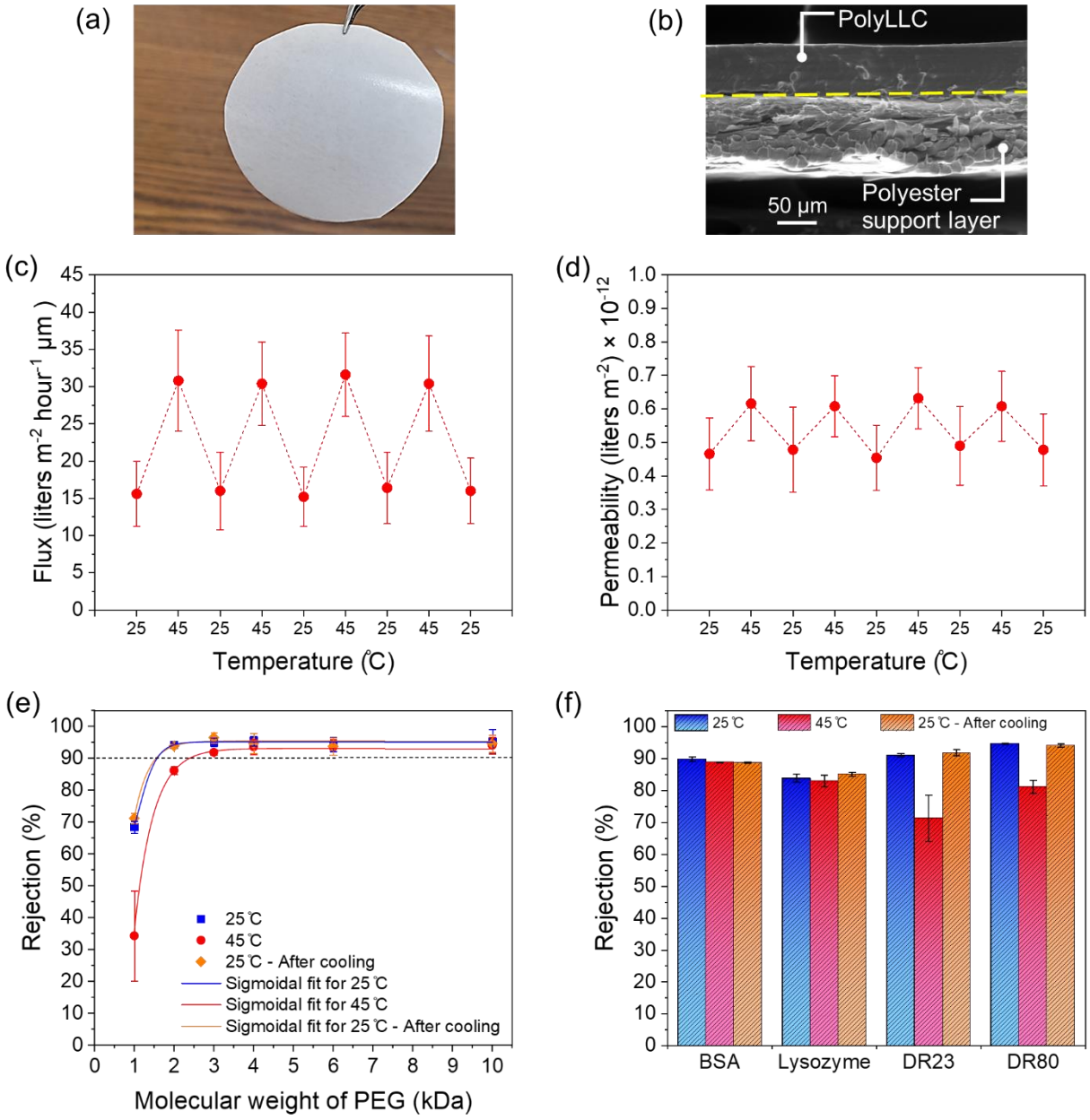

Figure 5-6. (a) A supported polyLLC membrane with a circular cut and (b) typical cross-sectional SEM image of the membrane. Cyclical changes of (c) thickness-normalized flux and (d) permeability with changes in temperature. (e) MWCO and (f) rejection of BSA, lysozyme, DR23, and DR80 measured at 25 °C, after increasing the temperature to 45 °C, and after cooling back down to 25 °C.

To evaluate the salt rejection capability of the H_1-structured NF membrane, we performed a single salt rejection experiment using different salts containing monovalent, divalent, and trivalent

anions. Aqueous solutions of these salts (without adjusting the pH) were prepared at ionic strengths of 1, 5, 10, 50, and 100 mM and were passed through the membrane. The results are displayed in Figure 5-7a, indicating that the membrane exhibits higher rejection rates for divalent and trivalent species compared to monovalent ones. Additionally, rejection rate decreases as the ionic strength is increased. The separation of ionic species by NF membranes is typically influenced by three primary mechanisms: size-exclusion, solution diffusion, and electrostatic interactions.[281] In membranes where the pore size is larger than the hydrated diameter of the ions, the primary controlling factor in separation is the electrostatic repulsion due to the electrical double layer being larger than the pore diameter.[123] In our membrane, separation mainly occurs based on the electrostatic repulsions between the COO^- group of copolymerized AAc and the anion of the salt. Based on the electroneutrality principle, therefore, the cation of the salt is also rejected to maintain the neutral ionic conditions on both sides of the membrane. Consequently, the rejection rate is higher for divalent and trivalent species since they induce stronger electrostatic interactions. With an increase in salt content (ionic strength), electrostatic screening reduces the electrical double layer thickness (Debye length), leading to lower rejection rates. Debye length, κ^{-1}, can be calculated theoretically using following equation:

$$\kappa^{-1} = \sqrt{\frac{\varepsilon_r \varepsilon_0 RT}{2F^2 I}} \qquad (5\text{-}1)$$

Where ε_r, ε_0, R, T, F and I are dielectric constant (with a value of 78.5), permittivity of the vacuum (equal to 8.85×10^{-12} C/V.m), gas constant (measuring 8.314 C.V/mol.K), absolute temperature (at 298 K), Faraday constant (at 9.65×10^4 C/mol) and ionic strength of the solution, respectively.[291] By employing this formula, one can determine Debye lengths of 9.6, 4.3, 3, 1.3, and 0.96 nm for ionic strengths of 1, 5, 10, 50, and 100 mM, respectively. When the ionic strength

is less than 50 mM, the calculated Debye length surpasses the size of the membrane pores, aligning with the observed higher salt rejection values. Conversely, for ionic strengths of 50 and 100 mM, the Debye length notably diminishes, falling within the range of the membrane pore size, resulting in decreased rejection rates.

As depicted in the inset of Figure 5-7a, $MgSO_4$ exhibits lower rejection rates at low ionic strengths compared to the salts containing similar anion. Such behavior can be attributed to the stronger electrostatic screening effect caused by the higher charge density of magnesium ions (more than 10 times) when compared to sodium and potassium cations.[292] Moreover, the membrane exhibits limited rejection rates for salts containing chloride ion compared to sulfate, which enables the selective separation of anions such as sulfate over chloride. Therefore, our membrane is an ideal candidate for salt fractionation, particularly in cases where the separation of chloride ion from other ions like sulfate is desired.[280]

To test the pH-dependent rejection capability of the polyLLC membrane for ionic species, we prepared aqueous solutions of Na_2SO_4, K_2SO_4 and $MgSO_4$ with an ionic strength of 5 mM at different pH values and passed them through the membrane. As typical experiment, the permeate flux of K_2SO_4 was also continuously monitored. Figure 5-7b demonstrates that the rejection rate for the tested salts (e.g., Na_2SO_4, K_2SO_4 and $MgSO_4$) is high and steady in neutral and alkaline solutions, but significantly decreases when the pH drops to 4. Moreover, the consistent flux observed at various pH values suggests that the pore size of the membrane does not change with pH. This finding is in agreement with the SAXS data (see Figure 5-5), which demonstrates unnoticeable structural variation in the polyLLC at different pH values. Thus, the change in rejection rates with pH can be attributed to the isoelectric point of COOH of copolymerized AAc, which is approximately 4.5.[293] As a result, when the pH drops below 4, COOH groups on the

polymer chains become undissociated, leading to weakened electrostatic repulsion and subsequently lower rejection rate.

To further investigate the pH response, we passed aqueous solutions containing 500 ppm of anionic dyes including OG, AF, and AR1 through the membrane at different pH values (4, 6, and 9). The results obtained from the experiment (as depicted in Figure 5-7d-g) demonstrate that at pH values of 6 and 9, a rejection rate close to 85% is observed for all the dyes. In contrast, when the pH is set at 4, the rejection rate drops to 6%, 10%, and 30% for AR1, OG, and AF, respectively. As control experiment, we also tested OG rejection performance of the commercially available NF270 membrane at different pH values. Figure F3 (see Appendix F) confirms that the rejection of NF270 remains constant regardless of the pH change, as the separation is primarily dependent on size-exclusion due to the smaller pore size of NF270 (~0.8 nm).[294] The outcomes of these experiments verify that the polyLLC membrane has pH-responsive separation of ionic species.

To assess whether thermoresponsiveness affects pH-dependent selectivity for ionic species, we conducted rejection experiments for K_2SO_4 (at 5 mM ionic strength) while varying both pH and temperature simultaneously. The results, depicted in Figure 5-7c, demonstrate that the rate of salt rejection remains constant at both tested pH values despite a change in temperature from 25 to 45 °C. This indicates that altering the pore size with temperature within the studied range has negligible effect on the rejection rate of ionic species driven by electrostatic repulsion. This outcome is somewhat expected as the polyLLC membrane does not reject studied ions by size-exclusion. Furthermore, at the temperature of 45 °C, the membrane pore size, which is ~2.6 nm from SAXS measurements and MWCO analysis, is still smaller than the computed Debye length of 4.3 nm for an ionic strength of 5 mM. This observation provides additional confirmation that

such pore expansion resulting from the membrane thermal response has negligible impact on the membrane ability to reject ionic species.

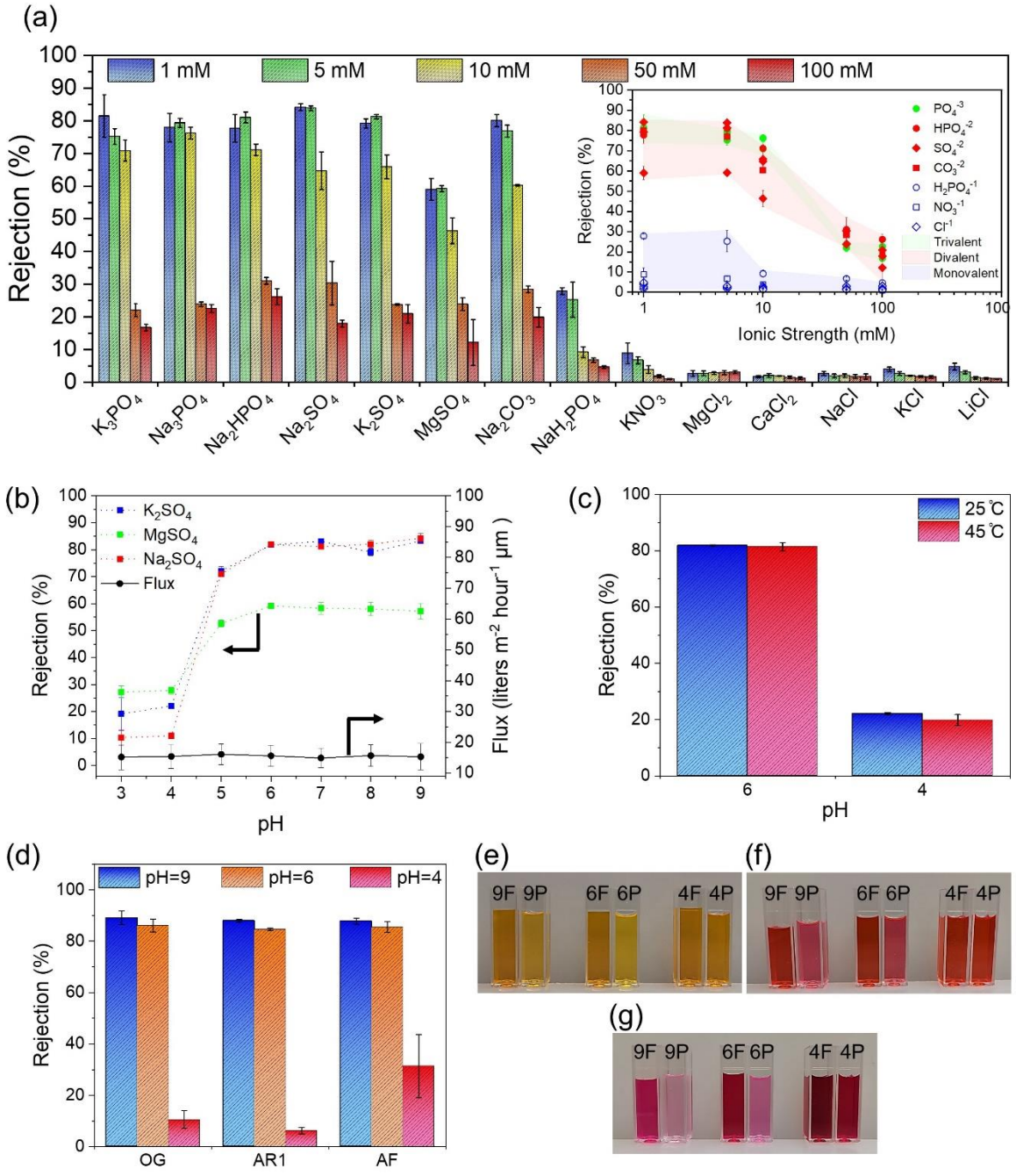

Figure 5-7. (a) The results of single salt rejection experiments are presented for different salts and concentrations. The range of rejection observed for different anions is indicated by the shaded areas in the

inset. (b) The rejection of different dissolved salts varies with pH. The membrane flux (for K_2SO_4) at different pH values is also presented in the figure. (c) The variation of K_2SO_4 rejection is demonstrated in response to changes in temperature and pH. (d) The pH-dependent rejection rate for different anionic dyes is displayed. Photos of the feed and permeate at different pH values are provided for (e) OG, (f) AR1, and (g) AF. In these photos, the pH value (9, 6, or 4) is indicated by a number and the letter indicates whether it is feed (F) or permeate (P). It should be noted that the color of the feed for AF changes as the pH is altered since this dye is a pH indicator.

5.3.2.3 Contact angle and fouling resistance

Fouling is a major challenge in membrane separation processes as it can lead to reduced membrane performance and lifespan. A membrane is particularly susceptible to fouling when it is utilized for filtering feed streams containing species such as proteins, bacteria, and viruses.[4] Increasing the surface hydrophilicity of membranes is a key strategy for mitigating fouling.[276] Therefore, we evaluated the surface hydrophilicity of the polyLLC membrane through measuring its water contact angle.[276] The results of the measurement are depicted in Figure 5-8a, showing an average contact angle of 33° for the polyLLC membrane when swollen at 25 to 45 °C. This suggests that the membrane has a highly hydrophilic surface, which can effectively enhance its resistance to fouling.

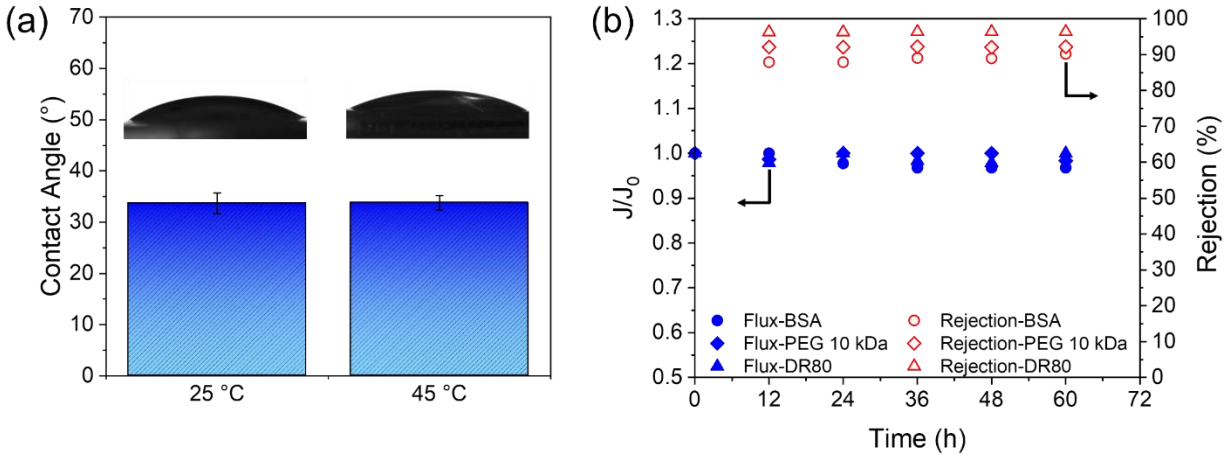

Figure 5-8. (a) The contact angle of the polyLLC membrane when swelled with water at 25 and 45 °C. (b) The evolution of the ratio of membrane flux at a given time (J) to the initial flux with DI water (J_0) (represented by filled symbols) and rejection rate of various solutes (represented by open symbols) for the polyLLC membrane.

We assessed the fouling resistance using the same procedure outlined in our previous work (see Chapter 4).[289] In brief, we passed solutions of three different species through the membrane. The filtration setup was kept at 25°C for a period of 60 h while the flux was measured at 12-h intervals. We also monitored the rejection rate with time to ensure that the membrane was performing consistently. As demonstrated in Figure 5-8b, the membrane flux decreased by less than 4% after 60 h, indicating exceptional resistance to fouling, which can be attributed to the highly hydrophilic surface of the membrane. Comparable findings were reported for polyLLC membranes without AAc in our previous work (see Chapter 4).[289] Additionally, the constant rejection rate confirms the reliable and consistent performance of the polyLLC membrane. It is important to note that the membrane is expected to exhibit similar fouling resistance at 45 °C due to its comparable surface hydrophilicity to that observed at 25 °C (with the same contact angle of 33°).

5.3.2.4 Mechanisms of thermal and pH response

Figure 5-9 schematically explains the thermo- and pH-responsiveness mechanisms of the polyLLC membrane. As can be seen, by increasing temperature, the chemically bonded polymer network de-swells, increasing the intermicellar distance, resulting in larger pore sizes. De-swelling is triggered by the LCST of the Pluronic, which makes the PPO block hydrophobic. It is worth noting that such changes in the polymer structure are reversible upon rehydration through cooling the system down to 25 °C.

The polyLLC membrane exhibits pH-responsiveness when the pH of the feed solution is lowered to 4, which is close to the isoelectric point of copolymerized AAc. At this pH, there is a weak electrostatic repulsion between the membrane and the ionic solute due to the fact that COOH group on polymer chains become undissociated. Thus, as the membrane separates ionic species primarily based on electrostatic repulsion, the rejection rate decreases considerably.

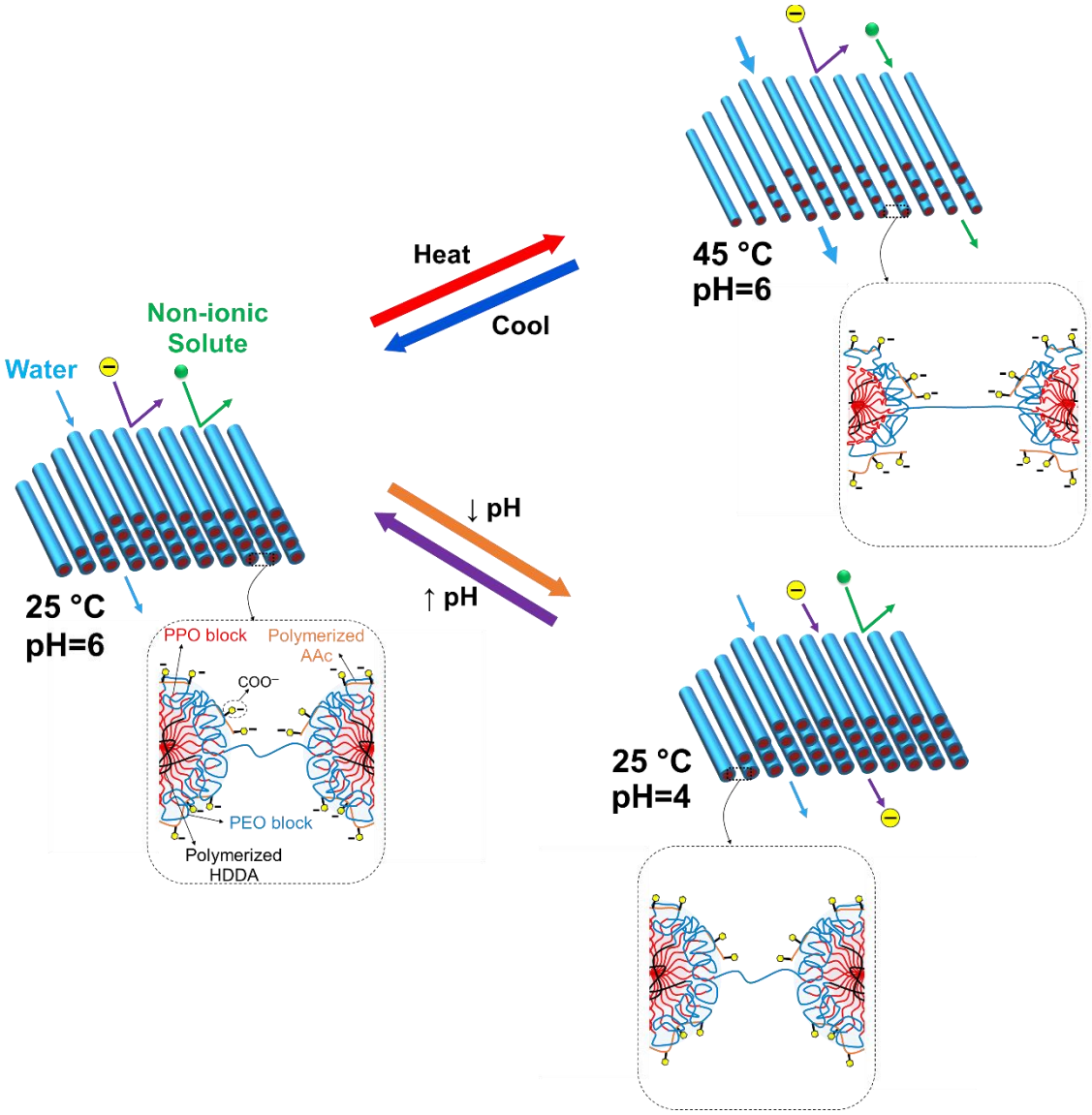

Figure 5-9. Schematic illustration of thermos- and pH-responsiveness mechanism of the polyLLC membrane.

5.4 Conclusion

In this chapter, we demonstrate the creation of a thermo- and pH-responsive NF membrane by using H_1 LLC as the template. Experimental studies show that this membrane has the capability to modify the separation characteristics in response to changes in temperature and pH. The formulation of the membrane includes P84DA, which acts as both the monomer and structure-directing amphiphile and is also responsible for changes in membrane pore size with temperature. Additionally, AAc was copolymerized with P84DA in the template, thus, facilitating ion separation through Donnan exclusion and imparting pH-responsive behavior. Our experiments indicate that the thickness-normalized flux and membrane MWCO can be increased from 16 to 31 liters m^{-2} $hour^{-1}$ μm and from 1,600 to 2,400 Da by raising the temperature from 25 to 45 °C, respectively. Furthermore, the developed membrane exhibits excellent performance in removing dissolved salts containing trivalent and divalent anion at neutral and alkaline pH levels, and its ion rejection capability can be turned off by lowering the feed pH to 4. We also observe remarkable sulfate over chloride ion selectivity, which is ideal for salt fractionation applications. Additionally, the membrane demonstrates exceptional resistance to fouling by various solutes due to its highly hydrophilic surface.

CHAPTER 6: CONCLUSIONS AND FUTURE WORKS

6.1 Summary

LLCs are mesoscopic structures that exhibit long-range periodic order ranging from 2 to 50 nm, formed via self-assembly of amphiphiles in selective solvents. LLC templating (polymerization in LLC templates) is a highly effective method for creating nanostructured polymers that can be utilized in various technical domains, specifically molecular separation. LLCs offer a diverse range of nanostructures, but our focus is on the lamellar and normal hexagonal phases because they provide continuous transport paths in two and three dimensions, respectively. Multi-directional continuous transport paths in nanometer range are especially advantageous for membrane applications. The normal hexagonal phase is particularly desirable because it eliminates the need for structural alignment. This dissertation provides a comprehensive study on transcriptive and synergistic LLC templating approaches to synthesize stimuli-responsive membranes, which can change their separation performance in response to an external stimulus (e.g., temperature and pH).

When using transcriptive LLC templating, polymerization kinetics has a critical role for maintaining the structure after polymerization. Therefore, the initiator-dependent thermal polymerization kinetics is studied in this approach. The results demonstrate that the IFW system exhibits faster reaction rates than IFO under varying conditions while also preserving the structure.

We propose that the gradual increase of propagating chains in the monomer phase, leading to a lower termination rate, may account for the faster polymerization rate. Additionally, a higher initiator efficiency could be another contributing factor. We further demonstrate that polymers cured with the IFW system exhibit improved mechanical properties compared to other initiation systems, even at similar monomer conversions. The polymerization at the polar/apolar interface in the IFW system may explain this difference.

Two-step thermoresponsive UF membranes can be produced by using transcriptive templating with the IFW system. The thermal response is triggered by thermoresponsive F127 block copolymer, which is combined with water and hydrophobic monomers to create an LLC with a lamellar structure. After the templating process, the resulting cross-linked network fixes the F127 molecules in place, preventing their removal by water. We demonstrate that the resulting membrane can adjust its pore size from 34.6 nm to 45.7 nm and 59.6 nm by increasing the temperature from 25 °C to 35 °C and 50 °C, respectively. Consequently, the membrane permeability and MWCO increase by elevating the temperature. The two-step thermal response appears to be due to the LCST of F127 at 35 °C and the melting of the PEO crystalline structure at 50 °C. Our investigation suggests that cleaning efficiency and membrane lifespan can be improved by cleaning the contaminated membrane at high temperatures due to the porosity change in response to temperature.

By replacing the OH groups at both ends of thermoresponsive Pluronic surfactants with acrylates, they can be functionalized and become polymerizable for use in synergistic LLC templating. This process yields P84DA, which is used to create H_1-structured mesophases that can create a thermoresponsive UF membrane upon polymerization. Our studies demonstrate that the resulting membrane can adjust its thickness-normalized flux from 28 to 68 liters m^{-2} $hour^{-1}$ µm

and pore size from 2.5 to 3.2 nm when the temperature is increased from 25 to 45 °C, respectively. Furthermore, the membrane exhibits excellent fouling resistance, as its permeability remains almost unchanged after 60 hours of filtration of various charged and uncharged solutes. Highly hydrophilic surface of the membrane appears to be the main reason for its antifouling behavior.

The addition of AAc in the H_1-structured LLC formulation during synergistic templating using P84DA can provide the membrane with additional functionality. The resulting NF membrane not only effectively separates dissolved salts containing trivalent and divalent anion from water but also displays thermo- and pH-responsive behavior. The presence of copolymerized AAc, as the charged component, enables ion separation through Donnan exclusion and contributes to pH responsive behavior for the separation of ionic species. The experimental results indicate that the thickness-normalized flux and membrane pore size can be increased from 16 to 31 liters m^{-2} $hour^{-1}$ µm and from 2.2 to 2.6 nm, respectively, by increasing the temperature from 25 to 45 °C. The developed membrane also exhibits excellent performance in removing dissolved salts containing trivalent and divalent anion at neutral and alkaline pH levels, with the ion rejection capability adjustable by reducing the feed pH to 4. It further exhibits remarkable selectivity for sulfate over chloride ions, making it ideal for salt fractionation applications. Moreover, the membrane demonstrates exceptional resistance to fouling from various solutes owing to its highly hydrophilic surface.

As discussed in Chapter 1, synergistic templating has been commonly utilized for the synthesis of UF and NF membranes, with only a few studies, including ours,[263] exploring transcriptive templating for this purpose. Our research[263] on the transcriptive approach demonstrates the ability to fabricate two-step thermoresponsive UF membranes with a pore size of 34.6 nm at 25 °C, which can be expanded to 45.7 and 59.6 nm by heating to 35 and 50 °C, respectively. In contrast, Qavi

et al. have reported the production of transcriptive-templated UF membranes with a pore size ranging from 2 to 4 nm at 25 °C without verifying their thermoresponsiveness.[32,142]

The average pore size and thickness-normalized flux (at 30 psi) values obtained for membranes synthesized through synergistic LLC templating have been summarized in Figure 6-1a. It is evident that using H_1 structure to synthesize the desired membrane results in a significant improvement in membrane flux compared to Q_1 or H_2 phases at a similar pore size. Additionally, our work has not only expanded the range of possible membrane pore sizes through synergistic templating but also successfully produced stimuli-responsive H_1-structured polyLLC membranes, which is a unique accomplishment. Figure 6-1b exhibits the selectivity/permeability trade-off for the synergistic LLC-templated membranes. We have employed 1/pore size as the separation factor representing the membrane selectivity. Hagen–Poiseuille equation[295] has been used to estimate the theoretical permeability for membranes having different tortuosity (τ) values (τ=1 for an ideal membrane with straight capillary tube pores across the membrane and τ=1.5-2.5 as the typical tortuosity range reported for different membranes[296]). As can be seen, H_1-structured membranes (including the ones developed in the current study) represent a more balanced permeability-selectivity feature over the samples with Q_1 and H_2 structures as they exhibit data points closer to the estimated ideal selectivity/permeability curve (τ=1), making them an ideal candidate for different application opportunities.

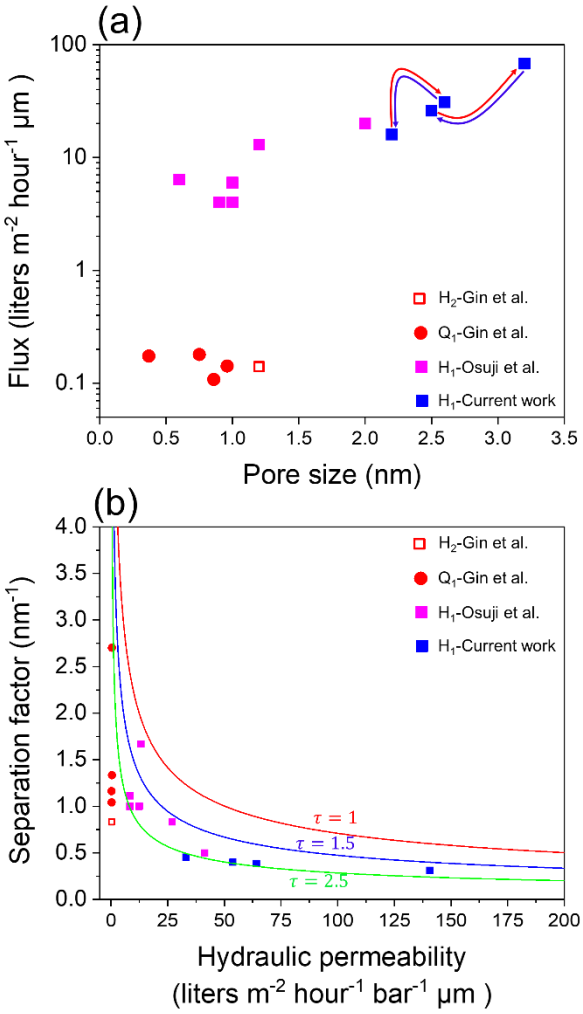

Figure 6-1. (a) The average pore size and thickness-normalized flux (at 30 psi) values of the membranes created via synergistic LLC templating using different LLC structures, as reported by Gin et al.,[34,93,118–120] Osuji et al.,[31,125,297] and the present study. (b) Selectivity/permeability trade-off for the synergistic LLC-templated membranes. 1/pore size has been used as the separation factor representing the membrane selectivity. Hagen–Poiseuille equation has been used to estimate the theoretical permeability for membranes having different tortuosity (τ) values (τ=1 for an ideal membrane with straight capillary tube pores across the membrane and τ=1.5-2.5 as the typical tortuosity range reported for different membranes[296]). Notably, the membranes produced in the current research exhibit the ability to alter their pore size and thus selectivity/permeability in response to temperature change from 25 to 45 °C. The red and blue arrows depicted in (a) denote the heating and cooling cycles, respectively. The membrane having 2.2 nm at 25 °C shows pH-responsiveness in addition to thermoresponsiveness, changing its selectivity towards ionic species with a change in pH.

6.2 Future work

Although this dissertation has made significant progress in using LLC templating to produce stimuli-responsive UF and NF membranes, there are still opportunities to enhance their performance and explore the potential of polyLLCs in other applications within the field. The following sections will briefly discuss these opportunities.

6.2.1 Mesophases with domain sizes beyond-20 nm

The amphiphiles discussed in this work typically have a molecular weight below 13 kDa, which inherently restricts the sizes of their lyotropic mesophases to below 20 nanometers, often falling into the sub-10-nanometer range. This limitation can restrict the potential applications for polyLLCs derived from these materials. As previously discussed in section 1.7, common strategies to tackle this challenge involve the use of giant surfactants and swelling LLCs by incorporating charged lipids. However, there is a paucity of research on utilizing such mesophases for synergistic or transcriptive templating. Consequently, further investigation is required to develop LLCs with different structures featuring domain sizes exceeding 20 nanometers and to employ them as templates for polymerization. The effect of larger domain sizes on polymerization kinetics, mechanical properties and mesophase stability after polymerization can be studied.

6.2.2 Membranes with less than 1 μm active layer thickness

While the thickness-normalized flux of the membranes produced in this study is comparable to those reported in the literature (as shown in Figure 6-1), reducing the thickness of the active layer from ~40 μm to less than 1 μm is critical to address the trade-off between permeability and selectivity and make these membranes commercially viable. Recently, Osuji et al. have achieved H_1-structured membranes with a thickness of nearly 100 nm using a combination of solution casting and spin coating. These membranes have effective pore sizes in the 1 nm range and a

permeability of around 20 liters m^{-2} $hour^{-1}$ bar^{-1}, which is higher than that of commercially available NF membranes.[297] To achieve the desired membrane thickness for the synergistic templating formulations developed in this study, a combination of heating (to lower the viscosity of the LLC) and spin coating can be utilized. Another option is to use a combination of solution casting and spin coating since our preliminary experiments indicate that we can create a ~60 wt% solution of LLC (the formulation studied in Chapter 4) in acetone (laboratory reagent, ≥99.5%, Sigma-Aldrich), and upon evaporation of acetone, the desired LLC structure can be obtained (as confirmed by CPLM). The effect of different active layer thicknesses on selectivity, permeability, fouling resistance and stimuli-responsiveness can be further studied.

6.2.3 Synthesizing positively charged NF membranes

As explained in Chapter 5, the incorporation of AAc into LLCs can generate negatively charged polyLLC membranes, which can separate dissolved salts from water based on electrostatic repulsion between the membrane and their anions. These membranes also exhibit excellent selectivity for sulfate ions over chloride ions. However, in some salt fractionation applications, separation based on cations is preferred because it provides an opportunity to separate valuable metals like lithium and magnesium from other less valuable species like sodium.[298] Therefore, synthesizing positively charged polyLLC membranes can be considered as the next step in improving the formulation for synergistic LLC templating. Incorporating monomers such as 2-(dimethylamino)ethyl methacrylate (DMAEMA) that contain amine groups in their structure into the LLC formulation could be one approach to achieve the goal of synthesizing positively charged polyLLC membranes. Another way to introduce a positive charge into the membrane is by incorporating amino-functionalized Pluronic into the formulation. There is a literature procedure available for amino-functionalizing Pluronics.[299] The relationship between the content or nature of

cationic specie incorporated into the membrane and the membrane selectivity towards various ions can be explored.

6.2.4 PolyLLCs for heavy metal ions removal from wastewater

The contamination of water resources by toxic heavy metals is a significant environmental issue related to the large-scale production of materials such as energy storage devices, paint and coating, and pharmaceuticals.[300] These substances can cause several health problems for humans. For example, lead ion accumulation in the body can lead to blood disorders, anorexia, and kidney malfunction.[301] To address this issue, scientists have developed various methods for removing toxic components from wastewater, including ion exchange, precipitation, flotation, adsorption, and membrane separation. Among these methods, adsorption is known for its excellent efficiency, relative simplicity, and recyclability.[302]

The efficient adsorption process for removing toxic heavy metals from wastewater usually involves two main steps: diffusion of the adsorbate into the adsorbent and chelation of the metal ion via the chelating sites of the adsorbent. The former step can be regulated through the porosity of the adsorbent, while the latter is controlled by the quantity and accessibility of the functional sites.[303] Porous polymer hydrogels are excellent candidates for this purpose as they offer high transport rates and contain functional groups like carboxyl (−COOH), hydroxyl (−OH), and amine (−NH2), which can act as chelating sites. Moreover, the molecular chains of hydrogels are highly stretched upon swelling with water, resulting in an excellent accessibility of chelating sites to metal ions.[303] We believe that the adsorption capacity and ion removal efficiency of polymeric hydrogels can be further improved by using well-ordered nanoporous hydrogels synthesized in LLC templates. The LLC formulation that was developed in Chapter 5 and contains AAc is a promising candidate for this application, as hydrogels synthesized with AAc have been extensively used in

the adsorption of various heavy metal ions (e.g., Cu^{2+}, Cd^{2+}, Cr^{6+}, Cd^{2+}, Mn^{2+}, Fe^{3+} and Zn^{2+}).[302] LLC formulations incorporating DMAEMA or amino-functionalized Pluronics can also be utilized, as hydrogels with amine functional groups have been shown to efficiently remove heavy metal ions like Cu^{2+}, Cd^{2+} and Pb^{2+} from water.[304] The synthesized product can be powdered or used as hydrogel films for the adsorption tests. Effect of adsorbent content, contact time, initial metal ion concentration, pH, temperature, and AAc, DMEMA and amino-functionalized Pluronic content on the adsorption capacity and efficiency of different heavy metal ions can be investigated. Additionally, the adsorbent can be regenerated and reused for several cycles to evaluate its recyclability. The polyLLCs discussed above can also serve as adsorptive membranes[304] for targeted heavy metal ion removal and can be regenerated and reused once they become saturated.[303]

References

(1) Chimene, D.; Alge, D. L.; Gaharwar, A. K. Two-Dimensional Nanomaterials for Biomedical Applications: Emerging Trends and Future Prospects. *Adv. Mater.* **2015**, *27* (45), 7261–7284. https://doi.org/10.1002/adma.201502422.

(2) Bardhan, N. M. 30 Years of Advances in Functionalization of Carbon Nanomaterials for Biomedical Applications: A Practical Review. *J. Mater. Res.* **2017**, *32* (1), 107–127. https://doi.org/10.1557/jmr.2016.449.

(3) Iskandar, F. Nanoparticle Processing for Optical Applications - A Review. *Adv. Powder Technol.* **2009**, *20* (4), 283–292. https://doi.org/10.1016/j.apt.2009.07.001.

(4) Werber, J. R.; Osuji, C. O.; Elimelech, M. Materials for Next-Generation Desalination and Water Purification Membranes. *Nat. Rev. Mater.* **2016**, *1* (5), 16018. https://doi.org/10.1038/natrevmats.2016.18.

(5) Wandera, D.; Wickramasinghe, S. R.; Husson, S. M. Stimuli-Responsive Membranes. *J. Memb. Sci.* **2010**, *357* (1–2), 6–35. https://doi.org/10.1016/j.memsci.2010.03.046.

(6) Zhang, Q.; Uchaker, E.; Candelaria, S. L.; Cao, G. Nanomaterials for Energy Conversion and Storage. *Chem. Soc. Rev.* **2013**, *42* (7), 3127–3171. https://doi.org/10.1039/c3cs00009e.

(7) Gin, D. L.; Lu, X.; Nemade, P. R.; Pecinovsky, C. S.; Xu, Y.; Zhou, M. Recent Advances in the Design of Polymerizable Lyotropic Liquid-Crystal Assemblies for Heterogeneous Catalysis and Selective Separations. *Adv. Funct. Mater.* **2006**, *16* (7), 865–878. https://doi.org/10.1002/adfm.200500280.

(8) Hu, H.; Gopinadhan, M.; Osuji, C. O. Directed Self-Assembly of Block Copolymers: A Tutorial Review of Strategies for Enabling Nanotechnology with Soft Matter. *Soft Matter* **2014**, *10* (22), 3867. https://doi.org/10.1039/c3sm52607k.

(9) Hyde, S. T. Identification of Lyotropic Liquid Crystalline Mesophases. In *Handbook of Applied Surface and Colloid Chemistry*; 2001; pp 299–332.

(10) Tachibana, T.; Mori, T.; Hori, K. Chiral Mesophases of 12-Hydroxyoctadecanoic Acid in Jelly and in the Solid State. I. A New Type of Lyotropic Mesophase in Jelly with Organic Solvents. *Bull. Chem. Soc. Jpn.* **1980**, *53* (6), 1714–1719. https://doi.org/10.1246/bcsj.53.1714.

(11) Atkin, R.; Bobillier, S. M. C.; Warr, G. G. Propylammonium Nitrate as a Solvent for Amphiphile Self-Assembly into Micelles, Lyotropic Liquid Crystals, and Microemulsions. *J. Phys. Chem. B* **2010**, *114* (3), 1350–1360. https://doi.org/10.1021/jp910649a.

(12) Robertson, L. A.; Schenkel, M. R.; Wiesenauer, B. R.; Gin, D. L. Alkyl-Bis(Imidazolium) Salts: A New Amphiphile Platform That Forms Thermotropic and Non-Aqueous Lyotropic Bicontinuous Cubic Phases. *Chem. Commun.* **2013**, *49* (82), 9407–9409. https://doi.org/10.1039/c3cc44452j.

(13) López-Barrón, C. R.; Chen, R.; Wagner, N. J.; Beltramo, P. J. Self-Assembly of Pluronic F127 Diacrylate in Ethylammonium Nitrate: Structure, Rheology, and Ionic Conductivity before and after Photo-Cross-Linking. *Macromolecules* **2016**, *49* (14), 5179–5189. https://doi.org/10.1021/acs.macromol.6b00205.

(14) Nagarajan, R. Molecular Packing Parameter and Surfactant Self-Assembly: The Neglected Role of the Surfactant Tail †. *Langmuir* **2002**, *18* (1), 31–38. https://doi.org/10.1021/la010831y.

(15) Lutz-Bueno, V.; Isabettini, S.; Walker, F.; Kuster, S.; Liebi, M.; Fischer, P. Ionic Micelles and Aromatic Additives: A Closer Look at the Molecular Packing Parameter. *Phys. Chem. Chem. Phys.* **2017**, *19* (32), 21869–21877. https://doi.org/10.1039/C7CP03891G.

(16) Lee, Y. C.; Taraschi, T. F.; Janes, N. Support for the Shape Concept of Lipid Structure Based on a Headgroup Volume Approach. *Biophys. J.* **1993**, *65* (4), 1429–1432. https://doi.org/10.1016/S0006-3495(93)81206-2.

(17) Huang, Y.; Gui, S. Factors Affecting the Structure of Lyotropic Liquid Crystals and the Correlation between Structure and Drug Diffusion. *RSC Adv.* **2018**, *8* (13), 6978–6987. https://doi.org/10.1039/c7ra12008g.

(18) Soni, S. S.; Brotons, G.; Bellour, M.; Narayanan, T.; Gibaud, A. Quantitative SAXS Analysis of the P123/Water/Ethanol Ternary Phase Diagram. *J. Phys. Chem. B* **2006**, *110* (31), 15157–15165. https://doi.org/10.1021/jp062159p.

(19) Rajabalaya, R.; Musa, M. N.; Kifli, N.; David, S. R. Oral and Transdermal Drug Delivery Systems: Role of Lipid-Based Lyotropic Liquid Crystals. *Drug Des. Devel. Ther.* **2017**, *Volume11*, 393–406. https://doi.org/10.2147/DDDT.S103505.

(20) Meng, Y.; Gu, D.; Zhang, F.; Shi, Y.; Cheng, L.; Feng, D.; Wu, Z.; Chen, Z.; Wan, Y.; Stein, A.; Zhao, D. A Family of Highly Ordered Mesoporous Polymer Resin and Carbon Structures from Organic-Organic Self-Assembly. *Chem. Mater.* **2006**, *18* (18), 4447–4464. https://doi.org/10.1021/cm060921u.

(21) Jayaraman, A.; Zhang, D. Y.; Dewing, B. L.; Mahanthappa, M. K. Path-Dependent Preparation of Complex Micelle Packings of a Hydrated Diblock Oligomer. *ACS Cent. Sci.* **2019**, *5* (4), 619–628. https://doi.org/10.1021/acscentsci.8b00903.

(22) Baez-Cotto, C. M.; Mahanthappa, M. K. Micellar Mimicry of Intermetallic C14 and C15 Laves Phases by Aqueous Lyotropic Self-Assembly. *ACS Nano* **2018**, *12* (4), 3226–3234. https://doi.org/10.1021/acsnano.7b07475.

(23) Jennings, J.; Green, B.; Mann, T. J.; Guymon, C. A.; Mahanthappa, M. K. Nanoporous

Polymer Networks Templated by Gemini Surfactant Lyotropic Liquid Crystals. *Chem. Mater.* **2018**, *30* (1), 185–196. https://doi.org/10.1021/acs.chemmater.7b04183.

(24) Jayaraman, A.; Mahanthappa, M. K. Counterion-Dependent Access to Low-Symmetry Lyotropic Sphere Packings of Ionic Surfactant Micelles. *Langmuir* **2018**, *34* (6), 2290–2301. https://doi.org/10.1021/acs.langmuir.7b03833.

(25) Moriguchi, I.; Ozono, A.; Mikuriya, K.; Teraoka, Y.; Kagawa, S.; Kodama, M. Micelle-Templated Mesophases of Phenol-Formaldehyde Polymer. *Chem. Lett.* **1999**, No. 11, 1171–1172. https://doi.org/10.1246/cl.1999.1171.

(26) Hentze, H.-P.; Co, C. C.; McKelvey, C. A.; Kaler, E. W. Templating Vesicles, Microemulsions, and Lyotropic Mesophases by Organic Polymerization Processes. In *Topics in Current Chemistry*; 2003; pp 197–223. https://doi.org/10.1007/3-540-36408-0_7.

(27) Worthington, K. S.; Baguenard, C.; Forney, B. S.; Guymon, C. A. Photopolymerization Kinetics in and of Self-Assembling Lyotropic Liquid Crystal Templates. *J. Polym. Sci. Part B Polym. Phys.* **2017**, *55* (6), 471–489. https://doi.org/10.1002/polb.24296.

(28) Wang, C.; Chen, D.; Jiao, X. Lyotropic Liquid Crystal Directed Synthesis of Nanostructured Materials. *Sci. Technol. Adv. Mater.* **2009**, *10* (2), 023001. https://doi.org/10.1088/1468-6996/10/2/023001.

(29) Gin, D. L.; Gu, W.; Pindzola, B. A.; Zhou, W.-J. Polymerized Lyotropic Liquid Crystal Assemblies for Materials Applications. *Acc. Chem. Res.* **2001**, *34* (12), 973–980. https://doi.org/10.1021/ar000140d.

(30) Mauter, M. S.; Elimelech, M.; Osuji, C. O. Nanocomposites of Vertically Aligned Single-Walled Carbon Nanotubes by Magnetic Alignment and Polymerization of a Lyotropic Precursor. *ACS Nano* **2010**, *4* (11), 6651–6658. https://doi.org/10.1021/nn102047j.

(31) Feng, X.; Imran, Q.; Zhang, Y.; Sixdenier, L.; Lu, X.; Kaufman, G.; Gabinet, U.; Kawabata, K.; Elimelech, M.; Osuji, C. O. Precise Nanofiltration in a Fouling-Resistant Self-Assembled Membrane with Water-Continuous Transport Pathways. *Sci. Adv.* **2019**, *5* (8), eaav9308. https://doi.org/10.1126/sciadv.aav9308.

(32) Qavi, S.; Lindsay, A. P.; Firestone, M. A.; Foudazi, R. Ultrafiltration Membranes from Polymerization of Self-Assembled Pluronic Block Copolymer Mesophases. *J. Memb. Sci.* **2019**, *580*, 125–133. https://doi.org/10.1016/j.memsci.2019.02.060.

(33) Dischinger, S. M.; Rosenblum, J.; Noble, R. D.; Gin, D. L.; Linden, K. G. Application of a Lyotropic Liquid Crystal Nanofiltration Membrane for Hydraulic Fracturing Flowback Water: Selectivity and Implications for Treatment. *J. Memb. Sci.* **2017**, *543*, 319–327. https://doi.org/10.1016/j.memsci.2017.08.028.

(34) Zhou, M.; Nemade, P. R.; Lu, X.; Zeng, X.; Hatakeyama, E. S.; Noble, R. D.; Gin, D. L. New Type of Membrane Material for Water Desalination Based on a Cross-Linked Bicontinuous Cubic Lyotropic Liquid Crystal Assembly. *J. Am. Chem. Soc.* **2007**, *129* (31), 9574–9575. https://doi.org/10.1021/ja073067w.

(35) Gin, D. L.; Bara, J. E.; Noble, R. D.; Elliott, B. J. Polymerized Lyotropic Liquid Crystal Assemblies for Membrane Applications. *Macromol. Rapid Commun.* **2008**, *29* (5), 367–389. https://doi.org/10.1002/marc.200700707.

(36) Guymon, C. A.; Lester, C. L. Photopolymerization Kinetics of Nanostructured Polymers Templated by Lyotropic Liquid Crystals. *ACS Symp. Ser.* **2003**, *847*, 378–388. https://doi.org/10.1021/bk-2003-0847.ch032.

(37) Lester, C. L.; Smith, S. M.; Jarrett, W. L.; Allan Guymon, C. Effects of Monomer Organization on the Photopolymerization Kinetics of Acrylamide in Lyotropic Liquid

Crystalline Phases. *Langmuir* **2003**, *19* (22), 9466–9472. https://doi.org/10.1021/la0300784.

(38) McLaughlin, J. R.; Abbott, N. L.; Guymon, C. A. Responsive Superabsorbent Hydrogels via Photopolymerization in Lyotropic Liquid Crystal Templates. *Polymer* **2018**, *142*, 119–126. https://doi.org/10.1016/j.polymer.2018.03.016.

(39) DePierro, M. A.; Olson, A. J.; Guymon, C. A. Effect of Photoinitiator Segregation on Polymerization Kinetics in Lyotropic Liquid Crystals. *Polymer* **2005**, *46* (2), 335–345. https://doi.org/10.1016/j.polymer.2004.11.007.

(40) DePierro, M. A.; Carpenter, K. G.; Guymon, C. A. Influence of Polymerization Conditions on Nanostructure and Properties of Polyacrylamide Hydrogels Templated from Lyotropic Liquid Crystals. *Chem. Mater.* **2006**, *18* (23), 5609–5617. https://doi.org/10.1021/cm061969a.

(41) Forney, B. S.; Baguenard, C.; Guymon, C. A. Effects of Controlling Polymer Nanostructure Using Photopolymerization within Lyotropic Liquid Crystalline Templates. *Chem. Mater.* **2013**, *25* (15), 2950–2960. https://doi.org/10.1021/cm4004849.

(42) Forney, B. S.; Baguenard, C.; Allan Guymon, C. Improved Stimuli-Response and Mechanical Properties of Nanostructured Poly(N-Isopropylacrylamide-Co-Dimethylsiloxane) Hydrogels Generated through Photopolymerization in Lyotropic Liquid Crystal Templates. *Soft Matter* **2013**, *9* (31), 7458–7467. https://doi.org/10.1039/c3sm50556a.

(43) Lester, C. L.; Colson, C. D.; Guymon, C. A. Photopolymerization Kinetics and Structure Development of Templated Lyotropic Liquid Crystalline Systems. *Macromolecules* **2001**, *34* (13), 4430–4438. https://doi.org/10.1021/ma001853e.

(44) Lester, C. L.; Smith, S. M.; Colson, C. D.; Guymon, C. A. Physical Properties of Hydrogels Synthesized from Lyotropic Liquid Crystalline Templates. *Chem. Mater.* **2003**, *15* (17), 3376–3384. https://doi.org/10.1021/cm021703d.

(45) McCormick, D. T.; Stovall, K. D.; Guymon, C. A. Photopolymerization in Pluronic Lyotropic Liquid Crystals: Induced Mesophase Thermal Stability. *Macromolecules* **2003**, *36* (17), 6549–6558. https://doi.org/10.1021/ma030037e.

(46) Clapper, J. D.; Guymon, C. A. Nanostructured Hydrogels via Photopolymerization in Lyotropic Liquid Crystalline Systems. *Mol. Cryst. Liq. Cryst.* **2009**, *509* (1), 30/[772]-38/[780]. https://doi.org/10.1080/15421400903065002.

(47) López-Barrón, C. R.; Chen, R.; Wagner, N. J. Ultrastretchable Iono-Elastomers with Mechanoelectrical Response. *ACS Macro Lett.* **2016**, *5* (12), 1332–1338. https://doi.org/10.1021/acsmacrolett.6b00790.

(48) Xie, Y.; Xie, R.; Yang, H. C.; Chen, Z.; Hou, J.; López-Barrón, C. R.; Wagner, N. J.; Gao, K. Z. Iono-Elastomer-Based Wearable Strain Sensor with Real-Time Thermomechanical Dual Response. *ACS Appl. Mater. Interfaces* **2018**, *10* (38), 32435–32443. https://doi.org/10.1021/acsami.8b10672.

(49) Gu, W.; Zhou, W. J.; Gin, D. L. A Nanostructured, Scandium-Containing Polymer for Heterogeneous Lewis Acid Catalysis in Water. *Chem. Mater.* **2001**, *13* (6), 1949–1951. https://doi.org/10.1021/cm0101531.

(50) Smith, R. C.; Fischer, W. M.; Gin, D. L. Ordered Poly(p-Phenylenevinylene) Matrix Nanocomposites via Lyotropic Liquid-Crystalline Monomers. *J. Am. Chem. Soc.* **1997**, *119* (17), 4092–4093. https://doi.org/10.1021/ja963837w.

(51) Gray, D. H.; Hu, S.; Juang, E.; Gin, D. L. Highly Ordered Polymer-Inorganic

Nanocomposites via Monomer Self-Assembly: In Situ Condensation Approach. *Adv. Mater.* **1997**, *9* (9), 731–736. https://doi.org/10.1002/adma.19970090912.

(52) McGrath, M. J.; Patterson, N.; Manubay, B. C.; Hardy, S. H.; Malecha, J. J.; Shi, Z.; Yue, X.; Xing, X.; Funke, H. H.; Gin, D. L.; Liu, P.; Noble, R. D. 110th Anniversary: The Dehydration and Loss of Ionic Conductivity in Anion Exchange Membranes Due to FeCl4- Ion Exchange and the Role of Membrane Microstructure. *Ind. Eng. Chem. Res.* **2019**, *58* (49), 22250–22259. https://doi.org/10.1021/acs.iecr.9b04592.

(53) Herz, J.; Reiss-Husson, F.; Rempp, P.; Luzzati, V. Quelques Exemples de Polymérisation En Phase Mésomorphe. *J. Polym. Sci. Part C Polym. Symp.* **2007**, *4* (2), 1275–1290. https://doi.org/10.1002/polc.5070040241.

(54) Ström, P.; Anderson, D. M. The Cubic Phase Region in the System Didodecyldimethylammonium Bromide-Water-Styrene. *Langmuir* **1992**, *8* (2), 691–709. https://doi.org/10.1021/la00038a065.

(55) Zhang, J.; Qiao, Z. A.; Mahurin, S. M.; Jiang, X.; Chai, S. H.; Lu, H.; Nelson, K.; Dai, S. Hypercrosslinked Phenolic Polymers with Well-Developed Mesoporous Frameworks. *Angew. Chemie - Int. Ed.* **2015**, *54* (15), 4582–4586. https://doi.org/10.1002/anie.201500305.

(56) Qavi, S.; Bandegi, A.; Firestone, M.; Foudazi, R. Polymerization in Soft Nanoconfinement of Lamellar and Reverse Hexagonal Mesophases. *Soft Matter* **2019**, *15* (41), 8238–8250. https://doi.org/10.1039/c9sm01565e.

(57) Friberg, S. E.; Thundathil, R.; Stoffer, J. O. Changed Lyotropic Liquid Crystalline Structure Due to Polymerization of the Amphiphilic Component. *Science (80-.).* **1979**, *205* (4406), 607–608. https://doi.org/10.1126/science.205.4406.607.

(58) Lee, Y. S.; Gleeson, J. T.; Yang, J. Z.; Sisson, T. M.; Frankel, D. A.; O'Brien, D. F.; Keller, S. L.; Aksay, E.; Gruner, S. M. Polymerization of Nonlamellar Lipid Assemblies. *J. Am. Chem. Soc.* **1995**, *117* (20), 5573–5578. https://doi.org/10.1021/ja00125a019.

(59) Young, C.-M.; Chang, C. L.; Chen, Y.-H.; Chen, C.-Y.; Chang, Y.-F.; Chen, H.-L. Dendrimer-Mediated Columnar Mesophase of Surfactants. *Soft Matter* **2021**, *17* (2), 397–409. https://doi.org/10.1039/D0SM01506G.

(60) Soberats, B.; Yoshio, M.; Ichikawa, T.; Zeng, X.; Ohno, H.; Ungar, G.; Kato, T. Ionic Switch Induced by a Rectangular–Hexagonal Phase Transition in Benzenammonium Columnar Liquid Crystals. *J. Am. Chem. Soc.* **2015**, *137* (41), 13212–13215. https://doi.org/10.1021/jacs.5b09076.

(61) Pindzola, B. A.; Jin, J.; Gin, D. L. Cross-Linked Normal Hexagonal and Bicontinuous Cubic Assemblies via Polymerizable Gemini Amphiphiles. *J. Am. Chem. Soc.* **2003**, *125* (10), 2940–2949. https://doi.org/10.1021/ja0208106.

(62) Qavi, S.; Firestone, M. A.; Foudazi, R. Elasticity and Yielding of Mesophases of Block Copolymers in Water-Oil Mixtures. *Soft Matter* **2019**, *15* (28), 5626–5637. https://doi.org/10.1039/c8sm02336k.

(63) Marquez Garcia, M. G. LYOTROPIC LIQUID CRYSTALS CONTAINING IONIC LIQUIDS FOR CO2 CAPTURE, New Mexico State University, 2020.

(64) Kim, S. A.; Jeong, K.-J.; Yethiraj, A.; Mahanthappa, M. K. Low-Symmetry Sphere Packings of Simple Surfactant Micelles Induced by Ionic Sphericity. *Proc. Natl. Acad. Sci.* **2017**, *114* (16), 4072–4077. https://doi.org/10.1073/pnas.1701608114.

(65) Frank, F. C.; Kasper, J. S. Complex Alloy Structures Regarded as Sphere Packings. I. Definitions and Basic Principles. *Acta Crystallogr.* **1958**, *11* (3), 184–190.

https://doi.org/10.1107/S0365110X58000487.

(66) Frank, F. C.; Kasper, J. S. Complex Alloy Structures Regarded as Sphere Packings. II. Analysis and Classification of Representative Structures. *Acta Crystallogr.* **1959**, *12* (7), 483–499. https://doi.org/10.1107/S0365110X59001499.

(67) Huang, M.; Yue, K.; Wang, J.; Hsu, C.-H.; Wang, L.; Cheng, S. Z. D. Frank-Kasper and Related Quasicrystal Spherical Phases in Macromolecules. *Sci. China Chem.* **2018**, *61* (1), 33–45. https://doi.org/10.1007/s11426-017-9140-8.

(68) Roux, D.; Coulon, C.; Cates, M. E. Sponge Phases in Surfactant Solutions. *J. Phys. Chem.* **1992**, *96* (11), 4174–4187. https://doi.org/10.1021/j100190a017.

(69) Angelov, B.; Angelova, A.; Mutafchieva, R.; Lesieur, S.; Vainio, U.; Garamus, V. M.; Jensen, G. V.; Pedersen, J. S. SAXS Investigation of a Cubic to a Sponge (L 3) Phase Transition in Self-Assembled Lipid Nanocarriers. *Phys. Chem. Chem. Phys.* **2011**, *13* (8), 3073–3081. https://doi.org/10.1039/C0CP01029D.

(70) Kent, B.; Garvey, C. J.; Cookson, D.; Bryant, G. The Inverse Hexagonal – Inverse Ribbon – Lamellar Gel Phase Transition Sequence in Low Hydration DOPC:DOPE Phospholipid Mixtures. *Chem. Phys. Lipids* **2009**, *157* (1), 56–60. https://doi.org/10.1016/j.chemphyslip.2008.10.003.

(71) Thundathil, R.; Stoffer, J. O.; Friberg, S. E. Polymerization in Lyotropic Liquid Crystals - 1. Change of Structure During Polymerization. *J. Polym. Sci. A1.* **1980**, *18* (8), 2629–2640. https://doi.org/10.1002/pol.1980.170180821.

(72) Shibasaki, Y.; Fukuda, K. Aggregation States and Polymerizabilities of Amphiphilic Monomer Molecules in Aqueous Systems with Different Water Contents. *Colloids and Surfaces* **1992**, *67* (C), 195–201. https://doi.org/10.1016/0166-6622(92)80298-G.

(73) McGrath, K. M.; Drummond, C. J. Polymerisation of Liquid Crystalline Phases in Binary Surfactant/Water Systems: Part 1. Allyldodecyldimethylammonium Bromide and Allyldidodecylmethylammonium Bromide. *Colloid Polym. Sci.* **1996**, *274* (4), 316–333. https://doi.org/10.1007/BF00654052.

(74) McGrath, K. M. Polymerisation of Liquid Crystalline Phases in Binary Surfactant/Water Systems. Part 3. Sodium 10-Undecenoate. *Colloid Polym. Sci.* **1996**, *274* (6), 499–512. https://doi.org/10.1007/BF00655224.

(75) McGrath, K. M. Polymerisation of Liquid Crystalline Phases in Binary Surfactant/Water Systems. Part 2. ω-Undecenyltrimethylammonium Bromide. *Colloid Polym. Sci.* **1996**, *274* (5), 399–409. https://doi.org/10.1007/BF00652461.

(76) Pawlowski, D.; Haibel, A.; Tieke, M. Γ-Ray Polymerization of Cationic Surfactant Methacrylates in Lyotropic Mesopnases. *Berichte der Bunsengesellschaft/Physical Chem. Chem. Phys.* **1998**, *102* (12), 1865–1869. https://doi.org/10.1002/bbpc.19981021217.

(77) Li, M.; Yang, W.; Chen, Z.; Qian, J.; Wang, C.; Fu, S. Phase Behavior and Polymerization of Lyotropic Phases. II. A Series of Polymerizable Amphiphiles with Systematically Varied Critical Packing Parameters. *J. Polym. Sci. Part A Polym. Chem.* **2006**, *44* (20), 5887–5897. https://doi.org/10.1002/pola.21573.

(78) Deng, H.; Gin, D. L.; Smith, R. C. Polymerizable Lyotropic Liquid Crystals Containing Transition-Metal and Lanthanide Ions: Architectural Control and Introduction of New Properties into Nanostructured Polymers. *J. Am. Chem. Soc.* **1998**, *120* (14), 3522–3523. https://doi.org/10.1021/ja9743654.

(79) Dwulet, G. E.; Gin, D. L. Ordered Nanoporous Lyotropic Liquid Crystal Polymer Resin for Heterogeneous Catalytic Aerobic Oxidation of Alcohols. *Chem. Commun.* **2018**, *54* (85),

12053–12056. https://doi.org/10.1039/c8cc05661g.

(80) Ringstrand, B. S.; Seifert, S.; Podlesak, D. W.; Firestone, M. A. Self-Assembly Directed Organization of Nanodiamond During Ionic Liquid Crystalline Polymer Formation. *Macromol. Rapid Commun.* **2016**, *37* (14), 1155–1167. https://doi.org/10.1002/marc.201600070.

(81) Peng, S.; Hartley, P. G.; Hughes, T. C.; Guo, Q. Enhancing Thermal Stability and Mechanical Properties of Lyotropic Liquid Crystals through Incorporation of a Polymerizable Surfactant. *Soft Matter* **2015**, *11* (31), 6318–6326. https://doi.org/10.1039/c5sm01646k.

(82) Srisiri, W.; Sisson, T. M.; O'Brien, D. F.; McGrath, K. M.; Han, Y.; Gruner, S. M. Polymerization of the Inverted Hexagonal Phase. *J. Am. Chem. Soc.* **1997**, *119* (21), 4866–4873. https://doi.org/10.1021/ja970052x.

(83) Reppy, M. A.; Gray, D. H.; Pindzola, B. A.; Smithers, J. L.; Gin, D. L. A New Family of Polymerizable Lyotropic Liquid Crystals: Control of Feature Size in Cross-Linked Inverted Hexagonal Assemblies via Monomer Structure. *J. Am. Chem. Soc.* **2001**, *123* (3), 363–371. https://doi.org/10.1021/ja002462i.

(84) Hoag, B. P.; Gin, D. L. Cross-Linkable Liquid Crystal Monomers Containing Hydrocarbon 1,3-Diene Tail Systems. *Macromolecules* **2000**, *33* (23), 8549–8558. https://doi.org/10.1021/ma000812f.

(85) Pindzola, B. A.; Hoag, B. P.; Gin, D. L. Polymerization of a Phosphonium Diene Amphiphile in the Regular Hexagonal Phase with Retention of Mesostructure. *J. Am. Chem. Soc.* **2001**, *123* (19), 4617–4618. https://doi.org/10.1021/ja0058583.

(86) Batra, D.; Hay, D. N. T.; Firestone, M. A. Formation of a Biomimetic, Liquid-Crystalline

Hydrogel by Self-Assembly and Polymerization of an Ionic Liquid. *Chem. Mater.* **2007**, *19* (18), 4423–4431. https://doi.org/10.1021/cm062992z.

(87) Batra, D.; Seifert, S.; Firestone, M. A. The Effect of Cation Structure on the Mesophase Architecture of Self-Assembled and Polymerized Imidazolium-Based Ionic Liquids. *Macromol. Chem. Phys.* **2007**, *208* (13), 1416–1427. https://doi.org/10.1002/macp.200700174.

(88) Grubjesic, S.; Seifert, S.; Firestone, M. A. Cytoskeleton Mimetic Reinforcement of a Self-Assembled N,N ′-Dialkylimidazolium Ionic Liquid Monomer by Copolymerization. *Macromolecules* **2009**, *42* (15), 5461–5470. https://doi.org/10.1021/ma900905k.

(89) Sievens-Figueroa, L.; Guymon, C. A. Cross-Linking of Reactive Lyotropic Liquid Crystals for Nanostrueture Retention. *Chem. Mater.* **2009**, *21* (6), 1060–1068. https://doi.org/10.1021/cm803383d.

(90) Becht, G. A.; Sofos, M.; Seifert, S.; Firestone, M. A. Formation of a Liquid-Crystalline Interpenetrating Poly(Ionic Liquid) Network Hydrogel. *Macromolecules* **2011**, *44* (6), 1421–1428. https://doi.org/10.1021/ma102146r.

(91) Ndefru, B. G.; Ringstrand, B. S.; Diouf, S. I. Y.; Seifert, S.; Leal, J. H.; Semelsberger, T. A.; Dreier, T. A.; Firestone, M. A. Multiscale Additive Manufacturing of Polymers Using 3D Photo-Printable Self-Assembling Ionic Liquid Monomers. *Mol. Syst. Des. Eng.* **2019**, *4* (3), 580–585. https://doi.org/10.1039/c8me00106e.

(92) Jin, J.; Nguyen, V.; Gu, W.; Lu, X.; Elliott, B. J.; Gin, D. L. Cross-Linked Lyotropic Liquid Crystal-Butyl Rubber Composites: Promising “Breathable” Barrier Materials for Chemical Protection Applications. *Chem. Mater.* **2005**, *17* (2), 224–226. https://doi.org/10.1021/cm040342u.

(93) Zhou, M.; Kidd, T. J.; Noble, R. D.; Gin, D. L. Supported Lyotropic Liquid-Crystal Polymer Membranes: Promising Materials for Molecular-Size-Selective Aqueous Nanofiltration. *Adv. Mater.* **2005**, *17* (15), 1850–1853. https://doi.org/10.1002/adma.200500444.

(94) Bara, J. E.; Kaminski, A. K.; Noble, R. D.; Gin, D. L. Influence of Nanostructure on Light Gas Separations in Cross-Linked Lyotropic Liquid Crystal Membranes. *J. Memb. Sci.* **2007**, *288* (1–2), 13–19. https://doi.org/10.1016/j.memsci.2006.09.023.

(95) Xu, Y.; Gu, W.; Gin, D. L. Heterogeneous Catalysis Using a Nanostructured Solid Acid Resin Based on Lyotropic Liquid Crystals. *J. Am. Chem. Soc.* **2004**, *126* (6), 1616–1617. https://doi.org/10.1021/ja038501i.

(96) Sievens-Figueroa, L.; Guymon, C. A. Polymerization Kinetics and Nanostructure Evolution of Reactive Lyotropic Liquid Crystals with Different Reactive Group Position. *Macromolecules* **2009**, *42* (23), 9243–9250. https://doi.org/10.1021/ma901318f.

(97) Lester, C. L.; Guymon, C. A. Ordering Effects on the Photopolymerization of a Lyotropic Liquid Crystal. *Polymer* **2002**, *43* (13), 3707–3715. https://doi.org/10.1016/S0032-3861(02)00188-X.

(98) Sievens-Figueroa, L.; Allan Guymon, C. Aliphatic Chain Length Effects on Photopolymerization Kinetics and Structural Evolution of Polymerizable Lyotropic Liquid Crystals. *Polymer* **2008**, *49* (9), 2260–2267. https://doi.org/10.1016/j.polymer.2008.02.047.

(99) DePierro, M. A.; Baguenard, C.; Allan Guymon, C. Radical Polymerization Behavior and Molecular Weight Development of Homologous Monoacrylate Monomers in Lyotropic Liquid Crystal Phases. *J. Polym. Sci. Part A Polym. Chem.* **2016**, *54* (1), 144–154. https://doi.org/10.1002/pola.27783.

(100) Gray, D. H.; Gin, D. L. Polymerizable Lyotropic Liquid Crystals Containing Transition-

Metal Ions as Building Blocks for Nanostructured Polymers and Composites. *Chem. Mater.* **1998**, *10* (7), 1827–1832. https://doi.org/10.1021/cm970830k.

(101) Hentze, H. P.; Krämer, E.; Berton, B.; Förster, S.; Antonietti, M.; Dreja, M. Lyotropic Mesophases of Poly(Ethylene Oxide)-O-Poly(Butadiene) Diblock Copolymers and Their Cross-Linking to Generate Ordered Gels. *Macromolecules* **1999**, *32* (18), 5803–5809. https://doi.org/10.1021/ma9904058.

(102) Yang, J.; Wegner, G. Polymerization in Lyotropic Liquid Crystals. 2. Synthesis of Photo-Cross-Linkable PEO-PDMS-PEO Triblock Copolymers and Permanent Stabilization of Their Supermolecular Structures in Lyotropic Mesophases. *Macromolecules* **1992**, *25* (6), 1791–1795. https://doi.org/10.1021/ma00032a027.

(103) Ringstrand, B.; Seifert, S.; Firestone, M. A. Preparation of a Solution-Processable, Nanostructured Ionic Polyacetylene. *J. Polym. Sci. Part B Polym. Phys.* **2013**, *51* (16), 1215–1227. https://doi.org/10.1002/polb.23321.

(104) Imai, M.; Sakai, K.; Kikuchi, M.; Nakaya, K.; Saeki, A.; Teramoto, T. Kinetic Pathway to Double-Gyroid Structure. *J. Chem. Phys.* **2005**, *122* (21), 214906. https://doi.org/10.1063/1.1905585.

(105) Grubjesic, S.; Lee, B.; Seifert, S.; Firestone, M. A. Preparation of a Self-Supporting Cell Architecture Mimic by Water Channel Confined Photocrosslinking within a Lamellar Structured Hydrogel. *Soft Matter* **2011**, *7* (20), 9695. https://doi.org/10.1039/c1sm06364b.

(106) Hartmann, P. C.; Sanderson, R. D. Templating Polymerization of Dodecylammonium Surfactants with Polymerizable (Meth)Acrylate Counter Ions. *Macromol. Symp.* **2005**, *225* (1), 229–237. https://doi.org/10.1002/masy.200550718.

(107) Wiesenauer, B. R.; Gin, D. L. Nanoporous Polymer Materials Based on Self-Organized,

Bicontinuous Cubic Lyotropic Liquid Crystal Assemblies and Their Applications. *Polym. J.* **2012**, *44* (6), 461–468. https://doi.org/10.1038/pj.2012.15.

(108) Srisiri, W.; Benedicto, A.; O'Brien, D. F.; Trouard, T. P.; Orädd, G.; Persson, S.; Lindblom, G. Stabilization of a Bicontinuous Cubic Phase from Polymerizable Monoacylglycerol and Diacylglycerol. *Langmuir* **1998**, *14* (7), 1921–1926. https://doi.org/10.1021/la970897m.

(109) Mueller, A.; O'Brien, D. F. Supramolecular Materials via Polymerization of Mesophases of Hydrated Amphiphiles. *Chem. Rev.* **2002**, *102* (3), 727–757. https://doi.org/10.1021/cr000071g.

(110) Yang, D.; O'Brien, D. F.; Marder, S. R. Polymerized Bicontinuous Cubic Nanoparticles (Cubosomes) from a Reactive Monoacylglycerol. *J. Am. Chem. Soc.* **2002**, *124* (45), 13388–13389. https://doi.org/10.1021/ja026085g.

(111) O'Brien, D. F.; Armitage, B.; Benedicto, A.; Bennett, D. E.; Lamparski, H. G.; Lee, Y. S.; Srisiri, W.; Sisson, T. M. Polymerization of Preformed Self-Organized Assemblies. *Acc. Chem. Res.* **1998**, *31* (12), 861–868. https://doi.org/10.1021/ar970140m.

(112) Dwulet, G. E.; Dischinger, S. M.; McGrath, M. J.; Basalla, A. J.; Malecha, J. J.; Noble, R. D.; Gin, D. L. Breathable, Polydopamine-Coated Nanoporous Membranes That Selectively Reject Nerve and Blister Agent Simulant Vapors. *Ind. Eng. Chem. Res.* **2019**, *58* (47), 21890–21893. https://doi.org/10.1021/acs.iecr.9b04738.

(113) McGrath, M. J.; Hardy, S. H.; Basalla, A. J.; Dwulet, G. E.; Manubay, B. C.; Malecha, J. J.; Shi, Z.; Funke, H. H.; Gin, D. L.; Noble, R. D. Polymerization of Counteranions in the Cationic Nanopores of a Cross-Linked Lyotropic Liquid Crystal Network to Modify Ion Transport Properties. *ACS Mater. Lett.* **2019**, *1* (4), 452–458. https://doi.org/10.1021/acsmaterialslett.9b00244.

(114) Dischinger, S. M.; Rosenblum, J.; Noble, R. D.; Gin, D. L. Evaluation of a Nanoporous Lyotropic Liquid Crystal Polymer Membrane for the Treatment of Hydraulic Fracturing Produced Water via Cross-Flow Filtration. *J. Memb. Sci.* **2019**, *592*, 117313. https://doi.org/10.1016/j.memsci.2019.117313.

(115) Lu, X.; Nguyen, V.; Zhou, M.; Zeng, X.; Jin, J.; Elliott, B. J.; Gin, D. L. Crosslinked Bicontinuous Cubic Lyotropic Liquid-Crystal/Butyl-Rubber Composites: Highly Selective, Breathable Barrier Materials for Chemical Agent Protection. *Adv. Mater.* **2006**, *18* (24), 3294–3298. https://doi.org/10.1002/adma.200601156.

(116) Kerr, R. L.; Miller, S. A.; Shoemaker, R. K.; Elliott, B. J.; Gin, D. L. New Type of Li Ion Conductor with 3D Interconnected Nanopores via Polymerization of a Liquid Organic Electrolyte-Filled Lyotropic Liquid-Crystal Assembly. *J. Am. Chem. Soc.* **2009**, *131* (44), 15972–15973. https://doi.org/10.1021/ja905208f.

(117) Liang, X.; Lu, X.; Yu, M.; Cavanagh, A. S.; Gin, D. L.; Weimer, A. W. Modification of Nanoporous Supported Lyotropic Liquid Crystal Polymer Membranes by Atomic Layer Deposition. *J. Memb. Sci.* **2010**, *349* (1–2), 1–5. https://doi.org/10.1016/j.memsci.2009.11.067.

(118) Hatakeyama, E. S.; Wiesenauer, B. R.; Gabriel, C. J.; Noble, R. D.; Gin, D. L. Nanoporous, Bicontinuous Cubic Lyotropic Liquid Crystal Networks via Polymerizable Gemini Ammonium Surfactants. *Chem. Mater.* **2010**, *22* (16), 4525–4527. https://doi.org/10.1021/cm1013027.

(119) Hatakeyama, E. S.; Gabriel, C. J.; Wiesenauer, B. R.; Lohr, J. L.; Zhou, M.; Noble, R. D.; Gin, D. L. Water Filtration Performance of a Lyotropic Liquid Crystal Polymer Membrane with Uniform, Sub-1-Nm Pores. *J. Memb. Sci.* **2011**, *366* (1–2), 62–72.

https://doi.org/10.1016/j.memsci.2010.09.028.

(120) Carter, B. M.; Wiesenauer, B. R.; Hatakeyama, E. S.; Barton, J. L.; Noble, R. D.; Gin, D. L. Glycerol-Based Bicontinuous Cubic Lyotropic Liquid Crystal Monomer System for the Fabrication of Thin-Film Membranes with Uniform Nanopores. *Chem. Mater.* **2012**, *24* (21), 4005–4007. https://doi.org/10.1021/cm302027s.

(121) Carter, B. M.; Wiesenauer, B. R.; Noble, R. D.; Gin, D. L. Thin-Film Composite Bicontinuous Cubic Lyotropic Liquid Crystal Polymer Membranes: Effects of Anion-Exchange on Water Filtration Performance. *J. Memb. Sci.* **2014**, *455*, 143–151. https://doi.org/10.1016/j.memsci.2013.12.056.

(122) Lester, C. L.; Guymon, C. A. Phase Behavior and Polymerization Kinetics of a Semifluorinated Lyotropic Liquid Crystal. *Macromolecules* **2000**, *33* (15), 5448–5454. https://doi.org/10.1021/ma000197f.

(123) Zhang, Y.; Dong, R.; Gabinet, U. R.; Poling-Skutvik, R.; Kim, N. K.; Lee, C.; Imran, O. Q.; Feng, X.; Osuji, C. O. Rapid Fabrication by Lyotropic Self-Assembly of Thin Nanofiltration Membranes with Uniform 1 Nanometer Pores. *ACS Nano* **2021**, acsnano.1c00722. https://doi.org/10.1021/acsnano.1c00722.

(124) McGrath, K. M.; Drummond, C. J. Polymerisation of Liquid Crystalline Phases in Binary Surfactant/Water Systems. Part 4. Dodecyldimethylammoniumethylmethacrylate Bromide. *Colloid Polym. Sci.* **1996**, *274* (7), 612–621. https://doi.org/10.1007/BF00653057.

(125) Zhang, Y.; Kim, D.; Dong, R.; Feng, X.; Osuji, C. O. Tunable Organic Solvent Nanofiltration in Self-Assembled Membranes at the Sub–1 Nm Scale. *Sci. Adv.* **2022**, *8* (11). https://doi.org/10.1126/sciadv.abm5899.

(126) Li, P.; Johnson, C.; Dyer, S. S.; Osuji, C. O.; Gin, D. L. A PH- and Light-Responsive

Nanoporous Lyotropic Gyroid Polymer Network. *Adv. Mater. Interfaces* **2022**, 2201761. https://doi.org/10.1002/admi.202201761.

(127) Imran, O. Q.; Li, P.; Kim, N. K.; Gin, D. L.; Osuji, C. O. Stable Cross-Linked Lyotropic Gyroid Mesophases from Single-Head/Single-Tail Cross-Linkable Monomers. *Chem. Commun.* **2021**, *57* (83), 10931–10934. https://doi.org/10.1039/D1CC04211D.

(128) Li, M. H.; Yang, W. L.; Qian, J.; Wang, C. C.; Fu, S. K. Polymerization of Lyotropic Phases: 1. Isotropic Fluid Phase of Two New Polymerizable Amphiphiles. *Des. Monomers Polym.* **2004**, *7* (6), 505–519. https://doi.org/10.1163/1568555042474077.

(129) Feng, X.; Tousley, M. E.; Cowan, M. G.; Wiesenauer, B. R.; Nejati, S.; Choo, Y.; Noble, R. D.; Elimelech, M.; Gin, D. L.; Osuji, C. O. Scalable Fabrication of Polymer Membranes with Vertically Aligned 1 Nm Pores by Magnetic Field Directed Self-Assembly. *ACS Nano* **2014**, *8* (12), 11977–11986. https://doi.org/10.1021/nn505037b.

(130) Bodkin, L. N.; Li, P.; Dyer, S. S.; Krajnak, Z. A.; Malecha, J. J.; Noble, R. D.; Gin, D. L. Improved Mechanical Compliance in Bicontinuous Cubic Lyotropic Membranes Based on a Cross-Linking Gemini Monomer via Copolymerization with a Non-Cross-Linkable Analog. *ACS Appl. Polym. Mater.* **2022**, *4* (11), 8026–8031. https://doi.org/10.1021/acsapm.2c01478.

(131) Burns, C. T.; Lee, S.; Seifert, S.; Firestone, M. A. Thiophene-Based Ionic Liquids: Synthesis, Physical Properties, Self-Assembly, and Oxidative Polymerization. *Polym. Adv. Technol.* **2008**, *19* (10), 1369–1382. https://doi.org/10.1002/pat.1200.

(132) Welch, P. M.; Dreier, T. A.; Magurudeniya, H. D.; Frith, M. G.; Ilavsky, J.; Seifert, S.; Rahman, A. K.; Rahman, A.; Singh, A. J.; Ringstrand, B. S.; Hanson, C. J.; Hollingsworth, J. A.; Firestone, M. A. 3D Volumetric Structural Hierarchy Induced by Colloidal

Polymerization of a Quantum-Dot Ionic Liquid Monomer Conjugate. *Macromolecules* **2020**, *53* (8), 2822–2833. https://doi.org/10.1021/acs.macromol.0c00011.

(133) Pecinovsky, C. S.; Hatakeyama, E. S.; Gin, D. L. Polymerizable Photochromic Macrocyclic Metallomesogens: Design of Supramolecular Polymers with Responsive Nanopores. *Adv. Mater.* **2008**, *20* (1), 174–178. https://doi.org/10.1002/adma.200702210.

(134) Zhou, W.; Gu, W.; Xu, Y.; Pecinovsky, C. S.; Gin, D. L. Assembly of Acidic Amphiphiles into Inverted Hexagonal Phases Using an L-Alanine-Based Surfactant as a Structure-Directing Agent. *Langmuir* **2003**, *19* (16), 6346–6348. https://doi.org/10.1021/la0341759.

(135) Pecinovsky, C. S.; Nicodemus, G. D.; Gin, D. L. Nanostructured, Solid-State Organic, Chiral Diels - Alder Catalysts via Acid-Induced Liquid Crystal Assembly. *Chem. Mater.* **2005**, *17* (20), 4889–4891. https://doi.org/10.1021/cm0514995.

(136) Antonietti, M.; Caruso, R. A.; Göltner, C. G.; Weissenberger, M. C. Morphology Variation of Porous Polymer Gels by Polymerization in Lyotropic Surfactant Phases. *Macromolecules* **1999**, *32* (5), 1383–1389. https://doi.org/10.1021/ma9812478.

(137) Zhang, J.; Xie, Z.; Hill, A. J.; She, F. H.; Thornton, A. W.; Hoang, M.; Kong, L. X. Structure Retention in Cross-Linked Poly(Ethylene Glycol) Diacrylate Hydrogel Templated from a Hexagonal Lyotropic Liquid Crystal by Controlling the Surface Tension. *Soft Matter* **2012**, *8* (7), 2087–2094. https://doi.org/10.1039/c1sm06526b.

(138) Zhang, J.; Xie, Z.; Hoang, M.; Hill, A. J.; Cong, W.; She, F. H.; Gao, W.; Kong, L. X. Retention of the Original LLC Structure in a Cross-Linked Poly(Ethylene Glycol) Diacrylate Hydrogel with Reinforcement from a Silica Network. *Soft Matter* **2014**, *10* (28), 5192–5200. https://doi.org/10.1039/c4sm00589a.

(139) Zhang, J.; Xie, Z.; Hill, A. J.; Cong, W.; She, F. H.; Gao, W.; Hoang, M.; Kong, L. X.

Effects of a Volatile Solvent with Low Surface Tension Combining with the Silica Network Reinforcement on Retention of LLC Structure in Polymer Matrix. *Polym. Bull.* **2018**, *75* (2), 581–595. https://doi.org/10.1007/s00289-017-2041-z.

(140) Clapper, J. D.; Guymon, C. A. Compatibilization of Immiscible Polymer Networks through Photopolymerization in a Lyotropic Liquid Crystal. *Adv. Mater.* **2006**, *18* (12), 1575–1580. https://doi.org/10.1002/adma.200502608.

(141) Tousley, M. E.; Feng, X.; Elimelech, M.; Osuji, C. O. Aligned Nanostructured Polymers by Magnetic-Field-Directed Self-Assembly of a Polymerizable Lyotropic Mesophase. *ACS Appl. Mater. Interfaces* **2014**, *6* (22), 19710–19717. https://doi.org/10.1021/am504730b.

(142) Qavi, S. RHEOLOGY, CHEMORHEOLOGY, AND MEMBRANE APPLICATION of AMPHIPHILIC BLOCK COPOLYMER/ WATER/OIL MESOPHASES, New Mexico State University, 2019.

(143) Liang, C.; Dai, S. Synthesis of Mesoporous Carbon Materials via Enhanced Hydrogen-Bonding Interaction. *J. Am. Chem. Soc.* **2006**, *128* (16), 5316–5317. https://doi.org/10.1021/ja060242k.

(144) Ghimbeu, C. M.; Sopronyi, M.; Sima, F.; Vaulot, C.; Vidal, L.; Le Meins, J. M.; Delmotte, L. "Light-Assisted Evaporation Induced Self-Assembly": An Efficient Approach toward Ordered Carbon Materials. *RSC Adv.* **2015**, *5* (4), 2861–2868. https://doi.org/10.1039/c4ra14246b.

(145) Herou, S.; Ribadeneyra, M. C.; Madhu, R.; Araullo-Peters, V.; Jensen, A.; Schlee, P.; Titirici, M. Ordered Mesoporous Carbons from Lignin: A New Class of Biobased Electrodes for Supercapacitors. *Green Chem.* **2019**, *21* (3), 550–559. https://doi.org/10.1039/c8gc03497d.

(146) Wang, X.; Liang, C.; Dai, S. Facile Synthesis of Ordered Mesoporous Carbons with High Thermal Stability by Self-Assembly of Resorcinol-Formaldehyde and Block Copolymers under Highly Acidic Conditions. *Langmuir* **2008**, *24* (14), 7500–7505. https://doi.org/10.1021/la800529v.

(147) Bandegi, A.; Bañuelos, J. L.; Foudazi, R. Formation of Ion Gels by Polymerization of Block Copolymer/Ionic Liquid/Oil Mesophases. *Soft Matter* **2020**, *16* (26), 6102–6114. https://doi.org/10.1039/D0SM00850H.

(148) Bandegi, A.; Kim, K.; Foudazi, R. Ion Transport in Polymerized Lyotropic Liquid Crystals Containing Ionic Liquid. *J. Polym. Sci.* **2021**, *59* (20), 2334–2344. https://doi.org/10.1002/pol.20210440.

(149) Clapper, J. D.; Guymon, C. A. Nanostructured Biodegradable Polymer Composites Generated Using Lyotropic Liquid Crystalline Media. *Macromolecules* **2007**, *40* (22), 7951–7959. https://doi.org/10.1021/ma071070u.

(150) Clapper, J. D.; Iverson, S. L.; Guymon, C. A. Nanostructured Biodegradable Polymer Networks Using Lyotropic Liquid Crystalline Templates. *Biomacromolecules* **2007**, *8* (7), 2104–2111. https://doi.org/10.1021/bm070167l.

(151) Anderson, D. M.; Ström, P. Polymerization of Lyotropic Liquid Crystals; ACS Symposium Series, 1989; pp 204–224. https://doi.org/10.1021/bk-1989-0384.ch013.

(152) Jung, M.; German, A. L.; Fischer, H. R. Polymerisation in Lyotropic Liquid-Crystalline Phases of Dioctadecyldimethylammonium Bromide. *Colloid Polym. Sci.* **2001**, *279* (2), 105–113. https://doi.org/10.1007/s003960000382.

(153) Anderson, D. M.; Ström, P. Polymerized Lyotropic Liquid Crystals as Contact Lens Materials. *Phys. A Stat. Mech. its Appl.* **1991**, *176* (1), 151–167.

https://doi.org/10.1016/0378-4371(91)90438-I.

(154) Laversanne, R. Polymerization of Acrylamide in Lamellar, Hexagonal, and Cubic Lyotropic Phases. *Macromolecules* **1992**, *25* (1), 489–491. https://doi.org/10.1021/ma00027a077.

(155) Forney, B. S.; Allan Guymon, C. Fast Deswelling Kinetics of Nanostructured Poly(N-Isopropylacrylamide) Photopolymerized in a Lyotropic Liquid Crystal Template. *Macromol. Rapid Commun.* **2011**, *32* (9–10), 765–769. https://doi.org/10.1002/marc.201100046.

(156) DePierro, M. A.; Guymon, C. A. Photoinitiation and Monomer Segregation Behavior in Polymerization of Lyotropic Liquid Crystalline Systems. *Macromolecules* **2006**, *39* (2), 617–626. https://doi.org/10.1021/ma0518196.

(157) Forney, B. S.; Guymon, C. A. Nanostructure Evolution during Photopolymerization in Lyotropic Liquid Crystal Templates. *Macromolecules* **2010**, *43* (20), 8502–8510. https://doi.org/10.1021/ma101418e.

(158) Hentze, H. P.; Göltner, C. G.; Antonietti, M. Synthesis of Organic Polymer Gels in Microemulsions and Lyotropic Mesophases. *Berichte der Bunsengesellschaft/Physical Chem. Chem. Phys.* **1997**, *101* (11), 1699–1702. https://doi.org/10.1002/bbpc.19971011130.

(159) DePierro, M. A.; Carpenter, K. G.; Guymon, C. A. Nanostructure Development of Polymers Templated from Lyotropic Liquid Crystals. *Radtech Tech. Proc.* **2006**.

(160) Meier, W. Polymer Networks with Lamellar Structure. *Macromolecules* **1998**, *31* (7), 2212–2217. https://doi.org/10.1021/ma971728b.

(161) Antonietti, M.; Göltner, C.; Hentze, H. P. Polymer Gels with a Micron-Sized, Layer-like Architecture by Polymerization in Lyotropic Cocogem Phases. *Langmuir* **1998**, *14* (10),

2670–2672. https://doi.org/10.1021/la971054y.

(162) Lester, C. L.; Smith, S. M.; Guymon, C. A. Acceleration of Polyacrylamide Photopolymerization Using Lyotropic Liquid Crystals. *Macromolecules* **2001**, *34* (25), 8587–8589. https://doi.org/10.1021/ma011314p.

(163) Hulvat, J. F.; Stupp, S. I. Liquid-Crystal Templating of Conducting Polymers. *Angew. Chemie - Int. Ed.* **2003**, *42* (7), 778–781. https://doi.org/10.1002/anie.200390206.

(164) Hulvat, J. F.; Stupp, S. I. Anisotropic Properties of Conducting Polymers Prepared by Liquid Crystal Templating. *Adv. Mater.* **2004**, *16* (7), 589–592. https://doi.org/10.1002/adma.200306263.

(165) Ghosh, S.; Remita, H.; Ramos, L.; Dazzi, A.; Deniset-Besseau, A.; Beaunier, P.; Goubard, F.; Aubert, P.-H.; Brisset, F.; Remita, S. PEDOT Nanostructures Synthesized in Hexagonal Mesophases. *New J. Chem.* **2014**, *38* (3), 1106–1115. https://doi.org/10.1039/C3NJ01349A.

(166) Wadekar, M. N.; Pasricha, R.; Gaikwad, A. B.; Kumaraswamy, G. Polymerization in Surfactant Liquid Crystalline Phases. *Chem. Mater.* **2005**, *17* (9), 2460–2465. https://doi.org/10.1021/cm048240r.

(167) DePierro, M. A.; Olson, A. J.; Guymon, C. A. Effect of Photoinitiator Solubility on Polymerization in Lyotropic Liquid Crystalline Media. *Radtech Tech. Proc.* **2004**.

(168) Depierro, M. A.; Guymon, C. A. Polymer Structure Development in Lyotropic Liquid Crystalline Solutions. *Macromolecules* **2014**, *47* (16), 5728–5738. https://doi.org/10.1021/ma500823q.

(169) Clapper, J. D.; Allan Guymon, C. Physical Behavior of Cross-Linked PEG Hydrogels Photopolymerized within Nanostructured Lyotropic Liquid Crystalline Templates. *Macromolecules* **2007**, *40* (4), 1101–1107. https://doi.org/10.1021/ma0622377.

(170) Li, Z.; Yan, W.; Dai, S. A Novel Vesicular Carbon Synthesized Using Amphiphilic Carbonaceous Material and Micelle Templating Approach. *Carbon N. Y.* **2004**, *42* (4), 767–770. https://doi.org/10.1016/j.carbon.2004.01.044.

(171) Liu, D. Y.; Krogstad, D. V. Self-Assembly and Phase Transformation of Block Copolymer Nanostructures in Ionic Liquid-Cured Epoxy. *Macromolecules* **2021**, *54* (2), 988–994. https://doi.org/10.1021/acs.macromol.0c02214.

(172) Ghosh, S.; Ramos, L.; Remita, S.; Dazzi, A.; Deniset-Besseau, A.; Beaunier, P.; Goubard, F.; Aubert, P.-H.; Remita, H. Conducting Polymer Nanofibers with Controlled Diameters Synthesized in Hexagonal Mesophases. *New J. Chem.* **2015**, *39* (11), 8311–8320. https://doi.org/10.1039/C5NJ00826C.

(173) Floresyona, D.; Goubard, F.; Aubert, P.-H.; Lampre, I.; Mathurin, J.; Dazzi, A.; Ghosh, S.; Beaunier, P.; Brisset, F.; Remita, S.; Ramos, L.; Remita, H. Highly Active Poly(3-Hexylthiophene) Nanostructures for Photocatalysis under Solar Light. *Appl. Catal. B Environ.* **2017**, *209*, 23–32. https://doi.org/10.1016/j.apcatb.2017.02.069.

(174) Dutt, S.; Siril, P. F. Morphology Controlled Synthesis of Polyaniline Nanostructures Using Swollen Liquid Crystal Templates. *J. Appl. Polym. Sci.* **2014**, *131* (18), 40800. https://doi.org/10.1002/app.40800.

(175) Castellano, J. A. Surface Anchoring of Liquid Crystal Molecules on Various Substrates. *Mol. Cryst. Liq. Cryst.* **1983**, *94* (1–2), 33–41. https://doi.org/10.1080/00268948308084245.

(176) Feng, X.; Nejati, S.; Cowan, M. G.; Tousley, M. E.; Wiesenauer, B. R.; Noble, R. D.; Elimelech, M.; Gin, D. L.; Osuji, C. O. Thin Polymer Films with Continuous Vertically Aligned 1 Nm Pores Fabricated by Soft Confinement. *ACS Nano* **2016**, *10* (1), 150–158.

https://doi.org/10.1021/acsnano.5b06130.

(177) Guo, Y.; Shahsavan, H.; Davidson, Z. S.; Sitti, M. Precise Control of Lyotropic Chromonic Liquid Crystal Alignment through Surface Topography. *ACS Appl. Mater. Interfaces* **2019**, *11* (39), 36110–36117. https://doi.org/10.1021/acsami.9b12943.

(178) Qavi, S.; Foudazi, R. Rheological Characteristics of Mesophases of Block Copolymer Solutions. *Rheol. Acta* **2019**, *58* (8), 483–498. https://doi.org/10.1007/s00397-019-01162-y.

(179) Yue, K.; Liu, C.; Guo, K.; Wu, K.; Dong, X.-H.; Liu, H.; Huang, M.; Wesdemiotis, C.; Cheng, S. Z. D.; Zhang, W.-B. Exploring Shape Amphiphiles beyond Giant Surfactants: Molecular Design and Click Synthesis. *Polym. Chem.* **2013**, *4* (4), 1056–1067. https://doi.org/10.1039/C2PY20881D.

(180) Yu, X.; Li, Y.; Dong, X.-H.; Yue, K.; Lin, Z.; Feng, X.; Huang, M.; Zhang, W.-B.; Cheng, S. Z. D. Giant Surfactants Based on Molecular Nanoparticles: Precise Synthesis and Solution Self-Assembly. *J. Polym. Sci. Part B Polym. Phys.* **2014**, *52* (20), 1309–1325. https://doi.org/10.1002/polb.23571.

(181) Reynhout, I. C.; Cornelissen, J. J. L. M.; Nolte, R. J. M. Synthesis of Polymer−Biohybrids: From Small to Giant Surfactants. *Acc. Chem. Res.* **2009**, *42* (6), 681–692. https://doi.org/10.1021/ar800143a.

(182) Yu, X.; Yue, K.; Hsieh, I.-F.; Li, Y.; Dong, X.-H.; Liu, C.; Xin, Y.; Wang, H.-F.; Shi, A.-C.; Newkome, G. R.; Ho, R.-M.; Chen, E.-Q.; Zhang, W.-B.; Cheng, S. Z. D. Giant Surfactants Provide a Versatile Platform for Sub-10-Nm Nanostructure Engineering. *Proc. Natl. Acad. Sci.* **2013**, *110* (25), 10078–10083. https://doi.org/10.1073/pnas.1302606110.

(183) Yoon, W.-J.; Lee, K. M.; Evans, D. R.; McConney, M. E.; Kim, D.-Y.; Jeong, K.-U. Giant

Surfactants for the Construction of Automatic Liquid Crystal Alignment Layers. *J. Mater. Chem. C* **2019**, *7* (28), 8500–8514. https://doi.org/10.1039/C9TC00422J.

(184) Angelov, B.; Angelova, A.; Ollivon, M.; Bourgaux, C.; Campitelli, A. Diamond-Type Lipid Cubic Phase with Large Water Channels. *J. Am. Chem. Soc.* **2003**, *125* (24), 7188–7189. https://doi.org/10.1021/ja034578v.

(185) Barriga, H. M. G.; Tyler, A. I. I.; McCarthy, N. L. C.; Parsons, E. S.; Ces, O.; Law, R. V.; Seddon, J. M.; Brooks, N. J. Temperature and Pressure Tuneable Swollen Bicontinuous Cubic Phases Approaching Nature's Length Scales. *Soft Matter* **2015**, *11* (3), 600–607. https://doi.org/10.1039/C4SM02343A.

(186) Tyler, A. I. I.; Barriga, H. M. G.; Parsons, E. S.; McCarthy, N. L. C.; Ces, O.; Law, R. V.; Seddon, J. M.; Brooks, N. J. Electrostatic Swelling of Bicontinuous Cubic Lipid Phases. *Soft Matter* **2015**, *11* (16), 3279–3286. https://doi.org/10.1039/C5SM00311C.

(187) Bruinsma, R. Elasticity and Excitations of Minimal Crystals. *J. Phys. II* **1992**, *2* (3), 425–451. https://doi.org/10.1051/jp2:1992142.

(188) Kim, H.; Song, Z.; Leal, C. Super-Swelled Lyotropic Single Crystals. *Proc. Natl. Acad. Sci.* **2017**, *114* (41), 10834–10839. https://doi.org/10.1073/pnas.1710774114.

(189) Leung, S. S. W.; Leal, C. The Stabilization of Primitive Bicontinuous Cubic Phases with Tunable Swelling over a Wide Composition Range. *Soft Matter* **2019**, *15* (6), 1269–1277. https://doi.org/10.1039/C8SM02059K.

(190) Zabara, A.; Chong, J. T. Y.; Martiel, I.; Stark, L.; Cromer, B. A.; Speziale, C.; Drummond, C. J.; Mezzenga, R. Design of Ultra-Swollen Lipidic Mesophases for the Crystallization of Membrane Proteins with Large Extracellular Domains. *Nat. Commun.* **2018**, *9* (1), 544. https://doi.org/10.1038/s41467-018-02996-5.

(191) Chen, C.; Wang, S.; Grady, B. P.; Harwell, J. H.; Shiau, B.-J. Oil-Induced Viscoelasticity in Micellar Solutions of Alkoxy Sulfate. *Langmuir* **2019**, *35* (37), 12168–12179. https://doi.org/10.1021/acs.langmuir.9b01969.

(192) Choi, J.-Y.; Yun, T.; Kwak, S.-Y. Two-Step Thermoresponsive Membrane with Tunable Separation Properties and Improved Cleaning Efficiency. *J. Memb. Sci.* **2018**, *554*, 117–124. https://doi.org/10.1016/j.memsci.2018.02.060.

(193) Simone, P. M.; Lodge, T. P. Lyotropic Phase Behavior of Polybutadiene-Poly (Ethylene Oxide) Diblock Copolymers in Ionic Liquids. *Macromolecules* **2008**, *41* (5), 1753–1759. https://doi.org/10.1021/ma702252v.

(194) Panday, A.; Mullin, S.; Gomez, E. D.; Wanakule, N.; Chen, V. L.; Hexemer, A.; Pople, J.; Balsara, N. P. Effect of Molecular Weight and Salt Concentration on Conductivity of Block Copolymer Electrolytes. *Macromolecules* **2009**, *42* (13), 4632–4637. https://doi.org/10.1021/ma900451e.

(195) Wanakule, N. S.; Panday, A.; Mullin, S. A.; Gann, E.; Hexemer, A.; Balsara, N. P. Ionic Conductivity of Block Copolymer Electrolytes in the Vicinity of Order-Disorder and Order-Order Transitions. *Macromolecules* **2009**, *42* (15), 5642–5651. https://doi.org/10.1021/ma900401a.

(196) Singh, M.; Odusanya, O.; Wilmes, G. M.; Eitouni, H. B.; Gomez, E. D.; Patel, A. J.; Chen, V. L.; Park, M. J.; Fragouli, P.; Iatrou, H.; Hadjichristidis, N.; Cookson, D.; Balsara, N. P. Effect of Molecular Weight on the Mechanical and Electrical Properties of Block Copolymer Electrolytes. *Macromolecules* **2007**, *40* (13), 4578–4585. https://doi.org/10.1021/ma0629541.

(197) Hoarfrost, M. L.; Tyagi, M. S.; Segalman, R. A.; Reimer, J. A. Effect of Confinement on

Proton Transport Mechanisms in Block Copolymer/Ionic Liquid Membranes. *Macromolecules* **2012**, *45* (7), 3112–3120. https://doi.org/10.1021/ma202741g.

(198) Virgili, J. M.; Hoarfrost, M. L.; Segalman, R. A. Effect of an Ionic Liquid Solvent on the Phase Behavior of Block Copolymers. *Macromolecules* **2010**, *43* (12), 5417–5423. https://doi.org/10.1021/ma902804e.

(199) Young, W.-S.; Kuan, W.-F.; Epps, T. H. Block Copolymer Electrolytes for Rechargeable Lithium Batteries. *J. Polym. Sci. Part B Polym. Phys.* **2014**, *52* (1), 1–16. https://doi.org/10.1002/polb.23404.

(200) Ghosh, S.; Ramos, L.; Remita, H. Swollen Hexagonal Liquid Crystals as Smart Nanoreactors: Implementation in Materials Chemistry for Energy Applications. *Nanoscale* **2018**, *10* (13), 5793–5819. https://doi.org/10.1039/C7NR08457A.

(201) Fan, X.; Zhang, Z.; Li, G.; Rowson, N. A. Attachment of Solid Particles to Air Bubbles in Surfactant-Free Aqueous Solutions. *Chem. Eng. Sci.* **2004**, *59* (13), 2639–2645. https://doi.org/10.1016/j.ces.2004.04.001.

(202) Thomas, A.; Goettmann, F.; Antonietti, M. Hard Templates for Soft Materials: Creating Nanostructured Organic Materials †. *Chem. Mater.* **2008**, *20* (3), 738–755. https://doi.org/10.1021/cm702126j.

(203) Wang, X.; Lin, K. S. K.; Chan, J. C. C.; Cheng, S. Direct Synthesis and Catalytic Applications of Ordered Large Pore Aminopropyl-Functionalized SBA-15 Mesoporous Materials. *J. Phys. Chem. B* **2005**, *109* (5), 1763–1769. https://doi.org/10.1021/jp045798d.

(204) Zhao, X. S.; Lu, G. Q. (Max); Millar, G. J. Advances in Mesoporous Molecular Sieve MCM-41. *Ind. Eng. Chem. Res.* **1996**, *35* (7), 2075–2090. https://doi.org/10.1021/ie950702a.

(205) da Silva, F. das C. M.; Costa, M. J. dos S.; da Silva, L. K. R.; Batista, A. M.; da Luz, G. E. Functionalization Methods of SBA-15 Mesoporous Molecular Sieve: A Brief Overview. *SN Appl. Sci.* **2019**, *1* (6), 654. https://doi.org/10.1007/s42452-019-0677-z.

(206) Ding, J. H.; Gin, D. L. Catalytic Pd Nanoparticles Synthesized Using a Lyotropic Liquid Crystal Polymer Template. *Chem. Mater.* **2000**, *12* (1), 22–24. https://doi.org/10.1021/cm990603d.

(207) Alexandridis, P.; Olsson, U.; Lindman, B. Self-Assembly of Amphiphilic Block Copolymers: The (EO)13(PO)30(EO)13-Water-p-Xylene System. *Macromolecules* **1995**, *28* (23), 7700–7710. https://doi.org/10.1021/ma00127a016.

(208) Alexandridis, P.; Olsson, U.; Lindman, B. Phase Behavior of Amphiphilic Block Copolymers in Water−Oil Mixtures: The Pluronic 25R4−Water− p -Xylene System. *J. Phys. Chem.* **1996**, *100* (1), 280–288. https://doi.org/10.1021/jp951626s.

(209) Holmqvist, P.; Alexandridis, P.; Lindman, B. Modification of the Microstructure in Poloxamer Block Copolymer−Water−"Oil" Systems by Varying the "Oil" Type. *Macromolecules* **1997**, *30* (22), 6788–6797. https://doi.org/10.1021/ma970625q.

(210) Alexandridis, P.; Olsson, U.; Lindman, B. A Record Nine Different Phases (Four Cubic, Two Hexagonal, and One Lamellar Lyotropic Liquid Crystalline and Two Micellar Solutions) in a Ternary Isothermal System of an Amphiphilic Block Copolymer and Selective Solvents (Water and Oil). *Langmuir* **1998**, *14* (10), 2627–2638. https://doi.org/10.1021/la971117c.

(211) Holmqvist, P.; Alexandridis, P.; Lindman, B. Modification of the Microstructure in Block Copolymer−Water−"Oil" Systems by Varying the Copolymer Composition and the "Oil" Type: Small-Angle X-Ray Scattering and Deuterium-NMR Investigation. *J. Phys. Chem. B*

1998, *102* (7), 1149–1158. https://doi.org/10.1021/jp9730297.

(212) Bodratti, A.; Alexandridis, P. Formulation of Poloxamers for Drug Delivery. *J. Funct. Biomater.* **2018**, *9* (1), 11. https://doi.org/10.3390/jfb9010011.

(213) Sinha, M. K.; Purkait, M. K. Preparation and Characterization of Novel Pegylated Hydrophilic PH Responsive Polysulfone Ultrafiltration Membrane. *J. Memb. Sci.* **2014**. https://doi.org/10.1016/j.memsci.2014.03.067.

(214) Capek, I. Inverse Emulsion Polymerization of Acrylamide Initiated by Oil- and Water-Soluble Initiators: Effect of Emulsifier Concentration. *Polym. J.* **2004**, *36* (10), 793–803. https://doi.org/10.1295/polymj.36.793.

(215) Alexandridis, P.; Olsson, U.; Lindman, B. Self-Assembly of Amphiphilic Block Copolymers: The (EO)13(PO)30(EO)13-Water-p-Xylene System. *Macromolecules* **1995**, *28* (23), 7700–7710. https://doi.org/10.1021/ma00127a016.

(216) Odian, G. Chain Copolymerization. In *Principles of Polymerization*; John Wiley & Sons, Inc.: Hoboken, NJ, USA, 2004. https://doi.org/10.1002/047147875X.ch6.

(217) Foudazi, R.; Gokun, P.; Feke, D. L.; Rowan, S. J.; Manas-Zloczower, I. Chemorheology of Poly(High Internal Phase Emulsions). *Macromolecules* **2013**, *46* (13), 5393–5396. https://doi.org/10.1021/ma401157b.

(218) Mortensen, K.; Brown, W.; Jørgensen, E. Lamellar Mesophase of Polyethylene Oxide)-Poly(Propylene Oxide)-Poly(Ethylene Oxide) Melts and Water-Swollen Mixtures. *Macromolecules* **1995**, *28* (5), 1458–1463. https://doi.org/10.1021/ma00109a016.

(219) Seo, M.; Hillmyer, M. A. Reticulated Nanoporous Polymers by Controlled Polymerization-Induced Microphase Separation. *Science (80-.).* **2012**, *336* (6087), 1422–1425. https://doi.org/10.1126/science.1221383.

(220) Sanz, B.; Ballard, N.; Asua, J. M.; Mijangos, C. Effect of Confinement on the Synthesis of PMMA in AAO Templates and Modeling of Free Radical Polymerization. *Macromolecules* **2017**, *50* (3), 811–821. https://doi.org/10.1021/acs.macromol.6b02282.

(221) Achilias, D. S. Investigation of the Radical Polymerization Kinetics Using DSC and Mechanistic or Isoconversional Methods. *J. Therm. Anal. Calorim.* **2014**, *116* (3), 1379–1386. https://doi.org/10.1007/s10973-013-3633-y.

(222) Zhao, H.; Simon, S. L. Methyl Methacrylate Polymerization in Nanoporous Confinement. *Polymer* **2011**, *52* (18), 4093–4098. https://doi.org/10.1016/j.polymer.2011.06.048.

(223) Strachota, B.; Matějka, L.; Sikora, A.; Spěváček, J.; Konefał, R.; Zhigunov, A.; Šlouf, M. Insight into the Cryopolymerization to Form a Poly(N-Isopropylacrylamide)/Clay Macroporous Gel: Structure and Phase Evolution. *Soft Matter* **2017**, *13* (6), 1244–1256. https://doi.org/10.1039/C6SM02278B.

(224) A., C.; K., S.; A., S.-M. J. F.; Q., W.; D., P. J. A.; J., M.-M. On the Stability and Chemorheology of a Urea Choline Chloride Deep-Eutectic Solvent as an Internal Phase in Acrylic High Internal Phase Emulsions. *RSC Adv.* **2016**, *6* (85), 81694–81702. https://doi.org/10.1039/C6RA18931H.

(225) Di Biase, M.; de Leonardis, P.; Castelletto, V.; Hamley, I. W.; Derby, B.; Tirelli, N. Photopolymerization of Pluronic F127 Diacrylate: A Colloid-Templated Polymerization. *Soft Matter* **2011**, *7* (10), 4928. https://doi.org/10.1039/c1sm05095h.

(226) Chow, A. W.; Sandell, J. F.; Wolfe, J. F. Reaction Kinetics and Chemo-Rheology of Poly(p-Phenylenebenzobisthiazole) Polymerization in the Ordered Phase. *Polymer* **1988**, *29* (7), 1307–1312. https://doi.org/10.1016/0032-3861(88)90061-4.

(227) Chow, A. W.; Hamlin, R. D.; Sandell, J. F.; Wolfe, J. F. Mesophase-Enhanced

Polymerization and Chemo-Rheology of Poly(p-Phenylenebenzobisthiazole). *MRS Proc.* **1988**, *134*, 95. https://doi.org/10.1557/PROC-134-95.

(228) Thickett, S. C.; Gilbert, R. G. Emulsion Polymerization: State of the Art in Kinetics and Mechanisms. *Polymer* **2007**, *48* (24), 6965–6991. https://doi.org/10.1016/j.polymer.2007.09.031.

(229) Maxwell, I. A.; Morrison, B. R.; Napper, D. H.; Gilbert, R. G. Entry of Free Radicals into Latex Particles in Emulsion Polymerization. *Macromolecules* **1991**, *24* (7), 1629–1640. https://doi.org/10.1021/ma00007a028.

(230) Xu, X.-H.; Li, Y.-X.; Zhou, L.; Liu, N.; Wu, Z.-Q. Precise Fabrication of Porous Polymer Frameworks Using Rigid Polyisocyanides as Building Blocks: From Structural Regulation to Efficient Iodine Capture. *Chem. Sci.* **2022**, *13* (4), 1111–1118. https://doi.org/10.1039/D1SC05361B.

(231) Baker, R. W. *Membrane Technology and Applications*; John Wiley & Sons, Ltd: Chichester, UK, 2012. https://doi.org/10.1002/9781118359686.

(232) Rektor, A.; Vatai, G. Membrane Filtration of Mozzarella Whey. *Desalination* **2004**, *162*, 279–286. https://doi.org/10.1016/S0011-9164(04)00052-9.

(233) Cassano, A.; Marchio, M.; Drioli, E. Clarification of Blood Orange Juice by Ultrafiltration: Analyses of Operating Parameters, Membrane Fouling and Juice Quality. *Desalination* **2007**, *212* (1–3), 15–27. https://doi.org/10.1016/j.desal.2006.08.013.

(234) Li, Q.; Bi, Q.; Lin, H.-H.; Bian, L.-X.; Wang, X.-L. A Novel Ultrafiltration (UF) Membrane with Controllable Selectivity for Protein Separation. *J. Memb. Sci.* **2013**, *427*, 155–167. https://doi.org/10.1016/j.memsci.2012.09.010.

(235) Zhao, X.; Su, Y.; Chen, W.; Peng, J.; Jiang, Z. PH-Responsive and Fouling-Release

Properties of PES Ultrafiltration Membranes Modified by Multi-Functional Block-like Copolymers. *J. Memb. Sci.* **2011**, *382* (1–2), 222–230. https://doi.org/10.1016/j.memsci.2011.08.014.

(236) Sinha, M. K.; Purkait, M. K. Preparation of a Novel Thermo Responsive PSF Membrane, with Cross Linked PVCL-Co-PSF Copolymer for Protein Separation and Easy Cleaning. *RSC Adv.* **2015**, *5* (29), 22609–22619. https://doi.org/10.1039/C4RA13863E.

(237) Fu, J.; Wang, X.; Ma, Z.; Wenming, H.; Li, J.; Wang, Z.; Wang, L. Photocatalytic Ultrafiltration Membranes Based on Visible Light Responsive Photocatalyst: A Review. *Desalin. WATER Treat.* **2019**, *168*, 42–55. https://doi.org/10.5004/dwt.2019.24403.

(238) Xiang, T.; Lu, T.; Zhao, W.-F.; Zhao, C.-S. Ionic Strength- and Thermo-Responsive Polyethersulfone Composite Membranes with Enhanced Antifouling Properties. *New J. Chem.* **2018**, *42* (7), 5323–5333. https://doi.org/10.1039/C8NJ00039E.

(239) Darvishmanesh, S.; Qian, X.; Wickramasinghe, S. R. Responsive Membranes for Advanced Separations. *Curr. Opin. Chem. Eng.* **2015**, *8*, 98–104. https://doi.org/10.1016/j.coche.2015.04.002.

(240) Roy, D.; Brooks, W. L. A.; Sumerlin, B. S. New Directions in Thermoresponsive Polymers. *Chem. Soc. Rev.* **2013**, *42* (17), 7214. https://doi.org/10.1039/c3cs35499g.

(241) Yu, J.-Z.; Zhu, L.-P.; Zhu, B.-K.; Xu, Y.-Y. Poly(N-Isopropylacrylamide) Grafted Poly(Vinylidene Fluoride) Copolymers for Temperature-Sensitive Membranes. *J. Memb. Sci.* **2011**, *366* (1–2), 176–183. https://doi.org/10.1016/j.memsci.2010.09.055.

(242) Chen, X.; Bi, S.; Shi, C.; He, Y.; Zhao, L.; Chen, L. Temperature-Sensitive Membranes Prepared from Blends of Poly(Vinylidene Fluoride) and Poly(N-Isopropylacrylamides) Microgels. *Colloid Polym. Sci.* **2013**, *291* (10), 2419–2428. https://doi.org/10.1007/s00396-

013-2985-y.

(243) Kahrs, C.; Schwellenbach, J. Membrane Formation via Non-Solvent Induced Phase Separation Using Sustainable Solvents: A Comparative Study. *Polymer* **2020**, *186*, 122071. https://doi.org/10.1016/j.polymer.2019.122071.

(244) Saadat, Y.; Imran, O. Q.; Osuji, C. O.; Foudazi, R. Lyotropic Liquid Crystals as Templates for Advanced Materials. *J. Mater. Chem. A* **2021**, *9* (38), 21607–21658. https://doi.org/10.1039/D1TA02748D.

(245) Saadat, Y.; Kim, K.; Foudazi, R. Initiator-Dependent Kinetics of Lyotropic Liquid Crystal-Templated Thermal Polymerization. *Polym. Chem.* **2021**, *12* (15), 2236–2252. https://doi.org/10.1039/D1PY00127B.

(246) Chatterjee, S.; Hui, P. C.; Wat, E.; Kan, C.; Leung, P.-C.; Wang, W. Drug Delivery System of Dual-Responsive PF127 Hydrogel with Polysaccharide-Based Nano-Conjugate for Textile-Based Transdermal Therapy. *Carbohydr. Polym.* **2020**, *236*, 116074. https://doi.org/10.1016/j.carbpol.2020.116074.

(247) CHATTERJEE, S.; Chi-leung HUI, P. Review of Stimuli-Responsive Polymers in Drug Delivery and Textile Application. *Molecules* **2019**, *24* (14), 2547. https://doi.org/10.3390/molecules24142547.

(248) Chatterjee, S.; Hui, P. C.; Kan, C.; Wang, W. Dual-Responsive (PH/Temperature) Pluronic F-127 Hydrogel Drug Delivery System for Textile-Based Transdermal Therapy. *Sci. Rep.* **2019**, *9* (1), 11658. https://doi.org/10.1038/s41598-019-48254-6.

(249) Thakral, S.; Kim, K. Small-Angle Scattering for Characterization of Pharmaceutical Materials. *TrAC Trends Anal. Chem.* **2021**, *134*, 116144. https://doi.org/10.1016/j.trac.2020.116144.

(250) R. C. Weast. *CRC Handbook of Chemistry and Physics*, 64th ed.; CRC Press: Boca Raton, FL, 1983.

(251) Davey, C. J.; Low, Z.-X.; Wirawan, R. H.; Patterson, D. A. Molecular Weight Cut-off Determination of Organic Solvent Nanofiltration Membranes Using Poly(Propylene Glycol). *J. Memb. Sci.* **2017**, *526*, 221–228. https://doi.org/10.1016/j.memsci.2016.12.038.

(252) Ho, D. L.; Hammouda, B.; Kline, S. R. Clustering of Poly(Ethylene Oxide) in Water Revisited. *J. Polym. Sci. Part B Polym. Phys.* **2003**, *41* (1), 135–138. https://doi.org/10.1002/polb.10340.

(253) Singh, S.; Khulbe, K. .; Matsuura, T.; Ramamurthy, P. Membrane Characterization by Solute Transport and Atomic Force Microscopy. *J. Memb. Sci.* **1998**, *142* (1), 111–127. https://doi.org/10.1016/S0376-7388(97)00329-3.

(254) Hammouda, B.; Ho, D. L. Insight into Chain Dimensions in PEO/Water Solutions. *J. Polym. Sci. Part B Polym. Phys.* **2007**, *45* (16), 2196–2200. https://doi.org/10.1002/polb.21221.

(255) Branca, C.; Magazù, S.; Maisano, G.; Migliardo, F.; Migliardo, P.; Romeo, G. Study of Conformational Properties of Poly(Ethylene Oxide) by SANS and PCS Techniques. *Phys. Scr.* **2003**, *67* (6), 551–554. https://doi.org/10.1238/Physica.Regular.067a00551.

(256) Grinberg, V. Y.; Burova, T. V.; Grinberg, N. V.; Dubovik, A. S.; Papkov, V. S.; Khokhlov, A. R. Energetics of LCST Transition of Poly(Ethylene Oxide) in Aqueous Solutions. *Polymer* **2015**, *73*, 86–90. https://doi.org/10.1016/j.polymer.2015.07.032.

(257) Cha, M.-H.; Choi, J.; Choi, B. G.; Park, K.; Kim, I. H.; Jeong, B.; Han, D. K. Synthesis and Characterization of Novel Thermo-Responsive F68 Block Copolymers with Cell-Adhesive RGD Peptide. *J. Colloid Interface Sci.* **2011**, *360* (1), 78–85. https://doi.org/10.1016/j.jcis.2011.04.041.

(258) Deliormanlı, A. M.; Türk, M. Flow Behavior and Drug Release Study of Injectable Pluronic F-127 Hydrogels Containing Bioactive Glass and Carbon-Based Nanopowders. *J. Inorg. Organomet. Polym. Mater.* **2020**, *30* (4), 1184–1196. https://doi.org/10.1007/s10904-019-01346-2.

(259) Saxena, A.; Tripathi, B. P.; Kumar, M.; Shahi, V. K. Membrane-Based Techniques for the Separation and Purification of Proteins: An Overview. *Adv. Colloid Interface Sci.* **2009**, *145* (1–2), 1–22. https://doi.org/10.1016/j.cis.2008.07.004.

(260) Fallahianbijan, F.; Emami, P.; Hillsley, J. M.; Motevalian, S. P.; Conde, B. C.; Reilly, K.; Zydney, A. L. Effect of Membrane Pore Structure on Fouling Behavior of Glycoconjugate Vaccines. *J. Memb. Sci.* **2021**, *619*, 118797. https://doi.org/10.1016/j.memsci.2020.118797.

(261) Salehi, F. Current and Future Applications for Nanofiltration Technology in the Food Processing. *Food Bioprod. Process.* **2014**, *92* (2), 161–177. https://doi.org/10.1016/j.fbp.2013.09.005.

(262) Güell, C.; Davis, R. H. Membrane Fouling during Microfiltration of Protein Mixtures. *J. Memb. Sci.* **1996**, *119* (2), 269–284. https://doi.org/10.1016/0376-7388(96)80001-J.

(263) Saadat, Y.; Kim, K.; Foudazi, R. Two-Step Thermoresponsive Ultrafiltration Membranes from Polymerization of Lyotropic Liquid Crystals. *ACS Appl. Polym. Mater.* **2022**, *4* (11), 8156–8165. https://doi.org/10.1021/acsapm.2c01095.

(264) Gin, D. L.; Carter, B. M.; Wiesenauer, B. R.; Hatakeyama, E. S.; Noble, R. D.; Barton, J. L. METHOD AND MEMBRANE FOR NANOPOROUS, BICONTINUOUS CUBIC LYOTROPIC LIOUID CRYSTAL POLYMER MEMBRANES THAT ENABLE EACLE FILM PROCESSING AND PORE SIZE CONTROL. US 2014/0154499 A1, 2006.

(265) Cellesi, F.; Tirelli, N.; Hubbell, J. A. Materials for Cell Encapsulation via a New Tandem

Approach Combining Reverse Thermal Gelation and Covalent Crosslinking. *Macromol. Chem. Phys.* **2002**, *203* (10–11), 1466–1472. https://doi.org/10.1002/1521-3935(200207)203:10/11<1466::AID-MACP1466>3.0.CO;2-P.

(266) Qavi, S.; Foudazi, R. Rheological Characteristics of Mesophases of Block Copolymer Solutions. *Rheol. Acta* **2019**, *58* (8), 483–498. https://doi.org/10.1007/s00397-019-01162-y.

(267) Chang, J.-H.; Ohno, M.; Esumi, K.; Meguro, K. Interaction of Iodine with Nonionic Surfactant and Polyethylene Glycol in Aqueous Potassium Iodide Solution. *J. Am. Oil Chem. Soc.* **1988**, *65* (10), 1664–1668. https://doi.org/10.1007/BF02912573.

(268) Kushan, E.; Senses, E. Thermoresponsive and Injectable Composite Hydrogels of Cellulose Nanocrystals and Pluronic F127. *ACS Appl. Bio Mater.* **2021**, *4* (4), 3507–3517. https://doi.org/10.1021/acsabm.1c00046.

(269) Lee, C.-F.; Tseng, H.-W.; Bahadur, P.; Chen, L.-J. Synergistic Effect of Binary Mixed-Pluronic Systems on Temperature Dependent Self-Assembly Process and Drug Solubility. *Polymers (Basel).* **2018**, *10* (1), 105. https://doi.org/10.3390/polym10010105.

(270) Marín San Román, P. P.; Sijbesma, R. P. Photo-Responsive Water Filtration Membranes Based on Polymerizable Columnar Liquid Crystals with Azo Moieties. *Adv. Mater. Interfaces* **2022**, *9* (19), 2200341. https://doi.org/10.1002/admi.202200341.

(271) Hernández, S.; Porter, C.; Zhang, X.; Wei, Y.; Bhattacharyya, D. Layer-by-Layer Assembled Membranes with Immobilized Porins. *RSC Adv.* **2017**, *7* (88), 56123–56136. https://doi.org/10.1039/C7RA08737C.

(272) Chudoba, R.; Heyda, J.; Dzubiella, J. Temperature-Dependent Implicit-Solvent Model of Polyethylene Glycol in Aqueous Solution. *J. Chem. Theory Comput.* **2017**, *13* (12), 6317–

6327. https://doi.org/10.1021/acs.jctc.7b00560.

(273) Özdemir, C.; Güner, A. Solution Thermodynamics of Poly(Ethylene Glycol)/Water Systems. *J. Appl. Polym. Sci.* **2006**, *101* (1), 203–216. https://doi.org/10.1002/app.23191.

(274) González Flecha, F. L.; Levi, V. Determination of the Molecular Size of BSA by Fluorescence Anisotropy. *Biochem. Mol. Biol. Educ.* **2003**, *31* (5), 319–322. https://doi.org/10.1002/bmb.2003.494031050261.

(275) Lin, J.; Ye, W.; Baltaru, M.-C.; Tang, Y. P.; Bernstein, N. J.; Gao, P.; Balta, S.; Vlad, M.; Volodin, A.; Sotto, A.; Luis, P.; Zydney, A. L.; Van der Bruggen, B. Tight Ultrafiltration Membranes for Enhanced Separation of Dyes and Na2SO4 during Textile Wastewater Treatment. *J. Memb. Sci.* **2016**, *514*, 217–228. https://doi.org/10.1016/j.memsci.2016.04.057.

(276) Rana, D.; Matsuura, T. Surface Modifications for Antifouling Membranes. *Chem. Rev.* **2010**, *110* (4), 2448–2471. https://doi.org/10.1021/cr800208y.

(277) Malmsten, M.; Linse, P.; Zhang, K. W. Phase Behavior of Aqueous Poly(Ethylene Oxide)/Poly(Propylene Oxide) Solutions. *Macromolecules* **1993**, *26* (11), 2905–2910. https://doi.org/10.1021/ma00063a040.

(278) Wang, K.; Wang, X.; Januszewski, B.; Liu, Y.; Li, D.; Fu, R.; Elimelech, M.; Huang, X. Tailored Design of Nanofiltration Membranes for Water Treatment Based on Synthesis–Property–Performance Relationships. *Chem. Soc. Rev.* **2022**, *51* (2), 672–719. https://doi.org/10.1039/D0CS01599G.

(279) Ahmad, N. N. R.; Ang, W. L.; Teow, Y. H.; Mohammad, A. W.; Hilal, N. Nanofiltration Membrane Processes for Water Recycling, Reuse and Product Recovery within Various Industries: A Review. *J. Water Process Eng.* **2022**, *45*, 102478.

https://doi.org/10.1016/j.jwpe.2021.102478.

(280) Roy, Y.; Lienhard, J. H. A Framework to Analyze Sulfate versus Chloride Selectivity in Nanofiltration. *Environ. Sci. Water Res. Technol.* **2019**, *5* (3), 585–598. https://doi.org/10.1039/C8EW00847G.

(281) Lu, D.; Yao, Z.; Jiao, L.; Waheed, M.; Sun, Z.; Zhang, L. Separation Mechanism, Selectivity Enhancement Strategies and Advanced Materials for Mono-/Multivalent Ion-Selective Nanofiltration Membrane. *Adv. Membr.* **2022**, *2*, 100032. https://doi.org/10.1016/j.advmem.2022.100032.

(282) Cao, Y.; Chen, G.; Wan, Y.; Luo, J. Nanofiltration Membrane for Bio-separation: Process-oriented Materials Innovation. *Eng. Life Sci.* **2021**, *21* (6), 405–416. https://doi.org/10.1002/elsc.202000100.

(283) Dong, X.; Al-Jumaily, A.; Escobar, I. Investigation of the Use of a Bio-Derived Solvent for Non-Solvent-Induced Phase Separation (NIPS) Fabrication of Polysulfone Membranes. *Membranes (Basel).* **2018**, *8* (2), 23. https://doi.org/10.3390/membranes8020023.

(284) Mohamat, R. Fabrication of Nanofiltration Membrane Utilising Surfactant Via Non-Solvent Induced Phase Separation Method. *SPEKTRA J. Kaji. Pendidik. Sains* **2019**, *5* (2), 129. https://doi.org/10.32699/spektra.v5i2.108.

(285) Zhang, L.; Zhang, R.; Ji, M.; Lu, Y.; Zhu, Y.; Jin, J. Polyamide Nanofiltration Membrane with High Mono/Divalent Salt Selectivity via Pre-Diffusion Interfacial Polymerization. *J. Memb. Sci.* **2021**, *636*, 119478. https://doi.org/10.1016/j.memsci.2021.119478.

(286) Li, X.; Cao, Y.; Yu, H.; Kang, G.; Jie, X.; Liu, Z.; Yuan, Q. A Novel Composite Nanofiltration Membrane Prepared with PHGH and TMC by Interfacial Polymerization. *J. Memb. Sci.* **2014**, *466*, 82–91. https://doi.org/10.1016/j.memsci.2014.04.034.

(287) Yuan, S.; Zhang, G.; Zhu, J.; Mamrol, N.; Liu, S.; Mai, Z.; Van Puyvelde, P.; Van der Bruggen, B. Hydrogel Assisted Interfacial Polymerization for Advanced Nanofiltration Membranes. *J. Mater. Chem. A* **2020**, *8* (6), 3238–3245. https://doi.org/10.1039/C9TA12984G.

(288) Zhang, R.; Zhu, Y.; Zhang, L.; Lu, Y.; Yang, Z.; Zhang, Y.; Jin, J. Polyamide Nanofiltration Membranes from Surfactant-Assembly Regulated Interfacial Polymerization: The Effect of Alkyl Chain. *Macromol. Chem. Phys.* **2021**, *222* (20), 2100222. https://doi.org/10.1002/macp.202100222.

(289) Saadat, Y.; Tabatabaei, S. M.; Kim, K.; Foudazi, R. Thermoresponsive Antifouling Ultrafiltration Membranes from Mesophase Templating. *J. Memb. Sci.* **2023**, *684*, 121861. https://doi.org/10.1016/j.memsci.2023.121861.

(290) Durpekova, S.; Di Martino, A.; Dusankova, M.; Drohsler, P.; Sedlarik, V. Biopolymer Hydrogel Based on Acid Whey and Cellulose Derivatives for Enhancement Water Retention Capacity of Soil and Slow Release of Fertilizers. *Polymers (Basel).* **2021**, *13* (19), 3274. https://doi.org/10.3390/polym13193274.

(291) Khademi, M.; Barz, D. P. J. Structure of the Electrical Double Layer Revisited: Electrode Capacitance in Aqueous Solutions. *Langmuir* **2020**, *36* (16), 4250–4260. https://doi.org/10.1021/acs.langmuir.0c00024.

(292) Rayner-Canham, G.; Overton, T. *Descriptive Inorganic Chemistry*, Sixth.; W. H. Freeman, 2013.

(293) Wiśniewska, M.; Urban, T.; Grządka, E.; Zarko, V. I.; Gun'ko, V. M. Comparison of Adsorption Affinity of Polyacrylic Acid for Surfaces of Mixed Silica–Alumina. *Colloid Polym. Sci.* **2014**, *292* (3), 699–705. https://doi.org/10.1007/s00396-013-3103-x.

(294) Boo, C.; Wang, Y.; Zucker, I.; Choo, Y.; Osuji, C. O.; Elimelech, M. High Performance Nanofiltration Membrane for Effective Removal of Perfluoroalkyl Substances at High Water Recovery. *Environ. Sci. Technol.* **2018**, *52* (13), 7279–7288. https://doi.org/10.1021/acs.est.8b01040.

(295) Wang, R.; Lin, S. Pore Model for Nanofiltration: History, Theoretical Framework, Key Predictions, Limitations, and Prospects. *J. Memb. Sci.* **2021**, *620*, 118809. https://doi.org/10.1016/j.memsci.2020.118809.

(296) Lee, A.; Elam, J. W.; Darling, S. B. Membrane Materials for Water Purification: Design, Development, and Application. *Environ. Sci. Water Res. Technol.* **2016**, *2* (1), 17–42. https://doi.org/10.1039/C5EW00159E.

(297) Zhang, Y.; Dong, R.; Gabinet, U. R.; Poling-Skutvik, R.; Kim, N. K.; Lee, C.; Imran, O. Q.; Feng, X.; Osuji, C. O. Rapid Fabrication by Lyotropic Self-Assembly of Thin Nanofiltration Membranes with Uniform 1 Nanometer Pores. *ACS Nano* **2021**, *15* (5), 8192–8203. https://doi.org/10.1021/acsnano.1c00722.

(298) Li, Y.; Zhao, Y.; Wang, H.; Wang, M. The Application of Nanofiltration Membrane for Recovering Lithium from Salt Lake Brine. *Desalination* **2019**, *468*, 114081. https://doi.org/10.1016/j.desal.2019.114081.

(299) Gyulai, G.; Magyar, A.; Rohonczy, J.; Orosz, J.; Yamasaki, M.; Bosze, S.; Kiss, E. Preparation and Characterization of Cationic Pluronic for Surface Modification and Functionalization of Polymeric Drug Delivery Nanoparticles. *Express Polym. Lett.* **2016**, *10* (3), 216–226. https://doi.org/10.3144/expresspolymlett.2016.20.

(300) Hosseinzadeh, H.; Pashaei, S.; Hosseinzadeh, S.; Khodaparast, Z.; Ramin, S.; Saadat, Y. Preparation of Novel Multi-Walled Carbon Nanotubes Nanocomposite Adsorbent via

RAFT Technique for the Adsorption of Toxic Copper Ions. *Sci. Total Environ.* **2018**, *640–641*, 303–314. https://doi.org/10.1016/j.scitotenv.2018.05.326.

(301) Abdullah, N.; Gohari, R. J.; Yusof, N.; Ismail, A. F.; Juhana, J.; Lau, W. J.; Matsuura, T. Polysulfone/Hydrous Ferric Oxide Ultrafiltration Mixed Matrix Membrane: Preparation, Characterization and Its Adsorptive Removal of Lead (II) from Aqueous Solution. *Chem. Eng. J.* **2016**, *289*, 28–37. https://doi.org/10.1016/j.cej.2015.12.081.

(302) Perumal, S.; Atchudan, R.; Edison, T. N. J. I.; Babu, R. S.; Karpagavinayagam, P.; Vedhi, C. A Short Review on Recent Advances of Hydrogel-Based Adsorbents for Heavy Metal Ions. *Metals (Basel).* **2021**, *11* (6), 864. https://doi.org/10.3390/met11060864.

(303) Chen, J.; Jiang, X.; Yin, D.; Zhang, W. Preparation of a Hydrogel-Based Adsorbent for Metal Ions through High Internal Phase Emulsion Polymerization. *ACS Omega* **2020**, *5* (32), 19920–19927. https://doi.org/10.1021/acsomega.9b03405.

(304) Vo, T. S.; Hossain, M. M.; Jeong, H. M.; Kim, K. Heavy Metal Removal Applications Using Adsorptive Membranes. *Nano Converg.* **2020**, *7* (1), 36. https://doi.org/10.1186/s40580-020-00245-4.

(305) Moad, G. A Critical Assessment of the Kinetics and Mechanism of Initiation of Radical Polymerization with Commercially Available Dialkyldiazene Initiators. *Prog. Polym. Sci.* **2019**, *88*, 130–188. https://doi.org/10.1016/j.progpolymsci.2018.08.003.

(306) Achilias, D. S.; Sideridou, I. D. Kinetics of the Benzoyl Peroxide/Amine Initiated Free-Radical Polymerization of Dental Dimethacrylate Monomers: Experimental Studies and Mathematical Modeling for TEGDMA and Bis-EMA. *Macromolecules* **2004**, *37* (11), 4254–4265. https://doi.org/10.1021/ma049803n.

(307) Schneider, M.; Graillat, C.; Boutti, S.; McKenna, T. F. Decomposition of APS and H2O2

for Emulsion Polymerisation. *Polym. Bull.* **2001**, *47* (3–4), 269–275. https://doi.org/10.1007/s289-001-8181-2.

(308) UI_NOROX_Broschüre_DS https://www.united-initiators.com/wp-content/uploads/2017/03/UI_NOROX_Broschüre_DS.pdf.

(309) Akzonobel. Initiators_for_High_Polymers http://www.neochemical.kz/File/Akzo_Data_110407-Initiators_for_High_Polymers.pdf.

(310) Lowell, A. I.; Price, J. R. Organic Peroxides. I. Initiation of Styrene Polymerization. *J. Polym. Sci.* **1960**, *43* (141), 1–12. https://doi.org/10.1002/pol.1960.1204314101.

(311) Zhu, W.; Wang, B.; Zhang, Y.; Ding, J. Preparation of a Thermosensitive and Biodegradable Microgel via Polymerization of Macromonomers Based on Diacrylated Pluronic/Oligoester Copolymers. *Eur. Polym. J.* **2005**, *41* (9), 2161–2170. https://doi.org/10.1016/j.eurpolymj.2005.04.006.

(312) Guo, C.; Liu, H.; Wang, J.; Chen, J. Conformational Structure of Triblock Copolymers by FT-Raman and FTIR Spectroscopy. *J. Colloid Interface Sci.* **1999**, *209* (2), 368–373. https://doi.org/10.1006/jcis.1998.5897.

(313) ISO-GUM. Evaluation of Measurement Data — Guide to the Expression of Uncertainty in Measurement. JCGM 100:2008, 2008.

APPENDIX A

NOMENCLATURE AND ACRONYMS

LC	Liquid crystal
LLC	Lyotropic liquid crystal
L_1	Normal micelles
I_1	Normal discontinuous cubic
H_1	Normal hexagonal
L_α	Lamellar
Q_1	Normal bicontinuous cubic
Q_2	Reverse bicontinuous cubic
H_2	Reverse hexagonal
I_2	Reverse discontinuous cubic
L_2	Reverse micelles
I_α	Discontinuous cubic
H_α	Hexagonal
Q_α	Bicontinuous cubic
CPP	Critical packing parameter
V	Lipophilic tail volume
a	'Effective' cross-sectional area of the hydrophilic head group
l	Extended lipophilic chain length
a_e	Geometrical cross-sectional area of the charged head group
CPLM	Cross polarized light microscopy
SAXS	Small-angle X-ray scattering
XRD	X-ray diffraction

NMR	Nuclear magnetic resonance
BCC	Body-centered cubic
FCC	Face-centered cubic
PolyLLC	Polymerized LLC
d	d-Spacing (also lattice parameter in lamellar phase)
a	Lattice parameter in hexagonal phase
R_m	Radius of micelle in hexagonal phase
R_c	Radius of confined phase in micelle in hexagonal phase
D_m	Intermicellar distance in hexagonal phase
$R_{h,max}$	Radius of the largest circle trapped between the micelles or confinement size in hexagonal phase
q^*	Position of the first Bragg peak in SAXS measurement
ϕ	Volume fraction of the dispersed phase (i.e., the phase confined in the cylindrical micelles)
ϕ_t	Volume fraction of the confined phase plus the volume fraction of the surfactant
δ_1	Thickness of the apolar domain in lamellar phase
δ_2	Thickness of the polar domain in lamellar phase
D_1	Intermicellar distance in apolar phase in lamellar structure
D_2	Intermicellar distance in polar phase in lamellar structure
$R_{1,max}$	Radii of the largest circles trapped between the micelles in apolar domain in lamellar phase
$R_{2,max}$	Radii of the largest circles trapped between the micelles in polar domain in lamellar phase
ϕ_1	Volume fraction of the apolar domain in lamellar phase
ϕ_2	Volume fraction of the polar domain in lamellar phase

D_L	Average intermicellar distance in lamellar structure
ϕ'	Volume fraction of the phases confined in the apolar domain in lamellar phase
ϕ''	Volume fraction of the phases confined in the polar domain in lamellar phase
Im3m or Q_{229}	Primitive lattice type for bicontinuous cubic phase
Pn3m or Q_{224}	Double-diamond lattice type for bicontinuous cubic phase
Ia3d or Q_{230}	Gyroid lattice type for bicontinuous cubic phase
$2l$	Thickness of the apolar domain in bicontinuous cubic phase
$2t_{polar}$	Polar domain thickness
d_{hkl}	Spacings
h, k, l	Miller indices
α_1	Polar domain size in discontinuous cubic phase
α_2	Apolar domain size in discontinuous cubic phase
R_c	Radius of the spherical micelles in discontinuous cubic phase
ϕ	Volume fraction of continuous domain in discontinuous cubic phase
F-K phases	Frank-Kasper phases
A15	Type of F-K phases
σ	Type of F-K phases
μ	Type of F-K phases
M	Type of F-K phases
P	Type of F-K phases
R	Type of F-K phases
Z	Type of F-K phases
C14 or C15 Laves	Type of F-K phases
L_3	'Sponge' phase
PPV	Poly(*p*-phenylenevinylene)

HPL	Hexagonal perforated lamellar
CMC	Critical micelle concentration
BR	Butyl rubber
MF	Microfiltration
NF	Nanofiltration
UF	Ultrafiltration
RO	Reverse osmosis
ALD	Atomic layer deposition
TFC	Thin film composite
AEM	Anion exchange membrane
TDS	Total dissolved solid
DOC	Dissolved organic carbon
FW	Flow back water
PDA	Polydopamine
CEES	2-Chloroethyl ethyl sulfide
DMMP	Dimethyl methylphosphonate
DOP	Dioctyl phthalate
ChO	Chemical oxidation
BCP	Block copolymer
OMC	Ordered mesoporous carbon
SWNT	Single-walled carbon nanotube
EP	Electropolymerization
PC	Polycondensation
Da	Dalton
PNIPAM	Poly(N-isopropylacrylamide)

LCST	Lowest critical solution temperature
PDMS	Polydimethylsiloxane
POSS	Polyhedral oligomeric silsesquioxane
MNP	Molecular nanoparticle
MW	Molecular weight
PEG	Poly(ethylene glycol)
NIPS	Non-solvent induced phase separation
nBA	n-Butyl acrylate
EGDMA	Ethylene glycol dimethacrylate
IFW	Initiation from water
IFO	Initiation from oil
APS	Ammonium persulfate
AIBN	Azobisisobutyronitrile
BPO	Benzoyl peroxide
DI	Deionized water
1D	One dimensional
2D	Two dimensional
3D	Three dimensional
DSC	Differential scanning calorimetry
$Q(t)$	Heat flow obtained from DSC analysis
R_p	Polymerization rate
$Q_{monomer}$	Theoretical heat of reaction of monomer
$Q_{crosslinker}$	Theoretical heat of reaction of crosslinker
M	Molar mass of monomer or crosslinker
$[M]_0$	Initial concentration of monomer or crosslinker

ΔH_p	Theoretical reaction enthalpy
n	Functionality of monomer or crosslinker
m	Total mass of monomer or crosslinker
p	Monomer conversion
ϕ_{Oil}	Volume fraction of oil
$\phi_{Pluronic}$	Volume fraction of Pluronic
ϕ_{Water}	Volume fraction of water
PEO	Poly(ethylene oxide)
PPO	Poly(propylene oxide)
R_g	Radius of gyration
k_d	Kinetics rate constant of initiator decomposition
k_p	Propagation rate constant
k_t	Termination rate constant
$[M]$	Monomer concentration
$[I]$	Initiator concentration
f	Initiator efficiency
$[I]_0$	Initial initiator concentration
$[R]$	Cumulative concentration of free radicals
t	Time
K'	Overall kinetics rate coefficient
E	Overall activation energy of the polymerization
X	Monomer conversion
G'	Storage moduli
G''	Loss moduli

PVDF	Polyvinylidenefluoride
PES	Polyethersulfone
F127	Pluronic F127
BSA	Bovine serum albumin
MWCO	Molecular weight cut-off
PAN	Polyacrylonitrile
AFM	Atomic force microscopy
Q	Flow rate
μ	Viscosity
A	Membrane area
ΔP	Pressure difference across the membrane
l	Membrane thickness
κ	Darcy's constant (intrinsic permeability)
μ_w	Kinetic viscosity of water
T	Temperature
TOC	Total organic carbon
r	Rejection
C_p	Concentration of solute in permeate
C_f	Concentration of solute in feed
DLS	Dynamic light scattering
a_{Stokes}	Stokes radius
M_w	Molecular weight
A_1	Initial value in Boltzmann sigmoidal equation
A_2	Final value in Boltzmann sigmoidal equation
x_0	center value in Boltzmann sigmoidal equation

m	Slope in Boltzmann sigmoidal equation
SANS	Small-angle neutron scattering
PCS	Photon correlation spectroscopy
P84	Pluronic P84
P84DA	Pluronic P84 diacrylate
[BMIM][BF_4]	1-Butyl-3-methylimidazolium tetrafluoroborate
HDDA	1,6-hexanediol diacrylate
DCM	Dichloromethane
HCPK	1-Hydroxycyclohexyl phenyl ketone
DR23	Direct red 23
DR80	Direct red 80
ATR-FTIR	Attenuated total reflectance-Fourier transform infrared spectroscopy
W_0	Weight of dry polyLLC
W_t	Weight of water-swollen polyLLC
SEM	Scanning electron microscope
Δq	Full width at half-maximum (FWHM) of the principal scattering peak at q*
ϕ_{PPO}	Volume fraction of PPO block in the Pluronic block copolymer
ϕ_{HDDA}	Volume fraction of HDDA
DMAEMA	2-(Dimethylamino)ethyl methacrylate

APPENDIX B

SUPPORTING INFORMATION FOR CHAPTER 1

Table B1. Amphiphiles, (co)monomers, cross-linkers and initiators used in LLC templating.

	No.	Name/Chemical Formula
Polymerizable Amphiphiles	P-A-1	Allyl dodecyldimethylammonium bromide
	P-A-2	Allyl didodecylmethylammonium bromide
	P-A-3	ω-Undecenyltrimethylammonium bromide
	P-A-4	(11-Methacry1oylundecyI)trimethylammonium bromide
	P-A-5	2-(Methacryloyloxy)ethyl dodecyl dimethyl ammonium bromide
	P-A-6	2-(Methacryloyloxy)ethyl tetradecyl dimethyl ammonium bromide
	P-A-7	2-(Methacryloyloxy)ethyl hexadecyl dimethyl ammonium bromide
	P-A-8	[2-(Acryloyloxy)ethyl]dimethyl tetradecyl ammonium bromide
	P-A-9	Dodecyldimethylammoniumethylmethacrylate bromide
	P-A-10	$C_9H_{18}(CH_2)_n\ NO^{2+}\ Br^-$
	P-A-11	N-(3-Methacrylamidopropyl)-N,N-dimethylhexadecan-1-aminium bromide
	P-A-12	(E)-N-(3-methacrylamidopropyl)-N,N-dimethyloctadeca-15,17-dien-1-aminium bromide
	P-A-13	(11-Acryloyloxy-undecyl)-dimethyl-[2-(methacryloyloxy)-ethyl]-ammonium bromide
	P-A-14	*N*,*N*-Di(11-acryloyloxy-undecyl)-*N*,*N*,*N*,*N*-tetramethyl-hexane-1,6-diammonium dibromide
	P-A-15	$C_{59}H_{66}NO_{22}^+\ Br^-$
	P-A-16	$C_{69}H_{90}N_3O_{24}^{3+}\ Br^{3-}$
	P-A-17	$C_{53}H_{74}N_3O_{17}^{3+}\ Br^{3-}$
	P-A-18	Sodium 10-undecenoate
	P-A-19	Zinc 10-undecenoate
	P-A-20	Dodecyl ammonium acrylate
	P-A-21	Dodecyl ammonium methacrylate
	P-A-22	*mon*-isoMeDenPE
	P-A-23	*bis*-isoMeDenPC
	P-A-24	$C_{48}H_{84}NO_8^+\ P^-$
	P-A-25	Hitenol BC-05
	P-A-26	$C_{27}H_{44}Na^+\ O_2^-$
	P-A-27	$C_{29}H_{49}NO_2\ Na^+\ SO_3^-$
	P-A-28	$C_{12}H_{14}(CH_2)_n\ (CH_2)_m\ Na^+O_3^-$
	P-A-29	$C_{49}H_{80}Na^+O_{11}^-$
	P-A-30	$C_{19}H_{14}(CH_2)_{3n}Na^+O_5^-$
	P-A-31	$C_{52}H_{88}NO_{13}S^-\ Li^+$
	P-A-32	$C_{58}H_{98}N_2O_{11}^+\ BF_4^-$
	P-A-33	$C_{58}H_{100}N_2O_{11}^+\ BF_4^-$
	P-A-34	$C_7H_{14}(CH_2)_n\ P^+\ Br^-$
	P-A-35	$C_{13}H_{22}(CH_2)_x\ (CH_2)_y\ P_2^{2+}\ Br_2^{2-}$
	P-A-36	$C_{13}H_{22}(CH_2)_x\ (CH_2)_y\ N_2^{2+}\ Br_2^{2-}$
	P-A-37	TMA-83u
	P-A-38	$C_{48}H_{84}\ N_4^{2+}\ Br_2^{2-}$
	P-A-39	$C_{48}H_{88}\ N_4^{2+}\ Br_2^{2-}$
	P-A-40	1-(8-(Acryloyloxy)octyl)-3-methylimidazolium Chloride 1-(10-(Acryloyloxy)decyl)-3-methylimidazolium Chloride
	P-A-41	1-(10-Thien-3-yl)decyl-3-methylimidazolium nitrate
	P-A-42	1-Decyl-3-methylimidazolium Acrylate

Table B1. *(Contd.)*

	No.	Name/Chemical Formula
Polymerizable Amphiphiles	P-A-43	1-Dodecyl-3-Propargylimidazolium Bromide
	P-A-44	3-Decyl-1-vinylimidazolium chloride
	P-A-45	Nanodiamond-[$COOC_{10}H_{20}VIm^{+}$][Br^{-}]
	P-A-46	Quantum-Dot-[$SC_{10}BrVIm^{+}$][Cl^{-}]
	P-A-47	$C_{330}H_{528}N_8O_{50}Pt_2P_4^{4+}$ $(PF_6^{-})_4$
	P-A-48	Monoacylglycerol
	P-A-49	1,2-Diacylglycerol
	P-A-50	Noigen RN-10
	P-A-51	α,ω-hydrophobically modified poly(oxyethylene)
	P-A-52	Ether-substituted perfluoroalkyl methacrylic acid
	P-A-53	$C_{52}H_{89}NO_{13}S$
	P-A-54	$C_{53}H_{89}NO_{12}$
	P-A-55	$C_{64}H_{103}N_3O_{11}$
	P-A-56	Poly(ethylene oxide)-*b*-poly(butadiene)
	P-A-57	MA-PEO-PDMS-PEO-MA
	P-A-58	PEO-b-PDMS-b-PEO-cinnamate triblock copolymer
	P-A-59	Pluronic diacrylate
	P-A-60	3-(2,4,13-(E,E)-tetradecatrienoyl)-*sn*-glycerol
Non-Polymerizable Amphiphiles	A-1	Didodecyldimethylammonium bromide
	A-2	Dioctadecyldimethylammonium bromide
	A-3	Dodecyltrimethylammonium bromide
	A-4	Tetradecyltrimethylammonium bromide
	A-5	Cetyltrimethylammonium bromide
	A-6	Octadecyltrimethylammonium bromide
	A-7	*N*,*N*-dimethyldodecylamine-*N*-oxide
	A-8	Dimyristoylphosphatidylcholine
	A-9	1-Decyl-3-methylimidazolium Chloride
	A-10	Sodium dodecyl sulfate
	A-11	Cetyltrimethylammonium tartrate
	A-12	Dioctyl sodium sulfosuccinate
	A-13	Brij 52
	A-14	Brij 56
	A-15	Brij 58
	A-16	Dodecyl poly(ethyleneglycol) ether
	A-17	PS-*b*-PEO (SE10/10)
	A-18	Poly(oxyethylene) oleyl ether
	A-19	Pluronic
	A-20	Tween 60
(Co)Monomers	M-1	Styrene
	M-2	Methyl methacrylate
	M-3	Methyl acrylate
	M-4	*n*-Butyl acrylate
	M-5	*n*-Hexyl acrylate
	M-6	*n*-Decyl acrylate
	M-7	*n*-Dodecyl methacrylate
	M-8	Glycidyl methacrylate
	M-9	Acrylamide
	M-10	*N*-Isopropylacrylamide
	M-11	*N*,*N*-Dimethylacrylamide

Table B1. *(Contd.)*

	No.	Name
(Co)Monomers	M-12	2-(Dimethylamino)ethyl methacrylate
	M-13	2-Hydroxyethyl methacrylate
	M-14	2-Carboxyethyl acrylate
	M-15	2-(Acrylamido)-2-methyl-1-propansulfonic acid
	M-16	Sodium acrylate
	M-17	Acrylic acid
	M-18	2,3-Dihydrothieno[3,4-b]-1,4-dioxin
	M-19	dimethyldimethoxysilane
	M-20	1,6-Hexanediol diacrylate
	M-21	Ethylene glycol dimethacrylate
	M-22	1,6-Hexanediol dimethacrylate
	M-23	Poly(ethylene glycol) dimethacrylate
	M-24	Poly(ethylene glycol) diacrylate
	M-25	Ethyloxy succinate dimethacrylate
	M-26	PLA-*b*-PEG-*b*-PLA diacrylate
	M-27	PLA-*b*-PEG-*b*-PLA dimethacrylate
	M-28	Caprolactone dimethacrylate
	M-29	Methacrylated poly(dimethylsiloxane)
	M-30	Poly(ethyleneglycol)-poly(lactic acid)-hexamethylene dimethacrylate
	M-31	3-Sulfopropyl acrylate
	M-32	[2-(Acryloyloxy)ethyl]trimethylammonium chloride
	M-33	Silver acrylate
	M-34	Phenol/formaldehyde
	M-35	3,9-Dioxidophenanthrene-1,5-dicarboxylate
	M-36	Phloroglucinol
	M-37	Resorcinol
	M-38	Bisphenol A diglycidyl ether
	M-39	1,4-Diphenylbutadiyne
	M-40	3-Hexylthiophene
	M-41	Aniline
	M-42	(E)-1’,3’,3’-Trimethyl-6-(octadeca-15,17-dien-1-yloxy)spiro[chromene-2,2’-indoline]
	M-43	2-((Z)-2-Hydroxy-5-(((E)-octadeca-15,17-dien-1-yl)oxy)styryl)-1,3,3-trimethyl-3H-indol-1-ium bromide
Cross-linkers	C-1	1,4-Divinylbenzene
	C-2	*N,N'*-Methylenebisacrylamide
	C-3	Neopentyl glycol diacrylate
	C-4	Methyltrimethoxysilane
	C-5	1,8-Octanediol dimethacrylate
	C-6	1,6-Hexanediol dimethacrylate
	C-7	1,4-Butanediol diacrylate
	C-8	Ethylene glycol dimethacrylate
	C-9	Poly(ethylene glycol) dimethacrylate
	C-10	Poly(ethylene glycol) diacrylate
	C-11	Diallylamine
	C-12	Formaldehyde
	C-13	Glyoxal
	C-14	1,4-Bis(chloromethyl)benzene
	C-15	1-Ethyl-3-methylimidazolium dicyanamide
	C-16	Pentaerythritol tetraacrylate
	C-17	1,10-Decanediol dimethacrylate
	C-18	1,6-Hexanediol diacrylate

Table B1. *(Contd.)*

	No.	Name
Initiators	I-1	2-Hydroxy-2-methylpropiophenone
	I-2	2,2-Dimethoxy-2-phenylacetophenone
	I-3	2-Methoxy-2-phenylacetophenone
	I-4	Diphenyl(2,4,6-trimethylbenzoyl)phosphine oxide
	I-5	2-Hydroxy-4′-(2-hydroxyethoxy)-2-methylpropiophenone
	I-6	2-Benzyl-2-dimethylamino-1-(4-morpholinophenyl)-butanone-1
	I-7	2-Hydroxy-2 methyl-1-4(1-methylvinyl)phenyl propanone
	I-8	Phenylbis(2,4,6-trimethylbenzoyl)phosphine oxide
	I-9	1-Hydroxycyclohexyl phenyl ketone
	I-10	2-Methyl-1-[4-(methylthio)phenyl]-2-(4-morpholinyl)-1-propanone
	I-11	Benzophenone
	I-12	4-(Dimethylamino)benzophenone
	I-13	Eosine Y/Triethanolamine
	I-14	Eosine/Methylene blue/Ethanolamine
	I-15	Azobisisobutyronitrile
	I-16	Hydrogen peroxide
	I-17	Ammonium persulfate
	I-18	Potassium persulfate
	I-19	Potassium persulfate/*L*-Cysteine
	I-20	Potassium persulfate/Sodium bisulfite
	I-21	Rhodium(III) chloride hydrate
	I-22	$FeCl_3$
	I-23	Benzoyl peroxide

APPENDIX C

SUPPORTING INFORMATION FOR CHAPTER 2

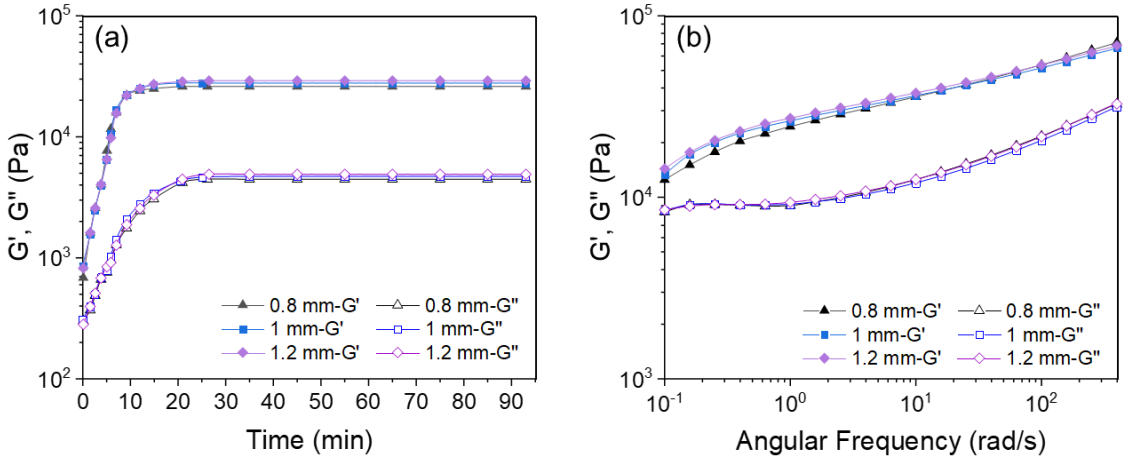

Figure C1. Confirming the absence of wall slip during rheological measurements: typical rheological behavior of the sample with lamellar LLC structure (a) during polymerization by APS and (b) after polymerization under different gaps between the measuring plates.

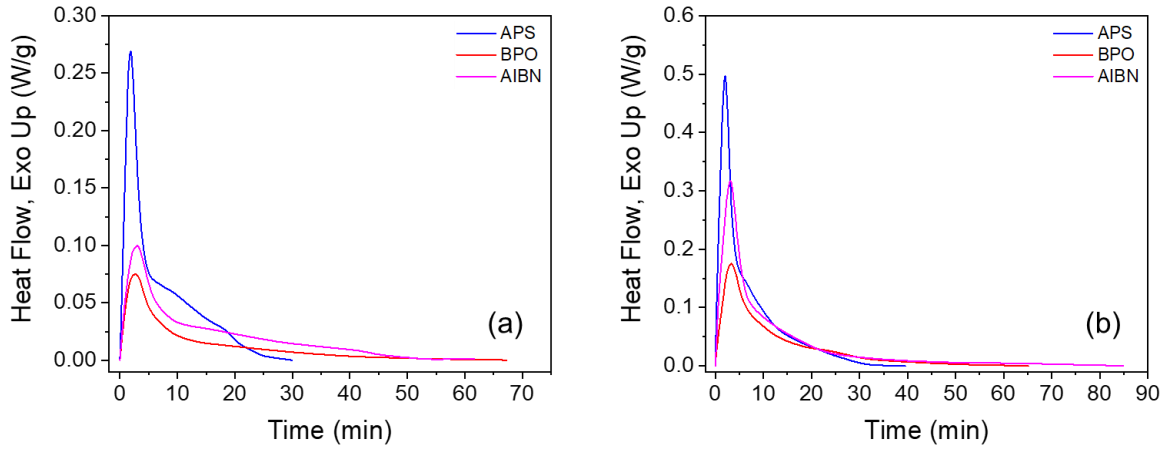

Figure C2. Typical raw DSC data for the polymerization in (a) lamellar and (b) hexagonal structures using different initiators. The heat flow has been normalized to the total weight of the mesophase used for the analysis (not total monomer content).

Theoretical concentration of the free radicals generated by different initiators over time

The theoretical cumulative concentration of free radicals generated through the decomposition of initiators was calculated by the following equation:[216]

$$[R] = 2f[I]_0\left(1-e^{-k_d t}\right) \quad \text{(C-1)}$$

where *[R]*, *f*, $[I]_0$, k_d and *t* are the cumulative concentration of free radicals, the initiator efficiency, initial concentration of the initiator, decomposition rate constant of the initiator, and time, respectively. The average value of 0.5 is commonly used for *f* in the case of AIBN.[305] However, there is not a firm average value reported in the literature for BPO[306] and APS.[307] Therefore, to cancel out the effect of *f*, we normalized *[R]* to *f*, resulting in the following equation:

$$\frac{[R]}{f} = 2[I]_0\left(1-e^{-k_d t}\right) \quad \text{(C-2)}$$

It should be noted that this calculation was made just to have a comparison among different initiators in terms of difference in the rate of free radical generation over time. So, the presented concentrations do not reflect the actual free radical concentration during LLC templating.

The calculation was made for the monomer content used in the formulation of lamellar structure (the calculation itself does not depend on the LLC structure) at three different temperatures. To do so, the values shown in Table C1 was used for k_d of different initiators. To calculate the k_d values, the activation energy, pre-exponential factor, and k_d at the reference temperature were obtained from the literature for different initiators.[305,307–310] k_d was then calculated at the desired temperature using Arrhenius equation. The initial concentration for all of the initiators was 0.33 M with respect to the total monomer content.

Table C1. Decomposition rate constant of different initiators at different temperatures.[305,307–310]

Initiator	***T* (°C)**	**k_d (s^{-1})**
APS	55	2.54×10^{-6}
	65	1.09×10^{-5}
	75	4.36×10^{-5}
AIBN	55	6.18×10^{-6}
	65	2.53×10^{-5}
	75	9.57×10^{-5}
BPO	55	2.04×10^{-6}
	65	7.85×10^{-6}
	75	2.79×10^{-5}

To make similar calculations for the systems in which the combination of two initiators with total concentration of 5 mol% is used (2.5 mol% APS + 2.5 mol% AIBN or 2.5 mol% APS + 2.5 mol% BPO), the following equation was used. In these samples, the initial concentration for each initiator was 0.165 M.

$$\frac{[R]}{f} = \frac{[R]_{APS}}{f_{APS}} + \frac{[R]_{AIBN\ or\ BPO}}{f_{AIBN\ or\ BPO}} \tag{C-3}$$

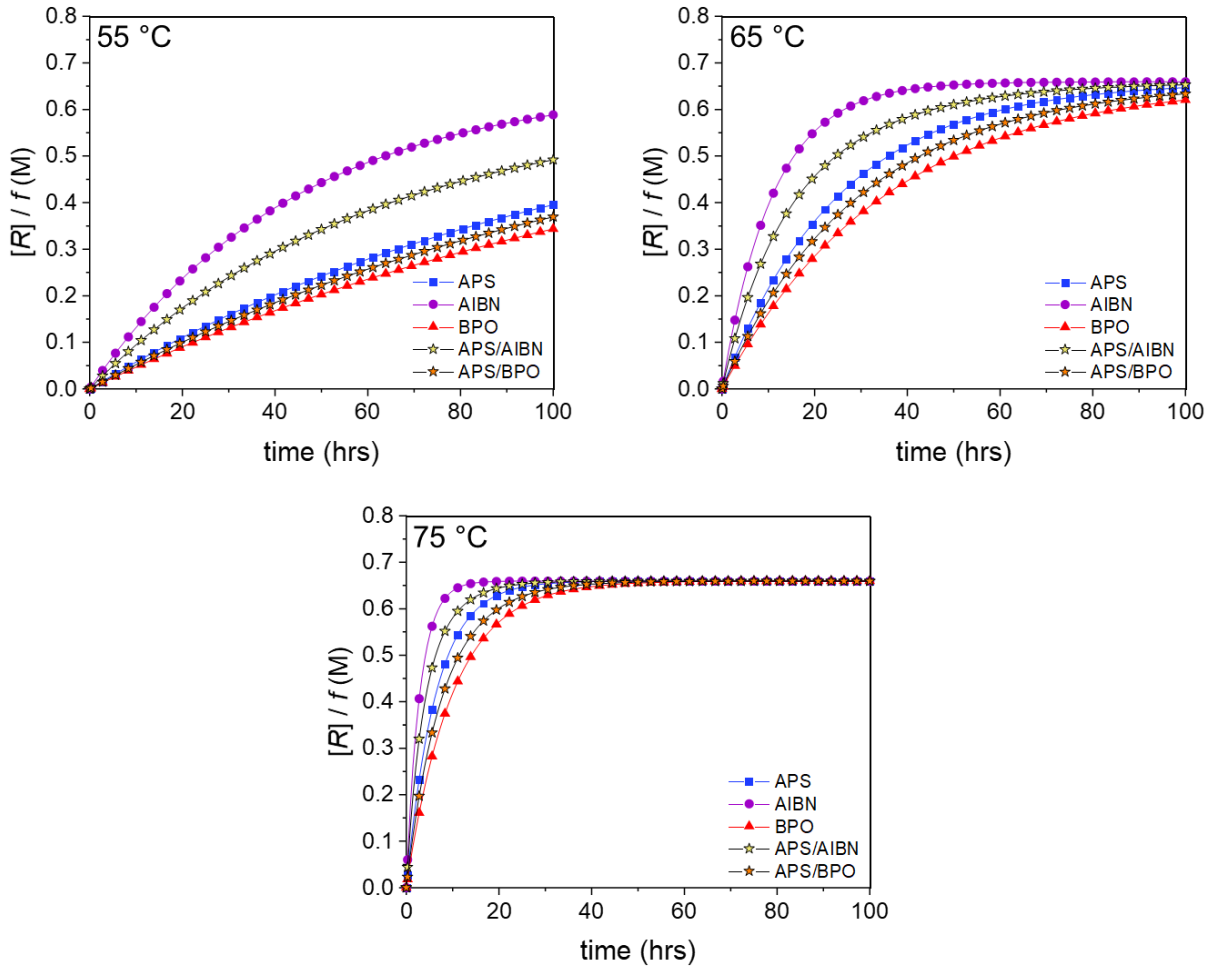

Figure C3. Normalized theoretical concentration of the free radicals generated by different initiators over time at three different temperatures.

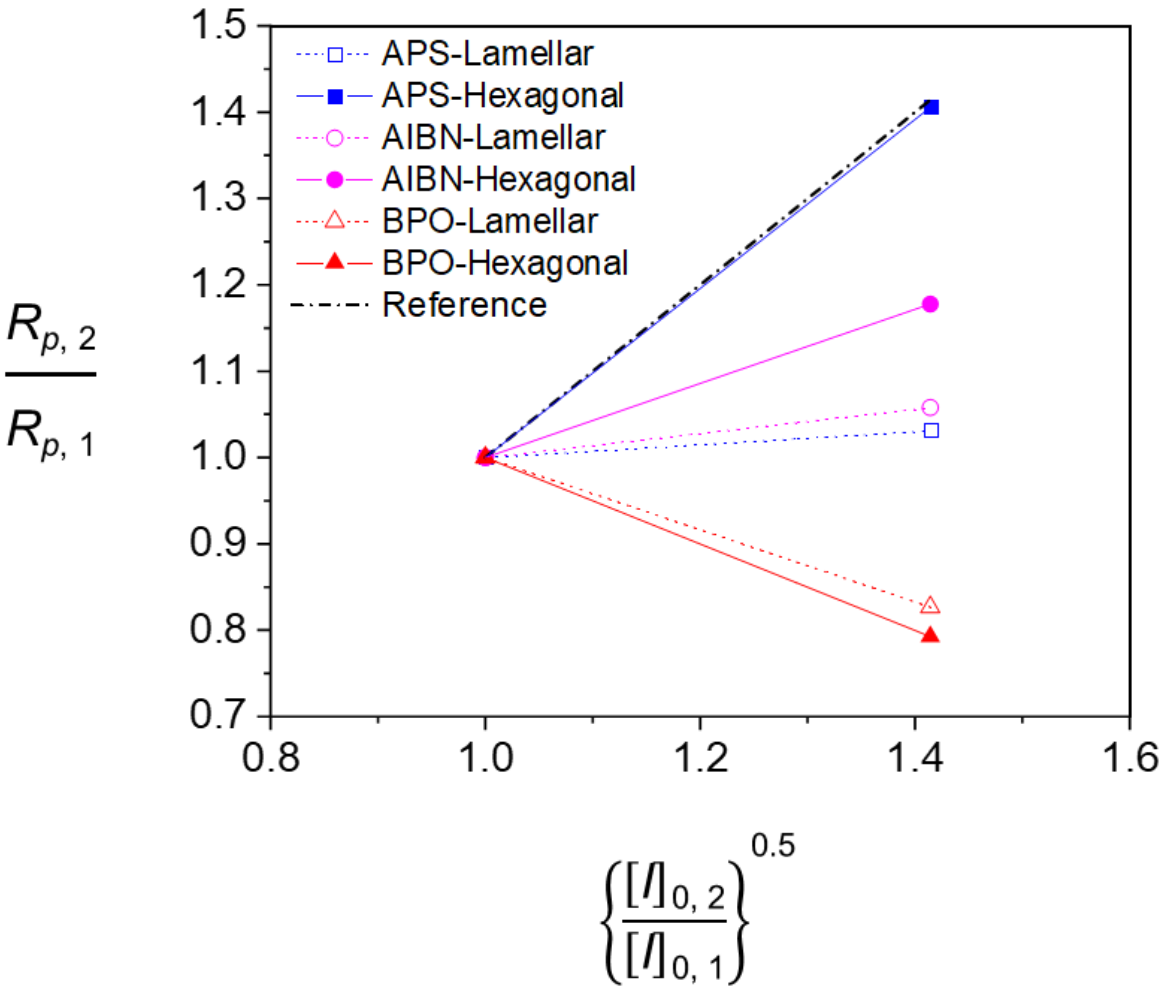

Figure C4. Change in maximum polymerization rate in lamellar and hexagonal structures with a change in the content of different initiators. $R_{p,1}$ and $R_{p,2}$ are the maximum polymerization rate when initial initiator content of $[I]_{0,1}$ and $[I]_{0,2}$ are used respectively. For different polymerization systems, $[I]_{0,1}$ and $[I]_{0,2}$ are initiator content of 2.5 and 5 mol% with respect to the total monomer content, respectively. In this figure, "Reference" represents the relation of reaction rate with the square root of initial initiator concentration, $R_p \propto ([I]_0)^{0.5}$. The lines connecting the data point are added as a guide for the eye.

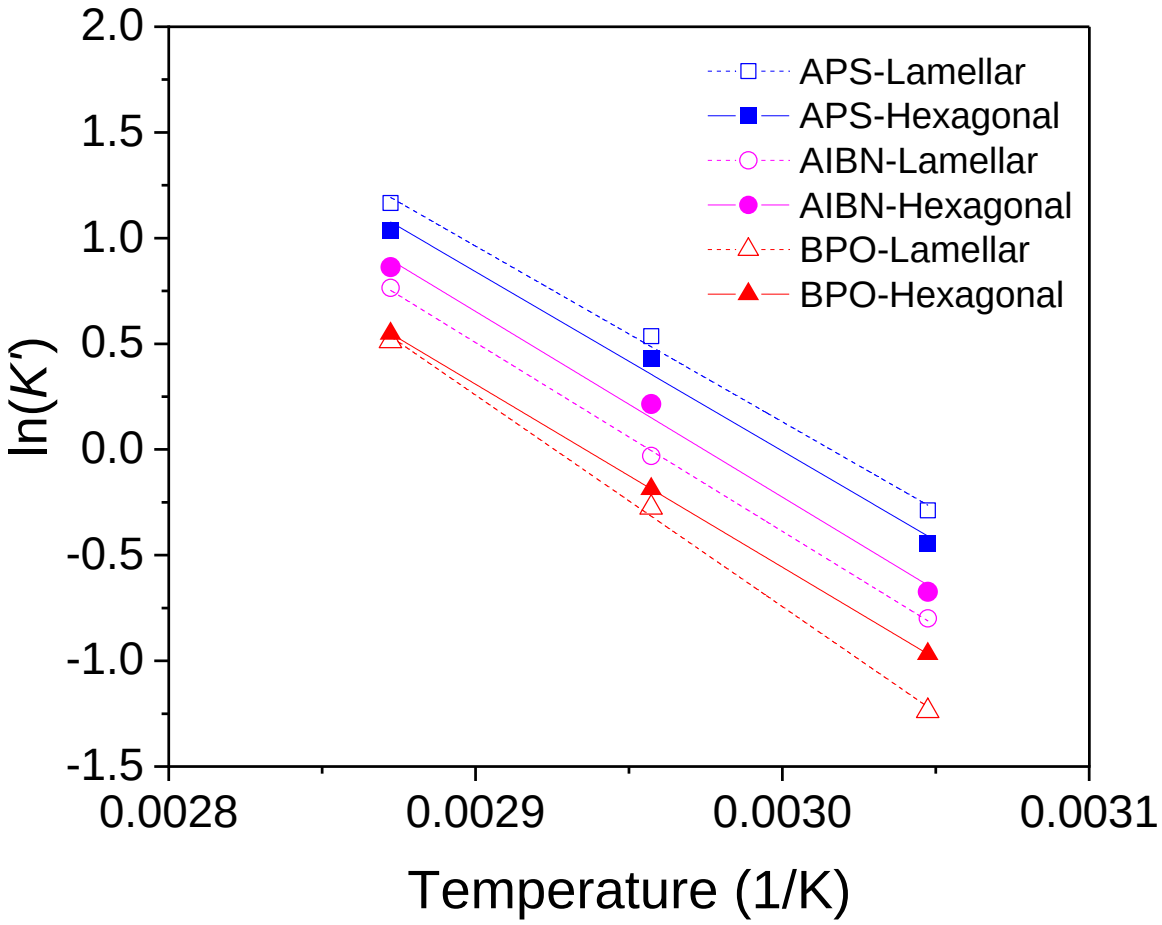

Figure C5. Overall kinetics rate coefficient vs temperature in lamellar and hexagonal structures using different initiators. Lines are linear fits to data. For APS-initiated system, *K*' are bigger in lamellar structure compared to hexagonal one in all of the temperatures. The opposite trend is observed for the reactions initiated by AIBN and BPO.

APPENDIX D

SUPPORTING INFORMATION FOR CHAPTER 3

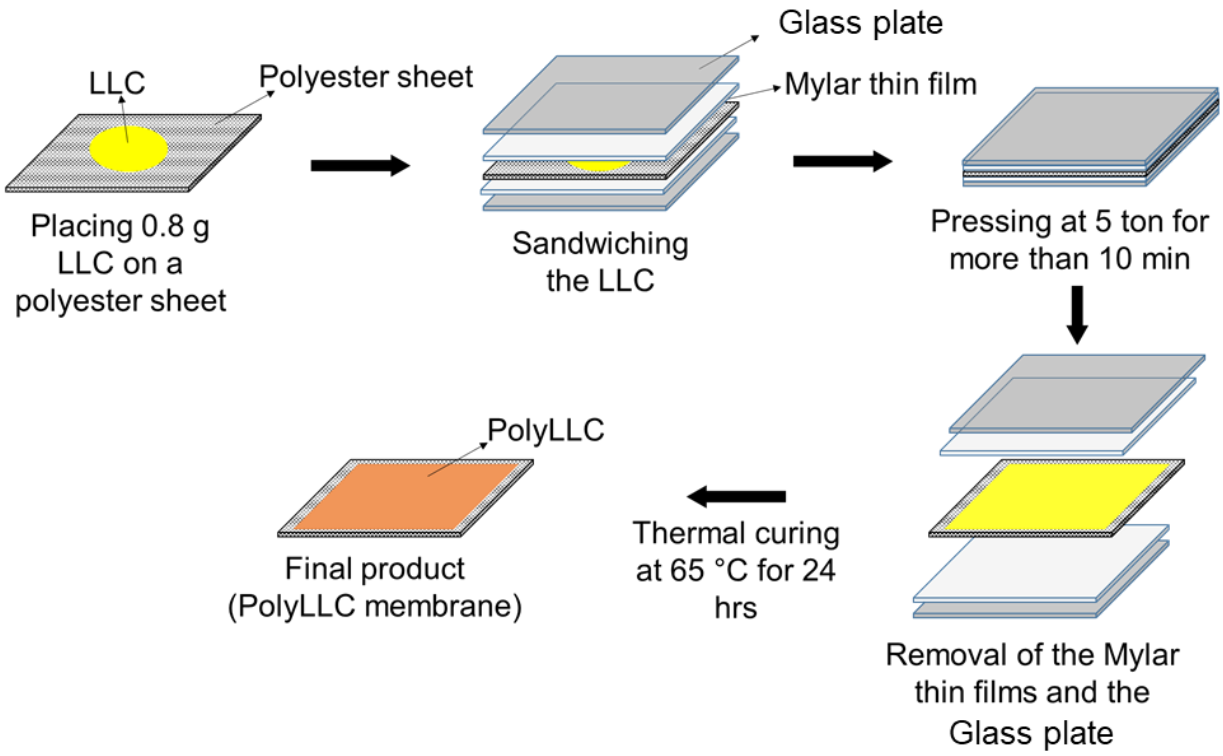

Figure D1. Schematic representation of polyLLC membrane preparation.

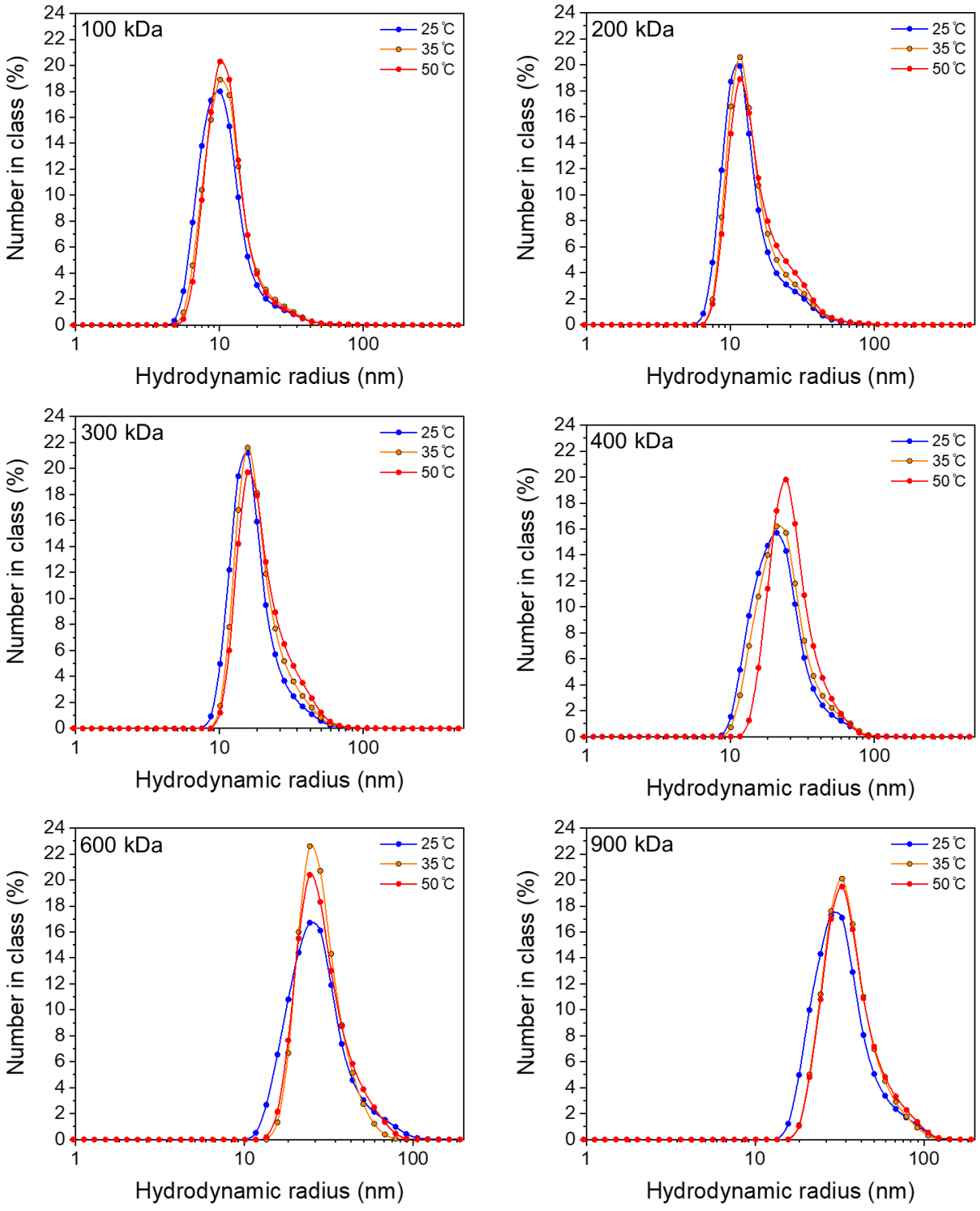

Figure D2. Temperature-dependent chain size distribution for PEO having different molecular weights.

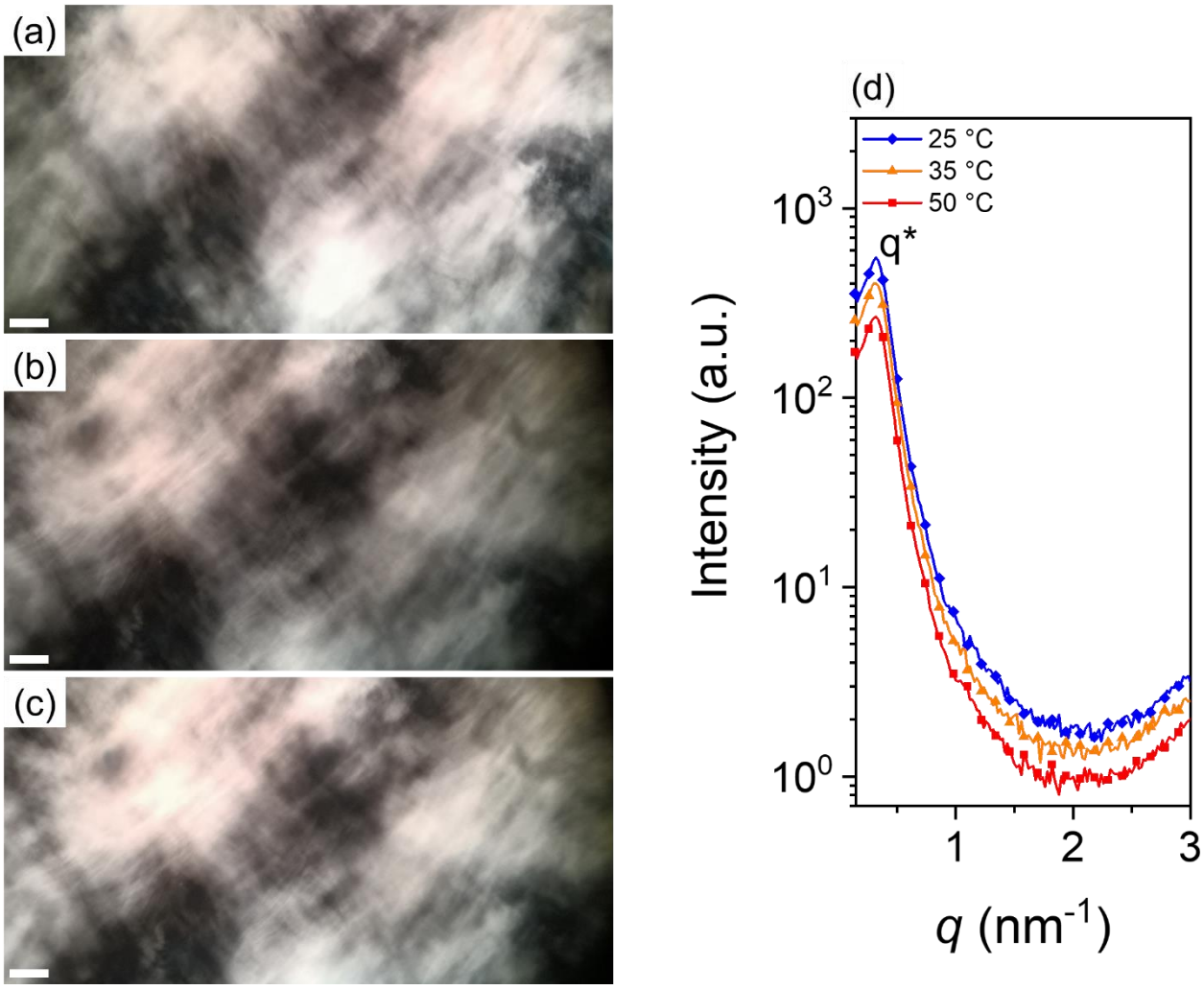

Figure D3. CPLM images of polyLLC with lamellar structure at (a) 25, (b) 35 and (c) 50 °C (scale bar: 50 μm). (d) 1D SAXS data for the polyLLC at 25, 35 and 50 °C (the plots are vertically shifted for clarity).

APPENDIX E

SUPPORTING INFORMATION FOR CHAPTER 4

ATR-FTIR and ^{1}H NMR results for P84 and P84DA

Figure E1 shows the chemical reaction based on which the diacrylation process is performed and (b) shows the ATR-FTIR spectrum of pure P84 and P84DA. The peak at 1725 cm^{-1}, which is not detected for pure P84, is a proof of diacrylation and shows the existance of C=O bond.[311] We can also see a peak at 1635 cm^{-1} which corresponds to C=C bonds that belong to acrylate groups. Other peaks present in both samples are attributed to other bonds like CH_2 (rocking at around 910 cm^{-1}, twisting at around 1281 cm^{-1} and scissor at around 1480 cm^{-1}), CO (stretch at around 924, 1064 and 1140 cm^{-1}).[312]

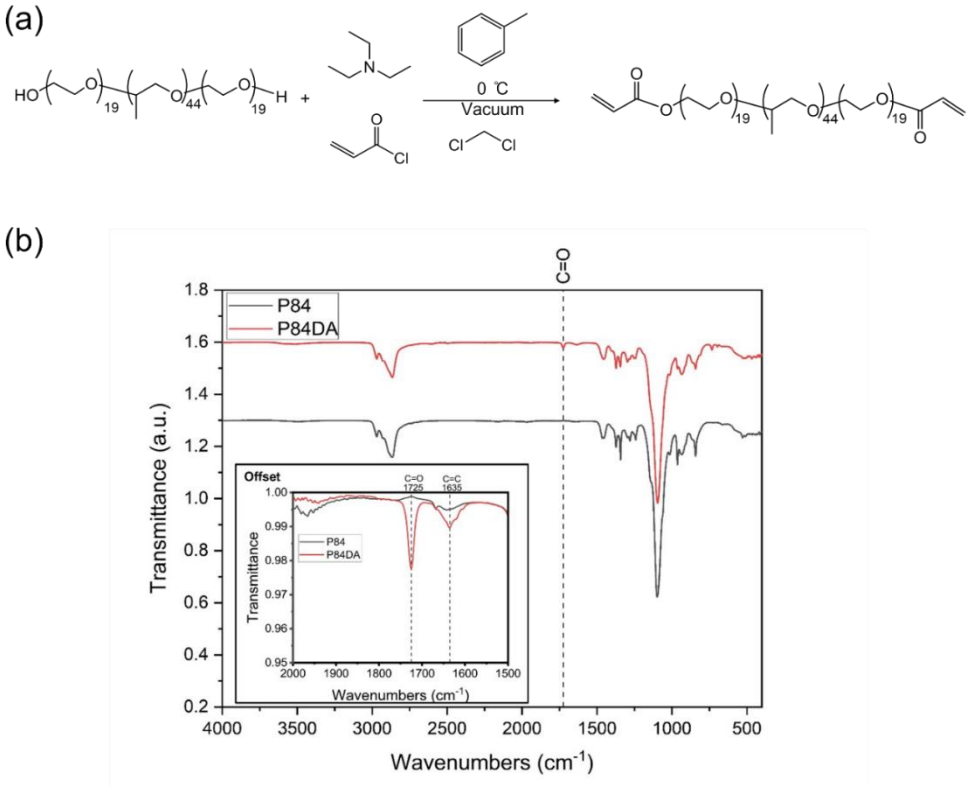

Figure E1. (a) Diacrylation reaction of P84DA with acryloyl chloride in the presence of triethylamine. (b) the ATR-FTIR spectrum of pure P84 and P84DA.

To further characterize the synthesized product, ^{1}H NMR analysis was performed on P84DA in deutrated chloroform as a solvent. Figure E2 shows the acquired result. Degree of diacrylation can be obtained by calculating the number of hydrogens corresponding to acrylate groups.[105] The theoritical number of those hydrogens assuming complete diacrylation should be 6. As can be seen in Figure E2, the total number of hydrogens of acrylate groups normalized to the number of methyl hydrogens of PPO blocks (which should be 129 for P84) is 2.94. This number shows around 50% diacrylation with respect to complete diacrylation with 6 acrylic hydrogens.

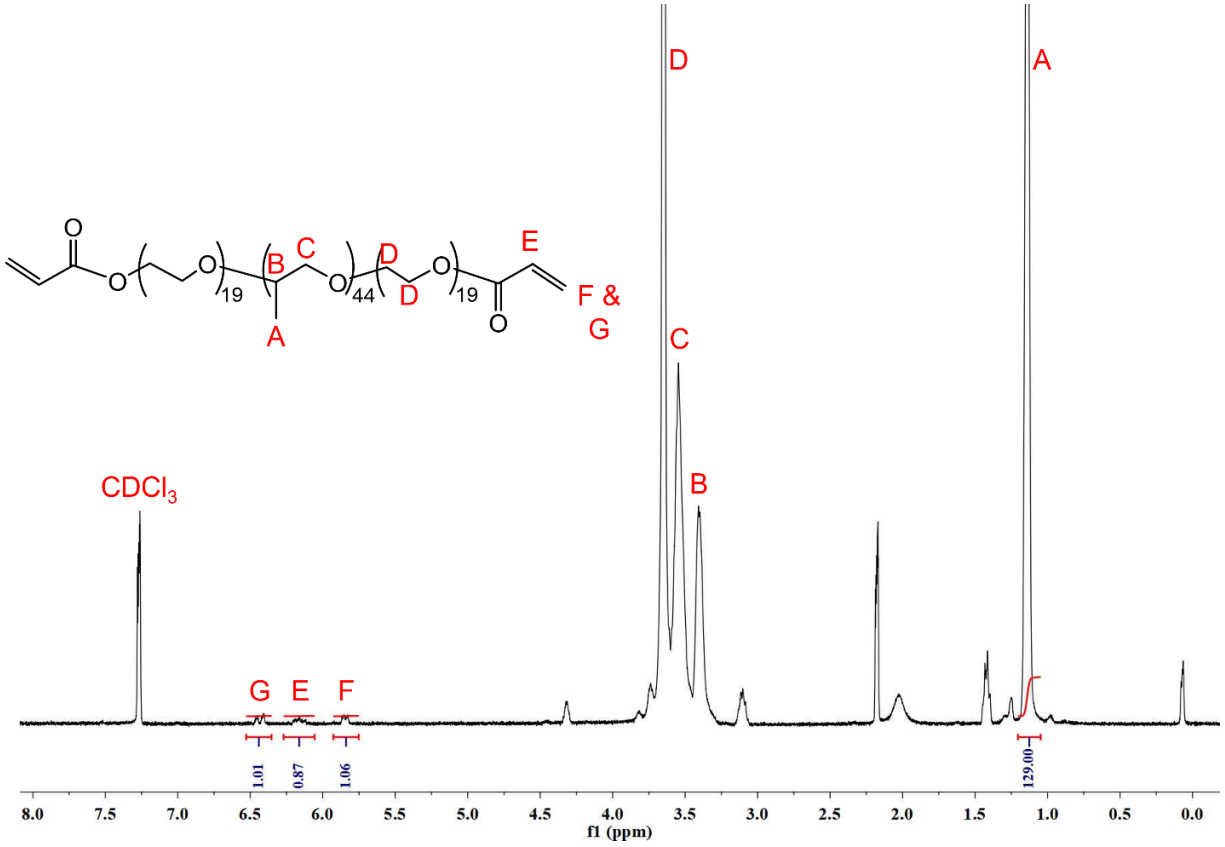

Figure E2. ^{1}H NMR spectrum of P84DA.

Reversible order-disorder structural transition of LLC upon heating and membrane preparation process

As shows in Figure E3, the obtained mesophase, which own H_1 structure (Bragg peaks with ratios of 1:$\sqrt{3}$:2:$\sqrt{7}$), undergoes structural changes upon heating. The structural transition happens as the temperature increases from 25 to 45 °C. Further increemnt of the temperature to 65 °C results in the formation of L_α structure having Bragg peaks with a ratio of 1:2. These strucutral changes are perfectly eversible upon cooling the heated mesophase.

Figure E4 shows how the viscosity of the mesophase changes due to this transition. As can be seen, the viscosity drops significantly as the mesophase is heated to 45 °C. By using such viscosity drop, we were able to use knife coating technique to coat the LLC on a polyester sheet to fabricate the supported polyLLC membrane (see Figure 4-1).

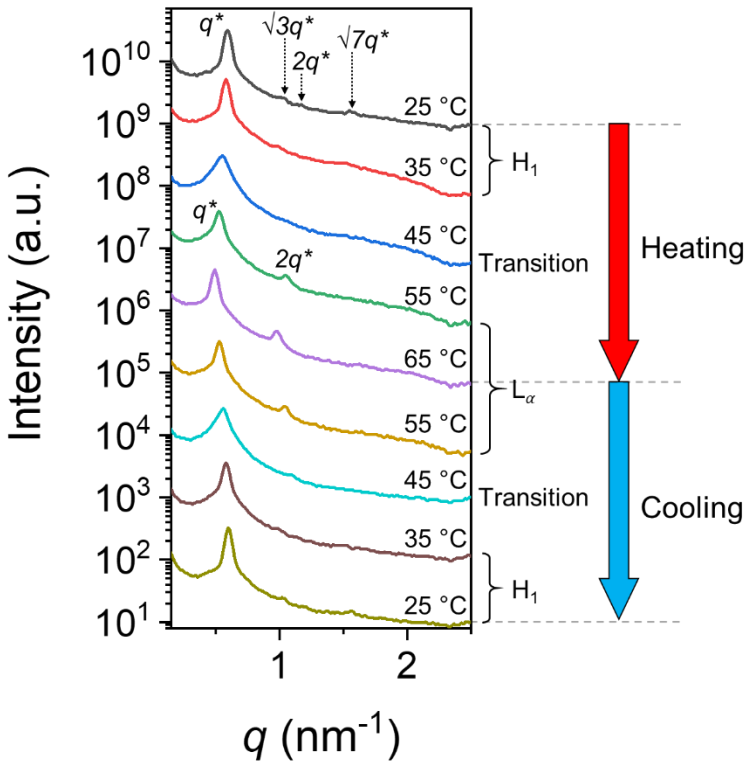

Figure E3. SAXS scattering profiles of the LLC (before polymerization) upon heating and cooling. The topmost data for 25 °C is the start point of the experiment (the plots are vertically shifted for clarity).

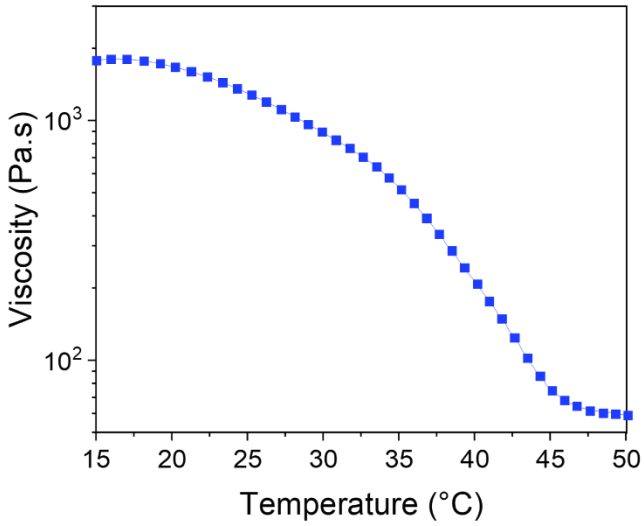

Figure E4. Complex viscosity vs. temperature for the obtained mesophase.

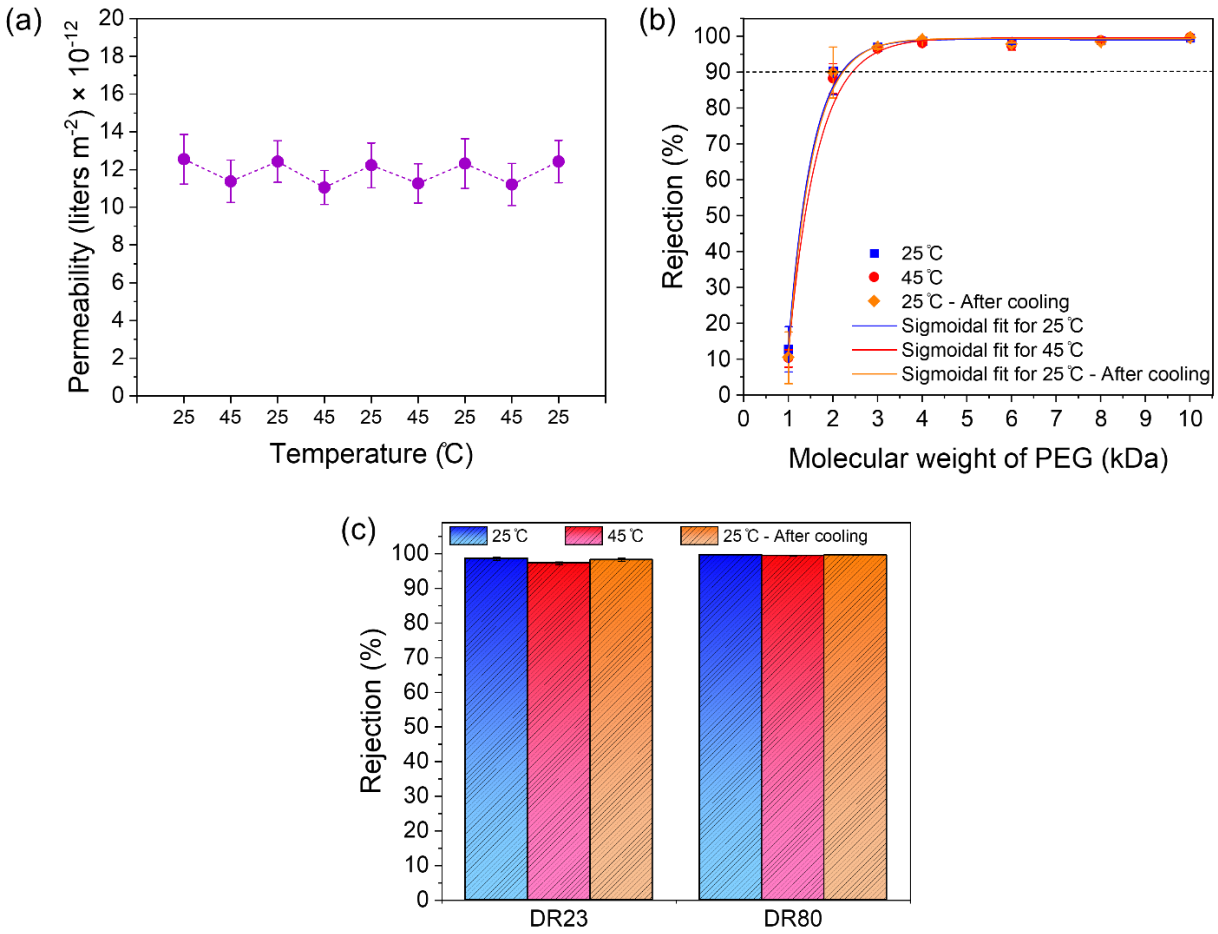

Figure E5. Temperature dependence of (a) permeability, (b) MWCO, and (c) red dyes rejection of a commercial non-thermoresponsive UF membrane.

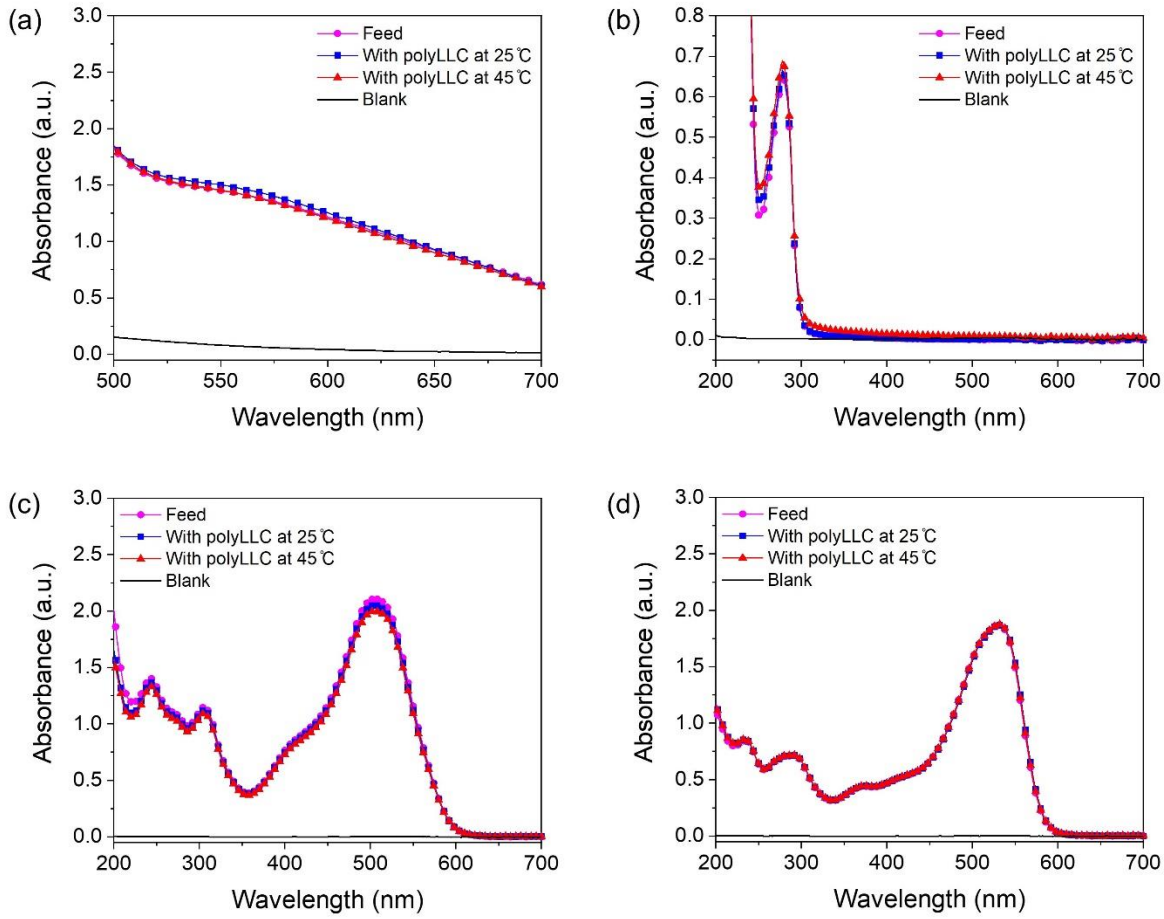

Figure E6. UV-Vis data for aqueous solutions of (a) PEG with 10 kDa molecular weight (containing the potassium iodide/iodine reagent), (b) BSA, (c) DR23, and (d) DR80 before and after contact with polyLLC for 48 hrs at two different temperatures.

APPENDIX F

SUPPORTING INFORMATION FOR CHAPTER 5

^{1}H NMR results for P84DA

P84DA was synthesized using the chemical reaction depicted in Figure F1a. The extent of functionalization was determined using ^{1}HNMR. To perform this analysis, 10 mg of the functionalized polymer was dissolved in 1 ml of deuterated chloroform as the solvent. Figure F1b displays the obtained result. The degree of diacrylation can be calculated by determining the number of hydrogens that correspond to the acrylate groups.[105] The expected number of these hydrogens assuming complete diacrylation is 6. As shown in Figure F1b, the total number of hydrogens in the acrylate groups normalized to the number of methyl hydrogens in the PPO blocks (which should be 129 for P84) is 3.65. This result indicates approximately 60% diacrylation in comparison to complete diacrylation with 6 acrylic hydrogens.

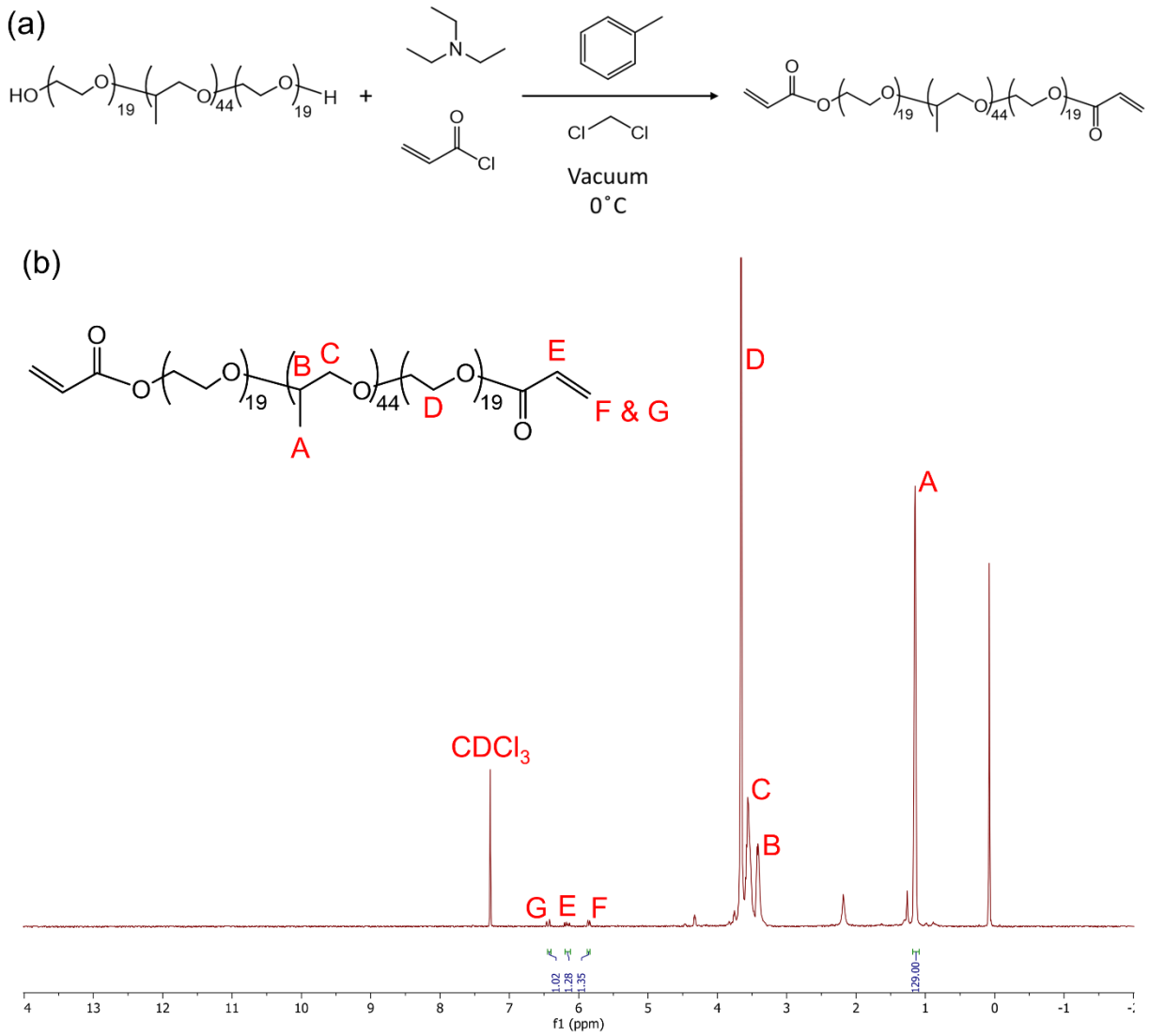

Figure F1. (a) Schematic of the chemical reaction used to synthesize P84DA. (b) 1HNMR results for the synthesized P84DA.

Structural changes of the mesophase under a heating-cooling cycle

The LLC containing AAc shows a change in structure, transitioning from H_1 at 25 °C to L_α at 65 °C. This mesophase transition is completely reversible when the sample is cooled down back to 25 °C.

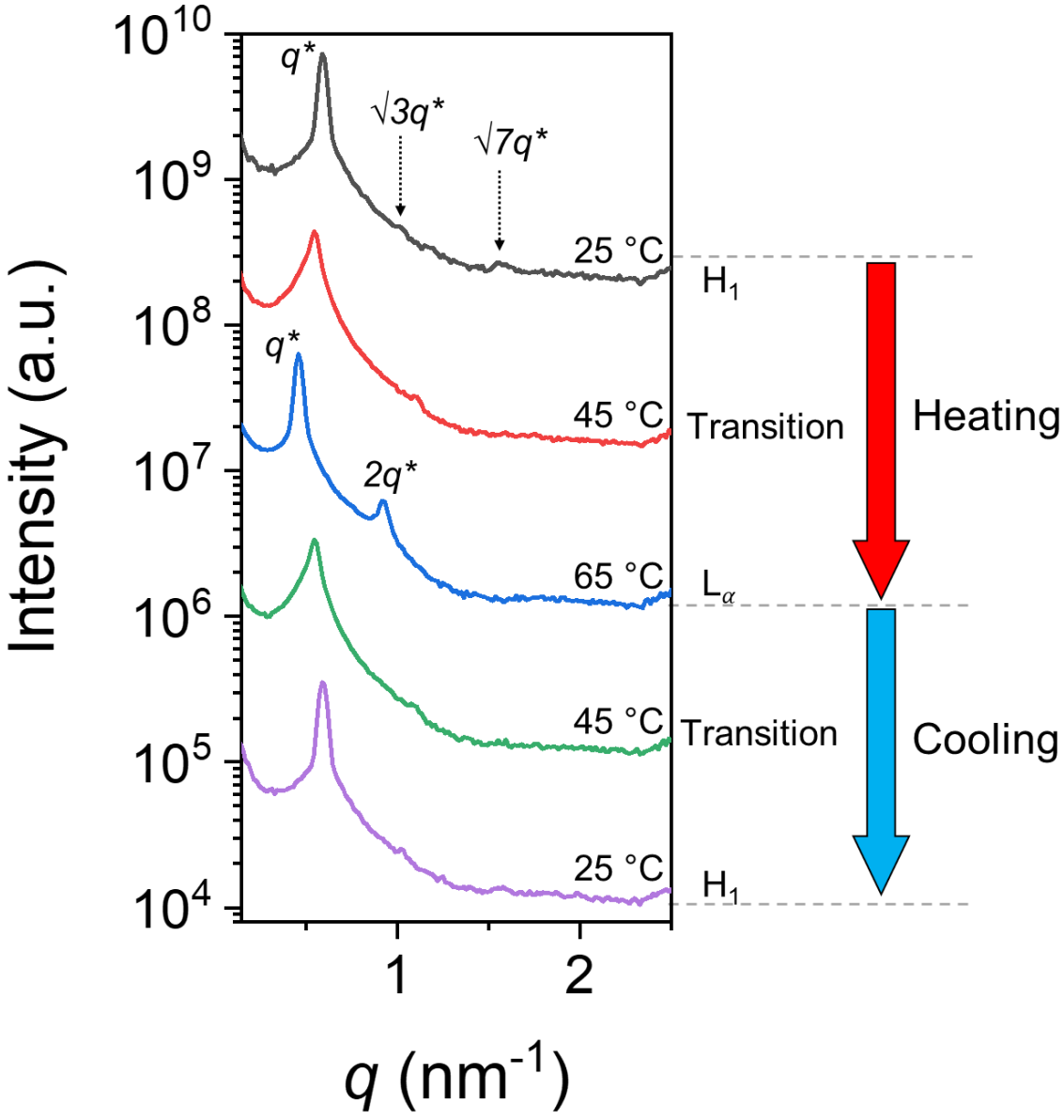

Figure F2. Structural changes of the LLC containing AAc upon heating and cooling. The plots have been vertically shifted to enhance clarity.

The rejection performance of commercially available NF270 membrane for OG at different pH values.

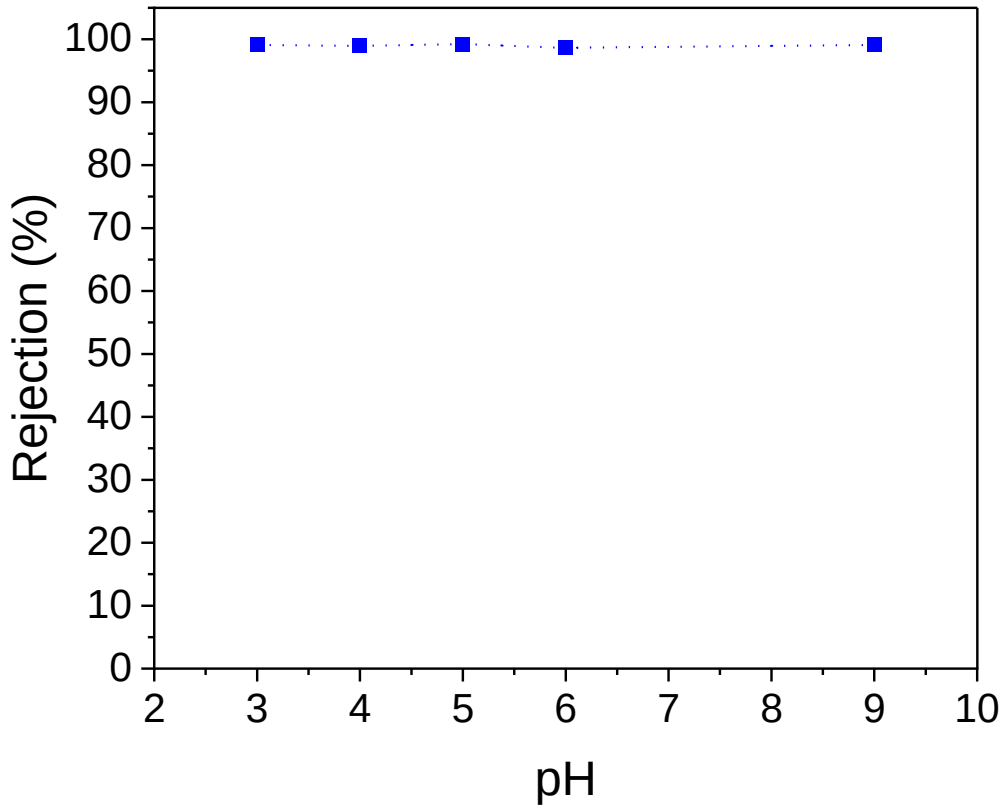

Figure F3. Variation of the rejection rate for OG with pH using commercially available NF270 membrane.

APPENDIX G

MEASUREMENTS UNCERTAINTY CACLULATIONS

From the law of propagation of uncertainties, we utilized the following equation[313] to determine the combined standard uncertainty, $u_c(y)$, in order to assess how the uncertainty of various measurement and controller devices impacted our reported data.

$$u_c(y) = \sqrt{\sigma_y{}^2 + \left[\frac{\Delta y}{\Delta x_1} u(x_1)\right]^2 + \left[\frac{\Delta y}{\Delta x_2} u(x_2)\right]^2 + ... + \left[\frac{\Delta y}{\Delta x_n} u(x_n)\right]^2} \qquad \text{(G-1)}$$

In this equation, y is the measured dependent quantity like membrane flux, σ_y is the uncertainty in the measured y due to the standard deviation, x is an independent variable like pressure and $u(x)$ is the absolute uncertainty of the device measuring or controlling the independent variable.

Pressure regulator, temperature controller, balance and pH meter are the main equipment employed in different characterization experiments. In some experiments, we utilized a UV-Vis spectrophotometer and a conductivity meter. However, since the linear calibration data obtained from these methods displayed an R-squared value of ≥0.999, indicating negligible measurement error, we excluded them from our combined uncertainty calculations.

Table G1 can be generated for the identified independent variables as the source of measurement uncertainties.

Table G1. $u(x)$ value for the equipment employed in different characterization experiments.

Equipment	***u(x)***
Pressure regulator	±0.1 psi
Temperature controller	±0.1 °C
Balance	±0.0001 g
pH meter	±0.001

Table G2 present the values of $\frac{\Delta y}{\Delta x}$ for various measured dependent quantities and independent variables in Chapter 1, as defined from the experimental data.

Table G2. Measured $\frac{\Delta y}{\Delta x}$ for different dependent quantities and independent variables in Chapter 1.

Independent variable	$\frac{\Delta y}{\Delta x}$				
	Hydration Capacity	Flux for polyLLC	Flux for PAN	Permeability for polyLLC	Permeability for PAN
Pressure	No correlation	5.3 liters m^{-2} $hour^{-1}$ psi^{-1}	6.8 liters m^{-2} $hour^{-1}$ psi^{-1}	0.065×10^{-10} liters m^{-2} psi^{-1}	0.12×10^{-10} liters m^{-2} psi^{-1}
Temperature	1.7 mg cm^{-3} $°C^{-1}$	2.8 liters m^{-2} $hour^{-1}$ $°C^{-1}$	1.2 liters m^{-2} $hour^{-1}$ $°C^{-1}$	0.02×10^{-10} liters m^{-2} $°C^{-1}$	0.002×10^{-10} liters m^{-2} $°C^{-1}$
Weight	0.1 mg cm^{-3}	0.001 liters m^{-2} $hour^{-1}$ g^{-1}	0.001 liters m^{-2} $hour^{-1}$ g^{-1}	0.001×10^{-10} liters m^{-2} g^{-1}	0.001×10^{-10} liters m^{-2} g^{-1}

As anticipated, our calculations indicate that the uncertainty of various measurement and controller devices had a negligible impact on our reported data. An example of this can be seen in the data points for polyLLC membrane flux at 25 °C, where the standard deviation of 8 liters m^{-2} h^{-1} corresponds to a combined standard uncertainty of 8.02 liters m^{-2} $hour^{-1}$. Consequently, the calculated combined standard uncertainty closely resembled the calculated standard deviation. In essence, using only the standard deviation is sufficient for reporting the uncertainty of our measurements. This method is also a widely accepted approach to data analysis that is commonly employed by other works in the literature within this field.[31,33,118,125,127]